UNIVERSITY OF SOUTHAMPTON

Faculty of Natural and Environmental Sciences

Ocean and Earth Sciences

Sea-level change, monsoon variability, and eastern Mediterranean climate over the Late Pleistocene

by

Katharine M. Grant

Thesis for the degree of Doctor of Philosophy

March 2013

Declaration Of Authorship

I, Katharine Grant, declare that this thesis entitled 'Sea-level change, monsoon variability, and eastern Mediterranean climate during the Late Pleistocene' and the work presented in it are my own, and have been generated by me as the result of my own original research.

I confirm that:

- This work was done wholly or mainly while in candidature for a research degree at this University;
- Where any part of this thesis has previously been submitted for a degree or any other qualification at this University or any other institution, this has been clearly stated;
- Where I have consulted the published work of others, this is always clearly attributed;
- Where I have quoted from the work of others, the source is always given. With the exception of such quotations, this thesis is entirely my own work;
- I have acknowledged all main sources of help;
- Where the thesis is based on work done by myself jointly with others, I have made clear exactly what was done by others and what I have contributed myself;
- Parts of this work have been published as:

Grant, K.M., Rohling, E.J., Bar-Matthews, Ayalon, A., Bronk Ramsey, C., M., Satow, C., Medina-Elizalde, M., Roberts, A.P. 2012. Rapid coupling between ice volume and polar temperature over the past 150,000 years. Nature 491, 744-747.

Lowe, J. and RESET team members. 2012. Volcanic ash layers illuminate the resilience of Neanderthals and early modern humans to natural hazards. Proceedings of the National Academy of Sciences 109, 13532-13537.

Roberts, A.P., Rohling, E.J., Grant, K.M., Larrasoaña, J.C., Liu, Q. 2011. Atmospheric dust variability from Arabia and China over the last 500,000 years. Quaternary Science Reviews 30, 3537-3541.

Signed: K Grant

Date: 8/3/13

Acknowledgments

First and foremost, my thanks go to Prof. Eelco Rohling for conceiving this project, offering me the opportunity to do a PhD, and excellent support and guidance. I also thank: Mike Bolshaw and Dave Spanner, for their conscientious technical support with stable isotope analyses; Prof. Andrew Roberts, for co-designing the project, critical feedback, and editing zeal; Dr Guy Rothwell, for allowing us to sample the archive halves of core LC21 and to use the BOSCORF facilities; Prof. Christophe Hemleben, for inviting us to the Tübingen core repository and allowing us to sample his Red Sea cores; Dr Mira Bar-Matthews, for providing comprehensive oxygen isotope and U/Th-dating information for Soreq Cave speleothems, including previously unpublished data; and, Dr Chris Satow, for his cheerful assistance with sampling core LC21, scanning and sampling ODP Site 967 cores, and advice on the tephrochronology of core LC21. I am also grateful to the RESET consortium members for their encouragement, enthusiasm, and good company. Finally, special thanks go to the ladies of 'Team Rohling' – Dr Fiona Hibbert, Felicity Williams, and Leah Cliff, for their continuous support and for being such a pleasure to work with.

UNIVERSITY OF SOUTHAMPTON

ABSTRACT

Faculty of Natural and Environmental Sciences
Ocean and Earth Sciences

Doctor of Philosophy

Sea-level change, monsoon variability, and eastern Mediterranean climate over the Late Pleistocene

by Katharine M. Grant

A new, radiometrically constrained chronology is developed for a continuous, high-resolution relative sea-level (RSL) record from the Red Sea that spans the past 500,000 years (500 ka BP). The method is based on indirect correlation of the RSL record with speleothem $\delta^{18}O$ records from Soreq cave, Israel (for the period 0-150 ka BP), and from Sanbao Cave, China (for the period 150-500 ka BP). The new RSL record allows ice-volume (sea-level) phase relationships with key climate-system variables to be examined, without bias from ice-core or orbital timescales. The effects of ice-volume changes on monsoon variability are also examined. In a separate development, the Soreq-synchronised interval of the RSL record is used to produce residual oxygen isotope ($\delta^{18}O$) records for the eastern Mediterranean; these represent regional environmental signals which are unbiased by ice-volume and source-water effects.

Results suggest that, over the last glacial cycle, changes in polar climate and ice-volume were tightly coupled, with centennial-scale response times, and rates of sea-level rise reached at least 1.2 m per century during periods of significant ice-volume reduction. Results also suggest that, at the last five glacial terminations, ice-volume changes generally lagged insolation and atmospheric CO_2 rises by ~2-7 kyr. This supports the Milankovitch theory of ice-age cycles, and disputes suggestions that CO_2-driven feedback processes initiated glacial terminations.

It is shown that ice-volume changes can partly explain East Asian monsoon (EAM) variability. In particular, rapid rates of ice-volume reduction at glacial terminations can account for rapid, millennial-scale variability in summer and winter EAM proxies. This observation is consistent with meltwater pulses into the North Atlantic at terminations leading to a delayed intensification of the summer EAM. Evidence also suggests that changes in different monsoon systems of the northern hemisphere were synchronous during periods of ice-volume minima. Regarding the East African summer monsoon (EAfSM), no systematic phasing is observed between precession minima and EAfSM maxima, and so the common use of a 3-kyr lag to date EAfSM records appears to be too generalised.

The new palaeo-environmental reconstructions for the Mediterranean presented here suggest that local precipitation did not increase substantially during the deposition of sapropels S1, S3 and S4, whereas net moisture availability may have been elevated during the interval of sapropel S5 deposition, and within colder glacial periods of the last glacial cycle. The most climatically variable period of the last glacial cycle in the Mediterranean (~30-60 ka BP) coincides with marine isotope stage (MIS) 3.

Contents

List of Figures

List of Tables

1 Introduction

Palaeo-environmental reconstructions can provide critical insights about climate-system processes. A prime example is the use of high-resolution time-series to reveal *i)* timing relationships between key components of the climate system, and *ii)* rates of change of environmental variables, such as atmospheric CO_2 concentrations and global ice volume. The reliability of inferred climate-system relationships and processes depends on the precision and accuracy of the age-model for the respective time-series, and on the physical and/or (bio-) geochemical understanding behind the proxy data.

Past changes in global ice volume can be approximated using sea-level reconstructions, so the development of continuous, high-resolution sea-level records with excellent age control is vital for palaeoclimate research. The primary aim of this thesis is therefore to develop a new chronology for the Red Sea relative sea-level (RSL) record (Siddall et al., 2003, 2004; Rohling et al., 2009) that is independent of ice-core age models and astronomical timescales (in contrast to previous chronologies for the Red Sea RSL record). Chapters 2 and 3 address this problem.

First, the 0-150 ka BP interval of the RSL record is re-dated by combining tephrochronology, Bayesian age modelling, and a dual correlation between eastern Mediterranean speleothem and planktonic foraminiferal $\delta^{18}O$ records, and between eastern Mediterranean $\delta^{18}O$ and RSL records (Chapter 2). The outcome of this approach is the first independently dated and continuous record of ice-volume variability over the last 150 kyr. This in turn allows phase relationships between changes in ice volume and polar climate (ice core records) to be examined (Chapter 2).

Next, the RSL chronology is improved for the interval 150-500 ka BP using different criteria (Chapter 3). Here, a Red Sea dust record (Roberts et al., 2011) – derived from the same core samples as the RSL record – is correlated to an East Asian summer monsoon proxy record at glacial terminations, and then the RSL and East Asian monsoon proxy records are correlated in between glacial terminations using signal covariance in the frequency band of precession. The resultant sea-level record provides the first radiometric dating of the sea-level/ice-volume signatures of terminations 3-5. Combined with the new 0-150 kyr RSL record, this permits a detailed examination of ice-volume phase relationships over five glacial cycles (Chapter 3).

Chapter 3 also explores the potential role of ice-volume changes in Asian summer and winter monsoon variability; this is facilitated by correlating a grain-size record from the Chinese Loess Plateau (Sun et al., 2006) to the Red Sea dust record after the latter was converted to the new (RSL) chronology.

The timing of monsoon variability is investigated further in Chapter 4, by returning to the eastern Mediterranean region where sapropel-bearing sediments reflect northward migration of the East African summer monsoon (EAfSM) rainbelt during precession minima (=EAfSM maxima). This study takes advantage of the new (eastern) Mediterranean-RSL chronology (Chapter 2) and an eastern Mediterranean sediment record of EAfSM maxima over five precession minima (Chapter 4), to examine timing relationships between EAfSM maxima and *i)* insolation maxima, *ii)* ice-volume changes, and *iii)* variations in proxy records of different monsoon systems.

The new Mediterranean-RSL chronology (Chapter 2) also provides a robust chronological context for climatic reconstructions of the (eastern) Mediterranean and Levant, and the opportunity to deconvolve eastern Mediterranean $\delta^{18}O$ records by removing ice-volume and source-water effects. These are related issues and they are the focus of Chapter 5. Here, 'residual' $\delta^{18}O$ records are calculated and analysed in conjunction with new clay mineralogical data for the eastern Mediterranean, and with a proxy record of local dust fluxes (Larrasoaña et al., 2003) that is adjusted to the new Mediterranean-RSL chronology. This multi-proxy suite of data allows interpretations about relative changes in humidity/aridity in the eastern Mediterranean over the last glacial cycle, which are unbiased by global ice-volume changes or monsoon-related freshwater run-off.

A summary of the key findings of Chapters 2-5 is presented in Chapter 6, followed by a discussion about possible avenues of future research, which will build on the results of the present study.

The chapters are presented either as published articles (Chapter 2) or as draft manuscripts to be submitted for publication in peer-reviewed journals, pending further refinements and discussions with co-authors. References are therefore presented in chapter-specific lists at the end of each chapter, rather than all together at the end of the thesis.

The main body of the thesis is complemented by three published articles (Appendices A-C). These present *i)* a broad overview of present-day and past climatic and hydrological conditions in the Mediterranean and Red Sea regions (Rohling et al., in press; Appendix A).

This provides an environmental context to the present work; *ii)* details of past changes in dust fluxes to the Red Sea (Roberts et al., 2011; Appendix B). This study underlies the hypothesis tested in Chapter 3; and finally *iii)* an example of how palaeoclimatic and archaeological data can be synchronised and subsequently exploited for anthropological research (Lowe et al., 2012; Appendix C).

References

Larrasoaña, J.C., Roberts, A.P., Rohling, E.J., Winklhofer, M., Wehausen, R. 2003. Three million years of monsoon variability over the northern Sahara. Climate Dynamics 21, 689-698.

Lowe, J., Barton, N., Blockley, S., Bronk Ramsey, C., Cullen, V.L., Davies, W., Gamble, C., Grant, K., Hardiman, M., Housley, R., Lane, C.S., Lee, S., Lewis, M., .MacLeod, A., Menzies, M.A., Müller, W., Pollard, M., Price, C., Roberts, A.P., Rohling, E.J., Satow, C., Smith, V.C., Stringer, C., Tomlinson, E.L., White, D., Albert, P.G., Arienzo, I., Barker, G., Borić, D., Carandente, A., Civetta, L., Ferrier, C., Gaudelli, J.L., Karkanas, P., Koumouzelis, M., Müller, U.C., Orsi, G., Pross, J., Rosi, M., Shalamanov-Korobar, L., Sirakov, N., Tzedakis, P.C. 2012. Volcanic ash layers illuminate the resilience of Neanderthals and early modern humans to natural hazards. Proceedings of the National Academy of Sciences, 109, 13532-13537.

Roberts, A.P., Rohling, E.J., Grant, K.M., Larrasoaña, J.C., Liu, Q. 2011. Atmospheric dust variability from Arabia and China over the last 500,000 years. Quaternary Science Reviews 30, 3537-3541.

Rohling, E.J., Grant, K., Bolshaw, M., Roberts, A.P., Siddall, M., Hemleben, Ch., Kucera, M. 2009. Antarctic temperature and global sea level closely coupled over the past five glacial cycles. Nature Geoscience 2, 500-504.

Rohling, E.J., Grant, K., Roberts, A.P., Larrasoaña, J.C. Palaeoclimate variability in the Mediterranean and Red Sea regions during the last 500,000 years; implications for hominin migrations. Current Anthropology (in press).

Siddall, M., Rohling, E.J., Almogi-Labin, A., Hemleben, Ch., Meischner, D., Schmeltzer, I., Smeed, D.A. 2003. Sea-level fluctuations during the last glacial cycle. Nature 423, 853-858.

Siddall, M., Smeed, D.A., Hemleben, Ch., Rohling, E.J., Schmeltzer, I., Peltier, W.R. 2004. Understanding the Red Sea response to sea level. Earth and Planetary Science Letters 225, 421-434.

Sun., Y., Clemens, S.C., An, Z, Yu, Z. 2006. Astronomical timescale and palaeoclimatic implication of stacked 3.6-Myr monsoon records from the Chinese Loess Plateau. Quaternary Science Reviews 25, 33-48.

Chapter 2

Rapid coupling between ice volume and polar temperature over the past 150,000 years

K. M. Grant, E. J. Rohling, M. Bar-Matthews, A. Ayalon, M. Medina-Elizalde, C. Bronk Ramsey, C. Satow, A. P. Roberts

Manuscript published in: Nature 491, 744-747 (2012)

Author affiliations and contributions are listed in the manuscript.

LETTER

doi:10.1038/nature11593

Rapid coupling between ice volume and polar temperature over the past 150,000 years

K. M. Grant[1], E. J. Rohling[1,2], M. Bar-Matthews[3], A. Ayalon[3], M. Medina-Elizalde[1]†, C. Bronk Ramsey[4], C. Satow[5] & A. P. Roberts[2]

Current global warming necessitates a detailed understanding of the relationships between climate and global ice volume. Highly resolved and continuous sea-level records are essential for quantifying ice-volume changes. However, an unbiased study of the timing of past ice-volume changes, relative to polar climate change, has so far been impossible because available sea-level records either were dated by using orbital tuning or ice-core timescales, or were discontinuous in time. Here we present an independent dating of a continuous, high-resolution sea-level record[1,2] in millennial-scale detail throughout the past 150,000 years. We find that the timing of ice-volume fluctuations agrees well with that of variations in Antarctic climate and especially Greenland climate. Amplitudes of ice-volume fluctuations more closely match Antarctic (rather than Greenland) climate changes. Polar climate and ice-volume changes, and their rates of change, are found to covary within centennial response times. Finally, rates of sea-level rise reached at least 1.2 m per century during all major episodes of ice-volume reduction.

During the past few million years, variability in global ice volume (sea level) has been one of the main feedback mechanisms in climate change (see, for example, refs 3, 4). However, detailed assessment of the role of ice volume in climate change is hindered by inadequacies in sea-level records and/or their chronologies. First, dated coral sea-level benchmarks are discontinuous before the last glacial maximum (LGM; ~22,000 years ago). Second, continuous sea-level records have insufficient chronological control; they rely on orbital tuning, correlations with ice-core records, or imperfect transfer of coral datings[1,2,5–7]. Orbital tuning assumes a systematic response between changes in ice volume and Earth's orbital parameters, so that the relationship between insolation forcing and global ice volume cannot be discerned from orbitally tuned records. In addition, the timing of any centennial-scale to millennial-scale fluctuations in ice volume will be poorly constrained in orbitally tuned sea-level records because the shortest orbital frequency is ~19,000 years. Transferring an ice-core chronology to a sea-level record requires an assumption that ice volume always varies in a systematic phase relationship with either Antarctic or Greenland climate, which may not be the case (see, for example, refs 1, 2, 8, 9).

We resolve these issues for the past 150,000 years using a novel approach to provide a detailed chronology to the continuous and highly resolved record of Red Sea relative sea-level (RSL)[2]. We exploit a 'basin isolation' concept, similar to that used for the Red Sea[1,2], in the nearby eastern Mediterranean, where marine sediments can be dated much more accurately. Because the hydrological cycle directly links the $\delta^{18}O$ of eastern Mediterranean surface waters and that of cave speleothems on bordering land masses downwind of this highly evaporative sea[10,11], we can directly relate our new high-resolution planktonic foraminiferal $\delta^{18}O$ record for the surface-dwelling species *Globigerinoides ruber* (white form) in eastern Mediterranean sediment core LC21 ($\delta^{18}O_{ruber}$) to the U–Th-dated Soreq Cave speleothem $\delta^{18}O$ record ($\delta^{18}O_{speleo}$) (Fig. 1; Methods and Supplementary Information).

Previous work demonstrated quantitatively that eastern Mediterranean $\delta^{18}O$ has a strong overprint of sea-level variability[12]; hence, considerable agreement is expected between $\delta^{18}O$ signals for the Red Sea and the eastern Mediterranean (Supplementary Information). Although the more complicated hydrological cycle in the Mediterranean (relative to the Red Sea) means that variations in eastern Mediterranean $\delta^{18}O$ cannot be used to determine the amplitudes of sea-level change precisely, the basin isolation effect imposes sufficient $\delta^{18}O$ signal similarity between the two seas to allow accurate transfer of the superior eastern Mediterranean chronology to the Red Sea record. This is achieved using our new $\delta^{18}O$ record from core LC21 for the subsurface-dwelling planktonic foraminifer *Neogloboquadrina pachyderma* (dextral) ($\delta^{18}O_{pac}$), which is known to minimize surface-water $\delta^{18}O$ overprints (Fig. 1, Methods and Supplementary Information).

Construction of the new RSL chronology involves two stages. First, we build an age model for eastern Mediterranean core LC21 by correlating its $\delta^{18}O_{ruber}$ record with the Soreq Cave $\delta^{18}O_{speleo}$ record over the interval 40–160 kyr BP (Fig. 1a and Supplementary Information). For the interval 0–40 kyr BP, our age model is constrained by 14 radiocarbon datings and two well-documented and independently dated tephra horizons from the Minoan[13] and Campanian Ignimbrite (CI)[14] eruptions. A Bayesian depositional model (constructed using OxCal[15]) comprising the original Soreq Cave chronology, the ^{14}C datings and the chronostratigraphic position of all Soreq–LC21 tie-points (Supplementary Information) then improves the accuracy of the Soreq Cave chronology and ^{14}C datings, and consequently that of core LC21, and rigorously determines the chronological uncertainties of the LC21 tie-points. Next, we transfer the new LC21 age model to the RSL record between 22,000 and 150,000 years ago using the $\delta^{18}O_{pac}$ record (Fig. 1b; Supplementary Information). For the younger interval (0–22,000 years ago), we correlate RSL with a recent sea-level probability curve based on radiometrically dated sea-level benchmarks[16]; this is a more direct correlation target than $\delta^{18}O_{speleo}$ for this interval (Fig. 1b). Our correlations reveal that Last Interglacial (LIG) sea levels peaked before the main (monsoonal) wet phase in the eastern Mediterranean (Fig. 1b). This is stratigraphically corroborated within Red Sea core KL09, in which runoff-related soil biomarkers appear after the LIG highstand signal[17] (Fig. 1b).

Age uncertainties are quantified for all correlations to allow full error propagation into the new RSL chronology. A root-mean-squares estimate at the 95% (2σ) probability level is calculated that fully accounts for errors associated with sample-spacing in the $\delta^{18}O_{speleo}$, $\delta^{18}O_{ruber}$, $\delta^{18}O_{pac}$ and RSL records, as well as the analytical error associated with the Soreq Cave U–Th and LC21 ^{14}C datings, and the 2σ confidence interval of the sea-level probability curve (Supplementary Information). We reinforce this by categorizing our chosen tie-points into three levels of confidence: category 1 is considered the most reliable and within the bounds of sample-spacing, category 2 tie-points may be moved by ±0.5 kyr, and category 3 tie-points are the most

[1]School of Ocean and Earth Science, University of Southampton, National Oceanography Centre, European Way, Southampton SO14 3ZH, UK. [2]Research School of Earth Sciences, The Australian National University, Canberra, ACT 0200, Australia. [3]Geological Survey of Israel, 30 Malchei Israel Street, Jerusalem 95501, Israel. [4]Research Laboratory for Archaeology and the History of Art, Dyson Perrins Building, University of Oxford, South Parks Road, Oxford OX1 3QY, UK. [5]Department of Geography, Queens Building, Royal Holloway University of London, Egham, Surrey TW20 0EX, UK. †Present address: Centro de Investigación Científica de Yucatán, Unidad Ciencias del Agua, Calle 8, No. 39, Mz. 29, S.M. 64 Cancun, Quintana Roo, CP 77500, México.

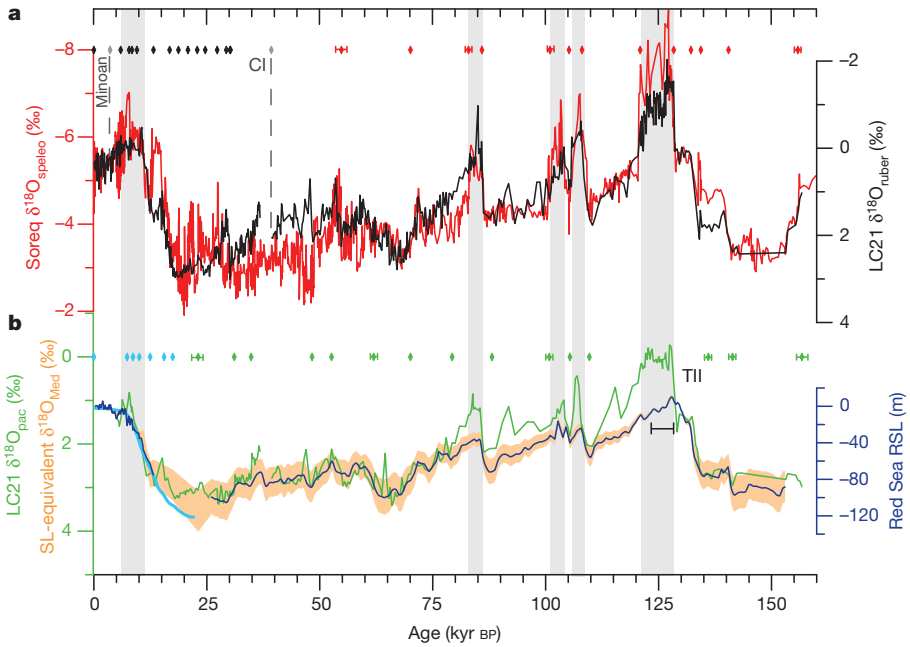

Figure 1 | Correlation of Soreq Cave and eastern Mediterranean (LC21) $\delta^{18}O$ signals and the Red Sea RSL record. **a**, New planktonic foraminiferal (*G. ruber*) $\delta^{18}O_{ruber}$ record from core LC21 (black), Soreq Cave $\delta^{18}O_{speleo}$ record (red) (Supplementary Information) and tie-points (red diamonds) used to correlate the LC21 and Soreq Cave records. Error bars (±0.5 and ±1 kyr) denote more ambiguous tie-points (Supplementary Information). Also indicated are ^{14}C datings (black diamonds), the Minoan and Campanian Ignimbrite (CI) tephra horizons (dashed black lines) and intervals of sapropel deposition (grey rectangles). **b**, Red Sea RSL record[2] (dark blue, 1-kyr moving Gaussian filter) after correlation with the LC21 (*N. pachyderma*) $\delta^{18}O_{pac}$ record (green) and with a highest-probability sea-level curve[16] (light blue). Correlation tie-points (green and light blue diamonds, with error bars as in **a**) and termination II (TII) are indicated. For a Mediterranean $\delta^{18}O$ ($\delta^{18}O_{Med}$) enrichment of 2.5 ± 0.5‰ per 120 m sea-level change[12], RSL was converted into equivalent $\delta^{18}O_{Med}$ values (orange shading). A LIG wet phase in the Red Sea (about 124–128 kyr BP; black bar) is also indicated[17]. RSL is not reliable for about 14–23 kyr BP because of an aplanktonic zone in Red Sea sediments (Supplementary Information).

contentious and may be moved by ±1 kyr (Fig. 1). On the basis of the total error of each RSL tie-point, we interpolate a 2σ age uncertainty for every data point in the RSL record (Supplementary Information). Finally, these age uncertainties are combined with methodological sea-level uncertainties (±12 m at the 2σ level[1]) in a probabilistic assessment of the RSL record (Fig. 2 and Supplementary Information). This reveals that, during the LIG, RSL at Hanish sill (gateway to the Red Sea) stood above 0 m at 126–130 or 120–133 kyr BP (95% confidence limits to the maximum-probability RSL (RSL_{Pmax}) and RSL data points, respectively), and peaked at 127–129 or 126–132 kyr BP (95% confidence limits to RSL_{Pmax} and RSL data points, respectively; Fig. 2). Although the depth of Hanish sill is implicit in the Red Sea sea-level method, the timing and magnitude of LIG sea levels in our RSL record may be expected to differ from eustatic sea level (ESL) as a result of isostatic effects at the sill[18]; our datings are therefore likely to be refined by detailed isostatic modelling of the sill.

We now compare our probabilistic sea-level curve with other key records of sea level and high-latitude climate (Fig. 2). Our new RSL record agrees well—within uncertainties—with coral sea-level benchmarks (Fig. 2b). Discrepancies in Marine Isotope Stages 5e and 5a may relate to uncertainties in coral position or depth habitat, tectonic/isostatic effects among sites, and/or isostatic effects at Hanish sill[18].

In general, our sea-level record agrees well with variability in ice volume suggested by deep-sea benthic foraminiferal $\delta^{18}O$, and with the major (orbital-scale) climate transitions recorded in Greenland and Antarctic ice cores (Fig. 2). Exceptions to this broad coherence are termination I in the benthic foraminiferal $\delta^{18}O$ record[5] of marine core MD95-2042 from the Iberian margin (Fig. 2d), and termination II and the Marine Isotope Stages 4–3 transition in a global benthic $\delta^{18}O$ stack[19] (Fig. 2c). Given that RSL agrees well with all other proxy records over these transitions, we surmise that these offsets are due to orbital tuning, lower sample resolution[19] and potential bias from deep-sea temperature changes[5] and isostatic effects.

Given that the eustatic glacial–interglacial sea-level range is implicitly accounted for in the Red Sea sea-level method, RSL is a good approximation of variations in ESL (ice volume)[1], although it may underestimate ESL variability by as much as 10% (ref. 18). Regarding polar climate variations, the structure and amplitude of Antarctic climate variations agree well with the record of highest-probability ice-volume fluctuations (Fig. 2e). This corroborates previous observations[1,2,5] but, crucially, is more conclusive because our new chronology is entirely independent of ice-core age models. The Antarctic–RSL relationship is most tenuous at about 95–115 kyr BP, at which RSL instead agrees better with Greenland climate fluctuations. Indeed, the timing of ice-volume changes is generally found to be close to that of Greenland climate variability (Fig. 2f). However, higher-amplitude Greenland $\delta^{18}O$ oscillations ('Dansgaard–Oeschger' events[20]) generally exceed concomitant ice-volume variability. In summary, at the maximum probability and 95% confidence levels for RSL, the timing and structure of large-scale sea-level variability reflects a global signature of climate changes recorded in both Antarctic and Greenland ice cores.

Phase relationships between changes in polar climate and ice volume are initially evaluated by lagged correlations between the ice-core data (European Project for Ice Coring in Antarctica (EPICA) Dronning Maud Land (EDML) $\delta^{18}O$ and North Greenland Ice-core Project (NGRIP) $\delta^{18}O$) and RSL (Supplementary Information). We find that ice-volume lags of 100–400 and 200–400 years produce the best correlations with Antarctic and Greenland climate changes, respectively (Fig. 3a, b and Supplementary Information). Rates of change in ice volume and in polar climate correlate most strongly within ±200 years (Fig. 3a, b). Further assessment with cross-spectral analyses of the EDML $\delta^{18}O$, NGRIP $\delta^{18}O$, and RSL records (and their derivatives) confirms that, for suborbital frequencies, peak coherences between Greenland climate and ice volume are associated with minimal phase offsets (±300 years), whereas phase offsets between Antarctic temperature and ice volume are potentially larger (400–700 years;

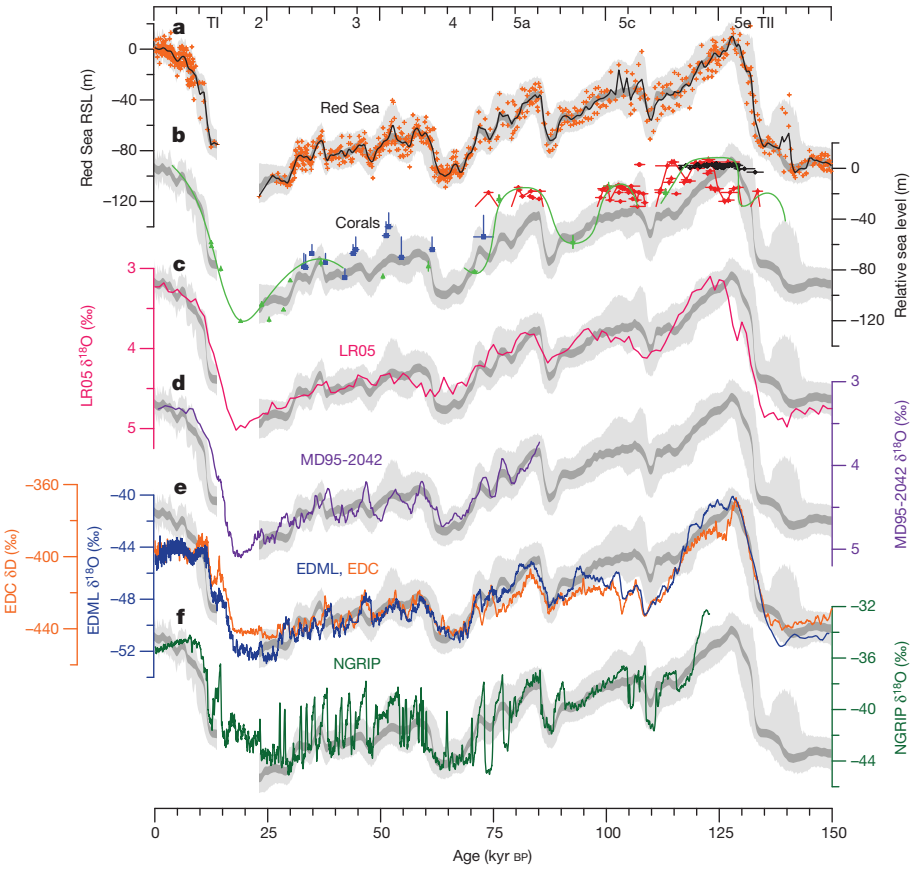

Figure 2 | Comparison of probabilistic assessment of RSL with other sea-level reconstructions and with Antarctic and Greenland climate variability. Confidence intervals of 95% for the RSL data (light grey) and probability maximum (dark grey) (Supplementary Information) are superimposed on: **a**, Red Sea RSL data on our new chronology (orange crosses; black line, 1 kyr moving Gaussian filter); **b**, coral sea-level data ($\pm 2\sigma$) (blue[24], green[25], red[26], black[27]); **c**, a global benthic foraminiferal $\delta^{18}O$ stack[19] (pink); **d**, benthic foraminiferal $\delta^{18}O$ record (five-point running mean) from marine core MD95-2042 (ref. 5) (purple); **e**, $\delta^{18}O$ record (seven-point running mean) from EPICA Dronning Maud Land (EDML)[28] (blue) and δD record (seven-point running mean) from EPICA Dome C (EDC)[29] (orange); and **f**, NGRIP $\delta^{18}O$ record (five-point running mean)[30] (green). The MD95-2042 $\delta^{18}O$ record is plotted here on the Greenland Ice Core Chronology (GICC05 (ref. 31) for 0–60 kyr BP, and on the NGRIP (2004) chronology[30] for 60–85 kyr BP, after synchronizing the co-registered (MD95-2042) planktonic foraminiferal $\delta^{18}O$ record with Greenland $\delta^{18}O$ variations. EDML $\delta^{18}O$ and EDC δD are plotted on the EDML1/EDC3 timescale[32]. NGRIP $\delta^{18}O$ is plotted on the GICC05 timescale for 0–60 kyr BP, and on its original timescale for 60–122 kyr BP (ref. 30). RSL is less reliable for about 14–23 kyr BP because of poor sampling resolution through an aplanktonic interval, and is therefore not shown. Marine Isotope Stages and terminations I and II (TI, TII) are indicated at the top of the figure.

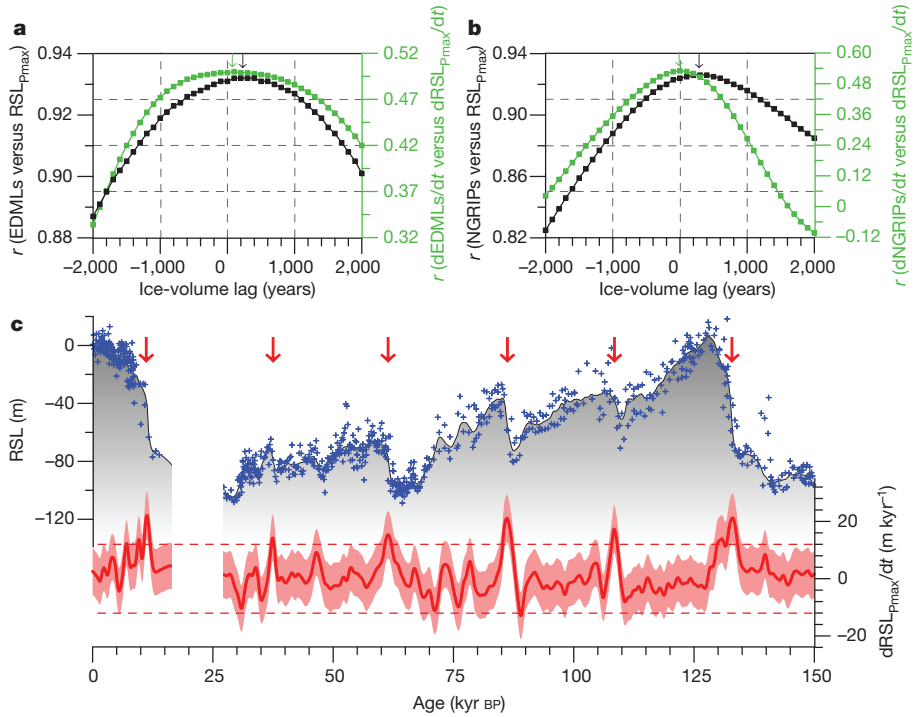

Figure 3 | Lagged correlations of Antarctic and Greenland climate versus ice volume (sea-level), and rates of sea-level change over the last full glacial cycle. **a**, **b**, Regression coefficients (r) (Supplementary Information) are plotted for the highest-probability sea-level curve and the smoothed (s) EDML and NGRIP $\delta^{18}O$ records (RSL_{Pmax}, EDMLs, NGRIPs; black squares, left-hand y axes) and for their first derivatives ($dRSL_{Pmax}/dt$, $dEDMLs/dt$, $dNGRIPs/dt$; green squares; right-hand y axes) for the regressions EDMLs versus RSL_{Pmax} and $dEDMLs/dt$ versus $dRSL_{Pmax}/dt$ (**a**) and NGRIPs versus RSL_{Pmax} and $dNGRIPs/dt$ versus $dRSL_{Pmax}/dt$ (**b**). Negative values of ice-volume lag correspond to changes in ice volume leading changes in polar climate. Optimum correlations are indicated (black and green arrows). **c**, RSL_{Pmax} (grey shading), RSL data (blue crosses) and probability maximum of the first derivative of RSL (red) with 95% confidence interval (pink shading). Rates of sea-level change of +12 and −8 m kyr^{-1} are indicated (dashed lines). Red arrows mark peaks in sea-level rises of more than 12 m kyr^{-1} at 10.9–11.8 kyr BP, 37.4–37.5 kyr BP, 61.2–61.6 kyr BP, 85.5–86.9 kyr BP, 108.1–108.8 kyr BP and 132.1–133.8 kyr BP. Data from the Red Sea aplanktonic interval (about 14–23 kyr BP) are omitted.

Supplementary Information). We infer that Greenland climate closely tracks and/or is directly coupled with ice-volume changes, whereas Antarctic climate variability may lead ice-volume changes by up to 700 years (Supplementary Information).

Our new RSL chronology permits the first robust calculation of rates of relative sea-level change throughout the past 150,000 years (Fig. 3c). This reveals that rates of sea-level rise reached at least 1.2 m per century during all major phases of ice-volume reduction, and were typically up to 0.7 m per century (possibly higher, given the smoothing in our method) when sea-level exceeded 0 m during the LIG (Fig. 3c); the latter is consistent with independent estimates[21,22]. Rates of sea-level lowering rarely exceeded 0.8 m per century. Any differences between rates of change in ESL and RSL at Hanish Sill are likely to be captured within our uncertainties.

We have characterized and dated a continuous record of ice-volume variability throughout the last glacial cycle in a manner that is entirely independent of assumptions about the orbital insolation forcing of climate or about glaciological processes. We have also shown that, on suborbital timescales, polar climate and ice-volume changes were closely coupled in a quasi-direct phase relationship (within centuries). Our analyses hint that Antarctic climate change leads global ice-volume change by several centuries, which is a realistic timescale for ice-sheet adjustments[23]. Greenland climate, however, is found to change virtually simultaneously with ice volume, which may suggest a link of Greenland temperature to ice-volume change in the Northern Hemisphere through albedo feedback.

METHODS SUMMARY

For the Soreq Cave record, we present 440 new U–Th datings that were acquired by multi-collector inductively coupled plasma mass spectrometry at the Geological Survey of Israel (Supplementary Information). Sample ages were corrected for detrital ^{230}Th if ^{230}Th/^{232}Th activity ratios were less than 160; for ^{230}Th/^{232}Th activity ratios of more than 160–200 the correction factor was well within age uncertainties. Typical age uncertainties (2σ) are less than 1 kyr (0–35 kyr BP), less than 1.5 kyr (35–70 kyr BP), less than 2.5 kyr (70–120 kyr BP) and less than 4 kyr (120–160 kyr BP). Dating methods are further described in Supplementary Information. We applied Bayesian age modelling[15] to all U–Th datings ($\pm 2\sigma$), which typically reduced uncertainties to less than 0.5 kyr (0–60 kyr BP), less than 1 kyr (60–90 kyr BP) and less than 2 kyr (90–160 kyr BP) and had only minor impacts on absolute ages (generally less than 250 and less than 750 years for 0–70 and 70–160 kyr BP, respectively).

For the eastern Mediterranean record, continuous u-channel samples from the pristine archive half of core LC21 (35° 40′ N, 26° 35′ E; cruise MD81) were subsampled at 1-cm intervals. Stable isotope analyses of about 15–30 cleaned, similar-sized tests of *G. ruber* (white form) and *N. pachyderma* (dextral) from the greater than 300-μm and 150–300-μm sieved sediment fractions, respectively, were performed at the National Oceanography Centre, Southampton, on a Europa Geo2020 mass spectrometer fitted with an individual acid-bath carbonate preparation line. Standards (NBS-19 and an in-house Carrara marble) were run every 17 samples; external precision is less than 0.06‰.

Received 31 May; accepted 13 September 2012.
Published online 14 November 2012.

1. Siddall, M. *et al.* Sea-level fluctuations during the last glacial cycle. *Nature* **423,** 853–858 (2003).
2. Rohling, E. J. *et al.* Antarctic temperature and global sea level closely coupled over the past five glacial cycles. *Nature Geosci.* **2,** 500–504 (2009).
3. Hansen, J. *et al.* Climate change and trace gases. *Phil. Trans. R. Soc. A* **365,** 1925–1954 (2007).
4. Köhler, P. *et al.* What caused Earth's temperature variations during the last 800,000 years? Data-based evidence on radiative forcing and constraints on climate sensitivity. *Quat. Sci. Rev.* **29,** 129–145 (2010).
5. Shackleton, N. J., Hall, M. A. & Vincent, E. Phase relationships between millennial-scale events 64,000–24,000 years ago. *Paleoceanography* **15,** 565–569 (2000).
6. Waelbroeck, C. *et al.* Sea-level and deep water temperature changes derived from benthic foraminifera isotopic records. *Quat. Sci. Rev.* **21,** 295–305 (2002).
7. Bintanja, R., van de Wal, R. S. W. & Oerlemans, J. Modelled atmospheric temperatures and global sea levels over the past million years. *Nature* **437,** 125–128 (2005).
8. Cuffey, K. M. & Marshall, S. J. Substantial contribution to sea-level rise during the last interglacial from the Greenland ice sheet. *Nature* **404,** 591–594 (2000).
9. Otto-Bliesner, B. L. *et al.* Simulating Arctic climate warmth and icefield retreat in the Last Interglacial. *Science* **311,** 1751–1753 (2006).
10. Bar-Matthews, M., Ayalon, A., Gilmour, M., Matthews, A. & Hawkesworth, C. J. Sea–land oxygen isotopic relationships from planktonic foraminifera and speleothems in the Eastern Mediterranean region and their implication for paleorainfall during interglacial intervals. *Geochim. Cosmochim. Acta* **67,** 3181–3199 (2003).
11. Almogi-Labin, A. *et al.* Climatic variability during the last ~90 ka of the southern and northern Levantine Basin as evident from marine records and speleothems. *Quat. Sci. Rev.* **28,** 2882–2896 (2009).
12. Rohling, E. J. Environmental controls on salinity and δ^{18}O in the Mediterranean. *Paleoceanography* **14,** 706–715 (1999).
13. Manning, S. W. *et al.* Chronology for the Aegean Late Bronze Age 1700–1400 BC. *Science* **312,** 565–569 (2006).
14. De Vivo, B. *et al.* New constraints on the pyroclastic eruptive history of the Campanian volcanic plain (Italy). *Mineral. Petrol.* **73,** 47–65 (2001).
15. Bronk Ramsey, C. Deposition models for chronological records. *Quat. Sci. Rev.* **27,** 42–60 (2008).
16. Stanford, J. D. *et al.* Sea-level probability for the last deglaciation: a statistical analysis of far-field records. *Global Planet. Change* **79,** 193–203 (2011).
17. Trommer, G. *et al.* Sensitivity of Red Sea circulation to sea level and insolation forcing during the last interglacial. *Clim. Past* **7,** 941–955 (2011).
18. Lambeck, K. *et al.* Sea level and shoreline reconstructions for the Red Sea: isostatic and tectonic considerations and implications for hominin migration out of Africa. *Quat. Sci. Rev.* **30,** 3542–3574 (2011).
19. Lisiecki, L. E. & Raymo, M. E. A Plio-Pleistocene stack of 57 globally distributed benthic δ^{18}O records. *Paleoceanography* **20,** PA1003, doi:10.1029/2004PA001071 (2005).
20. Dansgaard, W. *et al.* Evidence for general instability of past climate from a 250-kyr ice-core record. *Nature* **364,** 218–220 (1993).
21. Kopp, R. E., Simons, F. J., Mitrovica, J. X., Maloof, A. C. & Oppenheimer, M. Probabilistic assessment of sea level during the last interglacial stage. *Nature* **462,** 863–868 (2009).
22. Thompson, W. G., Curran, H. A., Wilson, M. A. & White, B. Sea-level oscillations during the last interglacial highstand recorded by Bahamas corals. *Nature Geosci.* **4,** 684–687 (2011).
23. Gregory, J. M., Huybrechts, P. & Raper, S. C. B. Threatened loss of the Greenland ice-sheet. *Nature* **428,** 616 (2004).
24. Chappell, J. Sea level changes forced ice breakouts in the Last Glacial cycle: new results from coral terraces. *Quat. Sci. Rev.* **21,** 1229–1240 (2002).
25. Cutler, K. B. *et al.* Rapid sea-level fall and deep-ocean temperature change since the last interglacial period. *Earth Planet. Sci. Lett.* **206,** 253–271 (2003).
26. Thompson, W. G. & Goldstein, S. L. Open-system coral ages reveal persistent suborbital sea-level cycles. *Science* **308,** 401–404 (2005).
27. Dutton, A. & Lambeck, K. Ice volume and sea level during the last interglacial. *Science* **337,** 216–219 (2012).
28. EPICA Community Members. One-to-one coupling of glacial climate variability in Greenland and Antarctica. *Nature* **444,** 195–198 (2006).
29. Jouzel, J. *et al.* Orbital and millennial Antarctic climate variability over the past 800,000 years. *Science* **317,** 793–797 (2007).
30. North Greenland Ice Core Project Members. High-resolution record of Northern Hemisphere climate extending into the last interglacial period. *Nature* **431,** 147–151 (2004).
31. Svensson, A. *et al.* A 60 000 year Greenland stratigraphic ice core chronology. *Clim. Past* **4,** 47–57 (2008).
32. Parrenin, F. *et al.* The EDC3 chronology for the EPICA Dome C ice core. *Clim. Past* **3,** 485–497 (2007).

Supplementary Information is available in the online version of the paper.

Acknowledgements We thank A. Dutton for comments that improved the manuscript. S. Lee helped with the use of OxCal. This study contributes to UK Natural Environment Research Council (NERC) projects NE/H004424/1, NE/E01531X/1 and NE/I009906/1, to a Royal Society Wolfson Research Merit Award (E.J.R.), and to a 2012 Australian Laureate Fellowship FL120100050 (E.J.R.).

Author Contributions K.M.G. led the study. E.J.R. designed the study, contributed to statistical analyses and co-wrote the paper. M.B.-M. and A.A. developed the Soreq Cave speleothem record. M.M.E. contributed to the interpretations. C.B.R. supported the Bayesian age modelling. C.S. contributed the LC21 tephrachronology. A.P.R. contributed to the discussion of results and manuscript refinement.

Author Information Reprints and permissions information is available at www.nature.com/reprints. The authors declare no competing financial interests. Readers are welcome to comment on the online version of the paper. Correspondence and requests for materials should be addressed to K.M.G. (kxg@noc.soton.ac.uk).

doi:10.1038/nature11593

This supplement is divided into eight sections that explain our approach and calculations in more detail. In section 1 we introduce the conceptual background to our new method of dating the most recent composite Red Sea sea-level record (RSL; Rohling et al., 2009). In section 2 we detail new U/Th datings for the Soreq Cave speleothem $\delta^{18}O$ record. In sections 3 and 4 we describe how we developed an age model for eastern Mediterranean (eMed) core LC21 using Bayesian modelling to further improve our chronostratigraphy. Sections 5 and 6 focus on our new chronology for the RSL record, detailing the LC21-RSL correlation and error propagation. In section 7 we specify the parameters of our probabilistic assessment of the complete RSL dataset. Finally, in section 8 we explain the methods of our lagged correlations and phase analyses between polar climate records and RSL. Online Supplementary Data accompanies this supplement.

1. Conceptual background

We exploit two key properties of the Mediterranean Sea:

1) Eastern Mediterranean (eMed) surface waters are the moisture source for Levantine precipitation, and
2) Mediterranean seawater $\delta^{18}O$ ("$\delta^{18}O_{Med}$") is highly sensitive to sea-level change at the Strait of Gibraltar.

Importantly, these properties (detailed below) relate to well understood, quantifiable physical processes, so our approach has a robust, justifiable basis.

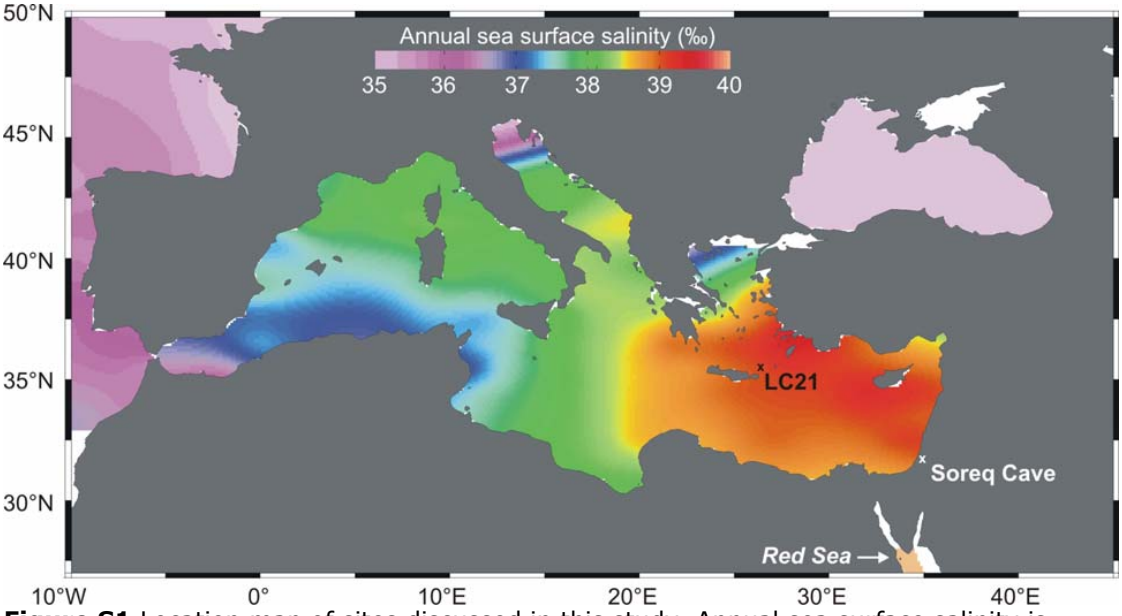

Figure S1 Location map of sites discussed in this study. Annual sea surface salinity is reconstructed from the World Ocean Atlas 2009 dataset using the Ocean Data View (Schlitzer, 2011) software. Areas lacking data are indicated in white.

Studies of terrestrial carbonates (speleothems and snail shells) from the Levant have shown that eMed surface waters are, and have been in the past, the source of moisture precipitating over the Levant (Goodfriend, 1991; Matthews et al., 2000; Bar-Matthews et al., 2000, 2003; McGarry et al., 2004; Almogi-Labin et al., 2009). Therefore, changes in the $\delta^{18}O$ of eMed speleothems are intrinsically linked via a "source water" effect to the $\delta^{18}O$ of eMed surface waters, and hence to

the $\delta^{18}O$ of surface-dwelling planktonic foraminifera. High-resolution speleothem $\delta^{18}O$ records from the Levant (e.g., Bar-Matthews et al., 2003; Gopher et al., 2010; Vaks et al., 2010) have excellent (U-series) age control. Surprisingly, however, there are no continuous, high-resolution records of eMed surface water $\delta^{18}O$ that extend back to the last interglacial (LIG) or further, to complement these speleothem records.

The highly evaporative and semi-enclosed Mediterranean basin is isolated from the open ocean by the narrow and shallow Strait of Gibraltar (284 m) (Fig. S1). These properties cause a "glacial concentration" effect on $\delta^{18}O_{Med}$ similar to that in the Red Sea, albeit to a less extreme extent (Rohling 1994, 1999) (Fig. S2). For example, the glacial-interglacial $\delta^{18}O$ contrast in the open ocean and in the Mediterranean and Red Seas is approximately 1.0, 2.5 and 5.5 ‰, respectively (Schrag et al., 1996; Rohling, 1999; Siddall et al., 2004). As a result, changes in global ice volume/sea-level are reflected in the $\delta^{18}O$ composition of Mediterranean foraminifera in an amplified manner relative to global seawater $\delta^{18}O$, especially in the easternmost sector of the basin where most evaporation occurs (Rohling, 1994, 1999).

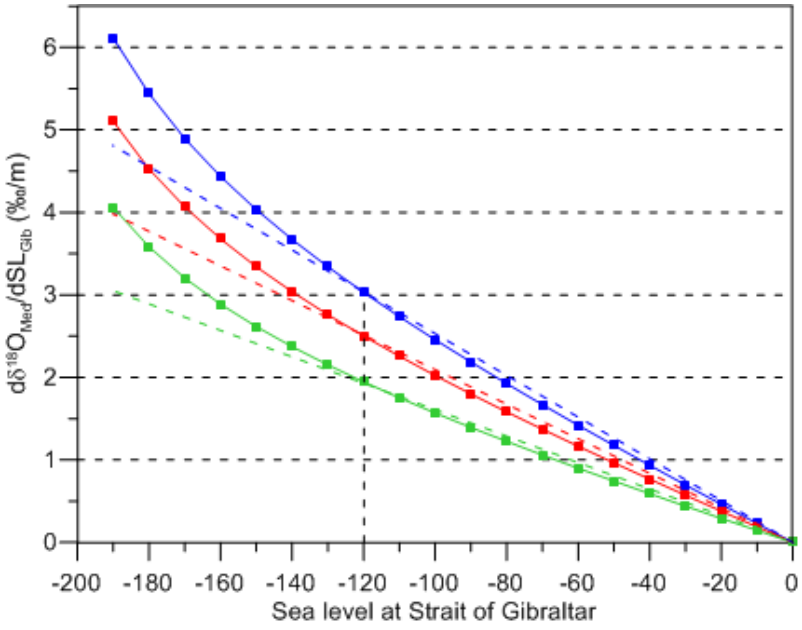

Figure S2 Sea-level sensitivity of Mediterranean $\delta^{18}O$. Changes in Mediterranean seawater $\delta^{18}O$ as a function of varying sea level at the Strait of Gibraltar ($d\delta^{18}O_{Med}/dSL_{Gib}$) are calculated for a relative humidity of 0.65 (blue), 0.70 (red) and 0.75 (green) (see Rohling (1999) for full details of model). For a sea-level change of 120 m (i.e., similar to the glacial-interglacial sea-level change), the relationship is closely approximated by a linear fit (coloured dashed lines) and a $\delta^{18}O_{Med}$ enrichment of 2.5 ± 0.5‰.

We have generated two high-resolution planktonic foraminiferal $\delta^{18}O$ records from a single set of samples from eMed core LC21 using: (1) the surface-dwelling species *Globigerinoides ruber* (white) ("$\delta^{18}O_{ruber}$"), and (2) the deeper-dwelling species *Neogloboquadrina pachyderma* (dextral) ("$\delta^{18}O_{pac}$"), which is commonly found at the base of the euphotic zone near the Deep Chlorophyll Maximum (Pujol and Vergnaud-Grazzini, 1995; Rohling et al., 2004). Core LC21 lies in the 'pool' of highest eMed salinities (Fig. S1) that is the evaporative region of greatest moisture supply to Levantine precipitation. We first, therefore, take advantage of the new $\delta^{18}O_{ruber}$ record, the Soreq Cave $\delta^{18}O$ speleothem record ("$\delta^{18}O_{speleo}$") (Supplementary Data), and the fact that the speleothem source-water derives from eMed surface waters, to transfer the speleothem U-series chronology from Soreq Cave to core LC21.

Next, we exploit the fact that there is a strong sea-level control on both eMed and Red Sea $\delta^{18}O$, to transfer the Soreq-synchronised LC21 chronology to the Red Sea RSL record. This is achieved by correlating RSL with $\delta^{18}O_{pac}$ (Section 4). Because *N. pachyderma* is not associated with surface water masses, any local changes in surface water $\delta^{18}O$ caused by evaporation, precipitation, temperature variations and riverine run-off have minimal effects on its shell $\delta^{18}O$

composition (Rohling et al., 2004), hence the glacial (sea-level) concentration effect will predominantly determine variations in $\delta^{18}O_{pac}$.

Given that the eustatic glacial-interglacial sea-level range is implicitly accounted for in the Red Sea sea-level method, RSL is a good approximation of eustatic sea-level (ESL) variations (Siddall et al., 2003). In this way, we produce the first continuous, high-resolution record of ESL/ice-volume changes over the last full glacial cycle with a detailed radiometric chronology, which is entirely independent of orbital tuning or ice-core timescales.

2. Soreq Cave speleothem U/Th dating

Soreq Cave is located ~60 km inland east of the Mediterranean Sea and 400 m above sea level. Numerous studies of speleothems and rainwater collected from Soreq Cave provide a thorough understanding of past and present speleothem isotopic signatures (e.g., Bar-Matthews et al., 1997, 2000, 2003; Ayalon et al., 1998; Kaufman et al., 1998; Affek et al., 2008). Most of these studies used speleothem datings based on thermal ionisation mass spectrometry (TIMS). The published Soreq Cave $\delta^{18}O$ record has now been updated based on 440 new (previously unpublished) U/Th ages acquired by multi-collector inductively coupled plasma mass spectrometry (MC-ICP-MS) (Supplementary Data). Paired MC-ICP-MS and TIMS datings strongly agree (Fig. S3a), and the new MC-ICP-MS datings substantially increase the dating density of the Soreq Cave age model (Fig. S3b; Supplementary Data). Results from the two approaches are strongly coherent (Fig. S3b), and would therefore produce virtually identical age models for the Soreq Cave $\delta^{18}O$ record, whether used separately or combined.

Speleothems from various locations within Soreq Cave were sampled according to standard procedures (Bar-Matthews et al., 1997). For dating purposes, 0.2-0.5 g of calcite powder was drilled along the speleothem growth axis using 0.8-4.0 mm diameter drill bits. All samples were totally dissolved, with a combination of 7 M HNO_3 and HF, and equilibrated with a mixed $^{229}Th/^{236}U$ spike that was calibrated with gravimetric standards (following Henderson et al., 2001). Both spiked isotopes supplied by Harwell are isotopically clean (^{229}Th>99.99%; ^{236}U=99.97%). Samples were loaded onto minicolumns containing 2 ml of Bio-Rad AG 1X8 200-400 mesh resin. U was eluted by 1 M HBr and Th with 6 M HCl. U and Th solutions were evaporated to dryness and the residues dissolved in 2 ml and 5 ml of 0.1 MHNO_3, respectively.

U/Th dating was performed using a Nu Instruments Ltd (UK) multi-collector inductively coupled plasma mass spectrometer (MC-ICP-MS) equipped with 12 Faraday cups and 3 ion counters. Each sample was introduced to the MC-ICP-MS through an Aridus® micro-concentric desolvating nebuliser sample introducing system. The instrumental mass bias was corrected (using an exponential equation) by measuring the $^{235}U/^{238}U$ ratio and correcting with the natural $^{235}U/^{238}U$ ratio (137.88). Calibration of ion counters relative to Faraday cups was performed using several cycles of measurement with different collector configurations in each particular analysis. Isotope ratios are given as activity ratios with 2σ uncertainties (Supplementary Data). Uncertainties are propagated from the in-run precision errors (0.4% at 2σ), weighing errors and uncertainties in spike concentrations and isotopic compositions. ^{230}Th and ^{234}U half lives are taken from Cheng et al. (2000). Uncertainties in the half lives of the U-series isotopes are not included in the error propagation.

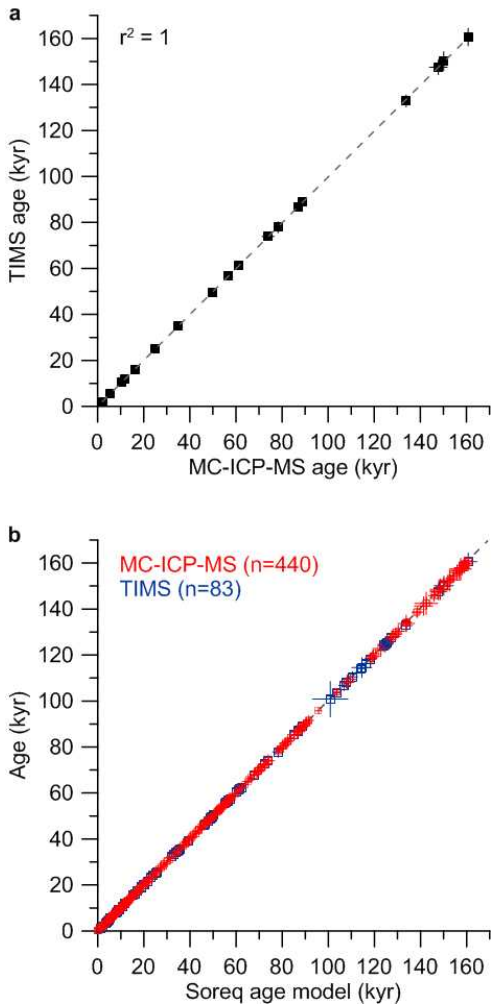

Figure S3 Comparison of MC-ICP-MS and TIMS datings. **a**, Paired MC-ICP-MS and TIMS datings (±2σ) with linear correlation (dashed line, r^2=1). **b**, All MC-ICP-MS (red) and TIMS (blue) datings (±2σ) compared to the Soreq age model (Supplementary Data, sheet 2, column A). All datings follow a linear fit (dashed line).

The U-Th method assumes that all ^{230}Th present in the calcite speleothem is formed *in situ* by radioactive decay of uranium that co-precipitated with the calcite. However, this component is often accompanied by detrital material such as clays, oxides and hydroxides (e.g., Richards and Dorale, 2003; Kaufman et al., 1998). For correction, a ^{232}Th/^{238}U atomic ratio of 1.8±0.25 in the detrital components was used; this value was measured using an isochron method for Soreq Cave speleothems (Kaufman et al., 1998).

3. Age model for core LC21

For the interval 0-40 ka BP, the LC21 age model is constrained by five previously generated radiocarbon datings (Casford et al., 2007), 9 new radiocarbon datings (Table S1), and conclusive identification of two well-dated tephra horizons (the Minoan and the Campanian Ignimbrite, CI, tephra layers) (Fig. S4). New ^{14}C datings (this study) were performed at the University of Oxford Radiocarbon Accelerator Unit on clean, hand-picked planktonic foraminiferal tests with no evidence of pyritization or overgrowth (see Bronk Ramsey et al. (2002) for details of the chemical pretreatment, target preparation and AMS measurement). Calibration of ^{14}C datings into calendar years requires a reservoir age correction, which is a combination of the averaged whole ocean reservoir age (405 yrs) and a local correction ("ΔR"). For Mediterranean marine calcite, ΔR is commonly taken to be 58±85 yrs (Reimer and McCormac, 2002) or 149±30 yrs (Facorellis et al., 1998) depending on whether dated samples were extracted from non-sapropel or sapropel horizons, respectively. A higher ΔR value for

periods of sapropel deposition reflects decreased rates of Mediterranean intermediate- and deep-water ventilation associated with such intervals. Three of our ^{14}C-dated samples were picked from a sapropel, so we use a ΔR value of 149±30 yrs to calibrate these samples and a ΔR value of 58±85 yrs for all other samples (Table S1). All datings (including those of Casford et al. (2007) were calibrated with OxCal (Bronk Ramsey, 2008) using the Marine09 radiocarbon calibration curve. The accuracy of our calibrated ^{14}C datings is further improved by combining sample age and depth information in a Bayesian deposition model (Section 4).

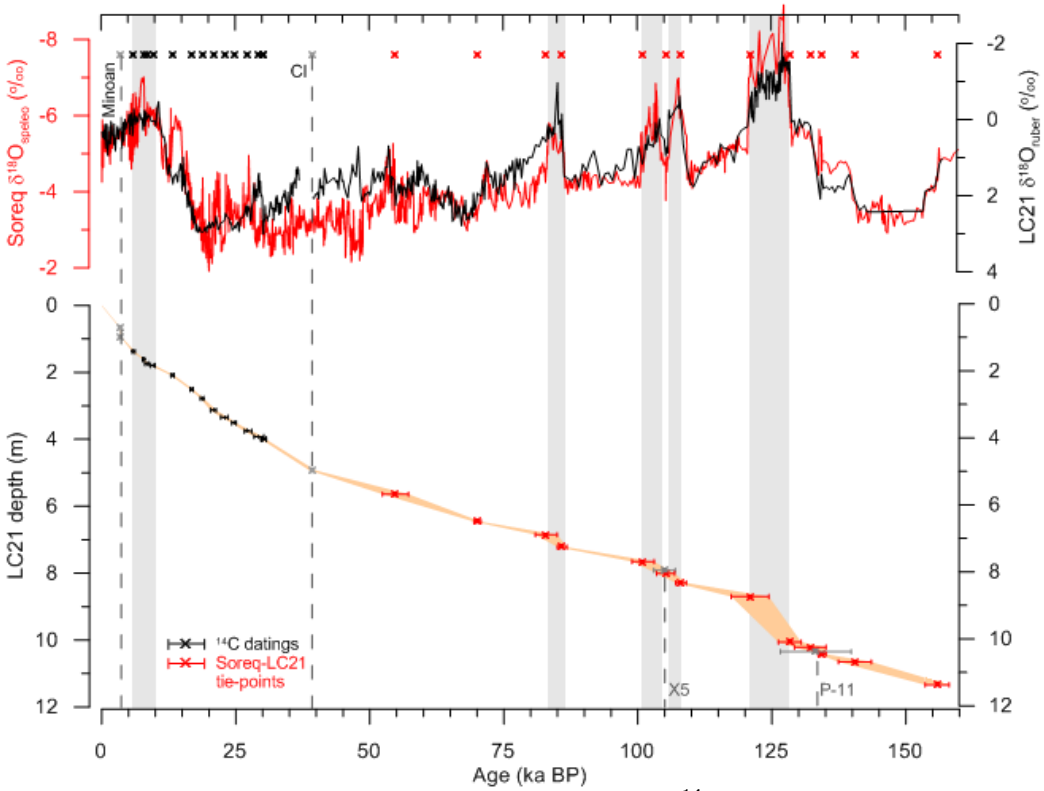

Figure S4 Construction of the LC21 age model. LC21 ^{14}C datings (black crosses) and correlation of the LC21 $\delta^{18}O_{ruber}$ (black) and Soreq Cave $\delta^{18}O_{speleo}$ (red) records, with OxCal-modelled correlation tie-points (red crosses). The Minoan, Campanian Ignimbrite (CI), X5 and P-11 tephra horizons (grey crosses and dashed lines) and intervals of sapropel deposition (grey rectangles) are also indicated. Superimposed on the LC21 age-depth model (orange fill) are the error margins of the ^{14}C datings, Soreq-LC21 tie-points and tephra horizons (black, red and grey error bars (2σ), respectively).

For the interval 40-150 ka BP, we used Analyseries (Paillard, 1996) to graphically correlate the $\delta^{18}O_{ruber}$ and $\delta^{18}O_{speleo}$ records (Fig. S4). As mentioned above, there is a direct physical process linking the $\delta^{18}O$ of calcite precipitated in eMed surface waters and in Levantine caves. It follows that there will be a signal common to both $\delta^{18}O_{ruber}$ and $\delta^{18}O_{speleo}$ on which any local $\delta^{18}O$ variations are superimposed. On long (orbital) timescales, eMed surface waters are periodically affected by intense freshening, and thus $\delta^{18}O$ depletion, caused by flooding of the Nile and North African wadi systems as a result of intensification and northward penetration of the African monsoon during precession minima (Rohling et al., 2002, 2004; Larrasoaña et al., 2003). These $\delta^{18}O$ depletions, together with sea level-controlled variations in $\delta^{18}O_{Med}$, are clearly evidenced by the good general agreement between $\delta^{18}O_{ruber}$ and $\delta^{18}O_{speleo}$. We therefore only correlate these major transitions in $\delta^{18}O_{ruber}$ and $\delta^{18}O_{speleo}$. In this way we transfer the U-series speleothem chronology to core LC21.

Our Soreq-LC21 correlation is validated by identification of two further tephra horizons at 7.915 m and 10.345 m in core LC21. These correlate with the X5 and P-11 tephras that have been dated at 105 ±2 ka BP (Kraml, 1997) and, indirectly, at 132.3 ±5.7 to 133.5 ±6.2 ka BP (Mahood and Hildreth, 1986), respectively (Fig. S4). Next, we applied a Bayesian deposition model using the OxCal programme (Bronk Ramsey, 2008), to derive a best-case chronology for LC21 with well-defined uncertainties.

4. OxCal Bayesian models

The chronostratigraphy of a sediment core is, in effect, a series of probability functions, and information of a probabilistic nature can be mathematically combined using the Bayes Theorem. OxCal achieves this using the Markov Chain Monte Carlo (MCMC) sampling method (Gilks et al., 1996) and Bayesian algorithms to create "*posterior*" probability densities for each point in a sedimentary sequence. Specifically, OxCal builds a "*prior*" model from information about the deposition of the sequence and the actual dates. Here we use the "Sequence" and "Poisson" OxCal models. The simple Sequence model allows wide variations in sedimentation rate and makes minimal *a priori* assumptions, assuming only that there are no age reversals in the sedimentary sequence. The Sequence model is also applicable when coherent depth information is lacking, as is the case for the Soreq Cave composite speleothem record. The Poisson model includes depth information and is therefore more appropriate for the LC21 datings. Previous studies have demonstrated that the Sequence and Poisson models can significantly improve the precision of an age model whilst retaining accuracy (Bronk Ramsey 2000; Blockley et al., 2007).

Our prior models consist of dates and uncertainties in the form of a normal (Gaussian) probability distribution (the "*likelihood*"), with an uncertainty σ about the mean μ. The dating information is from Soreq Cave (Supplementary Data), LC21 (Table S1) and from the Minoan (Manning et al., 2006) and CI (De Vivo et al., 2001) tephra horizons). The Soreq-LC21 tie-points were inserted into the OxCal Sequence model as a blank age and uncertainty at the relevant chronostratigraphic level obtained from the correlation, in order to determine a posterior probability density distribution for each tie-point.

OxCal assesses the statistical robustness of a model run by calculating an "Agreement Index" (AI), which is determined by the area of overlap between the probability density distributions of the *prior* (unmodelled) data and the posteriors. The higher the AI, the better the agreement, and the acceptance threshold for a posterior density is an AI >60% (Bronk Ramsey, 2008). In both of our models, overall agreement between the priors and the posteriors is high (AI >99% for most [97%] of the dates in the Sequence model; AI >87% for all dates in the Poisson model), which implies that our modelled ages and uncertainties are statistically robust. The final Soreq Cave chronology is accurate to within ±500 years for most of the dates (72%), and has a maximum uncertainty of ±2686 years. Only 3% of the dates have an uncertainty >1500 years.

The modelled ^{14}C dates and tephra ages were then used to establish the LC21 chronology (by linear interpolation) for the interval 0-40 ka BP. After rescaling the $\delta^{18}O_{speleo}$ record using the modelled U/Th dates, the $\delta^{18}O_{rub}$ and $\delta^{18}O_{speleo}$ records were re-synchronised for the interval 40-150 ka BP (see main-text Fig. 1a). Finally, the completed LC21 age model was used to date the $\delta^{18}O_{pac}$ record, and we were then ready to tune RSL to $\delta^{18}O_{pac}$ (see below).

5. New chronology for RSL

Our new chronology for the Red Sea sea-level record (RSL) is a product of two synchronisations: most of the record (22-150 ka BP) was tuned to the LC21 $\delta^{18}O_{pac}$ record,

whereas the last deglacial interval (0-22 ka BP) was correlated with the global sea-level probability curve of Stanford et al. (2011) (see main text and main-text Fig. 1b). We emphasise again that correlation of the RSL and $\delta^{18}O_{pac}$ records is justified on the basis of a sound, quantitative understanding of the common process (sea-level change) that causes first-order similarity between the records (Fig. S2 and main-text Fig. S1b).

To tune RSL to $\delta^{18}O_{pac}$ we limit our ties to clearly identifiable transitions common to both records, and minimise the number of ties (n=15) required for a good synchronisation (main-text Fig. 1). It is common practice, when graphically correlating records, to anchor them at the mid-point of corresponding transitions, rather than using peaks or troughs in the records. We follow this approach, but make one exception for the tie-point at the base of termination II (main-text Fig. 1). We chose this position (at 136 ka) because an unambiguous tie-point is lacking over the transition due to the different step-wise structures of the two records; the records are much more similar at the base of the transition which means that we can more confidently assign a tie-point here. We also avoid placing tie-points within the time intervals of sapropel deposition in core LC21. It is well known that periods of sapropel formation were associated with significant hydrological changes in the eMed, hence it is likely that $\delta^{18}O_{pac}$ does not solely reflect changes in sea level at these times (Rohling et al., 2004).

Tuning RSL over the last deglacial interval (0-22 ka BP) was straightforward owing to the smooth structure of the (target) probabilistic sea-level curve (main-text Fig. 1). The most contentious issue was where to anchor the base of this section of the RSL record, which lacks structure from 14 to 22 ka BP due to an aplanktonic zone in Red Sea sediments. The consequently increased uncertainty associated with the tie-points at 12.45, 15.55 and 17.45 ka BP is considered in our full propagation of age errors (section 6 below).

Next, we converted RSL (on its new chronology) into $\delta^{18}O_{Med}$-equivalent values using a scaling of 2.5±0.5 ‰ per 120 m sea-level change (main-text Fig. 1). This exercise demonstrates that for most of the last glacial cycle, $\delta^{18}O_{pac}$ varies within the uncertainties of a theoretical $\delta^{18}O_{Med}$-equivalent RSL curve, thus providing further evidence that lower frequency variations in $\delta^{18}O_{pac}$ correspond to the timing of sea-level change at the Strait of Gibraltar. In MIS 5a, 5c and 5e there are distinct intervals of $\delta^{18}O_{pac}$ 'overshoots', which largely coincide with deposition of sapropels S3, S4 and S5. This is to be expected and does not invalidate our tuning or approach because no tie-points were placed within these intervals (see above).

6. Propagation of RSL age uncertainties

We now rigorously determine the chronological uncertainties in our new RSL record. This involves propagating all uncertainties (a-k) from the three correlations (i-iii) as summarised below.

i) From the Soreq-LC21 correlation:
   a) radiometric dating error of Soreq Cave speleothems, LC21 planktonic foraminifera, and the Minoan and CI tephras,
   b) sample spacing in the Soreq $\delta^{18}O_{speleo}$ record,
   c) sample spacing in the LC21 $\delta^{18}O_{ruber}$ record, and
   d) extra uncertainty allowance for more ambiguous (category 2 and 3) tie-points.

ii) From the LC21-RSL correlation:
   e) total error carried over from the Soreq-LC21 correlation (i above),
   f) sample spacing in the RSL record (for the interval 22-150 ka BP),
   g) sample spacing in the $\delta^{18}O_{pac}$ record, and
   h) extra uncertainty allowance for category 2 and 3 tie-points.

iii) From the deglacial-RSL correlation:

j) methodological uncertainty in the Stanford et al. (2011) probabilistic sea-level curve, and
k) sample spacing in the RSL record (for the interval 0-22 ka BP).

These uncertainties are determined as follows: (a) is derived from our OxCal Sequence model; (b), (c), (f), (g) and (k) relate to the age difference between tie-points and nearest neighbouring samples in the $\delta^{18}O_{speleo}$, $\delta^{18}O_{ruber,}$ RSL and $\delta^{18}O_{pac}$ records, respectively. For (c), depth differences in core LC21 were converted into an equivalent age uncertainty; (e) is deduced by interpolation after combining uncertainties a-d (see below); (j) is taken from Stanford et al. (2011); (d) and (h) are imposed uncertainties and may be ±0.5 or ±1 kyr for category 2 and 3 tie-points, respectively (see main text, main-text Fig. 1, and Table S2).

We combined these uncertainties in a mean squared estimate (MSE) at the 95% probability level for the Soreq-LC21 correlation ("MSE_i"), the LC21-RSL correlation ("MSE_{ii}"), and the deglacial-RSL correlation ("MSE_{iii}"), as defined by:

$$MSE_i = \sqrt{\{a^2 + b^2 + (c+d)^2\}},$$
$$MSE_{ii} = \sqrt{\{e^2 + (f+g+h)^2\}}, \text{ and}$$
$$MSE_{iii} = \sqrt{\{j^2 + k^2\}}.$$

First, we calculated the total uncertainty for every Soreq-LC21 tie-point (MSE_i; red crosses and bars in Fig. S5). Next, we interpolated between successive lower and upper error margins of the Soreq-LC21 tie-points in order to produce a continuous error margin for the entire LC21 age-depth model (orange envelope in Fig. S5). We then determined the position of the LC21-RSL tie-points within the LC21 age-depth model, as well as their uncertainties (e) associated with the Soreq-LC21 correlation (green crosses and bars in Fig. S5). This involved converting the age of every LC21-RSL tie-point into an equivalent LC21 depth, and then linearly interpolating between each LC21-RSL tie-point and the error margins of its neighbouring Soreq-LC21 tie-points. We could now calculate MSE_{ii} (Table S2).

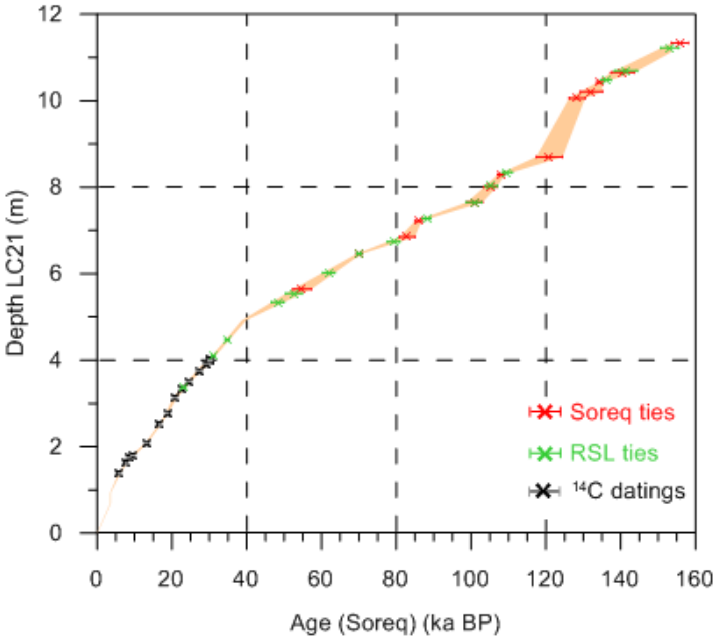

Figure S5 Interpolation of uncertainties for RSL. LC21 age-depth model (orange fill) with tie-points and 2σ uncertainties for the Soreq-LC21 (red crosses and bars) and LC21-RSL (green crosses and bars) correlations. LC21 ^{14}C datings are also shown (black crosses and 2σ error bars).

Determining MSE_{iii} required no imposed uncertainties for sample spacing because our RSL record and the Stanford et al. (2011) probabilistic sea-level curve both follow the same broad

trend, without any ambiguous peaks/troughs with respect to potential correlation points (Table S2). Finally, linear interpolation between the total LC21-RSL and deglacial-RSL tie-point uncertainties (MSE_{ii} and MSE_{iii}) produced a chronological uncertainty for every datapoint in the full RSL record. The latter is needed before we can produce a probabilistic analysis of the sea-level curve for the last full glacial cycle (see below).

7. Probabilistic analysis of Red Sea sea-level record

In order to determine confidence limits to RSL that fully account for the combined uncertainties in both age and sea-level reconstruction (main-text Fig. 2), we have defined normal distributions around each datapoint, based on the mean datapoint values and their standard deviations in both the age and sea-level directions (where the standard deviation for each point in the sea-level reconstruction method is ±6 m; Siddall et al., 2003, 2004). These probability intervals account for all of the combined uncertainties in both age and sea-level values and represent "worst case" propagation scenarios, given that no correlation was considered between any of the uncertainties. We then made N=1000 new records using independent random perturbations of all points within their probability distributions. This gives a 'sample' of 1000 RSL 'realisations' per equally spaced time step of 125 years (close to the average time resolution of the original data). For each 'sample', we determine the 95% confidence limit (from percentile counts) and the RSL value of the probability maximum ("$RSL_{P\text{-}max}$"); the latter provides the 'best fit' RSL curve from the Red Sea data. The record of $RSL_{P\text{-}max}$ from the 1000 realisations per time step has been smoothed with a moving 500-year Gaussian filter to remove spurious jumps, and is determined with a precision of ±7 m (95%).

The 95% confidence limits from the 1000 RSL realisations provide insight into the tolerance to scatter of any new sea-level data (with their own uncertainties) relative to the Red Sea sea-level record presented here. If new data consistently fall outside the limits, they may need to be subjected to a detailed outlier analysis, whereas if they fall inside the limits, they may be considered coherent with the Red Sea sea-level information.

For each individual RSL realisation, we also calculated the rates of change. This was achieved after smoothing each realisation with a 500-year moving Gaussian filter in order to remove sample-to-sample noise that would produce spurious rate jumps. We determined, per time step, the 95% confidence limit and the probability maximum of the rates of change ("$dRSL_{P\text{-}max}/dt$"). Based on 1000 realisations, we find that $dRSL_{P\text{-}max}/dt$ has a precision of ±8 m/kyr, at the 95% confidence level (main-text Fig. 3c).

8. Lagged correlations and phase analyses of ice-core records and RSL

We further investigate the relationship between changes in polar climate and global ice volume. We use $\delta^{18}O$ records from the European Project for Ice Coring in Antarctica (EPICA) Dronning Maud Land (EDML) (EPICA, 2006) and from the North Greenland Ice-core Project (NGRIP) (North Greenland Ice Core Project Members, 2004) as approximations of polar climate variations because they are the best-dated and most highly resolved ice-core climate records for the last glacial cycle. The RSL record closely approximates eustatic sea level (Siddall et al., 2003), and hence global ice-volume change.

First we regressed the ice-core records against RSL for intervals of both sea-level rise and fall. Our aim here is to establish whether the polar climate: ice-volume relationship varies between these intervals. We smoothed the RSL record with a 1 kyr moving Gaussian filter at 100 year age-steps ("RSLs") in order to remove sample-to-sample "noise" and reveal meaningful trends, and interpolated the EDML and NGRIP $\delta^{18}O$ records to the same 100 year age-steps. This

exercise demonstrates that the polar climate: sea-level relationship shows no significant hysteresis (Fig. S6), and means that we can investigate phase offsets throughout the entire records using lagged correlation and cross-spectral analyses (see below).

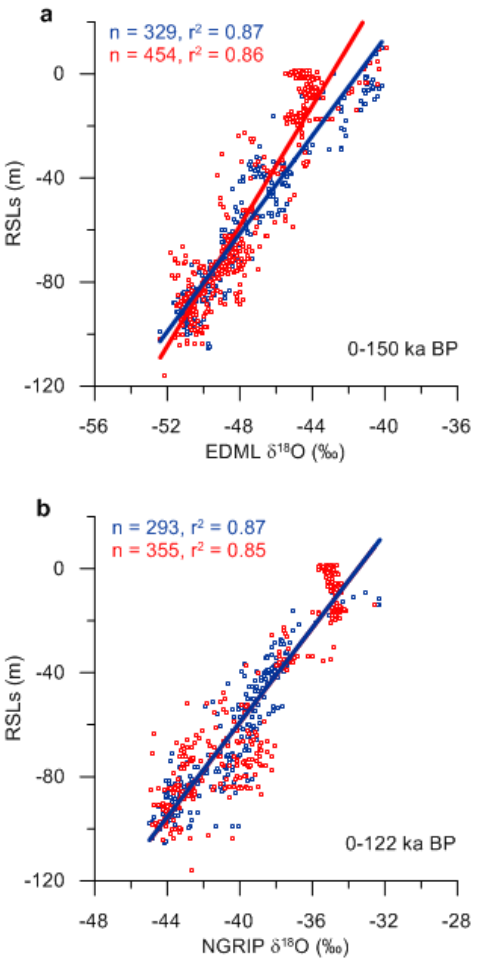

Figure S6 Regression plots of Antarctic and Greenland temperature versus the smoothed Red Sea sea-level record (RSLs). Optimum linear correlations and their coefficients (r^2) are given for datapoints (n) corresponding to intervals of rising (red) and falling (blue) sea level. **a**, EDML $\delta^{18}O$ against RSLs for the interval 0-150 ka BP. **b**, NGRIP $\delta^{18}O$ against RSLs for the interval 0-122 ka BP.

We applied the same Gaussian smoothing to the ice-core records (EDMLs, NGRIPs) in order to calculate their first derivatives (dEDMLs/dt, dNGRIPs/dt), and then performed a series of lagged correlations (0 to ±2000 years) at 100 yr intervals on: 1) EDMLs vs. RSL_{pmax}, 2) NGRIPs vs. RSL_{pmax}, 3) dEDMLs/dt vs. $dRSL_{pmax}/dt$, and 4) dNGRIPs/dt vs. $dRSL_{pmax}/dt$ (main-text Fig. 3a,b). This straightforward exercise allows us to see which phase offsets produce the best correlation between polar climate and ice volume, and between their rates of change; the absolute values of the correlation coefficients are therefore of secondary importance here.

We find optimum correlations when changes in ice volume (sea-level) lag changes in Antarctic and Greenland climate by 100-400 and 200-400 years, respectively (main-text Fig. 3a,b), which suggests that changes in ice volume are equally in phase with changes in both Antarctic and Greenland climate. The strongest correlation between rates of change in RSL and in Antarctic and Greenland climate is achieved with a 100-year and zero lag, respectively (main-text Fig. 3a,b). Taken together, these striking results suggest that a comparatively short (centennial-scale) response time characterises the polar climate-ice volume relationship. This finding requires further scrutiny, given its potentially far-reaching consequences in the context of current global warming trends. For that purpose, we take a more quantitative approach by performing Blackman-Tukey cross-spectral analyses (using the Analyseries software; Paillard, 1996) on the full EDML $\delta^{18}O$, NGRIP $\delta^{18}O$, and RSL records, as well as on RSLs and RSL_{pmax}, for the time

intervals 0-150 and 30-80 ka BP (Table S3). First we removed all frequencies less than 0.03 (this includes all obliquity and eccentricity-related frequencies) using a notch filter with bandwidth of 0.03 (= 33 kyr periodicity); the time series are not sufficiently long for meaningful spectral analyses of these orbital cycles. We therefore focus on sub-orbital and, to a lesser extent, precessional frequencies (our studied time interval contains six precession cycles, which is an inadequate number for a robust phase analysis).

We observe high coherence between changes in polar climate and ice volume at precessional and sub-precessional periodicities, with zero to multi-centennial response times (Table S4). Consistent results for the different RSL records and time intervals validate the precision of these analyses. Changes in Greenland climate and ice volume are tightly coupled at the 4.5 and ~9.6 kyr periodicities (zero lag) and are closely coupled at the 6.4 and precession periodicities (100-300 years ice-volume lead). At sub-precessional periodicities, rates of change in Greenland climate and in ice volume are also closely coupled (100-300 year ice-volume lead).

We observe larger phase offsets between ice-volume variability and Antarctic climate changes (rather than those of Greenland). Changes in ice volume lead Antarctic climate variability at the precession periodicity (by 400 years) and lag it at the half-precession and 6.8 kyr periodicities (by 600-700 years). A similar sign and magnitude of phase offset is observed between rates of change in ice volume and in Antarctic climate at the precession and half-precession periodicities.

The results of the phase analyses for the NGRIP record clearly uphold the results of our lagged correlations (main-text Fig. 3), and imply that ice-volume and Greenland temperature variability are tightly coupled. With respect to the phase relationship between Antarctic climate and ice volume variability, lagged correlations suggest a closer coupling than that indicated by cross-spectral phase analyses. However, given that there is a less distinct 'optimum' in the EPICA-RSL lagged correlations, and that uncertainty margins of the phase offsets may reach ±400 years, we conclude that the results of the two approaches are not incompatible and are dependent on the different frequencies of variability in the records.

Our regression and cross-spectral analyses demonstrate that changes in polar climate and ice volume are coupled, and that response times may be relatively rapid (centennial-scale). This type of phase analysis is possible for the first time because our new chronology has excellent centennial-multi-centennial age control, and because it is entirely independent of orbital tuning and ice-core age models.

References

Affek, H.P., Bar-Matthews, M., Ayalon, A., Matthews, A., Eiler, J.M. 2008. Glacial/interglacial temperature variations in Soreq Cave speleothems as recorded by 'clumped isotope' thermometry. Geochimica et Cosmochimica Acta 72, 5351-5360.

Almogi-Labin, A., Bar-Matthews, M., Shriki, D., Kolosovsky, E., Paterne, M., Schilman, B., Ayalon, A., Aizenshtat, Z., Matthews, A. 2009. Climatic variability during the last ~90 ka of the southern and northern Levantine Basin as evident from marine records and speleothems. Quaternary Science Reviews 28, 2882-2896.

Ayalon, A., Bar-Matthews, M., Sass, E. 1998. Rainfall-recharge relationships within a karstic terrain in the Eastern Mediterranean semi-arid region, Israel: $\delta^{18}O$ and δD characteristics. Journal of Hydrology 207, 18-31.

Bar-Matthews, M., Ayalon, A., Kaufman, 1997. A. Late Quaternary paleoclimate in the Eastern Mediterranean region from stable isotope analysis of speleothems at Soreq Cave, Israel. Quaternary Research 47, 155-168.

Bar-Matthews, M., M., Ayalon, A., Kaufman, A. 2000. Timing and hydrological conditions of sapropel events in the Eastern Mediterranean, as evident from speleothems, Soreq cave, Israel. Chemical Geology 169, 145-156.

Bar-Matthews, M., Ayalon, A., Gilmour, M., Matthews, A., Hawkesworth, C.J. 2003. Sea–land oxygen isotopic relationships from planktonic foraminifera and speleothems in the Eastern Mediterranean region and their implication for paleorainfall during interglacial intervals. Geochimica et Cosmochimica Acta 67, 3181-3199.

Bronk Ramsey, C. 2000. Comment on the use of Bayesian statistics for ^{14}C dates of chronologically ordered samples: a critical analysis. Radiocarbon 42, 199-202.

Bronk Ramsey, C., Higham, T.F.G., Owen, D.C., Pike, A.W.G., Hedges, R.E.M. 2002. Radiocarbon dates from the Oxford AMS system: Archaeometry Datelist 31. Archaeometry 44, Supplement 1, 1-150.

Bronk Ramsey, C. 2008. Deposition models for chronological records. Quaternary Science Reviews 27, 42-60.

Blockley, S.P.E., Blaauw, M., Bronk Ramsey, C., van der Plicht, J. 2007. Building and testing age models for radiocarbon dates in Lateglacial and Early Holocene sediments. Quaternary Science Reviews 26, 1915-1926.

Casford, J.S.L., Abu-Zied, R., Rohling, E.J., Cooke, S., Fontanier, Ch., Leng, M., Millard, A., Thomson, J. 2007. A stratigraphically controlled multi-proxy chronostratigraphy for the eastern Mediterranean. Paleoceanography 22, PA4215, doi:10.1029/2007PA001422.

Cheng, H., Edwards, R.L., Hoff, J., Gallup, C.D., Richards, D.A., Asmerom, Y. 2000. The half-lives of uranium-234 and thorium-230. Chemical Geology 169, 17-33.

Cleveland, W.S., Devlin, S.J. 1988. Locally-weighted regression: an approach to regression analysis by local fitting. Journal of the American Statistical Association 83, 596-610.

De Vivo, B., Rolandi, G., Gans, P.B., Calvert, A., Bohrson, W.A., Spera, F.J., Belkin, H.E. 2001. New constraints on the pyroclastic eruptive history of the Campanian volcanic plain (Italy). Mineralogy and Petrology 73, 47-65.

EPICA Community Members 2006. One-to-one coupling of glacial climate variability in Greenland and Antarctica. Nature 444, 195-198.

Facorellis, Y., Maniatis, Y., Kromer, B. 1998. Apparent ^{14}C ages of marine mollusk shells from a Greek island: calculation of the marine reservoir effect in the Aegean Sea. Radiocarbon 40, 963-973.

Gilks, W., Richardson, S., Spiegelhalter, D. (Eds.) 1996. Markov Chain Monte Carlo in Practice. Chapman & Hall, London.

Goodfriend, G.A. 1991. Holocene trends in ^{18}O in land snail shells from the Negev Desert and their implications for changes in rainfall source areas. Quaternary Research 35, 417-426.

Gopher, A., Ayalon, A., Bar-Matthews, M., Barkai, R., Frumkin, A., Karkanas, P., Shahack-Gross, R. 2010. The chronology of the late Lower Paleolithic in the Levant based on U-Th ages of speleothems from Qesem Cave, Israel. Quaternary Geochronology 5, 644-656.

Henderson, G.M., Slowey, N.C., Fleisher, M.Q. 2001. U-Th dating of carbonate platform and slope sediments. Geochimica et Cosmochimica Acta 65, 2757-2770.

Kaufman, A., Wasserburg, G.J., Porcelli, D., Bar-Matthews, M., Ayalon, A., Halicz, L. 1998. U-Th isotope systematics from the Soreq cave, Israel and climatic correlations. Earth and Planetary Science Letters 156, 141-155.

Kraml, M. 1997. Laser-$^{40}Ar/^{39}Ar$ Datierungen an distalen marinen Tephren des jung-quartären mediterranen Vulkanismus (Ionisches Meer, METEOR-Fahrt 25/4). Doctoral Thesis, Universität Freiburg im Breisgau, 216pp.

Larrasoaña, J.C., Roberts, A.P., Rohling, E.J., Winklhofer, M., Wehausen, R. 2003. Three million years of monsoon variability over the northern Sahara. Climate Dynamics 21, 689-698.

Mahood, G.A., Hildreth, W. 1986. Geology of the peralkaline volcano at Pantelleria, Strait of Sicily. Bulletin of Volcanology 48, 143-172.

Manning, S.W., Bronk Ramsey, C., Kutschera, W., Higham, T., Kromer, B., Steier, P., Wild, E.M. 2006. Chronology for the Aegean Late Bronze Age 1700-1400 BC. Science 312, 565-569.

Matthews, A., Ayalon, A., Bar-Matthews, M. 2000. D/H ratios of fluid inclusions of Soreq Cave (Israel) speleothems as a guide to the eastern Mediterranean meteoric line relationships in the last 120 ky. Chemical Geology 166, 183-191.

McGarry, S., Bar-Matthews, M., Matthews, A., Vaks, A., Schilman, B., Ayalon, A. 2004. Constraints on hydrological and paleotemperature variations in the eastern Mediterranean region in the last 140 ka given by the δD values of speleothem fluid inclusions. Quaternary Science Reviews 23, 919-934.

North Greenland Ice Core Project Members 2004. High-resolution record of Northern Hemisphere climate extending into the last interglacial period. Nature 431, 147-151.

Paillard, D. 1996. Macintosh Program performs time-series analysis. Eos Transactions, American Geophysical Union 77, 39.

Pujol, C., Vergnaud-Grazzini, C. 1995. Distribution patterns of live planktic foraminifers as related to regional hydrography and productive systems of the Mediterranean Sea. Marine Micropaleontology 25, 187-217.

Reimer, P.J., McCormac, F.G. 2002. Marine radiocarbon reservoir corrections for the Mediterranean and Aegean Seas. Radiocarbon 44, 159-166.

Richards, D.A., Dorale, J.A. 2003. Uranium-series chronology and environmental applications of speleothems. Reviews in Mineralogy and Geochemistry 52, 407-460.

Rohling, E.J. 1994. Review and new aspects concerning the formation of Mediterranean sapropels. Marine Geology 122, 1-28.

Rohling, E.J. 1999. Environmental control on Mediterranean salinity and $\delta^{18}O$. Paleoceanography 14, 706-715.

Rohling, E.J., Cane, T.R., Cooke, S., Sprovieri, M., Bouloubassi, I., Emeis, K.C., Schiebel, R., Kroon, D., Jorissen, F.J., Lorre, A., Kemp, A.E.S. 2002. African monsoon variability during the previous interglacial maximum. Earth and Planetary Science Letters 202, 61-75.

Rohling, E.J., Sprovieri, M., Cane, T.R., Casford, J.S.L., Cooke, S., Bouloubassi, I., Emeis, K.C., Schiebel, R., Hayes, A., Jorissen, F.J., Kroon, D. 2004. Reconstructing past planktic foraminiferal habitats using stable isotope data: a case history for Mediterranean sapropel S5. Marine Micropaleontology 50, 89-123.

Rohling, E.J., Grant, K., Bolshaw, M., Roberts, A.P., Siddall, M., Hemleben, C., Kucera, M. 2009. Antarctic temperature and global sea level closely coupled over the past five glacial cycles. Nature Geoscience 2, 500-504.

Schlitzer, R. 2011. Ocean Data View. http://odv.awi.de.

Schrag, D.P., Hampt, G., Murray, D.W. 1996. Pore fluid constraints on the temperature and oxygen isotopic composition of the glacial ocean. Science 272, 1930-1932.

Siddall, M., Smeed, D.A., Hemleben, C., Rohling, E.J., Schmelzer, I., Peltier, W.R. 2004. Understanding the Red Sea response to sea level. Earth and Planetary Science Letters 225, 421-434.

Stanford, J.D., Hemingway, R., Rohling, E.J., Challenor, P.G., Medina-Elizalde, M., Lester, A.J. 2011. Sea-level probability for the last deglaciation: a statistical analysis of far-field records. Global and Planetary Change 79, 193-203.

Vaks, A., Bar-Matthews, M., Matthews, A., Ayalon, A., Frumkin, A. 2010. Middle-Late Quaternary paleoclimate of northern margins of the Saharan-Arabian Desert: reconstruction from speleothems of Negev Desert, Israel. Quaternary Science Reviews 29, 2647-2662.

Table S1 Core LC21 radiocarbon dating results.

Depth in core (m)	Uncalibrated AMS ^{14}C age ±2σ (ka BP)	Calibrated ^{14}C age ±2σ (ka BP)	AI (%)	Reference
1.38	5.590 ± 0.120	5.936 ± 0.244	99.8	Casford et al. (2007)
1.62	7.480 ± 0.120	7.801 ± 0.146*	99.3	Casford et al. (2007)
1.74	8.120 ± 0.120	8.437 ± 0.140*	99.9	Casford et al. (2007)
1.80	9.010 ± 0.140	9.533 ± 0.174*	100.7	Casford et al. (2007)
2.09	11.770 ± 0.160	13.199 ± 0.236	102.5	Casford et al. (2007)
2.51	14.070 ± 0.100	16.769 ± 0.248	103.5	This study
2.78	15.970 ± 0.110	18.719 ± 0.182	99.9	This study
3.13	17.925 ± 0.140	20.821 ± 0.498	99.5	This study
3.34	19.625 ± 0.150	22.876 ± 0.512	99.7	This study
3.51	21.110 ± 0.180	24.655 ± 0.372	98.8	This study
3.76	23.010 ± 0.300	27.291 ± 0.660	99.6	This study
3.92	24.830 ± 0.920	29.315 ± 0.866	87.2	This study
3.99	25.730 ± 0.260	30.146 ± 0.480	101.6	This study
4.01	25.980 ± 0.280	30.242 ± 0.462	91.7	This study

AI = Agreement Index (see Section 3). Material extracted from sapropel S1 (*) has been calibrated using a ΔR value of 149 ± 30 years (Facorellis et al., 1998; see Section 3).

Table S2 Summary of RSL tie-point uncertainties (see Part 6 for definitions of uncertainties e, f, g, h, j and k).

a) RSL-$\delta^{18}O_{pac}$ correlation. Tie-points are classed as category 1 (black), 2 (blue) and 3 (red)

RSL tie-point	Uncertainty (e) (ka)	Uncertainty (f) (ka)	Uncertainty (g) (ka)	**MSE_{ii} (ka)**
1	0.6263	2.970	0.405	**5.84**
2	0.4786	0.214	0.197	**0.56**
3	0.5270	0.207	0.196	**0.60**
4	1.6636	0.310	0.868	**1.90**
5	2.1804	0.266	0.434	**2.24**
6	1.6103	0.270	0.373	**2.10**
7	0.6659	0.989	0.659	**1.36**
8	1.6511	0.682	0.659	**1.90**
9	1.0691	0.722	1.390	**1.90**
10	2.0634	0.374	1.026	**2.71**
11	1.6395	0.939	0.842	**2.07**
12	1.3088	0.434	1.260	**1.87**
13	1.3759	0.257	1.067	**2.16**
14	3.0228	0.194	0.896	**3.38**
15	2.3858	0.796	0.448	**3.79**

b) RSL-deglacial correlation

RSL tie-point	Uncertainty (j) (ka)	Uncertainty (k) (ka)	**MSE_{iii} (ka)**
1	0	0.069	**0.069**
2	0.20	0.129	**0.238**
3	0.20	0.206	**0.287**
4	0.10	0.584	**0.592**
5	0.20	1.504	**1.517**
6	0.35	3.593	**3.610**
7	0.75	3.593	**3.670**

Table S3 Summary of phase analyses of ice-core and RSL records. Lags (and 2σ uncertainties) ≥0.6 kyr are highlighted (red).

	Periodicity (kyr)	Coherency (%)	Lag (kyr)	Lag uncertainty (kyr)
EDML vs. RSL	25	91	-0.4	±0.4
	11.6	85	0.7	±0.3
	6.8	66	0.6	±0.3
dEDML/dt vs. dRSL/dt	26.3	92	-0.5	±0.4
	11.9	86	0.7	+0.3/-0.2
NGRIP vs. RSL	20.8	89	-0.2	±0.4
	9.6	68	0.1	-0.5/+0.4
	6.4	81	-0.3	-0.1/+0.2
	4.5	80	0.0	-0.1/+0.2
dNGRIP/dt vs. dRSL/dt	27.8	89	0.5	±0.5
	10	76	-0.3	±0.3
	7.5	88	-0.3	-0.2/+0.1
	6.4	85	-0.4	-0.2/+0.1
	4.5	78	0.1	-0.2/+0.1

Chapter 3

Timing of ice-volume and monsoon variations over five glacial cycles

K. M. Grant, E. J. Rohling, H. Cheng, L. Edwards, A. P. Roberts

Manuscript to be submitted to Science

Author contributions: KMG led the study and wrote the paper; EJR conceived the study and co-wrote the paper; HC and LE contributed the Sanbao Cave data; APR contributed to manuscript refinement. Author affiliations are listed in the manuscript.

Timing of ice-volume and monsoon variations over five glacial cycles

K.M. Grant[1], E.J. Rohling[2], H. Cheng[3,4], L. Edwards[3], A.P. Roberts[2]

1. School of Ocean and Earth Science, University of Southampton, National Oceanography Centre, European Way, Southampton SO14 3ZH, UK
2. Research School of Earth Sciences, The Australian National University, Canberra, ACT 0200, Australia
3. Department of Geology and Geophysics, University of Minnesota, Minneapolis, Minnesota 55455, USA
4. College of Geography Science, Nanjing Normal University, Nanjing 210097, China

Ice-sheet variability and monsoon circulation affect Earth's radiative budget and internal energy redistribution. However, process-understanding of interactions between these climate-system components remains elusive because of a lack of consistent age-control among long records of ice-volume and monsoon variability. We present a tight synchronisation among such records over the last 500,000 years, based on independent age-control over the last 150,000 years. We find that ice-volume reduction generally lags orbital forcing by 56±12° over 40- and 22-kyr cycles, and that - with differences in detail between each of the last five glacial terminations - ice volume follows rising boreal insolation and CO_2 by 2000-7000 years. We explain the lag of Asian summer monsoon intensification relative to insolation during glacial terminations by millennial-scale meltwater pulses into the North Atlantic.

Rapid climate shifts from glacial to interglacial conditions ("terminations") every ~100,000 years have long been related to variations in Earth's orbital parameters (Milankovitch, 1941; Hays et al., 1976), and in particular to boreal summer insolation (Alley et al., 2005; Kawamura et al., 2007; Cheng et al., 2006; Denton et al., 2010). However, lack of significant 100-kyr cyclicity in insolation (Imbrie et al., 1993; Shackleton, 2000; Paillard, 1998), evidence for southern hemisphere control of terminations (Petit et al., 1999; Huybers, 2011; Wolff et al., 2009), and debated relative importance of climate feedbacks and orbital forcing (Shackleton, 2000; Lisiecki, 2010; Imbrie et al., 2011), highlight unresolved questions about ice-volume-climate relationships.

Close coupling exists between variations in high-latitude and monsoon climate during terminations (Cheng et al., 2009; Denton et al., 2010). For example, ice-sheet calving episodes in the North Atlantic ('Heinrich Events'; Hemming, 2004) coincided with cold

anomalies in Greenland, southern hemisphere warming (Stocker and Johnsen, 2003; EPICA 2006), and $\delta^{18}O$ maxima in Chinese cave speleothems (Wang et al., 2001; Yuan et al., 2004; Cheng et al., 2009). Chinese cave $\delta^{18}O$ variations are influenced by summer and winter monsoon intensity, as well as by local and regional isotope fractionation (Cheng et al., 2009; Clemens et al., 2010; Lewis et al., 2010; Pausata et al., 2011), which reflect hydrological changes associated with monsoon circulation, the dominant mechanism for (inter) hemispheric moisture transfer. Moisture availability is critical for ice-sheet growth (Ruddiman et al., 1980), which in turn has been linked to Asian monsoon intensity (Barnett et al., 1988; Ding et al., 1995), but detailed understanding of the relationship between ice-volume and monsoon variability is lacking (Weber and Tuenter, 2011; Rohling et al., 2009a) because it requires robust records of both systems on a common timescale.

A commonly used ice-volume approximation - global benthic foraminiferal $\delta^{18}O$ - includes poorly understood deep-water temperature influences (Elderfield et al., 2012), and contains increased chronological uncertainties at terminations due to spatial gradients in benthic $\delta^{18}O$ (Skinner and Shackleton, 2005; Lisiecki and Raymo, 2009). This compromises the use of benthic foraminiferal $\delta^{18}O$ as an ice-volume proxy for investigating climatic relationships. In contrast, radiometrically dated relative sea-level (RSL) benchmarks - such as fossil coral terraces, submerged speleothems and paleoshoreline deposits - provide strong constraints on ice-volume reconstructions. However, prior to ~150,000 years (~150 kyr) ago, such data are scarce and are largely limited to interglacials, so they cannot constrain the timing, amplitude and rates of older ice-volume changes.

Here we present a U/Th-based chronology for a continuous, high-resolution record of Red Sea relative sea-level (RSL; Rohling et al., 2009b) over five complete glacial cycles, by developing a new criterion for synchronizing Red Sea RSL (Rohling et al., 2009b) and dust-flux data (Roberts et al., 2011) with U/Th-dated $\delta^{18}O$ variations in Sanbao Cave, China ($\delta^{18}O_{sanbao}$; Cheng et al., 2009, 2012). We then transpose this U/Th chronology to a record of Chinese loess deposition (MGSQ; Sun et al., 2006) by synchronization with Red Sea dust-flux variations. This extends a 150 kyr U/Th-based Red Sea RSL record (Grant et al., 2012), thereby providing independent dating constraints on terminations 1-5 as well as a consistent chronological framework for examining climate-system phase relationships throughout the last 500 kyr.

Ti/Ca and magnetically identified hematite ('Hem') abundance records from central Red Sea core KL09 reflect past variations in dust supply into the basin (Rohling et al., 2008; Roberts et al., 2011). These records and RSL data were obtained from the same sediment samples, so

timing relationships between dust supply and RSL are unambiguous. All five glacial terminations (T1-T5) contain a large, mid-termination dust peak, followed by a sharp drop toward the subsequent interglacials. A similar signal structure in Red Sea and Asian dust records suggests covariation in dust mobilization over these regions due to large-scale atmospheric circulation changes (Roberts et al., 2011). Red Sea dust fluxes are influenced by seasonal wind changes associated with Indian monsoon circulation (Jiang et al., 2009), which broadly covaries with East Asian monsoon dynamics (Rohling et al., 2003; Sinha et al., 2005; Fleitmann et al., 2007). We therefore hypothesize a close relationship between $\delta^{18}O_{sanbao}$ and Red Sea dust variations during terminations. We test our hypothesis by comparing Red Sea RSL data for 0-150 kyr on an independently-constrained chronology (RSL_{150}; Grant et al., 2012), with the same RSL data after synchronization between $\delta^{18}O_{sanbao}$ and KL09 Ti/Ca at T1-T5 (linearly interpolated between terminations) ($RSL_{dust\text{-}sanbao}$; Fig. 3.1; SOM). Good agreement warrants synchronization of $\delta^{18}O_{sanbao}$ and KL09 Ti/Ca to date T3-T5, and reveals scope for additional age control between terminations.

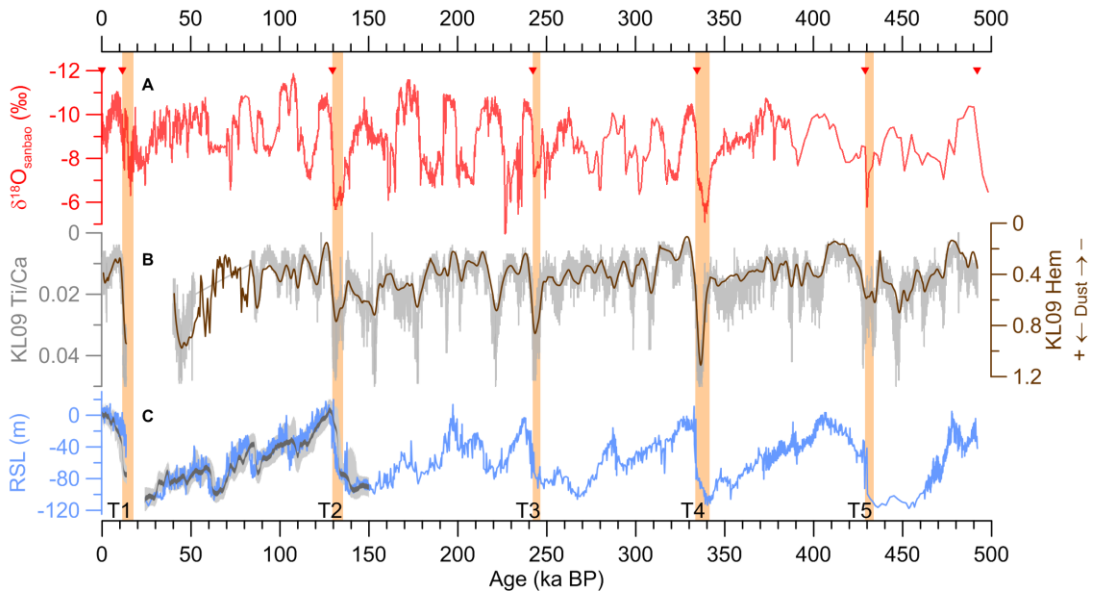

Figure 3.1 (A) Sanbao Cave speleothem $\delta^{18}O$; (B) and (C) core KL09 dust proxies (Hem, brown; Ti/Ca, grey) and co-registered Red Sea RSL record (blue) after synchronization with $\delta^{18}O_{sanbao}$ at terminations 1-5 (orange rectangles). Tie-points are indicated (red triangles). Independent dating of the Red Sea RSL record for 0-150 ka BP (Grant et al., 2012) is shown as 95% confidence intervals of the dataset (light gray) and probability maximum (dark gray). RSL and KL09 records are not reliable ca 14-23 ka BP and 14-40 ka BP, respectively, due to an indurated aplanktonic interval.

Cross-spectral analysis reveals strong covariance (90%) at precession-band frequencies (0.045 kyr^{-1}) between $\delta^{18}O_{sanbao}$ and $RSL_{dust\text{-}sanbao}$ (Fig. S3.3b). This is corroborated by analysis over 0-150 kyr using RSL_{150} (Fig. S3.3d). We utilize this agreement to improve our chronology of $RSL_{dust\text{-}sanbao}$ before 150 kyr ago. First, we apply a precession band-pass filter

(0.045 ±0.02 kyr^{-1}) to the records (Fig. S3.4a-c). Comparison of this band-pass component from RSL_{150} with that from $\delta^{18}O_{sanbao}$ reveals that offsets are minor (within ±1 kyr) and not systematic in direction or magnitude (SOM; Fig. S3.3c). Next, we synchronize the band-pass components in $RSL_{dust\text{-}sanbao}$ and $\delta^{18}O_{sanbao}$ before 150 kyr (RSL_{sanbao}), accounting for the observed (minor) phase offsets by allowing ±2 kyr uncertainty in each correlation tie-point. Finally, we combine all synchronization uncertainties between 150 and 500 kyr (SOM) with sea-level uncertainties (±12 m at 2σ; Siddall et al., 2003; Rohling et al., 2009b) in a probabilistic assessment (see Grant et al., 2012 for method). We then couple RSL_{150} with RSL_{sanbao} to give a complete probabilistic Red Sea RSL record over the last 500,000 years (Fig. 3.2a).

Red Sea RSL reasonably approximates global sea-level variability (Grant et al., 2012), as validated by strong chronological agreement with U/Th-dated coral sea-level benchmarks for past interglacials (marine isotope stages [MIS] 5e, 7c, 9c, 11), and with speleothem-based sea-level information (Fig. 3.2a). Interglacial timings from these records and ours (Table S3.2, SOM) may be refined in future pending developments in glacio-isostatic adjustment modeling over five full glacial cycles. Our RSL record also agrees with a global benthic $\delta^{18}O$ stack (Lisiecki and Raymo, 2005), with respect to both timing and amplitude of fluctuations (Fig. 3.2b). This suggests roughly proportional deep-sea temperature and ice-volume influences within this benthic $\delta^{18}O$ compilation.

Focussing on terminations (Fig. 3.2, 3.3), an initial and gradual sea-level rise ($SLrise_A$) was followed by a rapid rise ($SLrise_B$) for T2-T5. At T1, only $SLrise_B$ is adequately delineated in our RSL record because of a data-poor (aplanktonic) interval (Fenton et al., 2000).

We observe significant differences in the insolation:RSL relationship between T2 and the other terminations (T3, T4, T5, and likely T1). In the latter group, there is a clear tendency for $SLrise_A$ to coincide with or shortly follow increasing boreal summer insolation, while $SLrise_B$ occurs close to boreal summer insolation maximum (Fig. 3.2b, 3.3). For T2, $SLrise_A$ significantly pre-dates the rise in boreal summer insolation and instead tracks rising austral summer insolation, while $SLrise_B$ significantly pre-dates the boreal summer insolation maximum (Fig. 3.3). The T2 discrepancy for $SLrise_A$ may be due to insufficient RSL age control (Fig. 3.3), but this cannot explain the T2 discrepancy for $SLrise_B$. Hence, T3-T5 and T1 seem to best agree with the 'classical' boreal summer insolation theory for ice-volume changes (Milankovitch, 1941; Kawamura, et al., 2007), but T2 suggests that - in some cases - changes in austral summer insolation may be important (Schulz and Zeebe, 2006; Wolff et al., 2009; Huybers, 2011).

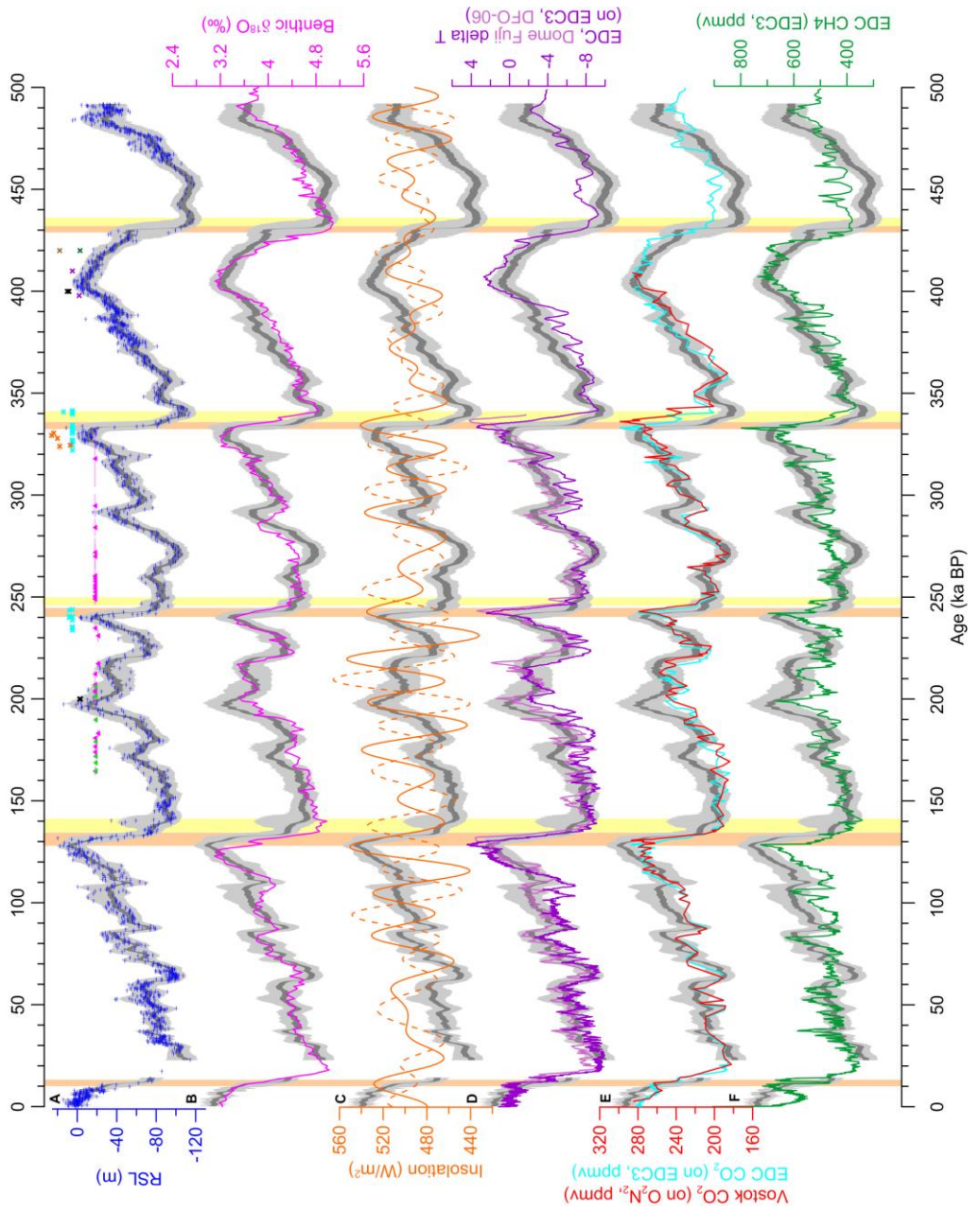

Figure 3.2 Probabilistic Red Sea RSL record [95% confidence intervals of the RSL dataset (light gray) and probability maximum (dark gray)] for 0-150 ka BP (Grant et al., 2012) and 150-500 ka BP (this study) plotted with: (A) Red Sea data and sea-level benchmarks (green triangles, Bard et al., 2002; pink triangles, Dutton et al., 2009; black crosses, Muhs et al., 2012; cyan crosses, Anderson et al., 2010; orange crosses, Stirling et al., 2001 [in Anderson et al., 2010]; red crosses, Schellmann and Radtke, 2004; brown cross, Hearty et al., 1999; green cross, Murray-Wallace, 2002), (B) benthic foraminifera $\delta^{18}O$ (Lisiecki and Raymo, 2005), (C) mid-summer insolation at 65°N (solid line) and 65°S (dashed line) (Berger, 1978), (D) Antarctic temperature records from Dome Fuji [lilac (Kawamura et al., 2007)] and EPICA Dome C [EDC, purple (Jouzel et al., 2007)], (E) CO_2 records from Vostok [red (Petit et al., 1999), on an O_2N_2 timescale (Bender and Suwa, 2007)] and from EDC [cyan (Siegenthaler et al., 2005), on the EDC3 timescale (Parrenin et al., 2007)], (F) CH_4 record from EDC (Loulergue et al., 2008). All records are plotted on their original timescales unless stated otherwise. Rectangles highlight sea-level rises A (yellow shading) and B (orange shading).

Sea-level rise at terminations closely coincides with CH_4 increases (Fig. 3.2f, 3.3). Given that CH_4 covaries with Greenland temperature (Blunier et al., 1998; Blunier and Brook, 2001; Barker et al., 2009), this corroborates previous findings of near-synchronous variations in Greenland climate and ice-volume (Grant et al., 2012). Antarctic temperature (T_{AA}) and CO_2 increases lead sea-level rises at terminations by 2-4 kyr ($SLrise_A$) and 4-7 kyr ($SLrise_B$), although the onsets of T_{AA} and CO_2 rises fall within dating uncertainties of $SLrise_A$ (Fig. 3.2d,e, 3.3). The magnitude of these leads is more ambiguous at T4 and T5, because the Dome Fuji T_{AA} and Vostok CO_2 records are offset from their EPICA Dome C (EDC) counterparts by ~3 kyr at T4 and do not reach T5 (Fig. 3.3d,e). If the T4 offset also applies to T5, then $SLrise_B$ at T5 would have lagged the T_{AA} and CO_2 increases by about 7 kyr, similar to the lags at T3 and T4. However, if the EDC3 chronology (Parrenin et al., 2007) is accurate for T5, then a reduced sea-level lag is implied, comparable to that at T1 and T2. To resolve this, better dating is needed of T5 in ice cores.

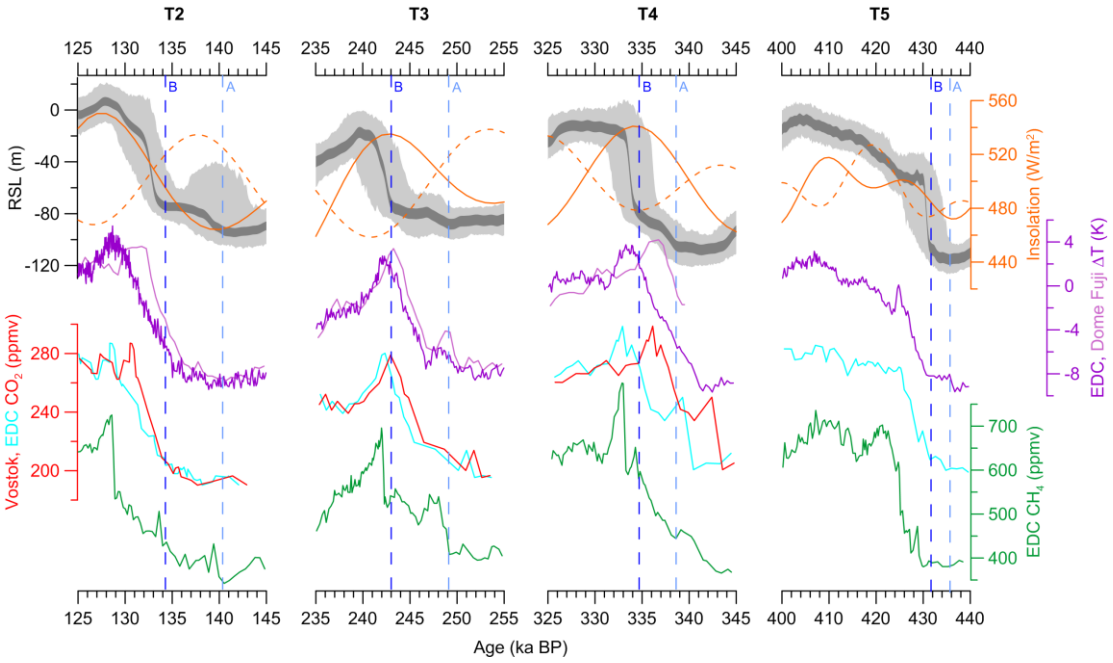

Figure 3.3 Enlargement of Fig. 3.2 for terminations 2-5 (T2-T5) (see Fig. 3.2 legend), with sea-level rises A and B indicated (dashed light and dark blue lines, respectively).

Overall, we observe subtle yet clear differences in phase relationships for terminations T1-T5. In particular, T3 and T4 have relatively long sea-level lags relative to boreal insolation, T_{AA} and CO_2, which significantly exceed our 95% confidence interval (Fig. 3.2c,d,e, 3.3). This rules out ice-volume related feedbacks on initial rises in T_{AA} and CO_2 for those terminations. There are also differences in the phasing of rates of sea-level change (dRSL) relative to orbital components (Fig. 3.4a,c). Maxima in dRSL correspond to precession minima at T1 and T3-T5, obliquity maxima at T1-T2 and T4, and rising eccentricity at T2-

T5. We infer that a 'one size fits all' approach to understanding termination mechanisms may not be appropriate.

Cross-spectral phase analyses quantify the mean ice-volume lead/lag relationships over the past 500 kyr at obliquity and precession frequencies (SOM; Table S3.3). Ice-volume changes are found to lag external climate forcing (obliquity, precession, insolation and rates of change in insolation) by 56±12˚, or ~6 and ~3 kyr at obliquity and precession periods, respectively. Shorter lags (0.5-1.8 kyr) are observed relative to T_{AA}, CO_2 and CH_4, and these lags differ by ~1 kyr for Antarctic records on different timescales (Table S3). Ice-volume and CO_2 changes are in phase (within uncertainties) at precession frequencies, and are either in phase (Vostok CO_2) or ice volume leads (EDC) CO_2 at obliquity frequencies (Table S3.3).

Finally, we explore the potential effects of past ice-volume variability on the Asian summer (ASM) and winter (AWM) monsoons (SOM). Previous work suggests that precession-paced ASM proxies lag insolation changes by 3-8 kyr (Clemens et al., 2010; Caley et al., 2011). The atmosphere has little thermal inertia so, in the absence of slow climatic feedbacks, its circulation should respond rapidly to climate forcing. However, northern hemisphere ice-sheet variability represents a slow feedback and affects atmospheric circulation, including the Asian monsoon (Barnett et al., 1988; Ding et al., 1995; Rohling et al., 2003). We therefore assess the extent to which ice-volume (RSL) variations and/or rates of ice-volume change (dRSL) may explain: (a) the lag between insolation changes and the $\delta^{18}O_{sanbao}$ proxy for ASM variations, where $\delta^{18}O_{sanbao}$ minima represent ASM maxima (Cheng et al., 2009), and (b) Chinese Loess Plateau dust-flux variability, which is linked to AWM intensity (Jin et al., 2007) and approximated by quartz grain-size variations (MGSQ (Sun et al., 2006)). Linear multivariate regressions allow straightforward evaluation of which combinations of orbital parameters (eccentricity, precession, and obliquity), RSL, and dRSL best agree with $\delta^{18}O_{sanbao}$ and MGSQ (SOM) (Fig. 3.4).

Our 'simulation' of $\delta^{18}O_{sanbao}$ ($Sanbao_{sim}$) shares 36% of variance with $\delta^{18}O_{sanbao}$. The main component in $Sanbao_{sim}$ is precession (sharing 18% of variance with $\delta^{18}O_{sanbao}$), but RSL and dRSL are also significant (Fig. 3.4d; Fig. S3.8). Sequential addition of various components in $Sanbao_{sim}$ reveals that variations are paced by orbital parameters (Fig. S3.8a), amplitude-modulated by ice volume (Fig. S3.8b), and become lagged due to the influence of rapid ice-volume change (Fig. S3.8c). Cross-spectral analyses confirm that the phase lag between insolation maxima and $\delta^{18}O_{sanbao}$ minima is reduced by 50% when considering $Sanbao_{sim}$ (a combination of insolation, RSL, and dRSL variability) instead of insolation alone (Table

S3.4, SOM). We infer that ice-volume fluctuations, and especially rates of ice-volume change, are important causes of the lagged ASM response to insolation.

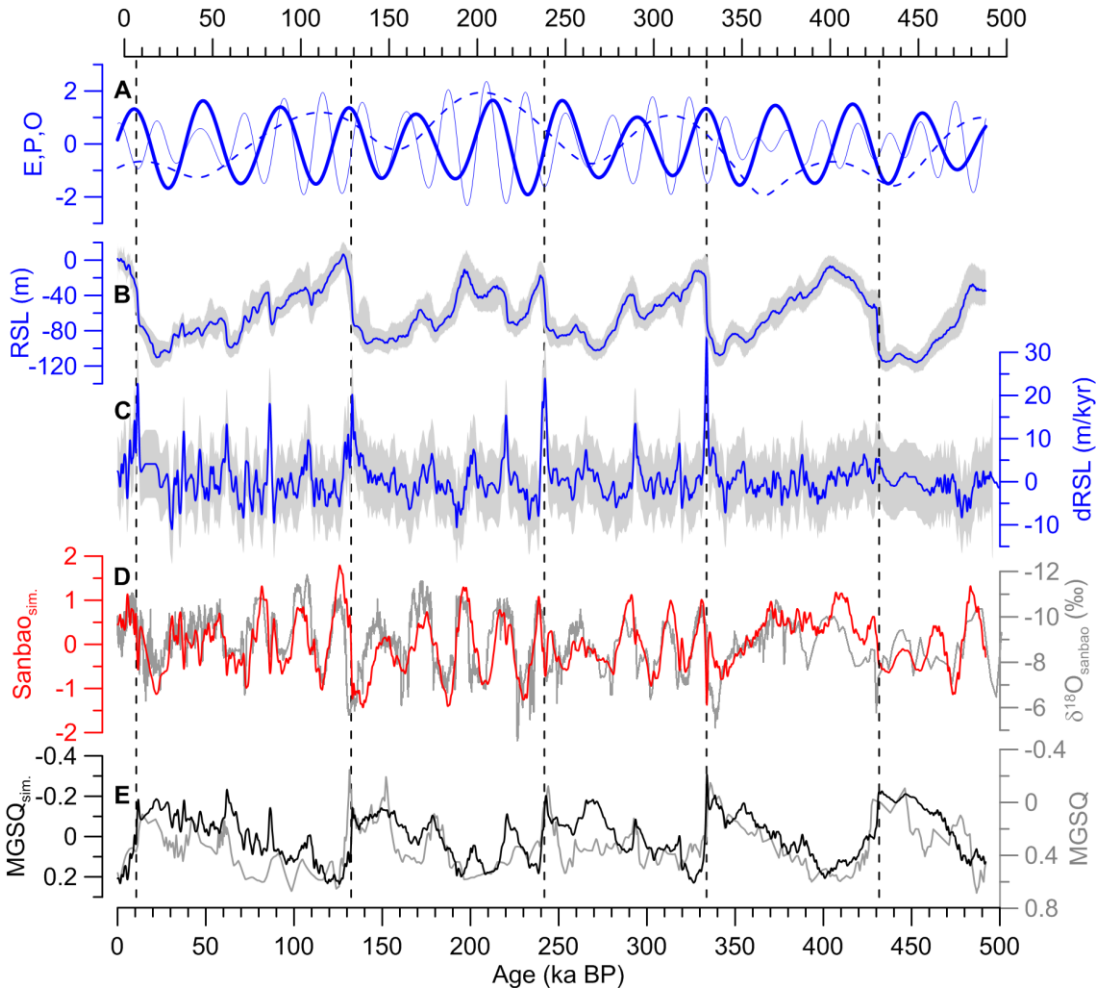

Figure 3.4 (A) Normalised eccentricity [E, dashed line], precession [P, thin line] and obliquity [O, solid line] (Berger, 1978), (B) composite Red Sea RSL record (Grant et al., 2012; this study) [probability maximum (blue) and 95% confidence interval of the RSL dataset (light gray)], (C) rates of RSL change (dRSL, blue) with 2σ uncertainties (gray), (D) $\delta^{18}O_{sanbao}$ (gray) and simulated $\delta^{18}O_{sanbao}$ (red), and (E) stacked grain-size record from the Chinese Loess Plateau [MGSQ, gray (Sun et al., 2006)] and simulated MGSQ (black). For explanation of construction of simulated records, see SOM.

A similar simulation of the Chinese loess MGSQ ($MGSQ_{sim}$) shares 43% of variance with MGSQ and is dominated by RSL, with minimal contribution from orbital components (Fig. 3.4e; Fig. S3.8d). We infer that spectral peaks at orbital frequencies in Chinese loess reflect indirect influences of orbital forcing via ice-sheet variability. A weak dRSL component accentuates dust flux maxima at terminations. Thus, dRSL appears to account for rapid, millennial-scale variability in ASM and AWM proxies during terminations.

To summarize, we provide the first continuous ice-volume record over five glacial cycles that is unbiased by orbital tuning, and is chronologically consistent with Asian monsoon proxy records. Our analysis reveals variable ice-volume:climate phase relationships at terminations, which suggests varying threshold conditions for termination onset/completion. Regarding millennial variability at terminations, we find that strong positive dRSL peaks (fast ice-volume reductions, or 'melt-water pulses') coincide with positive anomalies in $\delta^{18}O_{sanbao}$ (weak ASM), peaks in MGSQ (strong Asian dust flux) (Fig. 3.4c,d,e), and often a warm 'overshoot' in T_{AA} records (Fig. 3.2d). Together, these observations are consistent with a millennial-scale event that follows the bipolar see-saw concept, in which melt-water related slowing or shutdown of the North Atlantic overturning circulation causes abrupt Northern Hemisphere cooling and widespread Southern Hemisphere warming (Stocker and Johnsen, 2003; EPICA, 2006), with concomitant ASM weakening/failure (Cheng et al., 2009) and winter (monsoon) circulation intensification (Rohling et al., 2003, Jin et al., 2007).

References

Alley, R.B, Clark, P.U., Huybrechts, P., Joughlin, I. 2005. Ice-sheet and sea-level changes. Science 310, 456-460.

Andersen, M.B., Stirling, C.H., Potter, E.-K., Halliday, A.N., Blake, S.G., McCulloch, M.T., Bridget F., B.F., O'Leary, M.J. 2010. The timing of sea-level high-stands during Marine Isotope Stages 7.5 and 9: Constraints from the uranium-series dating of fossil corals from Henderson Island. Geochimica et Cosmochimica Acta 74, 3598-3620.

Bard, E., Antonioli, F., Silenzi, S. 2002. Sea-level during the penultimate interglacial period based on a submerged stalagmite from Argentarola Cave (Italy). Earth and Planetary Science Letters 196, 135-146.

Barker, S., Diz, P., Vautravers, M.J., Pike, J., Knorr, G., Hall, I.R., Broecker, W.S. 2009. Interhemispheric Atlantic seesaw response during the last deglaciation. Nature 457, 1097-1103.

Barnett, T.P., Dümenil, L., Schlese, U., Roeckner, E. 1988. The Effect of Eurasian Snow Cover on Global Climate. Science 239, 504-507.

Bender, M., Suwa, M. 2007. Trapped gas composition and chronology of the Vostok ice core. Boulder, Colorado USA: National Snow and Ice Data Center. Digital media.Berger, 1978.

Blunier, T., Brook, E. J. 2001. Timing of millennial-scale climate change in Antarctica and Greenland during the last glacial period. Science 291, 109-112.

Blunier, T., Chappellaz, J., Schwander, J., Dällenbach, A., Stauffer, B., Stocker, T.F., Raynaud, D., Jouzel, J., Clausen, H.B., Hammer, C.U., Johnsen, S.J. 1998. Asynchrony of Antarctic and Greenland climate change during the last glacial period. Nature 394, 739-743.

Bowen, D.Q. 2010. Sea level ~400 000 years ago (MIS 11): analogue for present and future sea-level? Climate of the Past 6, 19-29.

Caley, T., Malaizé, B., Revel, M., Ducassou, E., Wainer, K., Ibrahim, M., Shoeaib, D., Migeon, S., Marieu, V. 2011. Orbital timing of the Indian, East Asian and African boreal monsoons and the concept of a 'global monsoon'. Quaternary Science Reviews 30, 3705-3715.

Cheng, H., Edwards, R.L., Wang, Y., Kong, W., Ming, Y., Kelly, M.J., X. Wang., Gallup, C.D., Liu, W. 2006. A penultimate glacial monsoon record from Hulu Cave and two-phase glacial terminations. Geology 34, 217-220.

Cheng, H., Edwards, R.L., Broecker, W.S., Denton, G.H., Kong, X.G., Wang, Y.J., Zhang, R., Wang, X.F., 2009. Ice age terminations. Science 326, 248-252.

Cheng, H., Zhang, P.Z., Spötl, C., Edwards, R.L., Cai, Y. J., Zhang, D. Z. Sang, W.C., Tan, M., An, Z.S. 2012. The climatic cyclicity in semiarid-arid central Asia over the past 500,000 years. Geophysical research Letters 39, L01705, doi:10.1029/ 2011GL050202.

Clemens, S.C., Prell, W.L., Sun, Y. 2010. Orbital-scale timing and mechanisms driving Late Pleistocene Indo-Asian summer monsoons: Reinterpreting cave speleothem $\delta^{18}O$. Paleoceanography 25, PA4207, doi:10.1029/2010PA001926.

Denton, G.H., Anderson, R.F., Toggweiler, J.R., Edwards, R.L., Schaefer, J.M., Putnam, A.E. 2010. The last glacial termination. Science 328, 1652-1656.

Ding, Z.L., Liu, T.S., Rutter, N.W., Yu, Z.W., Guo, Z.T., Zhu, R.X. 1995. Ice-volume forcing of East Asian winter monsoon variation in the past 800,000 years. Quaternary Research 44, 140-159.

Dutton, A., Bard, E., Antonioli, F., Esat, T.M., Lambeck, K., McCulloch, M.T. 2009. Phasing and amplitude of sea-level and climate change during the penultimate interglacial. Nature Geoscience 2, 355-359.

Elderfield, H., Ferretti, P., Greaves, M., Crowhurst, S., McCave, I.N., Hodell, D., Piotrowski, A.M. 2012. Evolution of ocean temperature and ice volume through the mid-Pleistocene climate transition. Science 337, 704-709.

EPICA Community Members. One-to-one coupling of glacial climate variability in Greenland and Antarctica. Nature 444, 195-198 (2006).

Fleitmann, D., Burns, S.J., Mangini, A., Mudelsee, M., Kramers, J., Villa, I., Neff, U., Al-Subbary, A.A., Buettner, A., Hippler, D., Matter, A., 2007. Holocene ITCZ and

Indian monsoon dynamics recorded in stalagmites from Oman and Yemen (Socotra). Quaternary Science Reviews 26, 170-188.

Grant, K.M., Rohling, E.J., Bar-Matthews, Ayalon, A., Bronk Ramsey, C., M., Satow, C., Medina-Elizalde, M., Roberts, A.P. 2012. Rapid coupling between ice volume and polar temperature over the past 150,000 years. Nature 491, 744-747.

Hays, J.G., Imbrie, J., Shackleton, N.J. 1976. Variations in the Earth's orbit: pacemaker of the ice ages. Science 194, 1121-1132.

Hearty, P.J., Kindler, P., Cheng, H., Edwards, R.L. 1999. A +20m middle Pleistocene sea-level highstand (Bermuda and the Bahamas) due to partial collapse of Antarctic ice. Geology 27, 375-378.

Hemming, S.R. 2004. Heinrich events: Massive late Pleistocene detritus layers of the North Atlantic and their global climate imprint. Reviews of Geophysics 42, RG1005, doi:10.1029/2003RG000128.

Huybers, P. 2011. Combined obliquity and precession pacing of late Pleistocene deglaciations. Nature 480, 229-232.

Imbrie, J., Berger, A., Boyle, E.A., Clemens, S.C., Duffy, A., Howard, W.R., Kukla, G., Kutzbach, J., Martinson, D.G., McIntyre, A., Mix, A.C., Molfino, B., Morley, J.J., Peterson, L.C., Pisias, N.G., Prell, W.L., Raymo, M.E., Shackleton, N.J, Toggweiler, J.R. 1993. On the structure and origin of major glaciation cycles 2. The 100,000-year cycle. Paleoceanography 8, 699-735.

Imbrie, J.Z., Imbrie-Moore, A., Lisiecki, L.E. 2011. A phase-space model for Pleistocene ice volume. Earth and Planetary Science Letters 307, 94-102.

Jin, L., Chen, F., Ganopolski, A., Claussen, M. 2007. Response of East Asian climate to Dansgaard/Oeschger and Heinrich events in a coupled model of intermediate complexity. Journal of Geophysical Research 112, D06117, doi:10.1029/ 2006JD007316

Jiang, H., Farrar, J.T., Beardsley, R.C. Chen, R., Chen, C. 2009. Zonal surface wind jets across the Red Sea due to mountain gap forcing along both sides of the Red Sea. Gepphysical Research Letters 36, L19605, doi:10.1029/2009GL040008.

Jouzel, J., Masson-Delmotte, V., Cattani, O., Dreyfus, G., Falourd, S., Hoffmann, G., Minster, B., Nouet, J., Barnola, J.M., Chappellaz, J., Fischer, H., Gallet, J.C., Johnsen, S., Leuenberger, M., Loulergue, L., Luethi, D., Oerter, H., Parrenin, F., Raisbeck, G., Raynaud, D., Schilt, A., Schwander, J., Selmo, E., Souchez, R., Spahni, R., Stauffer, B., Steffensen, J.P., Stenni, B., Stocker, T.F., Tison, J.L., Werner, M., Wolff., E.W. 2007. Orbital and millennial antarctic climate variability over the past 800,000 years. Science 317, 793-797.

Kawamura, K., Parrenin, F., Lisiecki, L., Uemura, R., Vimeux, F., Severinghaus, J.P., Hutterli, M.A., Nakazawa, T., Aoki, S., Jouzel, J., Raymo, M.E., Matsumoto, K., Nakata, H., Motoyama, H., Fujita, S., Goto-Azuma, K., Fujii, Y., Watanabe, O. 2007. Northern hemisphere forcing of climatic cycles in Antarctica over the past 360,000 years. Nature 448, 912-917.

Lewis, S.C., LeGrande, A.N., Kelley, M., Schmidt, G.A. 2010. Water vapour source impacts on oxygen isotope variability in tropical precipitation during Heinrich events. Climate of the past 6, 325-343.

Lisiecki, L.E. 2010. Links between eccentricity forcing and the 100,000-year glacial cycle. Nature Geoscience 3, 349-352.

Lisiecki, L.E., Raymo, M.E. 2005. A Plio-Pleistocene stack of 57 globally distributed benthic $\delta^{18}O$ records. Paleoceanography 20, PA1003, doi:10.1029/2004PA001071.

Lisieki, L.E., Raymo, M.E. 2009. Diachronous benthic d18O responses during late Pleistocene terminations. Paleoceanography 24, PA3210, doi:10.1029/2009PA001732.

Loulergue, L., Schilt, A., Spahni, R., Masson-Delmotte, V., Blunier, T., Lemieux, B., Barnola, J.-M., Raynaud, D., Stocker, T.F., Chappellaz, J. 2008. Orbital and millennial-scale features of atmospheric CH_4 over the past 800,000 years. Nature 453, 383-386.

Milankovitch, M. 1941. Kanon der Erdbestrahlung und Seine Andwendung auf das Eiszeitenproblem (Royal Serbian Academy Special Publication 132, Belgrade, Serbia.

Muhs, D.R., Pandolfi, J.M., Simmons, K.R., Schumann, R.R. 2012. Sea-level history of past interglacial periods from uranium-series dating of corals, Curaçao, Leeward Antilles islands. Quaternary Research 78, 157-169.

Murray-Wallace, C.V. 2002. Pleistocene coastal stratigraphy, sea-level highstands and neotectonism of the southern Australian passive continental margin – a review. Journal of Quaternary Science 17, 469-489.

Paillard, D. 1998. The timing of Pleistocene glaciations from a simple multiple-state climate model. Nature 391, 378-381.

Parrenin, F., Barnola, J.-M., Beer, J., Blunier, T., Castellano, E., Chappellaz, J.A, Dreyfus, G., Fischer, H., Fujita, S., Jouzel, J., Kawamura, K., Lemieux-Dudon, B., Loulergue, L., Masson-Delmotte, V., Narcisi, B.M., Petit, J.-R., Raisbeck, G., Raynaud, D., Ruth, U., Schwander, J., Severi, M., Spahni, R., Steffensen, J.P., Svensson, A.M., Udisti, R., Waelbroeck, C., Wolff, E. 2007. The EDC3 chronology for the EPICA Dome C ice core. Climate of the Past 3, 485-497.

Pausata, S.F.R., Battisti, D.S., Kerim H. Nisancioglu, K.H., Bitz, C.M. 2011. Chinese stalagmite $\delta^{18}O$ controlled by changes in the Indian monsoon during a simulated Heinrich event. Nature Geoscience 4, 474-480.

Petit, J.R., Jouzel, J., Raynaud, D., Barkov, N.I., Barnola, J.M., Basile, I., Bender, M., Chappellaz, J., Davis, J., Delaygue, G., Delmotte, M., Kotlyakov, V.M., Legrand, M., Lipenkov, V., Lorius, C., Pépin, L., Ritz, C., Saltzman, E., Stievenard, M. 1999. Climate and atmospheric history of the past 420,000 years from the Vostok ice core, Antarctica. Nature 399, 429-436.

Roberts, A.P., Rohling, E.J., Grant, K.M., Larrasoaña, J.C., Liu, Q. 2011. Atmospheric dust variability from Arabia and China over the last 500,000 years. Quaternary Science Reviews 30, 3537-3541.

Rohling, E.J., Mayewski, P.A., Challenor, P. 2003. On the timing and mechanism of millennial-scale climate variability during the last glacial cycle. Climate Dynamics 20, 257-267.

Rohling, E.J., Liu, Q., Roberts, A.P., Stanford, J.D., Rasmussen, S.O., Langen, P.L., Siddall., M. 2009a. Controls on the East Asian monsoon during the last glacial cycle, based on comparison between Hulu Cave and polar ice-core records. Quaternary Science Reviews 28, 3291-3302.

Rohling, E.J., Grant, K., Bolshaw, M., Roberts, A.P., Siddall, M., Hemleben, Ch., Kucera, M. 2009b. Antarctic temperature and global sea level closely coupled over the past five glacial cycles. Nature Geoscience 2, 500-504.

Ruddiman, W.F. 2006. Ice-driven CO2 feedback on ice volume. Climate of the Past 2, 43-55.

Ruddiman, W.F., McIntyre, A., Niebler-Hunt, V., Durazzi, J.T., 1980. Oceanic evidence for the mechanism of rapid Northern Hemisphere glaciation. Quaternary Research, 13, 33-64.

Schellmann, G., Radtke, U. 2004. A revised morpho- and chronostratigraphy of the Late and Middle Pleistocene coral reef terraces on Southern Barbados (West Indies). Earth Science reviews 64, 157-187.

Schulz, K.G., Zeebe, R.E. 2006. Pleistocene glacial terminations triggered by synchronous changes in Southern and Northern hemisphere insolation: the insolation canon hypothesis. Earth and Planetary Science Letters 249, 326-336.

Siegenthaler, U., Stocker, T. F., Monnin, E., Lüthi, D., Schwander, J., Stauffer, B., Raynaud, D., Barnola, J.-M., Fischer, H., Masson-Delmotte, V., Jouzel, J. 2005. Stable carbon cycle-climate relationship during the late Pleistocene. Science 310 , 1313-1317.

Sinha, A., Cannariato, K.G., Stott, L.D., Li, H.-C., You, C.-F., Cheng, H., Edwards, R.L., Singh, I.B. 2005. Variability of Southwest Indian summer monsoon precipitation during the Bølling-Ållerød. Geology 33, 813-816.

Shackleton, N.J. 2000. The 100,000-year ice-age cycle identified and found to lag temperature, carbon dioxide, and orbital eccentricity. Science 289, 1897-1902.

Skinner, L.C., Shackleton, N.J. 2005. An Atlantic lead over Pacific deep-water change across Termination I: implications for the application of the marine isotope stage stratigraphy. Quaternary Science Reviews 24, 571-580.

Stirling, C.H., Esat T.M., Lambeck K., McCulloch M.T., Blake S.G., Lee D.C., Halliday, A.N. 2001. Orbital forcing of the marine isotope stage 9 interglacial. Science 91, 290-293.

Stocker, T.F., Johnson, S.J. 2003. A minimum thermodynamic model for the bipolar seesaw. Paleoceanography 18, doi:10.1029/2003PA000920.

Sun., Y., Clemens, S.C., An, Z, Yu, Z. 2006. Astronomical timescale and palaeoclimatic implication of stacked 3.6-Myr monsoon records from the Chinese Loess Plateau. Quaternary Science Reviews 25, 33-48.

Wang, Y.J., Cheng, H., Edwards, R.L., An, Z.S., Wu, J.Y., Shen, C.C., Dorale, J.A. 2001. A high-resolution absolute-dated Late Pleistocene monsoon record from Hulu Cave, China. Science 294, 2345-2348.

Weber, S.L., Tuenter, E. 2011. The impact of varying ice sheets and greenhouse gases on the intensity and timing of boreal summer monsoons. Quaternary Science Reviews 30, 469-479.

Wolff, E.W., Fischer, H., Röthlisberger, R. 2009. Glacial terminations as southern warmings without northern control. Nature Geoscience 2, 206-209.

Yuan, D., Cheng, H., Edwards, R.L., Dykoski, C.A., Kelly, M.J., Zhang, M., Qing, J., Lin, Y., Wang, Y., Wu, J., Dorale, J.A., An, Z., Yanjun Cai, Y. 2004. Timing, duration, and transitions of the last interglacial Asian monsoon. Science 304, 578.

Supplementary Online Information

Timing of ice-volume and monsoon variations over five glacial cycles

K. M. Grant, E. J. Rohling, H. Cheng, L. Edwards, A. P. Roberts

Supporting Online Material

Ice-volume and monsoon variability over five glacial cycles

K.M. Grant, E.J. Rohling, H. Cheng, L. Edwards, A.P. Roberts

This supporting material contains: a location map of the sites discussed in our study (Fig. S3.1); details of the synchronizations of Red Sea RSL records with Sanbao Cave $\delta^{18}O$ (Fig. S3.2-S3.4; Table S3.1) and with Chinese loess grain-size variations (Fig. S3.5); a summary of the timing of sea-level highstands in marine isotope stages (MIS) 7, 9, and 11 (Table S3.2); results of cross-spectral phase analyses between records of RSL and various climate parameters (Table S3.3); and 'simulations' of $\delta^{18}O_{sanbao}$ and Chinese loess records by multivariate regressions (Fig. S3.6, Table S3.4).

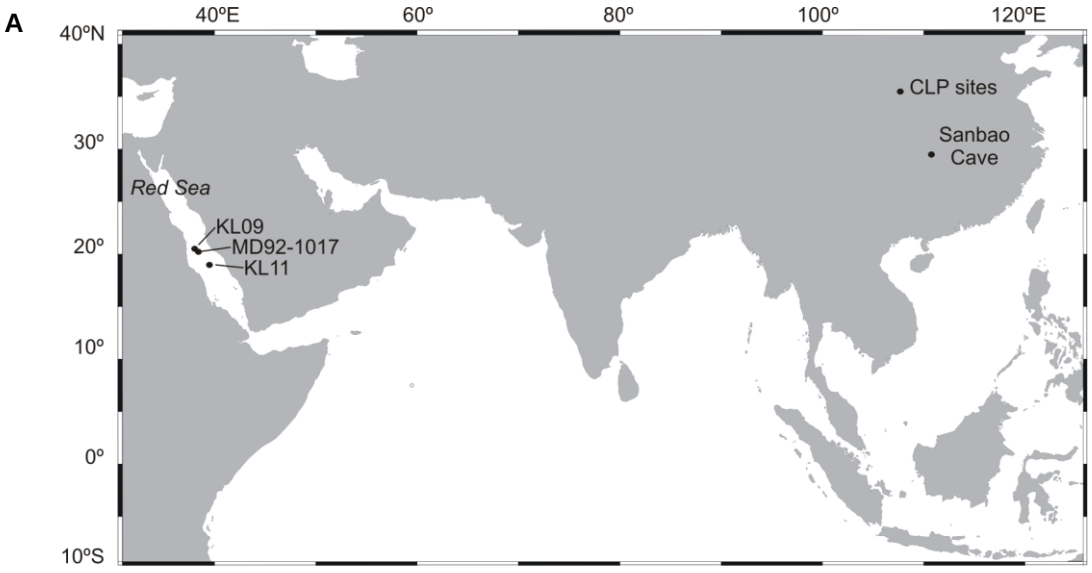

Figure S3.1 Map of sites and regions discussed in this study. (A) Location of Red Sea cores (KL09, MD92-1017, and KL11), Sanbao Cave, and the Chinese Loess Plateau (CLP) grain-size records. (B) Satellite image of an Arabian dust storm deflected over the Red Sea.

Correlation of Red Sea dust and RSL to Sanbao Cave $\delta^{18}O$

To establish a radiometrically-based chronology for the Red Sea RSL record back to 500 kyr ago, our method relies on two synchronisations. The first synchronisation, between core KL09 Ti/Ca and Sanbao Cave speleothem $\delta^{18}O$ ($\delta^{18}O_{sanbao}$), results in '$RSL_{dust\text{-}sanbao}$'. Here, the RSL record is indirectly synchronised to $\delta^{18}O_{sanbao}$ using the Red Sea dust record. The second synchronisation, between '$RSL_{dust\text{-}sanbao}$' and $\delta^{18}O_{sanbao}$, results in 'RSL_{sanbao}'. In this case, the first (indirect) RSL synchronisation to $\delta^{18}O_{sanbao}$ is 'fine-tuned' by directly correlating filtered orbital periodicities in $RSL_{dust\text{-}sanbao}$ and $\delta^{18}O_{sanbao}$ which are common to both records and which are directly in phase (within uncertainties).

For correlating Red Sea dust and $\delta^{18}O_{sanbao}$, we use the high-resolution Ti/Ca record of central Red Sea sediment core KL09. This has a 0.5-mm down-core sampling interval, compared to a 1-cm sampling interval for the environmental magnetic KL09 Hem record, which is smoothed by a 4-cm moving Gaussian window due to the width of the magnetometer response function (Roberts, 2006). We correlate mid-points of the rapid decreases in $\delta^{18}O_{sanbao}$ and KL09 Ti/Ca that follow their respective maxima at terminations. Use of these mid-points minimizes chronological uncertainties relating to potentially real offsets in the onset and end of the transitions (Shackleton, 2000). Mid-transition values correspond to ~-8‰ in $\delta^{18}O_{sanbao}$ and ~0.025 in Ti/Ca.

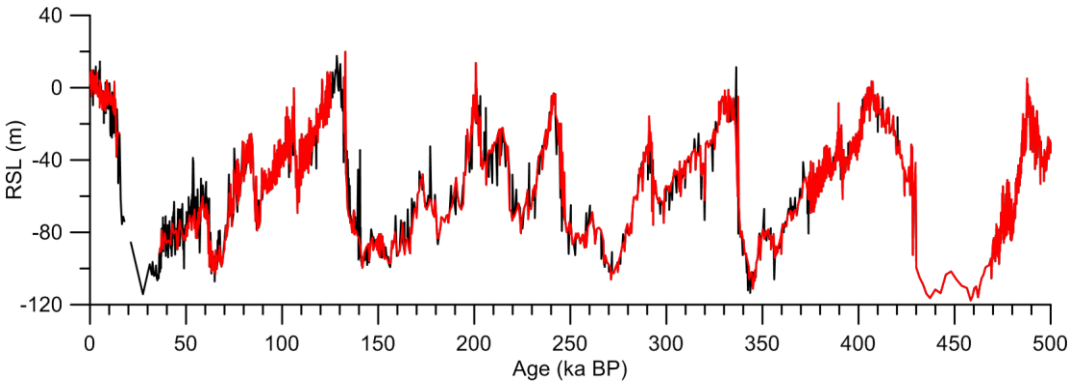

Figure S3.2 Red Sea relative sea-level (RSL) records. RSL records (from Rohling et al., 2009) derived from KL09 data only (red; n = 1404) and from KL09, KL11 and MD92-1017 data (black; n = 1938).

For correlation between Red Sea RSL and $\delta^{18}O_{sanbao}$, we use the Red Sea RSL record of Rohling et al. (2009, 2010). This record is predominantly based on RSL data from central Red Sea core KL09, supplemented with RSL data from nearby cores KL1l and MD92-1017. Key to our study is the known phase relationship between Red Sea dust and sea-level records, based on coupled measurements of the same samples from core KL09. The

composite (KL09 + KL11 + MD92-1017) and KL09-only RSL records yield identical timings of sea-level change (Fig. S3.2), so that inclusion of data from other cores in the RSL record does not produce spurious phase offsets between dust and RSL.

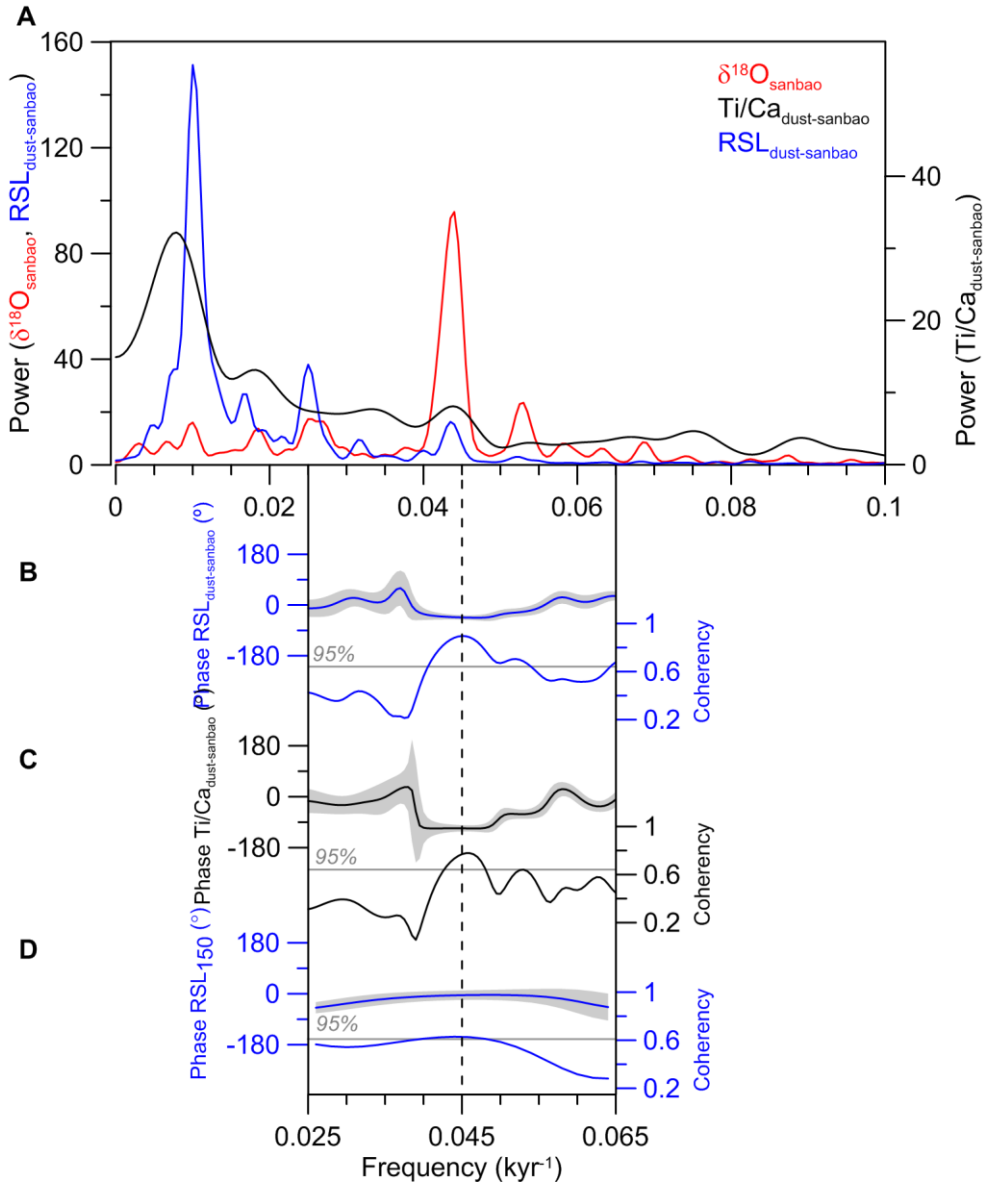

Figure S3.3 (A) Spectral analyses of $\delta^{18}O_{sanbao}$ (red), KL09 $Ti/Ca_{dust\text{-}sanbao}$ (black) and $RSL_{dust\text{-}sanbao}$ (blue) after the dust-$\delta^{18}O_{sanbao}$ correlation. All records have spectral peaks at a frequency of 0.042-0.045 kyr^{-1} (equivalent periodicity = 22.2-23.8kyr). (B-D) Phase relationships between $\delta^{18}O_{sanbao}$ and $RSL_{dust\text{-}sanbao}$, $Ti/Ca_{dust\text{-}sanbao}$, and RSL_{150}, respectively.

Synchronization of KL09 Ti/Ca (dust) and $\delta^{18}O_{sanbao}$, with straightforward linear interpolation between terminations, yields the '$Ti/Ca_{dust\text{-}sanbao}$' and '$RSL_{dust\text{-}sanbao}$' records. Their power spectra, and those for $\delta^{18}O_{sanbao}$, all have peaks at frequencies of 0.042-0.045 kyr^{-1}(~23 kyr periodicity), which is equivalent to the precession cycle (Fig. S3.3a). Spectral peaks are also observed for $Ti/Ca_{dust\text{-}sanbao}$ and $RSL_{dust\text{-}sanbao}$ at frequencies equivalent to

eccentricity (~0.01 kyr^{-1}; ~100 kyr periodicity), and for $RSL_{dust\text{-}sanbao}$ at obliquity frequencies (~0.025 kyr^{-1}; ~40 kyr periodicity) (Fig. S3.3a). Cross-spectral phase analyses of $Ti/Ca_{dust\text{-}sanbao}$ and $RSL_{dust\text{-}sanbao}$ with $\delta^{18}O_{sanbao}$ reveal strong covariance in the precession band (Fig. S3.3b,c), particularly between $RSL_{dust\text{-}sanbao}$ and $\delta^{18}O_{sanbao}$ (90% coherent). At maximum coherency (equivalent to a frequency of 0.045 kyr^{-1}), phase offsets between $\delta^{18}O_{sanbao}$ and $RSL_{dust\text{-}sanbao}$ are -2.7±0.4 kyr (Fig. S3.3b), but just -0.4±1 kyr when we use the same RSL data on a well-constrained chronology for the last 150 kyr (RSL_{150}; Grant et al., 2012) (Fig. S3.3d). The latter indicates that $\delta^{18}O_{sanbao}$ and RSL variations are in phase (within uncertainties) in the precession band. We use this observation to improve the Red Sea RSL and dust chronology over the time interval 150-500 kyr. For this, we apply a 0.045 kyr^{-1} band-pass filter to $\delta^{18}O_{sanbao}$ and $RSL_{dus\text{-}sanbao}$ (Fig. S3.4a-c), and then synchronize the filtered $\delta^{18}O_{sanbao}$ and $RSL_{dust\text{-}sanbao}$ records in the interval before 150 kyr (linearly interpolating between tie-points) (Fig. S3.4d); this yields 'RSL_{sanbao}'.

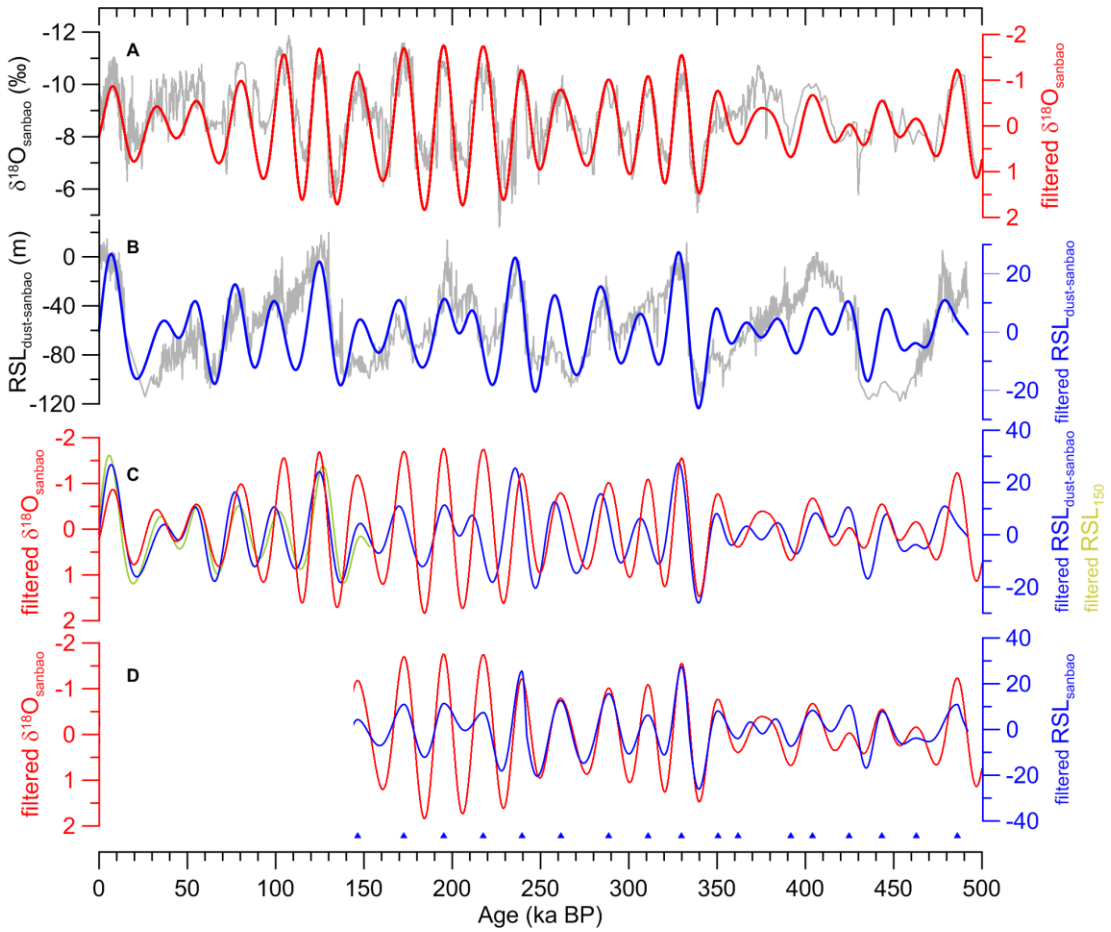

Figure S3.4 22-kyr band-pass filtered records of (A) $\delta^{18}O_{sanbao}$ (red) and (B) $RSL_{dust\text{-}sanbao}$ (blue) superimposed on $\delta^{18}O_{sanbao}$ and $RSL_{dust\text{-}sanbao}$ (gray). The lower panels contain the filtered RSL record before (C), and after (D) synchronization with the filtered $\delta^{18}O_{sanbao}$ record at 17 tie-points (blue triangles) for the interval 150-500 kyr. The filtered RSL_{150} record (green) is shown in (C).

We mostly correlate $RSL_{dust\text{-}sanbao}$ maxima to $\delta^{18}O_{sanbao}$ minima, although covariation of $RSL_{dust\text{-}sanbao}$ minima and $\delta^{18}O_{sanbao}$ maxima is more obvious at around 361.8 and 391.7 kyr (Fig. S3.4d). To account for uncertainties in phase offsets between these filtered records (-0.4±1 kyr, based on the well-dated RSL_{150}), we generously allow an extra ±2 kyr uncertainty for every correlation tie-point (see below).

Table S3.1 Sources of tie-point uncertainties in the dust-$\delta^{18}O_{sanbao}$ and RSL_{dust}-$\delta^{18}O_{sanbao}$ correlations for the interval 150-500 kyr ago. Red text denotes data relating to the band-pass filtered $\delta^{18}O_{sanbao}$ and RSL_{dust} records ($\delta^{18}O_{sanbao}$(F) and RSL_{dust}(F)). RMS = Root mean square. All uncertainties are quoted at 2σ and in kyr.

Tie-point Age (kyr)	U/Th dating	Sample spacing $\delta^{18}O_{sanbao}$ $\delta^{18}O_{sanbao}$(F)	Sample spacing KL09 Ti/Ca RSL_{dust}(F)	Extra 2 kyr	RMS (kyr)
146.39	1.48	0.20	0.40	2.00	2.53
172.69	1.50	0.20	0.40	2.00	2.54
195.15	2.54	0.10	0.40	2.00	3.26
217.59	2.10	0.20	0.40	2.00	2.93
239.39	0.25	0.20	0.40	2.00	2.06
242.16	0.27	0.07	0.03	2.00	2.02
261.39	0.32	0.20	0.40	2.00	2.07
288.59	0.69	0.20	0.40	2.00	2.16
310.89	1.00	0.20	0.40	2.00	2.28
329.89	0.63	0.20	0.40	2.00	2.14
334.37	1.00	0.06	0.03	2.00	2.24
350.40	0.90	0.20	0.40	2.00	2.24
361.80	1.00	0.20	0.40	2.00	2.28
391.70	1.34	0.20	0.40	2.00	2.45
404.10	2.82	0.20	0.40	2.00	3.49
424.90	2.00	0.20	0.40	2.00	2.86
429.00	2.00	3.00	0.03	2.00	4.12
443.40	2.00	0.20	0.40	2.00	2.86
462.70	2.98	0.20	0.40	2.00	3.62
486.00	4.24	0.20	0.40	2.00	4.71
492.00	4.96	5.00	0.02	2.00	7.32

.

A root mean square (RMS) calculation combines uncertainties associated with every tie-point in the two synchronisations (KL09 Ti/Ca-$\delta^{18}O_{sanbao}$ and $RSL_{dust\text{-}sanbao}$-$\delta^{18}O_{sanbao}$) for the interval 150-500 kyr (n = 21) (Table S3.1). This includes U/Th-dating uncertainties from the $\delta^{18}O_{sanbao}$ chronology (Cheng et al., 2009, 2012), sample-spacing uncertainties in the $\delta^{18}O_{sanbao}$, KL09 Ti/Ca, band-pass filtered $\delta^{18}O_{sanbao}$ and band-pass filtered $RSL_{dust\text{-}sanbao}$ records, and an additional ±2 kyr phase-offset uncertainty (see above). Radiometric dating

uncertainties for correlation tie-points were determined by interpolating between the 2σ values of the bracketing U/Th dates. Finally, after RMS propagation of all these chronological uncertainties for each tie-point, we calculate - through interpolation - a 2σ (chronological) uncertainty for every RSL_{sanbao} data-point. Combination of this chronological uncertainty with a vertical sea-level uncertainty for the RSL data (±12m at 2σ; Siddall et al., 2003, 2004; Rohling et al., 2009) then facilitates probabilistic RSL assessment as described by Grant et al. (2012). We also use this method to calculate the maximum probability (±2σ) of rates of sea-level change (dRSL) for the interval 150-500 kyr (main-text Fig. 3.4c). We have assumed no covariances between sources of uncertainty (i.e., the probability distribution for each datapoint is mutually exclusive), therefore, the confidence limits of our probabilistic sea-level records represent generous 'worst case' assessments.

The probabilistic RSL and dRSL assessments for the interval 150-500 kyr, as described above, are combined with similar probabilistic RSL and dRSL assessments for the last 150 kyr (Grant et al., 2012) which have more detailed time-control (main-text Fig. 3.2; Table S3.2). Together, these give continuous, probabilistic records of variations in sea-level and its rates of change over the last 500 kyr. This robust, independent age control enables - for the first time - estimation of rates of sea-level change for the last 500 kyr, without assumptions involved in tuning/correlation that underlie most such attempts in paleoclimate studies.

Table S3.2 Timing of sea-level highstands prior to the last interglacial (MIS 5e). RSL values are given for the maximum-probability sea level ($\mathbf{2\sigma_{pmax}}$), and for the 95% confidence limit of all RSL uncertainties ($2\sigma_{data}$).

	Stage	MIS 7		MIS 9	MIS 11
	Sub-stage	7a	7e	9e	
		(ka BP)	(ka BP)	(ka BP)	(ka BP)
RSL ≥0 m	$\mathbf{2\sigma_{pmax}}$	-	-	-	-
	$2\sigma_{data}$	194.9-200.3	-	327.4-334.3	400.1-408.4
RSL ≥-10 m	$\mathbf{2\sigma_{pmax}}$	**196.1-198.4**	-	**326.6-331.1**	**400.3-409.3**
	$2\sigma_{data}$	193.3-202.3	237.9-242.0	324.6-335.0	397.0-416.6
RSL ≥-20 m	$\mathbf{2\sigma_{pmax}}$	**194.5-199.9**	**238.8-241.3**	**325.3-333.3**	**398.0-417.3**
	$2\sigma_{data}$	191.5-207.4	236.5-242.9	322.6-335.9	394.9-421.8

Phase relationships between ice-volume and climate variability

Changes in the Red Sea RSL record approximate variations in global ice-volume (see Grant for detailed argument), so to quantify phase relationships between ice-volume and climate variability we perform cross-spectral analyses between RSL and Antarctic temperature (ΔT_{AA}), CO_2 and CH_4 records (Table S3.3). We use ice-core records from the European Project for Ice Coring in Antarctic (EPICA) Dome C (EDC) (Siegenthaler et al., 2005; Jouzel et al., 2007; Loulergue et al., 2008), from Dome Fuji (Kawamura et al., 2007), and from Vostok (Petit et al., 1999). The Dome Fuji and Vostok records are based on 'O_2N_2' timescales that are potentially more accurate than conventional ice-core chronologies (Kawamura et al., 2007; Bender and Suwa, 2007). All EDC records are presented here on the EDC3 timescale (Parrenin et al., 2007), after conversion of the original chronology where necessary.

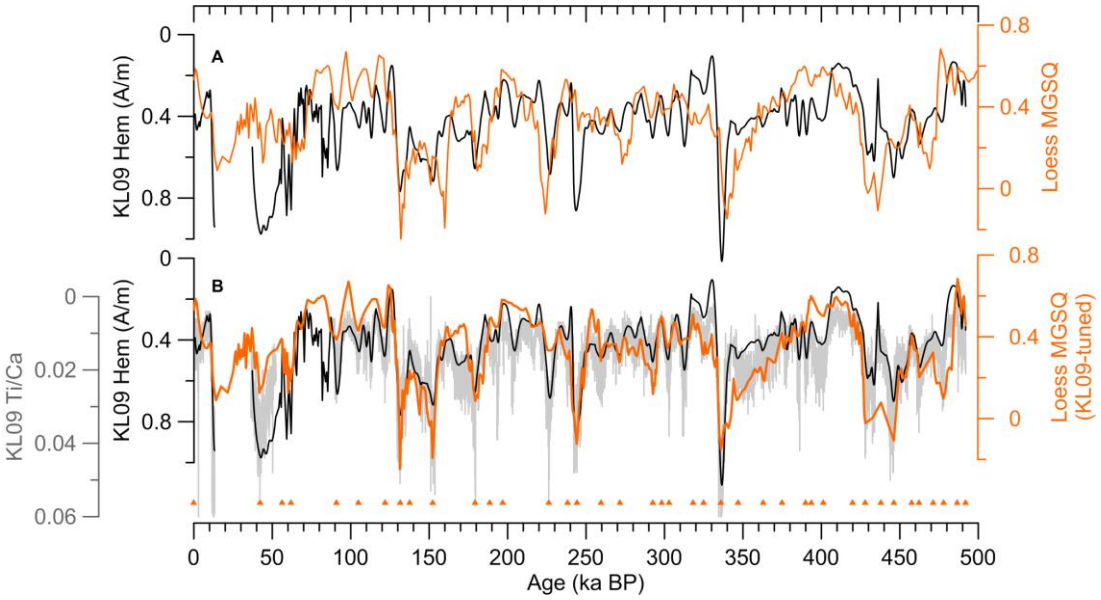

Figure S3.5 Synchronization of Chinese loess and Red Sea dust records. Red Sea core KL09 Hem (black) and Ti/Ca (grey) records, and the stacked 'mean quartz grain size' (MGSQ) record (orange) on its original chronology (Sun et al., 2006) (A) and after correlation with the Red Sea dust record (B). Correlation ties are indicated as orange triangles.

Correlation between Chinese loess and Red Sea dust records

Striking similarity between KL09 Hem and a stacked mean quartz grain-size record (MGSQ, Sun et al., 2006) from the Chinese Loess Plateau (Roberts et al., 2011) reflects a broadly synchronous response to atmospheric changes within the wider monsoon region (Fig. S3.5). Although the dynamic processes that link these records have not yet been explored in detail,

Table S3.3 Summary of phase analyses between key climate records and RSL. Phase lags correspond to the frequencies at which maximum coherency (Coh.) is observed between the analysed variables. Only statistically significant coherencies are tabled. Negative phases denote RSL changes leading those in the climate parameters. Red text denotes ice-volume phase offsets within uncertainties (±2σ). Insolation (Insol.) and rates of change in insolation (dInsol./dt) are for 65°N, 21 June (Berger, 1978).

	Obliquity (~41 kyr)			*Precession (~23 kyr)*			*Precession (~19 kyr)*		
	Coh. (%)	Phase ±2σ (°)	Phase ±2σ (kyr)	Coh. (%)	Phase ±2σ (°)	Phase ±2σ (kyr)	Coh. (%)	Phase ±2σ (°)	Phase ±2σ (kyr)
Obliquity	89	56±7	6.2±0.8	-	-	-	-	-	-
Precession	-	-	-	90	61±7	3.7±0.5	80	54±10	2.9±0.6
Insol.	89	51±7	5.7±0.8	91	56±6	3.5±0.4	79	54±11	2.9±0.6
dInsol./dt	93	51±6	5.9±0.7	93	54±5	3.3±0.4	-	-	-
ΔT_{EDC}	97	5.5±3.4	0.6±0.4	93	7.5±5.3	0.5±0.4	77	35±11	1.8±0.6
ΔT_{Fuji}	95	14±5	1.5±0.6	93	28±8	1.8±0.5	-	-	-
$CO_{2\ EDC}$	89	-12±7	-1.3±0.8	89	-5.6±7.1	-0.4±0.5	-	-	-
$CO_{2\ Vostok}$	88	-4.6±7.2	-0.5±0.8	88	6.5±7.3	0.4±0.5	-	-	-
$CH_{4\ EDC}$	93	7.1±5.3	0.8±0.6	93	20±6	1.3±0.4	67	24±15	1.3±0.8

their obvious visual similarity and association with monsoonal atmospheric circulation (see main text) strongly suggest that they can be synchronized. We use both Red Sea dust records (KL09 Ti/Ca and Hem) for tie-point guidance: the Hem and MGSQ records appear more similar in structure because they are of comparable resolution, but the higher-resolution Ti/Ca record more accurately determines tie-point ages (Fig. S3.5).

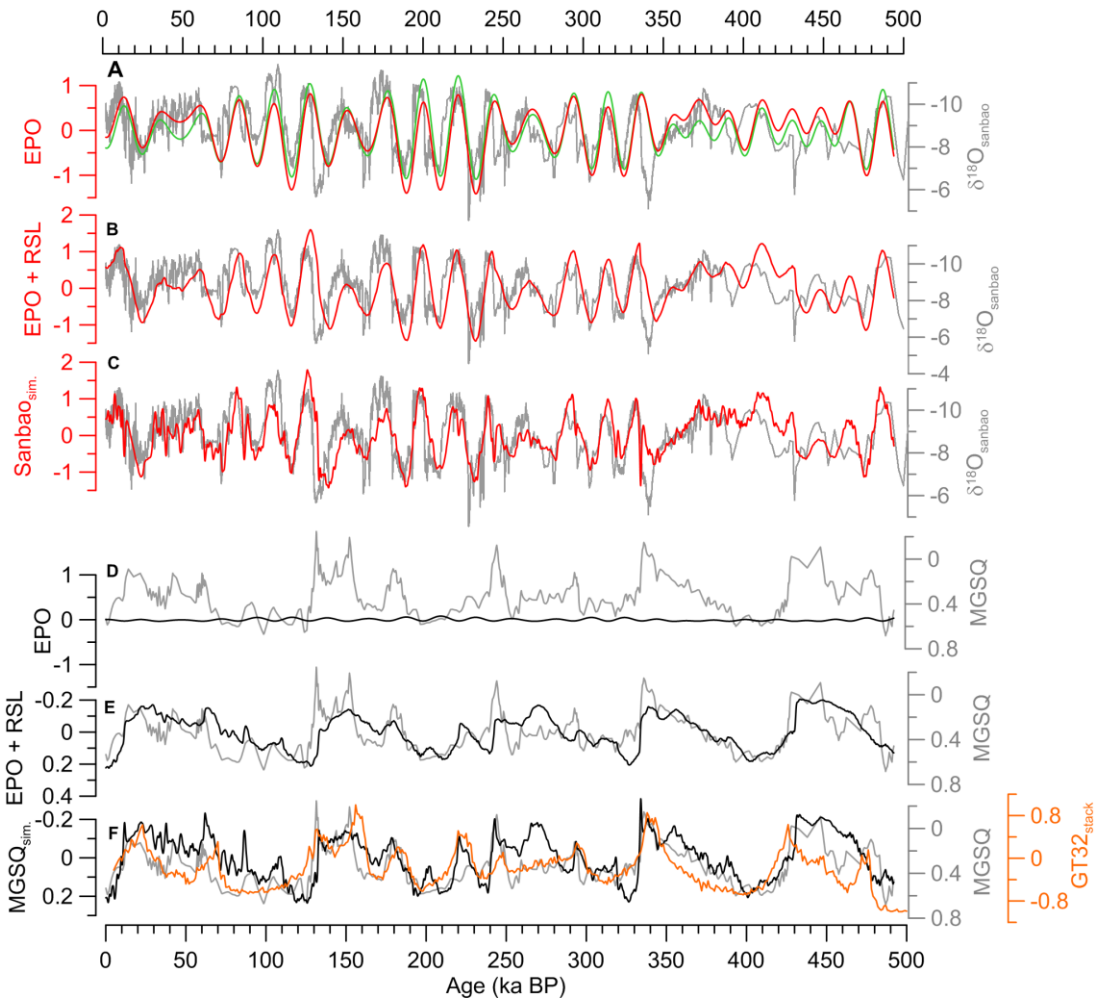

Figure S3.6 Simulations of (A-C) $\delta^{18}O_{sanbao}$ (red) and (D-F) MGSQ (black) superimposed on the original $\delta^{18}O_{sanbao}$ and MGSQ time-series (gray). Time-series for the orbital components (EPO) and for boreal mid-summer insolation (A, green) have been normalized to unit variance. A recently published grain-size record from the Chinese Loess Plateau is also shown (F, orange; Hao et al., 2012). Y-axes in (A) and (D) are scaled for comparison.

Simulating monsoon variability

Our multivariate regression-based 'simulations' of the $\delta^{18}O_{sanbao}$ ($Sanbao_{sim}$) and Chinese loess ($MGSQ_{sim}$) records utilize normalized series of the orbital components (eccentricity, E; precession, P; obliquity, O; Berger, 1978), and our new maximum-probability RSL and dRSL records (main-text Fig. 3.4; Fig. S3.6). Ignoring the intercepts, the factor loading

compositions are -0.205E -0.471P +0.131O +0.338RSL -0.289dRSL for $Sanbao_{sim}$ (Fig. S3.6c), and 0.014E +0.022P +0.00237O +0.102RSL -0.036dRSL for $MGSQ_{sim}$ (Fig. S3.6f). The combined orbital components within $Sanbao_{sim}$ have nearly identical variance to the record of boreal mid-summer insolation (Fig. S3.6a). Cross-spectral phase analyses of $\delta^{18}O_{sanbao}$ with the convolutions of $Sanbao_{sim}$ (e.g., orbital components alone, orbital components plus RSL, etc.) reveal the effects of the RSL and dRSL components on phase offsets between $\delta^{18}O_{sanbao}$ and insolation (EPO) (Table S3.4; main text).

Table S3.4 Summary of cross-spectral phase analyses between $\delta^{18}O_{sanbao}$ and convolutions of our '$Sanbao_{sim}$' record. See SOM text for factor loadings for the components of $Sanbao_{sim}$. Phases are shown for peak coherencies ('Coh.') between $\delta^{18}O_{sanabo}$ and the convolved records at periodicities equivalent to the precession cycle.

	Coh. (%)	Periodicity (kyr)	Phase ±2σ (°)	(kyr)
EPO	94	22.7	39.9±4.9	2.5±0.3
EPO + RSL	93	21.7	33.8±5.3	2.0±0.4
$Sanbao_{sim}$ (EPO + RSL – dRSL)	94	21.7	21.6±4.9	1.3±0.3

Overall, $Sanbao_{sim}$ explains 36% of the variance in $\delta^{18}O_{sanbao}$, compared to 18% explained by insolation alone, which suggests that variations in $\delta^{18}O_{sanbao}$ over the last five glacial cycles reflect equal parts 1) precession-paced insolation forcing and 2) fluctuations in global ice volume and its rates of change. The implications of these inferences depend on how accurately the $\delta^{18}O_{sanbao}$ record represents variations in Asian summer monsoon intensity (see Cheng et al., 2009; Clemens et al., 2010; Lewis et al., 2010; Pausata et al., 2011). In contrast, the largest component in $MGSQ_{sim}$ is ice volume (RSL), which explains 35% of the variance in MGSQ. The total $MGSQ_{sim}$ explains 43% of the variance in MGSQ, implying that the intensity of the Asian winter monsoon is far less sensitive to insolation changes and rates of ice-volume change than the Asian summer monsoon.

References for Supporting Materials:

Bender, M., Suwa, M. 2007. Trapped gas composition and chronology of the Vostok ice core. Boulder, Colorado USA: National Snow and Ice Data Center. Digital media.

Berger, A. 1978. Long-term variations of daily insolation and Quaternary Climatic Changes. Journal of Atmospheric Science 35, 2362-2367.

Cheng, H., Edwards, R.L., Broecker, W.S., Denton, G.H., Kong, X.G., Wang, Y.J., Zhang, R., Wang, X.F., 2009. Ice age terminations. Science 326, 248-252.

Cheng, H., Zhang, P.Z., Spötl, C., Edwards, R.L., Cai, Y. J., Zhang, D. Z. Sang, W.C., Tan, M., An, Z.S. 2012. The climatic cyclicity in semiarid-arid central Asia over the past 500,000 years. Geophysical research Letters 39, L01705, doi:10.1029/ 2011GL050202.

Clemens, S.C., Prell, W.L., Sun, Y. 2010. Orbital-scale timing and mechanisms driving Late Pleistocene Indo-Asian summer monsoons: Reinterpreting cave speleothem $\delta^{18}O$. Paleoceanography 25, PA4207, doi:10.1029/2010PA001926.

Grant, K.M., Rohling, E.J., Bar-Matthews, M., Ayalon, A., Medina-Elizalde, M., Bronk Ramsey, C., Satow, C., and Roberts, A.P. 2012. Rapid coupling between ice volume and polar temperature over the past 150 kyr. Nature 491, 744-747.

Hao, Q., Wang, L., Oldfield, F., Peng, S., Qin, L., Song, Y., Xu, B., Qiao, Y., Bloemendal, J., Guo, Z. 2012. Delayed build-up of Arctic ice sheets during 400,000-year minima in insolation variability. Nature 490, 393-396.

Jouzel, J., Masson-Delmotte, V., Cattani, O., Dreyfus, G., Falourd, S., Hoffmann, G., Minster, B., Nouet, J., Barnola, J.M., Chappellaz, J., Fischer, H., Gallet, J.C., Johnsen, S., Leuenberger, M., Loulergue, L., Luethi, D., Oerter, H., Parrenin, F., Raisbeck, G., Raynaud, D., Schilt, A., Schwander, J., Selmo, E., Souchez, R., Spahni, R., Stauffer, B., Steffensen, J.P., Stenni, B., Stocker, T.F., Tison, J.L., Werner, M., Wolff., E.W. 2007. Orbital and millennial antarctic climate variability over the past 800,000 years. Science 317, 793-797.

Kawamura, K., Parrenin, F., Lisiecki, L., Uemura, R., Vimeux, F., Severinghaus, J.P., Hutterli, M.A., Nakazawa, T., Aoki, S., Jouzel, J., Raymo, M.E., Matsumoto, K., Nakata, H., Motoyama, H., Fujita, S., Goto-Azuma, K., Fujii, Y., Watanabe, O. 2007. Northern hemisphere forcing of climatic cycles in Antarctica over the past 360,000 years. Nature 448, 912-917.

Lewis, S.C., LeGrande, A.N., Kelley, M., Schmidt, G.A. 2010. Water vapour source impacts on oxygen isotope variability in tropical precipitation during Heinrich events. Climate of the past 6, 325-343.

Loulergue, L., Schilt, A., Spahni, R., Masson-Delmotte, V., Blunier, T., Lemieux, B., Barnola, J.-M., Raynaud, D., Stocker, T.F., Chappellaz, J. 2008. Orbital and millennial-scale features of atmospheric CH_4 over the past 800,000 years. Nature 453, 383-386.

Parrenin, F., Barnola, J.-M., Beer, J., Blunier, T., Castellano, E., Chappellaz, J.A, Dreyfus, G., Fischer, H., Fujita, S; Jouzel, J., Kawamura, K., Lemieux-Dudon, B., Loulergue, L., Masson-Delmotte, V., Narcisi, B. M., Petit, J.-R., Raisbeck, G., Raynaud, D., Ruth, U., Schwander, J., Severi, M., Spahni, R., Steffensen, J. P., Svensson, A.M.,

Udisti, R., Waelbroeck, C., Wolff, E. 2007. The EDC3 chronology for the EPICA Dome C ice core. Climate of the Past 3, 485-497.

Pausata, S.F.R., Battisti, D.S., Kerim H. Nisancioglu, K.H., Bitz, C.M. 2011. Chinese stalagmite $\delta^{18}O$ controlled by changes in the Indian monsoon during a simulated Heinrich event. Nature Geoscience 4, 474-480.

Petit, J.R., Jouzel, J., Raynaud, D., Barkov, N.I., Barnola, J.M., Basile, I., Bender, M., Chappellaz, J., Davis, J., Delaygue, G., Delmotte, M., Kotlyakov, V.M., Legrand, M., Lipenkov, V., Lorius, C., Pépin, L., Ritz, C., Saltzman, E., Stievenard, M. 1999. Climate and atmospheric history of the past 420,000 years from the Vostok ice core, Antarctica. Nature 399, 429-436.

Roberts, A.P. 2006. High-resolution magnetic analysis of sediment cores: strengths, limitations and strategies for maximizing the value of long-core magnetic data. Physics of the Earth and Planetary Interiors 156, 162-178.

Roberts, A.P., Rohling, E.J., Grant, K.M., Larrasoaña, J.C., Liu, Q. 2011. Atmospheric dust variability from Arabia and China over the last 500,000 years. Quaternary Science Reviews 30, 3537-3541.

Rohling, E.J., Grant, K., Bolshaw, M., Roberts, A.P., Siddall, M., Hemleben, Ch., Kucera, M. 2009. Antarctic temperature and global sea level closely coupled over the past five glacial cycles. Nature Geoscience 2, 500-504.

Rohling, E.J., Braun, K., Grant, K., Kucera, M., Roberts, A.P., Siddall, M., and Trommer, G. 2010. Comparison between Holocene and Marine Isotope Stage-11 sea-level histories. Earth and Planetary Science Letters 291, 97-105.

Shackleton, N.J., 2000. The 100,000-year ice-age cycle identified and found to lag temperature, carbon dioxide, and orbital eccentricity. Science 289, 1897-1902.

Siddall, M., Rohling, E.J., Almogi-Labin, A., Hemleben, Ch., Meischner, D., Schmeltzer, I., Smeed, D.A. 2003. Sea-level fluctuations during the last glacial cycle. Nature 423, 853-858.

Siddall, M., Smeed, D.A., Hemleben, Ch., Rohling, E.J., Schmeltzer, I., Peltier, W.R. 2004. Understanding the Red Sea response to sea level. Earth and Planetary Science Letters 225, 421-434.

Siegenthaler, U., Stocker, T. F., Monnin, E., Lüthi, D., Schwander, J., Stauffer, B., Raynaud, D., Barnola, J.-M., Fischer, H., Masson-Delmotte, V., Jouzel, J. 2005. Stable carbon cycle-climate relationship during the late Pleistocene. Science 310 , 1313-1317.

Sun., Y., Clemens, S.C., An, Z, Yu, Z. 2006. Astronomical timescale and palaeoclimatic implication of stacked 3.6-Myr monsoon records from the Chinese Loess Plateau. Quaternary Science Reviews 25, 33-48.

Chapter 4

East African summer monsoon variability relative to insolation and ice-volume changes over the last glacial cycle

K. M. Grant, E. J. Rohling

Manuscript to be submitted to Quaternary Science Reviews

Author contributions: KMG led the study and wrote the paper; EJR contributed to manuscript refinement. Author affiliations are listed in the manuscript.

East African summer monsoon variability relative to insolation and ice-volume changes over the last glacial cycle

K.M. Grant[1,2], E.J. Rohling[1,2]

1. School of Ocean and Earth Science, University of Southampton, National Oceanography Centre, European Way, Southampton SO14 3ZH, UK
2. Research School of Earth Sciences, The Australian National University, Canberra, ACT 0200, Australia

Abstract

Model simulations and palaeo-environmental proxy records suggest that high-latitude climate and monsoon variability are tightly coupled on orbital timescales. Detailing this phase relationship is currently limited, however, by a lack of unbiased proxy data with excellent age control. A related issue is that the chronology of a widely-used archive of past monsoon variability – organic rich layers (sapropels) in Mediterranean sediments – is potentially biased by an assumed 3000 year (3 kyr) lag between precession minima and sapropel mid-points. Here we present evidence from an eastern Mediterranean sediment core (LC21), which has a well-constrained, radiometrically based chronology, to investigate the timing of sapropel deposition (=East African summer monsoon (EAfSM) variability) relative to changes in insolation, precession, sea level, and rates of sea-level change, during the last 150,000 years. We show that there is not a consistent 3-kyr lag between precession minima and sapropel mid-points, which are instead found to be directly in phase (zero lag) during periods of glacial inception. After glacial terminations, we find that both ice-volume changes and insolation determine the timing of sapropel onset. We also compare EAfSM variability with monsoon proxy records from different regions, and observe in-phase monsoon variability among these regions during the last (Holocene) and penultimate (Eemian) interglacials, and more pronounced regional timing offsets during glacial inception. We conclude that the concept of a 'global monsoon' is too simplistic; boreal monsoons appear to have been synchronous only during periods of ice-volume minima, implying ice-sheet control of monsoon variability at these times.

4.1 Introduction

Monsoon circulation is a key component of global climate dynamics due to its direct role in large-scale heat and moisture redistribution, and its indirect effect on land-albedo feedbacks.

Reconstructions of long-term (centennial to millennial to multi-millennial) variability in monsoon systems therefore represent important contributions toward the understanding of natural (pre-anthropogenic) climate changes. Over the last decade, evidence has accumulated for a tight coupling between (low-latitude) monsoon intensity and (high-latitude) ice-sheet and North Atlantic climate variability (e.g., Schulz et al., 1998; Leuschner and Sirocko, 2000; Wang et al., 2001, 2008; Rohling et al., 2003; Cheng et al., 2006, 2009). This may be expected, given that monsoon and ice-volume proxy records exhibit strong cyclicity in the orbital precession and obliquity periods (e.g., Clemens and Prell, 2003; Larrasoaña et al., 2003; Davis and Brewer, 2009), yet a detailed, mechanistic understanding of long-term monsoon dynamics in relation to orbital (insolation) forcing and global ice-volume changes is far from complete.

Until recently, quantification of monsoon:ice-volume phase relationships has been hindered by a lack of independently dated ice-volume records (i.e., independent from orbital timescales and/or ice-core chronologies). There is also a lack of clarity concerning monsoon phasing relative to precession-driven insolation changes, because different leads/lags are inferred from different types of monsoon proxies and from model simulations (Clemens and Prell, 2003; Kutzbach et al., 2008; Clemens et al., 2010; Ziegler et al., 2010a,b; Weber and Tuenter, 2011). As a result, it remains contested whether a synchronous "global monsoon" exists or not (Caley et al., 2011).

An important archive of past monsoon variability consists of the periodic occurrence of organic-rich sediment layers, or "sapropels", in the eastern Mediterranean (and to a lesser extent in the western and central Mediterranean) (for overviews, see Rossignol-Strick 1985; Rohling, 1994; Emeis et al., 1996, and references therein). The formation of these sapropels has been attributed to combinations of surface-water freshening, reduced deep-water ventilation, and increased export production (e.g., Rossignol-Strick et al., 1982; Rossignol-Strick, 1985; Rohling, 1994; Higgs et al., 1994; Emeis et al., 1996; Jorissen, 1999; Thomson et al., 1999; Mercone et al., 2001; Casford et al, 2003; Abu-Zied et al., 2008). The key driver behind these processes was a reduction of net evaporation over the basin, predominantly due to northward migration of the East African summer monsoon (EAfSM) rainbelt over North African wadi systems and river catchments that drain into the eastern Mediterranean (e.g., Rossignol-Strick et al., 1982; Rossignol-Strick, 1985; Rohling, 1999; Rohling and De Rijk, 1999; Rohling et al., 2002b, 2004; Larrasoana et al., 2003; Marino et al., 2007, 2009; Osborne et al., 2008, 2010). The northward migration of the EAfSM rainbelt was associated with northward migration of the intertropical convergence zone (ITCZ) in response to maximum boreal summer insolation at precession minima.

The exact timing of sapropel formation relative to insolation changes remains unclear because direct radiometric age constraints exist only for the most recent (early to middle Holocene) sapropel S1 (e.g., Lourens et al., 1996; Mercone et al., 2000; Casford et al., 2007; De Lange et al., 2008). On that limited basis, an astronomically-tuned timescale for Mediterranean sediments has been proposed that assumes a 3-kyr lag between precession minima and sapropel mid-points (Hilgen et al., 1993; Lourens et al., 1996, 2004). However, the assumed extrapolation of the specific phase relationship of S1 to older sapropels remains to be tested (e.g., Ziegler et al., 2010a). We have recently presented a radiometrically constrained chronology that spans four sapropels (Grant et al., 2012), which allows such a test to be performed.

Core LC21 in the eastern Mediterranean (Fig. 4.1) contains four sapropels (S1, S3, S4, S5), and – in addition to a radiometrically constrained chronology – has been synchronised with the Red Sea relative sea-level (RSL) record (Grant et al., 2012). Hence, it is an ideal platform for investigating phase relationships between monsoon variability, insolation forcing and global ice-volume fluctuations on orbital timescales. We use it to test the following hypotheses: 1) there is a consistent 3-kyr offset between precession minima and sapropel mid-points, 2) there is a systematic phasing between northward penetration of the EAfSM and changes in global ice volume, 3) the concept of a global monsoon is valid.

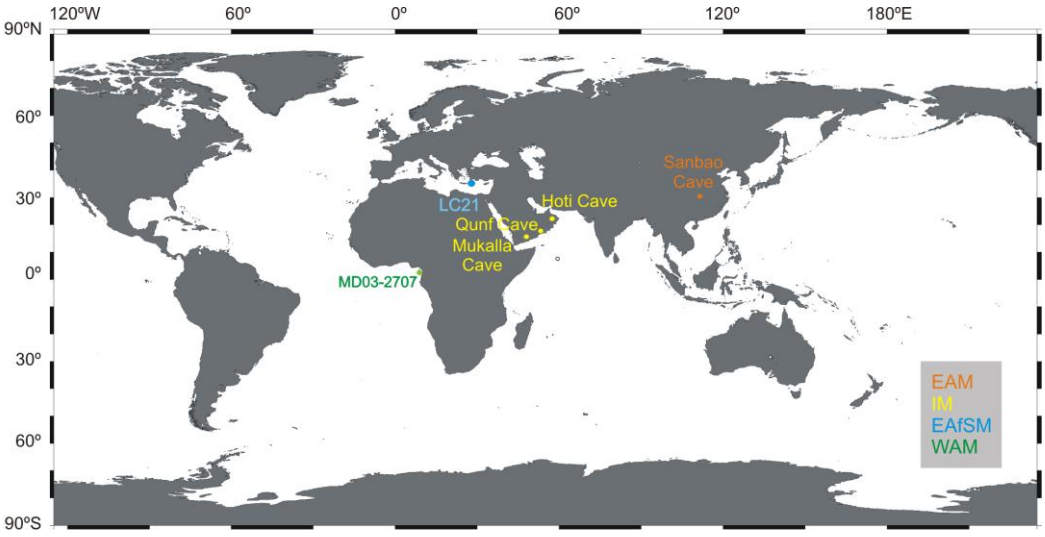

Figure 4.1 Locations of marine cores and speleothem caves discussed in this study, in the context of the East Asian monsoon (EAM), Indian monsoon (IM), East African summer monsoon (EAfSM) and West African monsoon (WAM).

4.2 Methods

Scanning x-ray fluorescence (XRF) elemental analyses of the archive halves of sediment core LC21 (southern Aegean Sea, 35° 40' N, 26° 35' E; Fig. 4.1), were performed at the British Ocean Sediment Core Research Facility (BOSCORF) at the National Oceanography Centre, Southampton, using an Itrax XRF core scanner from Cox Analytical Systems (Gothenburg, Sweden). XRF data were collected every 0.5mm down-core using a molybdenum tube set at 30 kV and 30mA, and a sampling time of 40 seconds directly at the core surface. The exposed core surface was covered with a 4 micron thin SPEX Certi Prep Ultralene1 foil to avoid contamination of the XRF measurement unit and desiccation of the sediment. Subsequent sub-sampling and stable isotope analyses of the same core halves have been described in Grant et al. (2012). The foraminiferal stable oxygen and carbon isotope records discussed below are for the surface-dwelling species *Globigerinoides ruber* (white) ($\delta^{18}O_{ruber}$, $\delta^{13}C_{ruber}$) and the sub-surface dwelling species *Neogloboquadrina pachyderma* (dextral) ($\delta^{18}O_{pac}$, $\delta^{13}C_{pac}$). Tests of these species were selected from >300 μm and 150-300 μm sieved sediment fractions (see Methods in Grant et al., 2012).

4.3 Results

Barium and stable isotope profiles are used to accurately delineate the depths of sapropel boundaries (Fig. 4.2), which are here used to define past intervals when the East African summer monsoon (EAfSM) penetrated north of ~21°N (see Rohling et al., 2002a, 2004; Larrasoaña et al., 2003; Osborne et al., 2008). Redox reactions at the sediment-seawater interface affect the preservation of organic-rich deposits. As a consequence, elements that are enriched in sapropels and which exhibit 'conservative' behaviour in sediments are most suitable for reconstructing down-core sapropel depths. Barium is ideal for this purpose because it is well-preserved in sediments (Dymond et al., 1992), and enriched in sapropels (Thomson et al., 1995; De Lange et al., 2008) due to its association with the decomposition of organic matter in the water column, which in turn is coupled to primary productivity (Dymond et al., 1992).

In core LC21, pronounced increases in Ba at sapropel horizons are accompanied by elevated Vanadium (V) and depleted $\delta^{18}O$ and $\delta^{13}C$ (Fig. 4.2).Vanadium is a redox-sensitive element and precipitates under reducing conditions, so although it should not be used alone to define sapropel boundaries, the good agreement between increases in V and Ba in core LC21 implies that – in this case – elevated V reliably indicates sapropel boundaries (see Thomson

et al., 1995; Nijenhuis et al., 1999). Strongly depleted $\delta^{18}O_{ruber}$ and $\delta^{18}O_{pac}$ values in LC21 sapropels far exceed inferred $\delta^{18}O$ changes associated with global ice-volume reduction at these times (see Fig. 1 in Grant et al., 2012), and are synchronous with negative excursions in $\delta^{13}C_{ruber}$ and $\delta^{13}C_{pac}$ (Fig. 4.2). The $\delta^{18}O_{ruber}$ and $\delta^{18}O_{pac}$ depletions are unlikely to primarily reflect warming of surface and sub-surface waters or an increase in net precipitation over evaporation because neither of these processes would result in a synchronous depletion in both surface- and subsurface-water $\delta^{13}C$. The observed trend is easily explained, however, by monsoon-driven flooding of the North African margin, which would result in a substantial input of isotopically light freshwater and terrestrial carbon into the eastern Mediterranean. Together, therefore, the LC21 Ba, V, $\delta^{18}O$ and $\delta^{13}C$ records effectively delineate the intervals of sapropel formation and preservation in core LC21, and thus the intervals of northward expansion of the EAfSM.

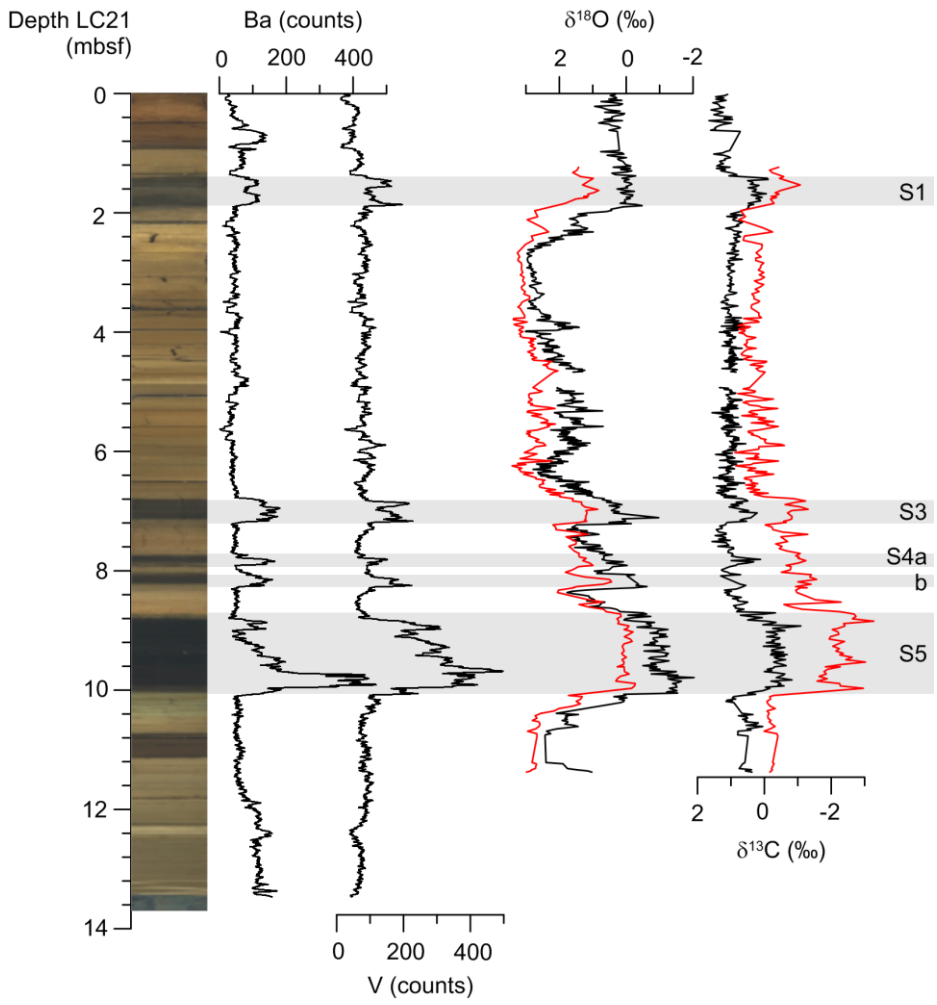

Figure 4.2 Photograph of core LC21 (in metres below sea floor, mbsf) with scanning XRF profiles (21-point moving average) of barium and vanadium, and planktonic foraminierfal $\delta^{18}O$ and $\delta^{13}C$ records from *G. ruber* (white) and *N. pachyderma* (d). Sapropels are indicated (grey rectangles).

4.4 Discussion

4.4.1 Sapropel deposition and insolation maxima/precession minima

Here we consider the timing of sapropel deposition relative to the summer inter-tropical insolation gradient ("SITIG", Fig. 4.3) and the precessional component of insolation. The advantage of using the SITIG rather than a specific latitudinal insolation curve is that it accounts for changes in tropical insolation in both hemispheres, and therefore best captures variability in the insolation forcing of the intertropical convergence zone (ITCZ), which in turn drives the intensity and spatial distribution of monsoon precipitation. We find that the onset of sapropels S3-S5 in core LC21 occurred ~1.5-3 kyr before insolation maxima/precession minima (Fig. 4.3b-d), whereas sapropel S1 deposition began 0.8 kyr after the Holocene insolation maximum/precession minimum (Fig. 4.3a). Previous studies inferred a lag of ~3 kyr between the mid-point of S1 and the nearest insolation maximum/precession minimum (Lourens et al., 1996; De Lange et al., 2008; Ziegler et al., 2010a). We find a comparable phase offset if we considering the S1 midpoint (Fig. 4.3a). It is clear that, regardless of whether sapropel bases or mid-points are used, the concept of a consistent 3-kyr phase offset between precession minima/insolation maxima is valid only within broad tolerances of a few thousand years.

The differences between phase relationships determined using either sapropel bases or mid-points are noteworthy. Sapropel mid-points give the average timing of sapropel formation/preservation and are therefore an appropriate approximation for cross-spectral phase analyses, which typically rely on peak-to-peak signal comparison at a specific frequency. However, the timing of a mid-point depends on the duration of a sapropel, and this clearly varies – both in absolute terms (number of years) and relative to insolation changes. For example, according to the radiometrically constrained chronology of LC21, sapropels S3 and S4 coincide with the interval of maximum insolation values (>520 W/m^2) (Fig. 4.3c,d), but sapropels S1 and S5 extend until insolation drops to ~500 W/m^2 (Fig. 4.3a,b).

The above strongly suggests that, during full interglacials (i.e., considering S1 and S5), EAfSM precipitation and/or northward expansion is sufficiently strong to prolong sapropel deposition under waning insolation, which is consistent with positive vegetation-albedo feedbacks on the meteorological conditions (Nicholson, 2009). Such changes in the duration of sapropels due to indirect (feedback) processes are unlikely to be the same for all sapropels, and this compromises the validity of the concept of a 'systematic' phase

relationship between precession and sapropel mid-points. Because vegetation-albedo feedbacks have not yet had the time to develop at around the time of onset of sapropel deposition, it seems more promising to evaluate phase relationships between precession and the onset/base of sapropels. By that criterion, the lagged onset of sapropel S1 (relative to peak insolation) is clearly unique relative to other sapropels within the last glacial cycle.

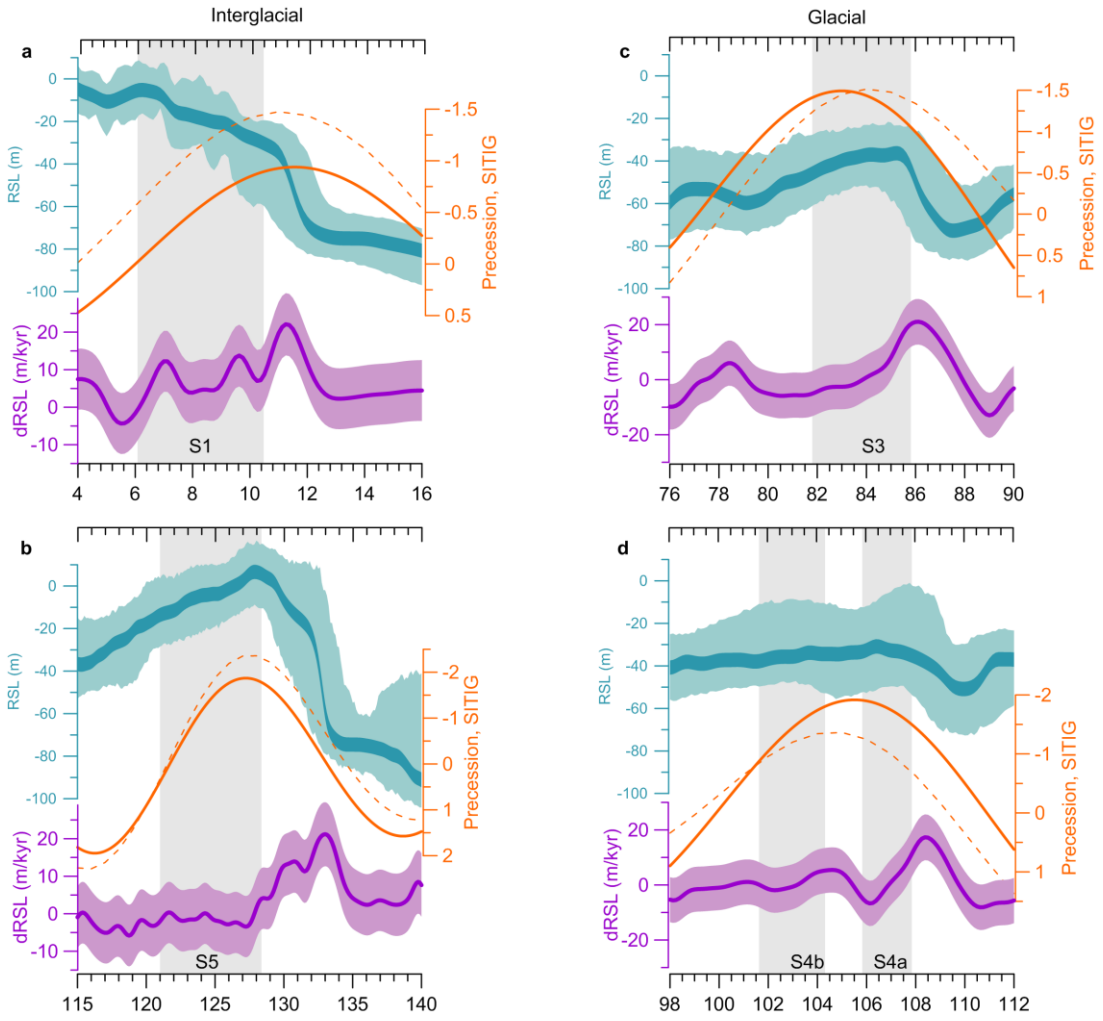

Figure 4.3 Insolation and ice-volume changes during sapropel deposition (= EAfSM maxima) under full interglacial conditions (a, b) and periods of glacial inceptions (c, d). A maximum probability sea-level curve (dark turquoise) with 95% confidence limits (pale turquoise) (Grant et al., 2012) is based on the Red Sea sea-level reconstruction method (Siddall et al., 2003, 2004; Rohling et al., 2009). The subtropical insolation gradient (SITIG, dashed orange) is calculated as the difference between mid-summer insolation at 23˚N and 23˚S, and has been normalised by unit variance, and then negated, in order to plot on the same axis as the normalised precession curve (orange).

Previous work has related the apparently 'delayed' onset of S1 to millennial-scale cooling in the North Atlantic affecting atmospheric circulation over the Mediterranean (Rohling, 1994; Ziegler et al., 2010a). Deep-water convection in the eastern Mediterranean is highly sensitive to cold northerly airflows (see Rohling et al., 2002b; Casford et al., 2003, and

references therein), and episodes of strengthened deep convection in the Mediterranean during the Holocene and last interglacial, relating to temporary weakenings/disruptions in the formation and/or preservation of sapropels S1 and S5, have been correlated with Greenland climate fluctuations (Mercone et al., 2001; Rohling et al., 2002a,b;Casford et al., 2003; Marino et al., 2007, 2009; Osborne et al., 2008).

Earlier studies inferred a link between North Atlantic climate variability and the strength of the Indian and Asian monsoons (Porter and An, 1995; Guo et al., 1996; Schulz et al., 1998; Leuschner and Sirocko, 2000; Rohling et al., 2003), and this has been corroborated by model simulations (Claussen et al., 2003; Jin et al., 2007). More recently, U/Th-dated speleothem records from Chinese caves have provided compelling evidence for a process-link between North Atlantic cold events triggered by meltwater discharges, and delayed onsets of the East Asian summer monsoon (e.g., Wang et al., 2001, 2008; Cheng et al., 2006, 2009). Using LC21, these inferences can now be tested for the first time with paired records of EAfSM and ice-volume variations over four precession minima (see below).

4.4.2 The EAfSM and global ice-volume changes

As previously mentioned, the sapropels in core LC21 correspond to periods when the EAfSM rainbelt reached its maximal northerly penetration. For simplicity, we here refer to these periods as "EAfSM maxima". During the last glacial cycle, the onsets of three EAfSM maxima (S3, S4, and S5) coincided (within ~1 kyr) with the onsets of sea-level highstands, despite differences in the height of these highstands (Fig. 4.3b-d). For sapropel S5 (Fig. 4.3d), this phasing is supported by observations that a somewhat wetter phase developed in the central Red Sea immediately after the last interglacial (LIG) sea-level highstand had been reached (Trommer et al., 2011). Conversely, the Holocene EAfSM maximum (S1) started at a time when sea level was still rising (~4 kyr before a highstand; Fig. 4.3a). These observations suggest that there was no systematic differentiation in EAfSM:ice-volume phase relationships between interglacial (sapropels S1 and S5) and glacial-inception (sapropels S3 and S4) conditions. This lack of systematic behaviour is further illustrated by the presence of an apparent disparity in the EAfSM:ice-volume phasing between the current and last interglacial periods (top panel of Fig. 4.3a,b).

When considering rates of sea-level change (dRSL) rather than RSL itself, however, we find a clear differentiation between EAfSM:ice-volume phasing (at precession minima) within interglacial and glacial-inception periods. In the interglacial cases, EAfSM maxima began after a 50-75% reduction in rates of sea-level rise from their peak rates, and after sea-levels

had risen ~90m (Fig. 4.3a,b). In glacial-inception cases, the onset of EAfSM maxima occurred just after the peak rates of sea-level rise, and after substantially smaller sea-level rises (~15-35m) (Fig. 4.3c,d).

The most obvious potential cause for different EAfSM:ice-volume phasings between the Holocene and LIG relates to the ice-volume histories since the preceding glacial maxima. Termination 1 saw a steady sea-level rise over approximately 120m, whereas Termination 2 was characterised by a steady rise of 90m, which followed an early rise and subsequent brief reversal (see Fig. 3.3 in Chapter 3). Clemens and Prell (2003) and Clemens et al. (2010) invoked large-scale ice-volume changes as the cause of a precession phase-lag in the Indo-Asian summer monsoon, due to their effect on sensible heating of the Asian Plateau. Similarly, past variations in an East Asian monsoon proxy record can be explained in part by changes in global ice volume, and in the rates of ice-volume reduction (see Fig. 3.4 in Chapter 3). However, the inclusion of variable northern hemisphere ice sheets in model simulations of monsoon variability (Ziegler et al., 2010b; Weber and Tuenter, 2011) produced zero phase lag in the precession band, in line with previous simulations based on stationary ice-sheets (Tuenter et al., 2005; Kutzbach et al., 2008). The evident discrepancy between model simulations and data may reflect model limitations, e.g., the crude resolution of ice sheets and ocean circulation, and lack of atmospheric mid-latitude dynamics (Weber and Tuenter, 2011).

The records presented here indicate that changes in the (ultimately precession-driven) northward expansion of the EAfSM were considerably affected by 1) global ice-volume in the interval preceding each precession minimum and, consequently, 2) the amount of subsequent ice-volume loss, as well as 3) the rates of ice-volume reduction. Given that precession-scale variability in the West African summer monsoon (Weldeab et al., 2007) and Indo-Asian summer monsoons (Clemens and Prell, 2003; Wang et al., 2001, 2008; Cheng et al., 2009) has also been linked to large-scale changes in global ice-volume, we now consider whether the changes in monsoon precipitation were synchronous across these different monsoon systems.

4.4.3 A 'global monsoon' during precession minima?

The EAfSM record from core LC21 is compared with six key 'summer monsoon' proxy records representing different monsoon systems of the northern hemisphere (Fig. 4.4). For the East Asian monsoon (EAM), we use a speleothem $\delta^{18}O$ record from Sanbao Cave ($\delta^{18}O_{sanbao}$), China (Cheng et al., 2009); for the Indo-Asian monsoon (IAM), we use a

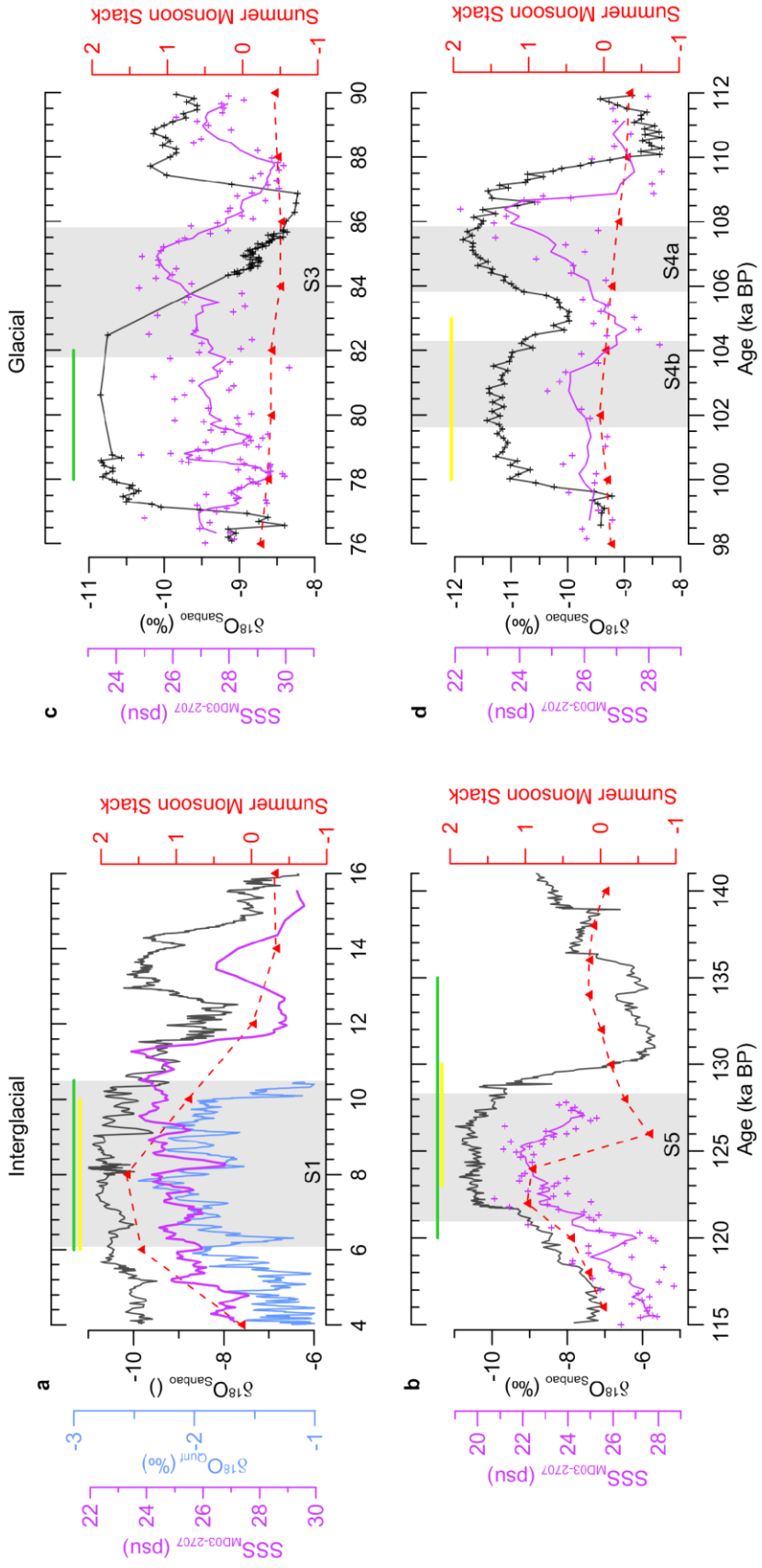

Figure 4.4 Proxy records for the East African summer monsoon (EAfSM; grey rectangles), for sapropels S1 and S5 (a, b) deposited during full interglacial conditions, and sapropels S3 and S4 (c, d) deposited during the last glacial inception. Also shown are: Sanbao Cave, China, speleothem $\delta^{18}O$ (black; Cheng et al., 2009, 2012); Qunf Cave, Oman, speleothem $\delta^{18}O$ (blue; Fleitmann et al., 2003a, 2007); stalagmite growth intervals indicating pluvial periods in Hoti Cave, Oman (green; Fleitmann et al., 2003b) and Mukalla Cave, Yemen (yellow; Fleitmann et al., 2011); an Indo-Asian 'summer monsoon stack' (red; Clemens and Prell, 2003) based on summer monsoon proxies from the northern Arabian Sea; estimated sea surface salinities (SSS) in sediment core MB03-2707 from the East Equatorial Atlantic (EEA) (purple, 3-point running average; Welddeab et al., 2007). Note that for $\delta^{18}O_{sanbao}$, a 9-point running average is plotted in (a), due to high sampling resolution, and datapoints are shown where sample resolution is lower (c, d).

composite 'summer monsoon stack' (SMS) record (Clemens and Prell, 2003); for the Indian monsoon (IM), we use a speleothem $\delta^{18}O$ record from Qunf Cave, Oman (Fleitmann et al., 2007), as well as periods of speleothem growth in Hoti Cave, Oman (Fleitmann et al., 2003a,b) and in Mukalla Cave, Yemen (Fleitmann et al., 2011); and for the West African monsoon (WAM) we use variations in sea surface salinity (SSS) in the East Equatorial Atlantic (EEA) (Weldeab et al., 2007).

First, it is important to note that these various monsoon proxy records reflect different processes. For example, speleothem growth periods in Arabian caves are determined by the position of the Indian monsoon rainbelt (Fleitmann et al., 2003a,b, 2011), while the speleothem $\delta^{18}O$ records reflect the amount and isotopic (source) composition of monsoon precipitation (Clemens et al., 2010; Pausata et al., 2011). However, these control processes are regional expressions of changes in summer monsoon precipitation due to changes in atmospheric circulation on a wide (hemispheric) scale. Hence, it remains instructive to compare the timing of these responses.

Second, we emphasise that the monsoon records are presented here using their original chronologies. As a consequence, any inferred phase relationships will contain age-model-related uncertainties, but we minimise these by focussing on records with sound radiometric age control. Although the WAM record is not radiometrically dated before ~40 ka BP, its chronology is well-constrained by correlation to a layer-counted ice-core between ~40-130 ka BP.

For the four time-slices considered here, we observe better agreement between the timings of change in the different monsoon systems during full interglacial conditions (Fig. 4.4a,b) than during periods of glacial inception (Fig. 4.4c,d). This is particularly noticeable for the Holocene (Fig. 4.4a), when the EAfSM maximum coincides closely (within a millennium) with pluvial periods in Arabia, minimum $\delta^{18}O_{sanbao}$, and highest SMS values. Lower EEA SSS also coincide with this interval, although the lowest values occur before the 'peak monsoon interval' in the other proxy records.

Although the timings of monsoon variations are spread slightly wider (~2 kyr) between the various records during the last interglacial, the main period of inferred summer monsoon intensification is similar (Fig. 4.4b). The only outliers are the two distinctly low SMS values at ~126 and 128 ka BP (Fig. 4.4b). Because sample resolution in the SMS record is relatively poor, this apparent disparity essentially hinges on the accuracy (in age and SMS value) of only one datapoint (at 126 ka BP). Given that all other monsoon proxy records

agree over this interval, we suggest that chronological uncertainties and/or proxy sensitivities in the SMS may explain this discrepancy.

The last period of glacial inception (Marine Isotope Stage [MIS] 5a-d) is generally characterised by larger offsets between the various monsoon proxy records (Fig. 4.4c,d). SMS values remain consistently low, which would imply little strengthening of the IAM. Furthermore, there appears to be an ~4 kyr offset between changes in the African and Indo-Asian monsoons in MIS 5a (Fig. 4.4c). This inferred offset is most clear between the intervals of sapropel S3 deposition and stalagmite growth in Hoti Cave, whereas the EEA SSS and $\delta^{18}O_{sanbao}$ records are more ambiguous; SSS was highly variable between 76 and 90 ka BP, and $\delta^{18}O_{sanbao}$ variations are poorly resolved between 79 and 84 ka BP, in spite of overlapping samples from two stalactites (Wang et al., 2008). Improved resolution in the latter records may further substantiate the potential ~4 kyr offset between African and Indo-Asian monsoon variability during MIS 5a.

In MIS 5c (Fig. 4.4d), there is good agreement between the timings of sapropel 4a and decreases in $\delta^{18}O_{sanbao}$ and EEA SSS, and of sapropel 4b, depleted $\delta^{18}O_{sanbao}$, and a pluvial period in Yemen. Also, proxy records for the WAM, EAFSM, and EAM all show an interruption in monsoon conditions at around 104-106 ka BP. Nonetheless, the onset of significantly reduced SSS in the EEA seems to have preceded the onset of the Yemeni pluvial period by ~4 kyr, in agreement with observations for MIS 5a (Fig. 4.4c). Overall, therefore, phase offsets between different monsoon systems appear to be minimal during interglacial periods, and to have increased during the period of glacial inception.

A previous investigation into the timing of WAM, EAfSM, IM, and EAM variability over the past 45 kyrs also found regional phase differences, especially with respect to precession and obliquity variations (Caley et al., 2011). This contrasts with inferences of recurrent episodes of near-synchronous (within age uncertainties) millennial-scale variability between the North Atlantic climate and the EAfSM, IM and EAM (e.g., Schulz et al., 1998; Wang et al., 2001; Rohling et al., 2002a). Weldeab et al. (2007) concluded that WAM and EAM variability was synchronous during the last deglaciation, but not during MIS 5, and Larrasoaña et al. (2003) noted the coincidence of (monsoon-related) dust flux minima, on precession timescales, between dust records from the western equatorial Atlantic and eastern Mediterranean – regions influenced by the WAM and EAfSM, respectively.

These diverse observations are not necessarily incompatible with our findings, and often reflect ‘average’ monsoon phasings based on time-series analyses or specific events. Here

we offer a more nuanced assessment based on well-constrained data for four time-slices corresponding to precession minima. Results from this study are consistent with the concept of a 'global monsoon' operating during interglacials, but regional differences appear to become more significant with the development of large ice sheets.

4.5 Conclusions

Results of this study strongly suggest that the notion of a systematic 3-kyr lag between precession minima and sapropel mid-points is unfounded, although such a lag does apply to the Holocene sapropel S1. The timing of sapropel mid-points appears to be directly in phase with precession minima (zero lag) during periods of glacial inception, whereas during full interglacials, the onset of sapropel formation is determined by ice-volume changes over the preceding glacial termination. In the latter case, sapropel formation appears to have been instigated after sea-levels had risen ~90m, and after rates of sea-level rise had dropped by at least 50% from their peak rates. Evidence from several more interglacial sapropels will be required to test the validity of – and further quantify – this apparent phase relationship.

These findings are therefore consistent with previous suggestions that ice-sheet variability affected the timing of boreal summer monsoons during periods of ice-volume minima. However, the concept of a 'global monsoon' on orbital timescales is too generalised; different monsoon systems appear to have been synchronised only during ice-volume minima, with regional timing offsets in monsoon variability becoming more significant as northern hemisphere ice sheets expanded. Variable response times to precession forcing likely reflect the sensitivity of environmental proxies to different processes and critical thresholds in specific localities.

References

Abu-Zied, R.H., Rohling, E.J., Jorissen, F.J., Fontanier, C., Casford, J.S.L. Cooke, S. 2008. Benthic foraminiferal response to changes in bottom water oxygenation and organic carbon flux in the eastern Mediterranean during LGM to Recent times. Marine Micropaleontology 67, 46-68.

Caley, T., Malaizé, B., Revel, M., Ducassou, E., Wainer, K., Ibrahim, M., Shoeaib, D., Migeon, S., Marieu, V. 2011. Orbital timing of the Indian, East Asian and African boreal monsoons and the concept of a 'global monsoon'. Quaternary Science Reviews 30, 3705-3715.

Casford, J.S.L., Rohling, E.J., Abu-Zied, R.H., Jorissen, F.J., Leng, M., Thomson, J. 2003. A dynamic concept for eastern Mediterranean circulation and oxygenation during sapropel formation. Palaeogeography, Palaeoclimatology, Palaeoecology 190, 103-119.

Casford, J.S.L., Abu-Zied, R., Rohling, E.J., Cooke, S., Fontanier, Ch., Leng, M., Millard, A., Thomson, J. 2007. A stratigraphically controlled multi-proxy chronostratigraphy for the eastern Mediterranean. Paleoceanography 22, PA4215, doi:10.1029/2007PA001422.

Cheng, H., Edwards, R.L., Wang, Y., Kong, W., Ming, Y., Kelly, M.J., X. Wang., Gallup, C.D., Liu, W. 2006. A penultimate glacial monsoon record from Hulu Cave and two-phase glacial terminations. Geology 34, 217-220.

Cheng, H., Edwards, R.L., Broecker, W.S., Denton, G.H., Kong, X.G., Wang, Y.J., Zhang, R., Wang, X.F., 2009. Ice age terminations. Science 326, 248-252.

Claussen, M., Ganopolski, A., Brovkin, V., Gerstengarbe, F.-W., Werner, P. 2003. Simulated global-scale response of the climate system to Dansgaard/Oeschger and Heinrich events. Climate Dynamics 21, 361-370.

Clemens, S.C., Prell, W.L. 2003. A 350,000 year summer-monsoon multi-proxy stack from the Owen ridge, Northern Arabian Sea. Marine Geology 201, 35-51.

Clemens, S.C., Prell, W.L., Sun, Y. 2010. Orbital-scale timing and mechanisms driving Late Pleistocene Indo-Asian summer monsoons: Reinterpreting cave speleothem $\delta^{18}O$. Paleoceanography 25, PA4207, doi:10.1029/2010PA001926.

Davis, B.A.S., Brewer, S. 2009. Orbital forcing and role of the latitudinal insolation/ temperature gradient. Climate Dynamics 32, 143-165.

De Lange, G.J., Thomson, J., Reitz, A., Slomp, C.P., Speranza Principato, M., Erba, E., Corselli, C. 2008. Synchronous basin-wide formation and redox-controlled preservation of a Mediterranean sapropel. Nature Geoscience 1, 606-610.

Emeis, K.-C., Robertson, A.H.F., Richter, C., and shipboard scientific party. 1996. Proceedings of the Ocean Drilling Program, Initial Reports, Leg 160. College Station, Texas.

Dymond, J., Suess, E., Lyle, M. 1992. Barium in deep-sea sediment: a geochemical proxy for paleoproductivity. Paleoceanography 7, 163-181.

Grant, K.M., Rohling, E.J., Bar-Matthews, Ayalon, A., Bronk Ramsey, C., M., Satow, C., Medina-Elizalde, M., Roberts, A.P. 2012. Rapid coupling between ice volume and polar temperature over the past 150,000 years. Nature 491, 744-747.

Fleitmann, D., Burns, S.J., Neff, U., Mangini, A., Matter, A., 2003a. Changing moisture sources over the last 330,000 years in Northern Oman from fluid-inclusion evidence in speleothems. Quaternary Research 60, 223-232.

Fleitmann, D., Burns, S.J., Mudelsee, M., Neff, U., Kramers, J., Mangini, A., Matter, A. 2003b. Holocene forcing of the Indian monsoon recorded in a stalagmite fromSouthern Oman. Science 300, 1737-1739.

Fleitmann, D., Burns, S.J., Mangini, A., Mudelsee, M., Kramers, J., Villa, I., Neff, U., Al-Subbary, A.A., Buettner, A., Hippler, D., Matter, A. 2007. Holocene ITCZ and Indian monsoon dynamics recorded in stalagmites from Oman and Yemen (Socotra). Quaternary Science Reviews 26, 170-188.

Fleitmann, D., Burns, S.J., Pekala, M., Mangini, A., Al-Subbary, A., Al-Aowah, M., Kramers, J., Matter, A. 2011. Holocene and Pleistocene pluvial periods in Yemen, southern Arabia. Quaternary Science Reviews 30, 783-787.

Grant, K.M., Rohling, E.J., Bar-Matthews, M., Ayalon, A., Medina-Elizalde, M., Bronk Ramsey, C., Satow, C., Roberts, A.P. 2012. Rapid coupling between ice volume and polar temperature over the past 150 kyr. Nature 491, 744-747.

Guo, Z., Liu, T., Guiot, J., Wu, N., Lü, H., Han, J., Liu, J., Gu, Z. 1996. High frequency pulses of East Asian monsoon climate in the last two glaciations: link with the North Atlantic. Climate Dynamics 12, 701-709.

Higgs, N.C., Thomson, J., Wilson, T.R.S., Croudace, I.W. 1994. Modification and complete removal of eastern Mediterranean sapropels by postdepositional oxidation. Geology 22, 423-426.

Hilgen, F.J., Lourens, L.J., Berger, A., Loutre, M.F. 1993. Evaluation of the astronomically calibrated time scale for the Late Pliocene and earliest Pleistocene. Paleoceanography 8, 549-565.

Jin, L., Chen,F., Ganopolski, A., Claussen, M. 2007. Response of East Asian climate to Dansgaard/Oeschger and Heinrich events in a coupled model of intermediate complexity. Journal of geophysical Research 112, D06117, doi:10.1029/ 2006JD007316.

Jorissen, F.J. 1999. Benthic foraminiferal successions across Late Quaternary Mediterranean sapropels. Marine Geology 153, 91-101.

Kutzbach, J.E. 1981. Monsoon climate of the Early Holocene: Climate experiment with the Earth's orbital parameters for 9000 years ago. Science 214, 59-61.

Kutzbach, J.E., Liu, X., Liu, Z., Chen, G. 2008. Simulation of the evolutionary response of global summer monsoons to orbital forcing over the past 280,000 years. Climate Dynamics 30, 567-579.

Larrasoaña, J.C., Roberts, A.P., Rohling, E.J., Winklhofer, M., Wehausen, R. 2003. Three million years of monsoon variability over the northern Sahara. Climate Dynamics 21, 689-698.

Leuschner, D.C., Sirocko, F. 2000. The low-latitude monsoon climate during Dansgaard-Oeschger cycles and Heinrich Events. Quaternary Science Reviews 19, 243-254.

Lourens, L.J., Antonarakou, A., Hilgen, F.J., van Hoof, A.A.M., Vergnaud-Grazzini, C.,Zachariasse, W.J. 1996. Evaluation of the Plio-Pleistocene astronomical timescale. Paleoceanography 11, 391-413.

Lourens, L.J., Hilgen, F., Shackleton, N. J., Laskar, J., Wilson, D. 2004. The Neogene Period. In: Gradstein, F. M., Ogg, J. G., Smith, A. G. (eds) A Geologic Timescale 2004, Cambridge University Press, 409-440.

Marino, G., Rohling, E.J., Rijpstra, W.I., Sangiorgi, F., Schouten, S., Sinninghe Damsté, J.S. 2007. Aegean Sea as driver for hydrological and ecological changes in the eastern Mediterranean. Geology 35, 675-678.

Marino, G., Rohling, E.J., Sangiorgi, F., Hayes, A., Casford, J.S.L., Lotter, A.F., Kucera, M., Brinkhuis, H. 2009. Early and middle Holocene in the Aegean Sea: interplaybetween high and low latitude climate variability. Quaternary Science Reviews 28, 3246-3262.

Mercone, D., Thomson, J., R.H., Croudace, I.W., Siani, G., Paterne, M., Troelstra, S. 2000. Duration of S1, the most recent Mediterranean sapropel, as indicated by AMS radiocarbon and geochemical evidence. paleoceanography 15, 336-347.

Mercone, D., Thomson, J., Abu-Zied, R.H., Croudace, I.W., Rohling, E.J. 2001. High-resolution geochemical and micropalaeontological profiling of the most recent eastern Mediterranean sapropel. Marine Geology 177, 25-44.

Nicholson, S.E. 2009. A revised picture of the structure of the “monsoon” and land ITCZ over West Africa. Climate Dynamics 32, 1155-1171.

Nijenhuis, I.A., Bosch, H.J., Sinnighe Damsté, J.S., Brumsack, H.-J., de Lange, G.J. 1999. Organic matter and trace element rich sapropels and black shales: a geochemical comparison. Earth and Planetary Science Letters 169, 277-290.

Osborne, A.H., Vance, D., Rohling, E.J., Barton, N., Rogerson, M., Fello, N. 2008. A humid corridor across the Sahara for the migration "Out of Africa" of early modern humans 120,000 years ago. Proceedings of the National Academy of Science, USA, 105, 16444-16447.

Osborne, A., Marino, G., Vance, D., Rohling, E.J. 2010. Eastern Mediterranean surface water Nd during Eemian sapropel S5: monitoring northerly (mid latitude) versus southerly (sub tropical) freshwater contributions. Quaternary Science Reviews 29, 2473-2483.

Pausata, F.S.R., Battisti, D.S., Nisancioglu, K.H., Bitz, C.M. 2011. Chinese stalagmite 18O controlled by changes in the Indian monsoon during a simulated Heinrich event. Nature Geoscience 4, 474-480.

Porter, S., An, Z.S. 1995. Correlation between climate events in the North Atlantic and China during the last glaciation. Nature 375, 305-308.

Reichart, G.J. 1997. Late Quaternary variability of the Arabian Sea monsoon and oxygen minimum zone. Geologica Ultraiectina 154, pp. 174.

Rohling, E.J. 1994. Review and new aspects concerning the formation of Mediterranean sapropels. Marine Geology 122, 1-28.

Rohling, E.J. 1999. Environmental control on Mediterranean salinity and $\delta^{18}O$. Paleoceanography 14, 706-715.

Rohling, E.J., De Rijk. S. 1999. The Holocene climate optimum and last glacial maximum in the Mediterranean: the marine oxygen isotope record. Marine Geology 153, 57-75.

Rohling, E.J., Cane, T.R., Cooke, S., Sprovieri, M., Bouloubassi, I., Emeis, K.-C., Schiebel, R., Kroon, D., Jorissen, F.J., Lorre, A., Kemp, A.E.S. 2002a. African monsoon variability during the previous interglacial maximum. Earth and Planetary Science Letters 202, 61-75.

Rohling, E.J., Mayewski, P.A., Hayes, A., Abu-Zied, R.H., Casford, J.S.L. 2002b. Holocene atmosphere-ocean interactions: records from Greenland and the Aegean Sea. Climate Dynamics 18, 587-593.

Rohling, E.J., Mayewski, P.A., Challenor, P. 2003. On the timing and mechanism of millennial-scale climate variability during the last glacial cycle. Climate Dynamics 20, 257-267.

Rohling, E.J., Grant, K., Bolshaw, M., Roberts, A.P., Siddall, M., Hemleben, Ch., Kucera, M. 2009. Antarctic temperature and global sea level closely coupled over the past five glacial cycles. Nature Geoscience 2, 500-504.

Rossignol-Strick, M. 1985. Mediterranean quaternary sapropels, an immediate response of the African monsoon to variation of insolation. Palaeogeography, Palaeoclimatology, Palaeoecology 49, 237-263.

Rossignol-Strick, M., Nesteroff, W., Olive, P., Vergnaud-Grazzini, C. 1982. After the deluge, Mediterranean stagnation and sapropel formation. Nature 295, 105-110.

Schulz, H., von Rad, U., Erlenkeuser, H. 1998. Correlation between Arabian Sea and Greenland climate oscillations of the past 110,000 years. Nature 393, 54-57.

Siddall, M., Rohling, E.J., Almogi-Labin, A., Hemleben, Ch., Meischner, D., Schmeltzer, I., Smeed, D.A. 2003. Sea-level fluctuations during the last glacial cycle. Nature 423, 853-858.

Siddall, M., Smeed, D.A., Hemleben, Ch., Rohling, E.J., Schmeltzer, I., Peltier, W.R. 2004. Understanding the Red Sea response to sea level. Earth and Planetary Science Letters 225, 421-434.

Thomson, J., Higgs, N.C., Wilson, T.R.S., Croudace, I.W., De Lange, G.J., van Santvoort, P.J.M. 1995. Redistribution and geochemical behaviour of redox sensitive elements around S1, the most recent Eastern Mediterranean sapropel. Geochimica et Cosmochimica Acta 59, 3487-3501.

Thomson. G., Mercone, D., de Lange, G.J., van Santvoort, P.J.M. 1999. Review of recent advances in the interpretation of Eastern Mediterranean sapropel S1 from geochemical evidence. Marine Geology 153, 77-89.

Trommer, G., Siccha, M., Rohling, E.J., Grant, K., van der Meer, M.T.J., Schouten, S., Baranowski, U., Kucera, M. 2011. Sensitivity of Red Sea circulation to sea level and insolation forcing during the last interglacial. Climate of the Past 7, 941-955.

Tuenter, E., Weber, S.L., Hilgen, F.J., Lourens, L.J., Ganopolski, A. 2005. Simulation of climate phase lags in response to precession and obliquity forcing and the role of vegetation. Climate Dynamics 24, 279-295.

Weber, S.L., Tuenter, E. 2011. The impact of varying ice sheets and greenhouse gases on the intensity and timing of boreal summer monsoons. Quaternary Science Reviews 30, 469-479.

Weldeab, S., Lea, D.W., Schneider, R.R., Andersen, N., 2007. 155,000 years of West African monsoon and ocean thermal evolution. Science 316, 1303-1307.

Wang, Y.J., Cheng, H., Edwards, R.L., An, Z.S., Wu, J.Y., Shen, C.C., Dorale, J.A. 2001. A high-resolution absolute-dated Late Pleistocene monsoon record from Hulu Cave, China. Science 294, 2345-2348.

Wang, Y., Cheng, H., Edwards, R.L., Kong, X., Xiaohua, S., Chen, S., Wu, J., Jiang, X., Wang, X., Zhisheng, A. 2008. Millennial- and orbital-scale changes in the East Asian monsoon over the past 224,000 years. Nature 28, 1090-1093.

Weber, S.L., Tuenter, E. 2011. The impact of varying ice sheets and greenhouse gases on the intensity and timing of boreal summer monsoons. Quaternary Science Reviews 30, 469-479.

Ziegler, M., Tuenter, E., Lourens, L.J. 2010a. The precession phase of the boreal summer monsoon as viewed from the eastern Mediterranean (ODP Site 968). Quaternary Science Reviews 29, 1481-1490.

Ziegler, M., Lourens, L.J., Tuenter, E., Hilgen, F.J., Reichart, G.J., Weber, S.L. 2010b. Precession phase offset between Arabian Sea biological productivity and the Indian summer monsoon. Paleoceanography 25, PA3213, doi:10.1029/2009PA001884.

Chapter 5

Changes in humidity in the eastern Mediterranean over the last 150,000 years

K. M. Grant, E. J. Rohling, R.B. Pearce, A. Hinchliff, R. Williams, J. Amies

Author contributions: KMG led the study and wrote the chapter; EJR contributed to chapter refinement; RBP, AH and RW performed clay mineralogical analyses; JA acquired new stable isotope data for ODP Site 967.

Changes in humidity in the eastern Mediterranean over the last 150,000 years

K.M. Grant, E.J. Rohling, R.B. Pearce, A. Hinchliffe, J. Amies, R. Williams

Abstract

The eastern Mediterranean is an important region for palaeoclimate and archaeological research, yet few high-resolution palaeo-environmental records from this region extend over the entire last glacial cycle. A related issue is that key Mediterranean $\delta^{18}O$ records have not been adequately deconvolved into their component environmental signals. We present high-resolution stable isotope, clay mineralogical, and Saharan dust-proxy records for the past 150,000 years. By synchronising these records with the U/Th-dated Soreq Cave speleothem $\delta^{18}O$ record, and with a continuous relative sea-level (RSL) record from the Red Sea, we are able to determine, for the first time, the isotope 'residuals' for speleothem and planktonic foraminiferal $\delta^{18}O$ records, which represent the regional environmental influences, after exclusion of source-water and ice-volume effects. Our multi-proxy dataset suggests that local precipitation in the Levant did not increase significantly during the deposition of sapropels S1, S3 and S4. Conversely, we find evidence for elevated levels of net moisture availability in the Levant during most of the Last Interglacial deposition of sapropel S5, although its onset may have coincided with a relatively arid spell in the Levant. We also infer that intervals of increased moisture availability in the eastern Mediterranean occurred during marine isotope stages (MIS) 2, 4, and 6, but we cannot (yet) distinguish between the influences of changes in evaporation and precipitation or resolve the seasonality of the inferred moisture changes. The results identify MIS 3 as the period of greatest climatic instability and/or spatial and temporal climatic contrasts in the eastern Mediterranean within the last 150,000 years.

5.1. Introduction

The eastern Mediterranean is a key region for palaeoclimate studies because it is sensitive to remote climate changes at both high/middle latitudes in the northern hemisphere (Rohling et al., 2002a; Casford et al., 2003; Mayewski et al., 2004; Clare et al., 2008; Kotthoff et al., 2011; Milner et al., 2013), and at low latitudes via drainage of African monsoon rainfall (Rossignol-Strick et al., 1982; Rossignol-Strick, 1985; Rohling et al., 2002b; Scrivner et al., 2004; Osborne et al., 2008). Hence, sedimentary archives from this basin offer the potential for disentangling variabilities in these major climate system components, and for establishing unambiguous phase relationships between these variabilities and the ecological and biogeochemical responses to them (e.g., Rohling et al., 2006; Abu-Zied et al., 2008;

Marino et al., 2009; Osborne et al., 2010; Grelaud et al., 2012; Schmiedl et al., 2010). The eastern Mediterranean is also an interesting region for study because it is a well-known site of convective deep-water formation and atmospheric cyclogenesis, and is characterised by sharply defined seasonal extremes of wet and drought (e.g., Rohling et al. 2009, and references therein).

Reconstructions of past changes in eastern Mediterranean climate have largely relied on foraminiferal, coccolith, dinoflagellate cyst and pollen census data, stable oxygen isotope ($\delta^{18}O$) records from cave speleothems and foraminifera, bulk sediment geochemical data, lake-level records in the Mediterranean borderlands, clay mineralogical studies, and organic geochemical data. Despite this abundance of information, a detailed understanding of eastern Mediterranean palaeoclimate changes over the last glacial cycle still remains to be established. To date, this has been impeded by issues associated with proxy limitations, a scarcity of continuous, high-resolution records with good chronological control, and a dearth of single sample series containing co-registered signals that can unambiguously detail phase relationships between different forcing processes.

Examples of proxy issues concerning $\delta^{18}O$-based climate reconstructions for the eastern Mediterranean are as follows. First, marine $\delta^{18}O$ records are commonly restricted to discrete sapropel intervals (e.g., Casford et al., 2002, 2003; Rohling et al., 2002a,b, 2004, 2006; Marino et al., 2007, 2009), or – if longer periods of time are covered – have a relatively low sample resolution (e.g., Fontugne and Calvert, 1992; Kroon et al., 1998; Lourens et al., 2004, and references therein). Second, glacial-interglacial sea-level fluctuations affect the $\delta^{18}O$ of Mediterranean seawater (Rohling, 1999), yet this ice-volume signal remains to be properly deconvolved from Mediterranean $\delta^{18}O$ timeseries. Third, speleothem $\delta^{18}O$ records from the Levant have generally been interpreted in terms of past changes in precipitation (Bar-Matthews et al., 2000; Vaks et al., 2006), yet there is a strong "source water" effect – from eastern Mediterranean surface water dilution – on Levantine speleothem $\delta^{18}O$ (Bar-Matthews et al., 2003; McGarry et al., 2004; Kolodny et al., 2005; Almogi-Labin et al., 2009) and this effect remains to be accounted for in palaeoclimate studies.

Examples concerning the reliability of pollen-based climate reconstructions for the eastern Mediterranean are that there is significant spatial variability in pollen taxa in this region (Bottema, 1995), that it may not be possible to distinguish between drought-resistant/intolerant species within a particular genus (Tzedakis, 2009), and that the chronology of some pollen records may be questioned (Tzedakis, 2009; Langgut et al., 2011). In addition, palaeo-vegetation (and lake-level) data reflect net moisture availability,

rather than precipitation *per se*, and so will be strongly overprinted by variations in evaporation that are determined by a different set of climatological control parameters than precipitation. Finally, most precipitation availability around the eastern Mediterranean is dominated by evaporative moisture supply from the eastern Mediterranean Sea, so that increased precipitation *per se* may be a signal of enhanced net water loss from the sea (given that some of the vapour will be transported outside the catchment area) (see Marino et al., 2009).

The present study focuses on highly resolved, co-registered signals, so that phase relationships may be determined without ambiguity, and uses multi-proxy evidence to overcome issues that affect individual proxy records. We take advantage of the fact that the Soreq Cave speleothem $\delta^{18}O$ record ("$\delta^{18}O_{speleo}$"), the planktonic foraminiferal (*Globigerinoides ruber*) $\delta^{18}O$ record from marine core LC21 ("$\delta^{18}O_{ruber}$") (Fig. 5.1), and the Red Sea relative sea-level (RSL) record have been chronologically synchronised to each other (Grant et al., 2012). We use these tightly constrained relationships to remove the source-water and ice-volume effects from these records, to produce the first deconvolved climate and hydrological records for the eastern Mediterranean, which extend over the entire last glacial cycle, have a high sampling resolution, and have excellent radiometric age control. We supplement these records with new clay mineralogical data from the same sample series of core LC21, and we also correlate a new surface-water $\delta^{18}O$ record from ODP Site 967 (Levantine Basin; Fig. 5.1) to the LC21 *G. ruber* $\delta^{18}O$ record, in order to synchronise a previously published dust record from ODP Site 967 (Larrasoaña et al., 2003) with the radiometrically constrained Soreq-LC21-RSL chronology. We then discuss this complete suite of records in the context of climate conditions with a focus on periods of sapropel deposition (equivalent to precession minima/boreal insolation maxima), and glacial intervals (marine isotope stages (MIS) 2-4 and 6).

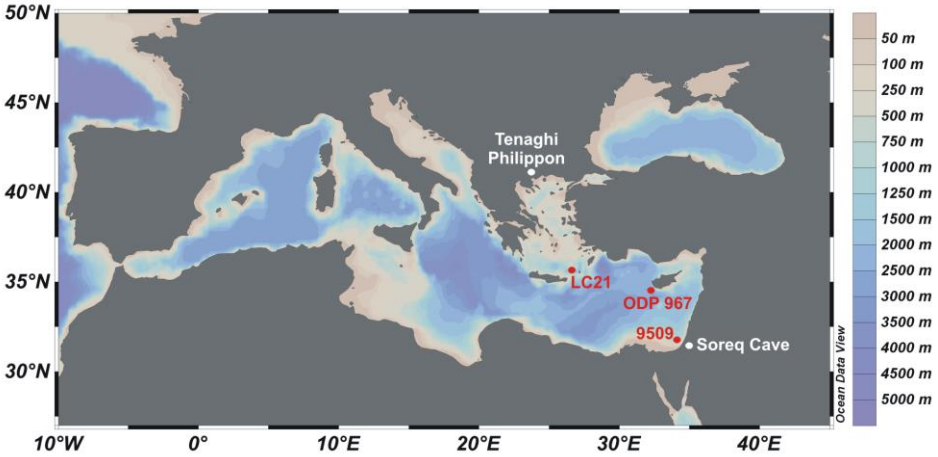

Figure 5.1 Bathymetric map of the Mediterranean showing locations of sites discussed in this study. Water depths are in metres (m).

5.2. Materials and methods

5.2.1. Clay mineralogical analyses

Sampling methods for the archive half of core LC21 have been described in Grant et al. (2012). Three hundred and fifty six of the sub-samples were then selected at 2-5 cm intervals for clay mineralogical analysis by X-ray diffraction (XRD) at the National Oceanography Centre, Southampton. The samples were treated with 1 M acetic acid to remove carbonate, and the <2μm fraction was separated by settling under gravity according to Stokes' Law. Next, the samples were saturated with magnesium ions, washed by centrifugation, smeared onto glass discs, and analysed using standard clay techniques using a PANalytical X'Pert pro diffractometer fitted with a Cu X-ray tube. The machine operating conditions were set at 35kV, 40mA utilising automatic slits, and a step size of 0.02º 2 Θ at 1 second per step. Samples were run as air-dried, ethylene glycolated, and heated preparations. Saturation with ethylene glycol confirms the presence or absence of expandable clay phases (=smectites), and heating to 550ºC assists with the identification of chlorite and/or kaolinite. The semi-quantitative analysis method for the clays was based on that detailed by Biscaye (1965), and the results are presented as closed sum calculations with a precision of ±5-10%.

5.2.2. ODP Site 967

For the magnetic susceptibility and stable isotope records of ODP Site 967, seven continuous u-channels were taken from Holes A B, and D. The u-channels were then sliced every 1 cm down-core to produce a continuous series of discrete, ~4 cm^3 (2x2x1 cm) sediment samples. Down-core sample depths for ODP Site 967 have been converted to "revised metres composite depth" (rmcd) (Sakamoto et al., 1998) in order to maintain a consistent down-core depth scale between different drill-holes at the same site. Each discrete sample was measured for magnetic susceptibility using an Agico KLY-4S Kappa Bridge, and then weighed and freeze-dried. For stable isotope analyses, tests of the surface-dwelling planktonic foraminifer *Globigerinoides ruber* (white) were selected from the >300 μm sieved fraction (see Methods in Grant et al., 2012), at a down-core sampling resolution of about 5 cm.

5.2.3. Chronology

The chronology of core LC21 has been established in Chapter 2 (Grant et al., 2012). The age model for ODP Site 967 is developed by graphic correlation of its $\delta^{18}O_{ruber}$ record with LC21 $\delta^{18}O_{ruber}$, using the Analyseries software (Paillard, 1996) (Fig. 5.2). Correlation tie-points have been selected on the basis of signal similarity and by examining (and minimising) changes in sedimentation rates (SRs) produced by different age-depth correlations. The well-defined sapropel stratigraphy in both cores has guided our correlation. Additional depth-age constraints in the ODP Site 967 age model have been obtained from two geochemically 'finger-printed' tephra layers (Satow, 2012): the Cape Riva (21.705±0.311 ka BP; Eriksen et al., 1990) and Kos Plateau Tuff (KPT) (166.1±2 ka BP; Bachmann et al., 2010) (Fig. 5.2).

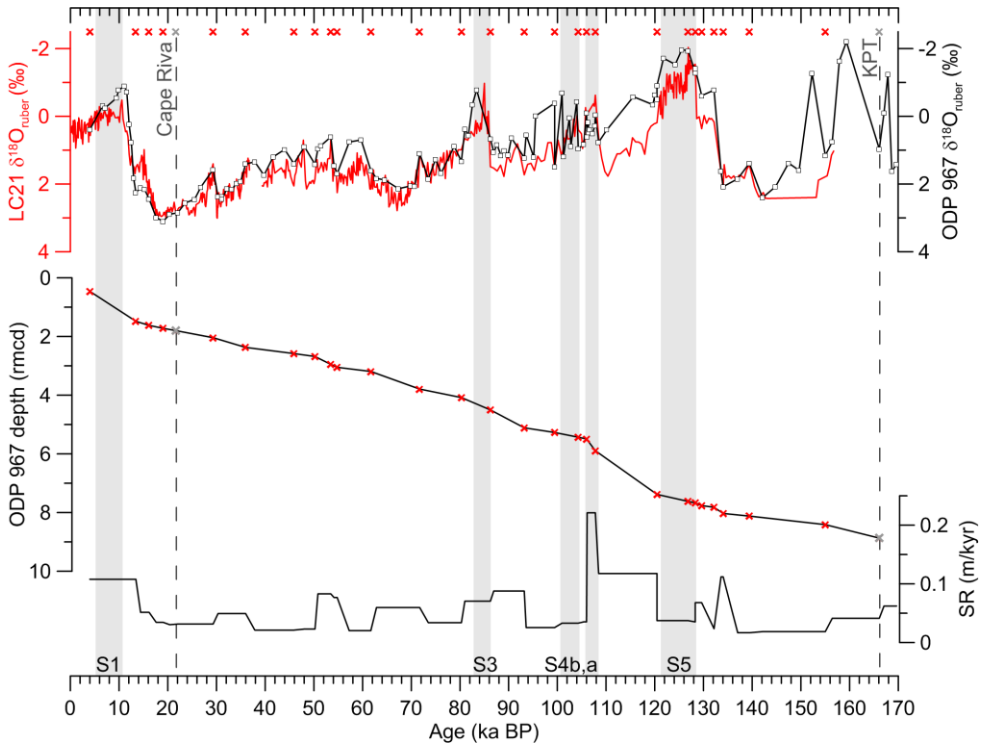

Figure 5.2 Construction of the ODP Site 967 age model. Top panel: Correlation of the ODP Site 967 $\delta^{18}O_{ruber}$ record (black) to the LC21 $\delta^{18}O_{ruber}$ record (red) at 27 tie-points (red crosses). The Cape Riva and Kos Plateau Tuff (KPT) tephra horizons (grey crosses and dashed lines) and intervals of sapropel deposition (grey rectangles) are also indicated. Bottom panel: Linearly interpolated sedimentation rates (SR, blue) and age-depth curve (black line with red crosses) derived from age control points in the top panel.

5.2.4. $\delta^{18}O$ residuals

As mentioned before, global ice-volume changes strongly affect Mediterranean seawater $\delta^{18}O$ due to the restriction of exchange flow through the Strait of Gibraltar with lowering of

sea level (Rohling, 1999). There also is a direct evaporation-precipitation link between the $\delta^{18}O$ composition of eastern Mediterranean surface waters and speleothems from the Levant (Matthews et al., 2000; Bar-Matthews et al., 2003; McGarry et al., 2004; Kolodny et al., 2005; Almogi-Labin et al., 2009; Marino et al., 2009; Grant et al., 2012). Therefore, both the Soreq cave $\delta^{18}O_{speleo}$ record and the LC21 $\delta^{18}O_{ruber}$ record contain an important sea-level component (2.5±0.5 ‰ at 2σ, for a full glacial-interglacial isotopic change equivalent to 120 m of sea-level change; Rohling, 1999; Grant et al., 2012).

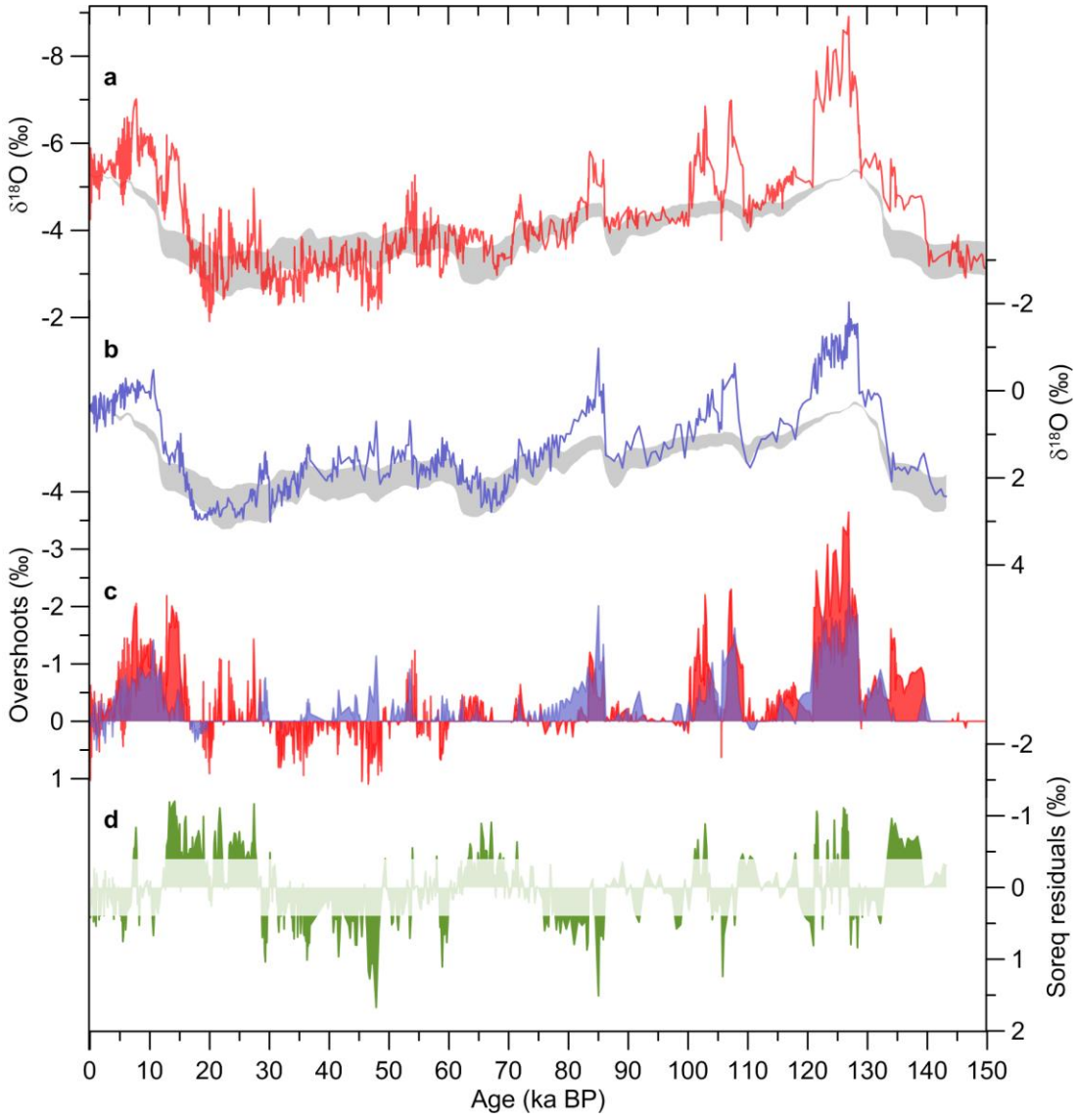

Figure 5.3 (**a** and **b**): Speleothem $\delta^{18}O$ record from Soreq cave (red) and planktonic foraminiferal (*G. ruber*) $\delta^{18}O$ record from core LC21 (blue), superimposed on a maximum probability sea-level record which has been converted into Mediterranean surface-water $\delta^{18}O$ values (grey shading; see Methods). (**c**) 'Overshoots' of the Soreq cave (red shading) and LC21 (blue shading) $\delta^{18}O$ records beyond the 95% confidence limits of sea-level-equivalent $\delta^{18}O$ variations (see Methods). Note that overlapping overshoots appear as purple. (**d**) Normalised (by unit variance) residual $\delta^{18}O$ signal for Soreq Cave (green shading) after removing variations in source-water $\delta^{18}O$. Variations within 2σ uncertainty limits (pale green) are not considered to be significant.

We use a (Soreq-synchronised) maximum probability relative sea-level (RSL) record (Grant et al., 2012) to remove the sea-level influence from the $\delta^{18}O_{speleo}$ and $\delta^{18}O_{ruber}$ records (Fig. 5.3a,b). This first required interpolation of the RSL record to the age-steps of the $\delta^{18}O_{speleo}$ and $\delta^{18}O_{ruber}$ records. Next, the RSL record was converted into eastern Mediterranean $\delta^{18}O$-equivalent values, using scalings of 2.0 ‰ (= +2σ) and 3.0 ‰ (= -2σ) per 120 m sea-level change; these records are defined as "$RSL_{eq+2\sigma}$" and "$RSL_{eq-2\sigma}$". Finally, $RSL_{eq+2\sigma}$ and $RSL_{eq-2\sigma}$ were normalised to the respective Holocene values of $\delta^{18}O_{ruber}$ and $\delta^{18}O_{speleo}$ (based on the average for each record over the interval 0-3 ka BP; Fig. 5.3a,b), and subtracted from $\delta^{18}O_{ruber}$ and $\delta^{18}O_{speleo}$. This produced records of 'overshoots' that are defined by $\delta^{18}O_{ruber}$ and $\delta^{18}O_{speleo}$ values lighter than $RSL_{eq+2\sigma}$ or heavier than $RSL_{eq-2\sigma}$ (Fig. 5.3c). The $\delta^{18}O_{ruber}$ overshoots represent glacial-cycle-corrected signals of surface-water $\delta^{18}O$ changes due to African monsoon run-off events and regional eastern Mediterranean climate variability. The $\delta^{18}O_{speleo}$ overshoots reflect these hydrological components of surface-water $\delta^{18}O$ change as well as local climatic overprints related to isotope fractionation during the pathway from evaporation of eastern Mediterranean source waters, through precipitation/ evapotranspiration, to cave-carbonate precipitation. Fractionation processes during this pathway are dominated by temperature and amount effects.

Finally, we determine the residual isotopic signal for $\delta^{18}O_{speleo}$ ("$Soreq_{residuals}$"), which isolates only the local climatic overprints, by removing the source-water component (Fig. 5.3d). This was achieved by interpolating the $\delta^{18}O_{speleo}$ and $\delta^{18}O_{ruber}$ records to the same age-steps, subtracting the mean from each record so that they are centred about a mean of zero, and then subtracting the zero-centralised $\delta^{18}O_{ruber}$ from the zero-centralised $\delta^{18}O_{speleo}$. The uncertainty of the $Soreq_{residuals}$ about the mean value (0±0.38 at 2σ) was calculated using a root mean squares calculation, and combines uncertainties for the average Holocene value of $\delta^{18}O_{speleo}$ (-5.22±0.29) and $\delta^{18}O_{ruber}$ (0.41±0.24). The $Soreq_{residuals}$ record gives, for the first time, a deconvolved local eastern Mediterranean climate signal, from which any bias related to monsoon run-off or global glacial cycles has been removed.

We present no 'overshoots' record for the ODP Site 967 $\delta^{18}O_{ruber}$ series because it is (as yet) measured at a much coarser resolution than the LC21 $\delta^{18}O_{ruber}$ record; the latter therefore is much more informative. However, similar $\delta^{18}O_{ruber}$ variations in core LC21 and at ODP Site 967 (Fig. 5.2) suggest that the LC21 overshoots represent basin-wide changes in eastern Mediterranean surface water $\delta^{18}O$.

5.3. Results

5.3.1. Clays

Illite is the dominant clay mineral in core LC21 (33-55%), followed closely by expandable clays (=smectites; 21-47%). Kaolinite and chlorite (8-17%) are minor constituents of the LC21 clay assemblage (Fig. 5.4). To minimise closed-sum effects and aid palaeo-environmental interpretations, clay mineral variations in LC21 are expressed as smectite/illite and kaolinite/chlorite ratios (e.g., Ehrmann et al., 2007a,b, and references therein) (Fig. 5.4). Illite is derived mainly from physical weathering in cooler and drier climates, and the predominant source of illite to the eastern Mediterranean is in fluvial discharges from southern Europe draining into the northern Aegean Sea (Ehrmann et al., 2007a,b; Poulos, 2009); aeolian transport of illite from southern Europe and the Sahara has also been proposed (Hamann et al., 2009). Smectites, however, are derived from chemical weathering under relatively warm and humid conditions, and they dominate the clay fraction in riverine inputs into the eastern Mediterranean from the Near East and the Nile (Ehrmann et al., 2007a,b; Hamann et al., 2009; Poulos, 2009). Smectite/illite ratios in eastern Mediterranean sediments therefore qualitatively reflect warm-wet versus cool-dry climate variations, as well as the relative input of fluvial discharges from the eastern/southeastern versus northern borderlands.

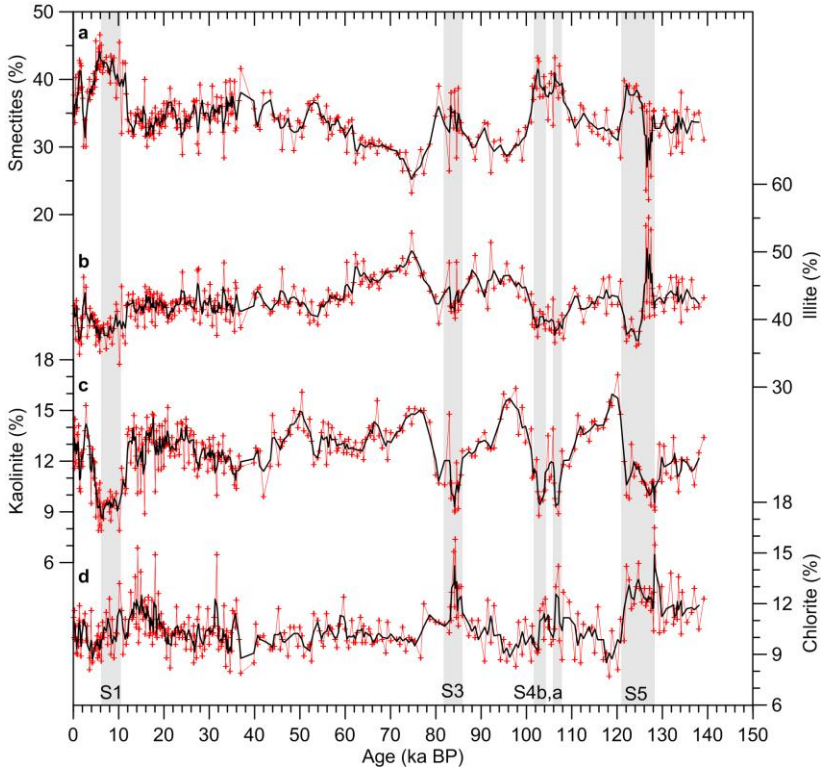

Figure 5.4 Percentage distributions of the main clay mineral groups in core LC21. For each group, a 3-point running mean (black) is superimposed on all datapoints (red). Sapropel intervals are illustrated (grey rectangles).

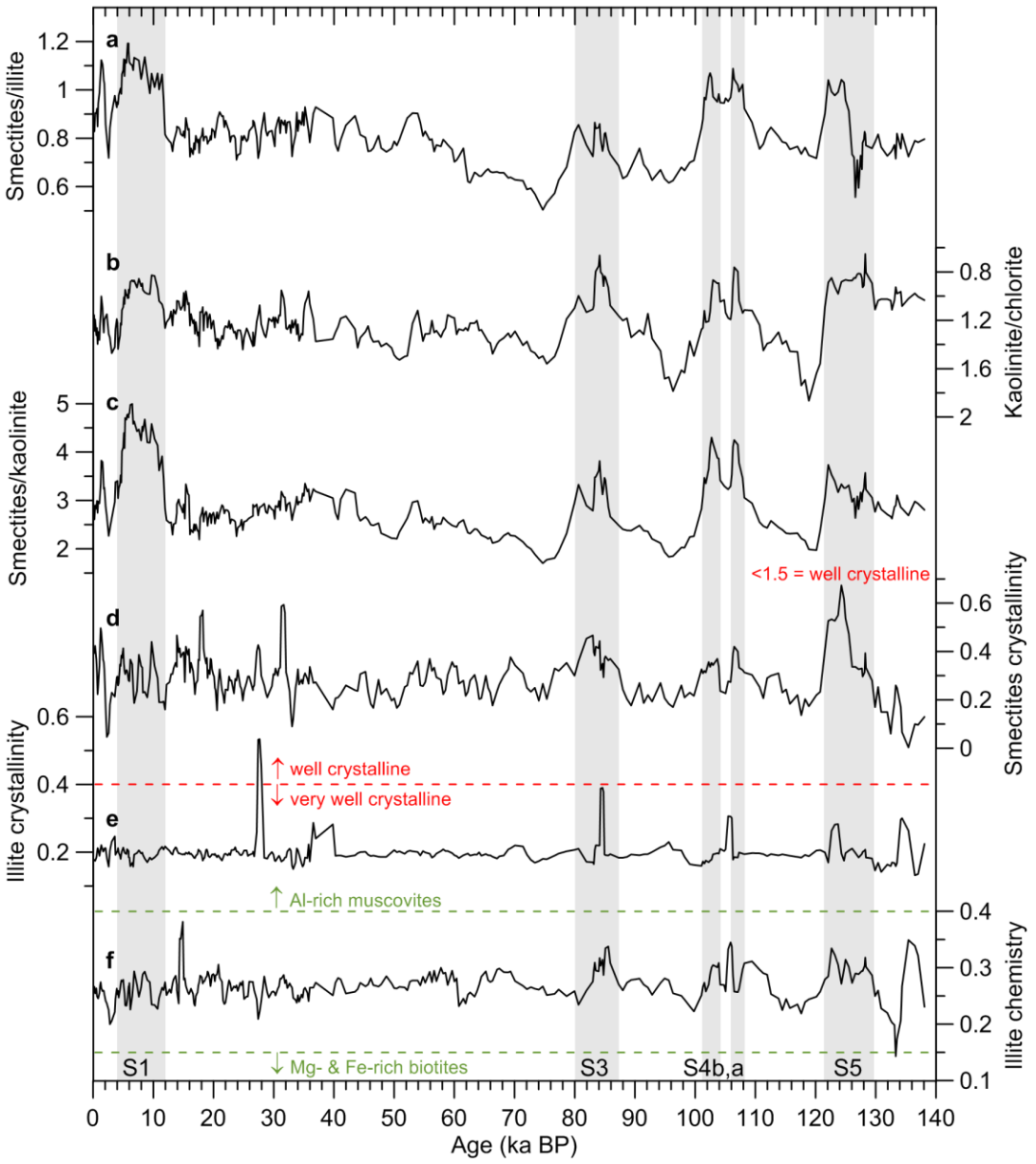

Figure 5.5 Clay mineral data from core LC21. Ratios of smectites/illite (**a**), kaolinite/chlorite (**b**), and smectites/kaolinite (**c**) are shown as 3-point running means. Crystallinities of smectites (**d**) and illite (**e**) are measured as half-height peak widths (Δ°2Θ); for illite, values <0.4 (red dashed line) indicate very well crystalline, and values of 0.4-0.6 indicate well crystalline. For smectite crystallinities, all values are well below 1.5 (threshold not shown) and are therefore well crystalline. For illite chemistry (peak areas, **f**), values >0.4 and <0.15 (green dashed lines) indicate Al-rich muscovites and Mg- and Fe-rich biotites, respectively. Sapropel intervals are illustrated (grey rectangles).

There is no dominant source of chlorite for the eastern Mediterranean and its concentrations are low throughout the Aegean (Ehrmann et al., 2007a,b). Kaolinite, however, is predominantly sourced from North Africa, and is transported into the Aegean and Levantine basins by the prevailing westerly winds and/or the Nile River discharge (Venkatarathnam and Ryan, 1971; Ehrmann et al., 2007a,b; Hamann et al., 2009; Poulos, 2009). Kaolinite is

formed by chemical weathering, which is enhanced in warmer and wetter climates, yet its erosion and subsequent aeolian transport from the African continent will be augmented under cooler, drier conditions. In core LC21, the near-inverse covariation between smectite/illite and kaolinite/chlorite ratios (Fig. 5.5a,b), suggests that kaolinite fluctuations mainly reflect aeolian rather than fluvial (Nile) transport processes.

Smectite and illite crystallinities are expressed as the half-height peak width ($\Delta°2\Theta$) of the smectite 17Å and illite 10Å peaks, whereby values <1.5 and <0.6 represent well-crystalline smectites and illites, respectively (Ehrmann et al., 2007a,b). In core LC21, half-height peak widths are <0.7 and <0.6 for smectites and illites, respectively (Fig. 5.5d,e), indicating highly crystalline minerals (Ehrmann et al., 2007a,b). Well-crystalline smectites characterise the clay composition of Nile discharge (Venkatarathnam and Ryan, 1971, Stanley and Wingerath, 1996; Ehrmann et al., 2007a,b), which suggests that LC21 smectites are predominantly sourced from the Nile. In the study region, illite crystallinity is a less useful parameter, because well-crystalline illites occur in both northern and southern Aegean sediments (Ehrmann et al., 2007a,b).

Information about illite chemistry can be revealed by the 5Å/10Å peak-area ratio, where values >0.4 are indicative of Al-rich illites (muscovites) while those <0.15 typify Mg- and Fe-rich illites (biotite) (Ehrmann et al., 2007a,b). In core LC21, 5Å/10Å peak area ratios are ~0.2-0.35 (Fig. 5.5f), so that illite deposition at this site over the last glacial cycle was not dominated by any specific mineral, which limits the usefulness of this measure in the study region.

5.3.2. Dust proxies

Larrasoaña et al. (2003) established an environmental magnetic proxy for down-core hematite fluctuations at ODP Site 967, based on measurements of isothermal remanent magnetism. We have now transposed this record ('Hem') to the Soreq-LC21-RSL chronology (Fig. 5.6e). Larrasoaña et al. (2003) demonstrated that their hematite proxy was a reliable indicator of past Saharan dust inputs to the eastern Mediterranean, in contrast to magnetic susceptibility measurements which, although useful for approximating past dust fluxes in some regions (e.g., Bloemendal and deMenocal, 1989; deMenocal, 1995; Hoogakker et al., 2004), also reflect the reduction and oxidation of magnetic minerals at sapropel boundaries in eastern Mediterranean sediments (Larrasoaña et al., 2008). However, our magnetic susceptibility results for ODP Site 967 generally agree well with variations in Hem, particularly during MIS 1 and 5 (Fig. 5.6e). This suggests that, for these intervals, the

magnetic susceptibility record may be used to clarify the timing of dust-flux changes because it is at a higher-resolution than the Hem record.

5.4. Discussion

5.4.1. Eastern Mediterranean climate during times of sapropel formation

Comparison of the $Soreq_{residuals}$ (Fig. 5.6b) with the $\delta^{18}O_{speleo}$ and $\delta^{18}O_{ruber}$ overshoots (Fig. 5.6c) for S1, S3 and S4 reveals strongly negative values for the overshoots, whereas the $Soreq_{residuals}$ show no statistically significant depletions within S3 and S4a, and only minor depletions in S1 and S4b. Hence, it is only during S5 that both residuals and overshoots exhibit a negative excursion. As mentioned before, the residuals are the best approximation of temperature-fractionation and amount effects affecting Soreq Cave $\delta^{18}O_{speleo}$, while the overshoots contain important influences from hydrological (notably African monsoon) impacts on eastern Mediterranean surface-water $\delta^{18}O$. Therefore, our observations for S1, S3, S4, and S5 strongly suggest that that three (S1, S3, S4) of these intervals of monsoon-flooding into the eastern Mediterranean did not coincide with significantly elevated local (net) humidity in the Levant; only the interval of S5 shows unequivocal evidence for this.

These inferences are consistent with: *(a)* model simulations, which suggest that northward penetration of the African monsoon rainbelt during precession minima did not extend as far as the North African coast (Tuenter et al., 2003); and *(b)* a comprehensive synthesis of Mediterranean palaeoclimatic data, which concluded that the onset of sapropel deposition during interglacials was not driven by fluvial discharges into the northern Mediterranean, when this region most likely experienced summer aridity (Tzedakis, 2009). Furthermore, for the period of sapropel S1, a multi-proxy study of laminated Lake Van sediments, Turkey, concluded that wettest conditions were established after 8.2 ka BP (Wick et al., 2003), well after the onset of S1 deposition. That also agrees with the most recent compilation of Lake Lisan (Dead Sea levels), which showed very low lake levels during the period of S1 deposition (Torfstein et al., 2013). Presumably, warm ambient conditions caused strong evaporative loss, so that while local precipitation may have been enhanced, the net freshwater budget remained more arid than today (see discussion of this balance in Frumkin et al., 2011, and references therein).

The clay mineralogy of LC21 offers supporting information. Higher smectite/illite ratios in most sapropel intervals (except for the first half of S5) also suggest that there was no substantial increase in (net) precipitation over river catchments draining into the northern

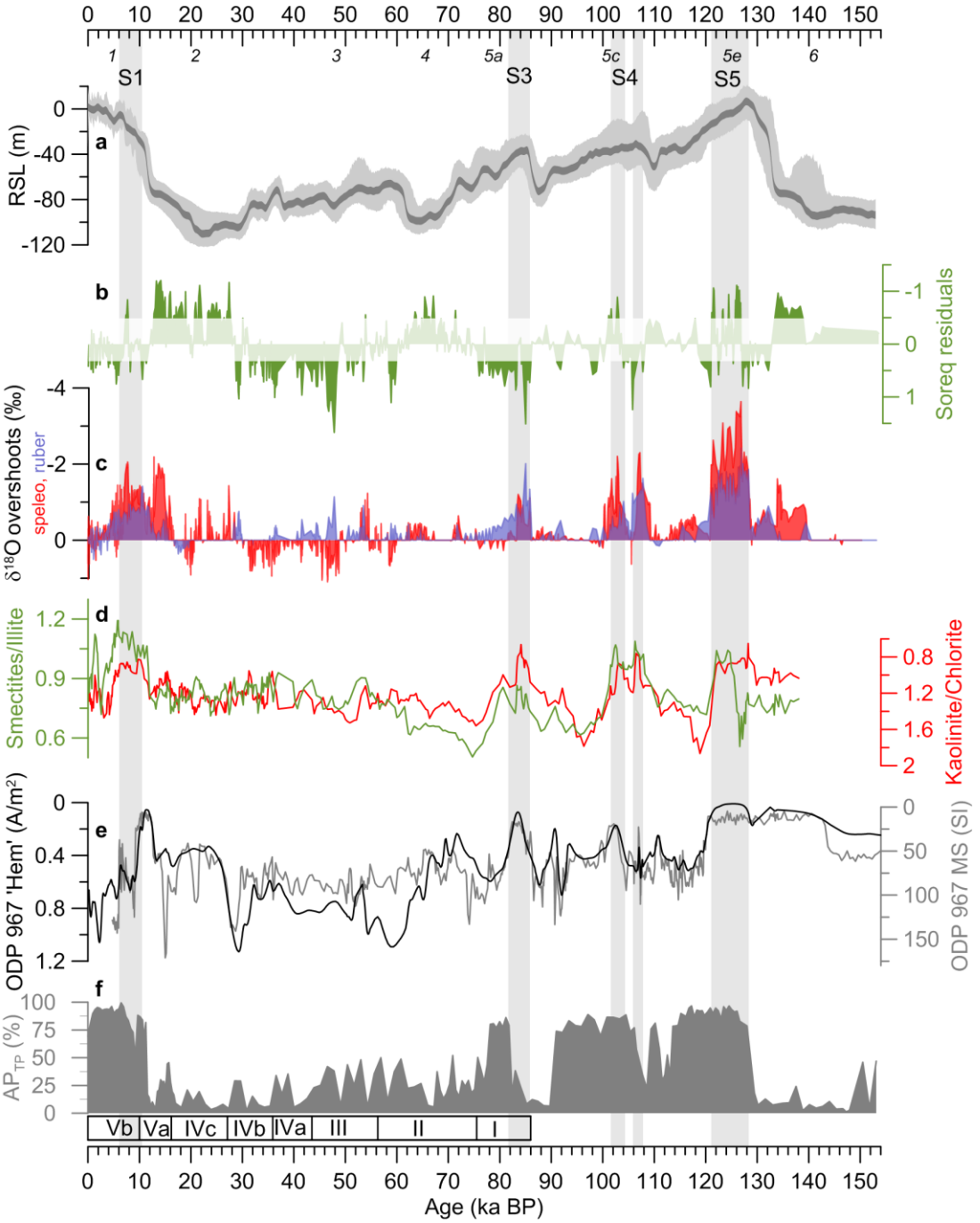

Figure 5.6 Palaeo-environmental records from core LC21, ODP Site 967, and Tenaghi Phillipon, Greece, in the context of glacial-interglacial climate changes. (**a**) Red Sea relative sea-level (RSL) curve, showing confidence intervals of 95% for all data (light grey) and for the probability maximum (dark grey). (**b**) Soreq Cave $\delta^{18}O$ residuals (green), as in Fig. 5.3d. (**c**) Soreq Cave (red) and LC21 (blue) $\delta^{18}O$ overshoots, as in Fig. 5.4c. (**d**) Smectite/illite (green) and kaolinite/chlorite (red) ratios in core LC21. (**e**) An aeolian dust record from ODP Site 967 ('Hem', black), based on an environmental magnetic parameter (see Larrasoaña et al., 2003), and variations in magnetic susceptibility (MS, grey) measured at higher resolution on the same core samples. Note the reversed y-axes. (**f**) Percentage arboreal pollen (AP) in a terrestrial core from Tenaghi Phillipon (TP), Greece (data from Lang and Wolff, 2011, after Tzedakis et al., 2006). Also indicated are: Marine isotope stages (MIS) 1-6, sapropel numbers (top) and pollen zonation scheme (I-V) of Langgut et al., 2011 (bottom).

Aegean Sea at these times. The marked low in the smectite/illite ratio at the onset of S5 is caused by an increase in the illite fraction of the LC21 clay assemblage to 55%. This coincides with the last interglacial (LIG) sea-level highstand and initially positive $Soreq_{residuals}$ that imply either: *(i)* an increased transport/supply of illite into the southern Aegean Sea from southern European rivers, or *(ii)* an increase in aridity that led to increased illite production from physical weathering. Although explanation *(i)* cannot be ruled out, it seems to disagree with positive $Soreq_{residuals}$. Conversely, explanation *(ii)* seems to be in agreement with those, and also with evidence for a peak in Mediterranean sclerophylls during the initial period (first ~2 kyr) of sapropel deposition in interglacials, which strongly suggests summer aridity (Tzedakis et al., 2002, 2003; Tzedakis, 2009, and references therein).

The above findings clearly contrast with previous suggestions of increased regional precipitation around the eastern Mediterranean during precession minima. For example, Kallel et al. (1997, 2000) inferred that the salinity of eastern Mediterranean surface waters (SSS) was homogenous during sapropel deposition, and suggested that this reflected an increase in local precipitation. Some model simulations of the Mediterranean freshwater budget during precession minima also suggest that the effects of enhanced river discharge into the northern Mediterranean, and enhanced net precipitation over the Mediterranean, are equal to or greater than the effect of increased Nile discharge (Meijer and Tuenter, 2007). Similarly, high percentages of arboreal pollen in the intervals of S1, S4b and S5 in mainland Greece (Fig. 5.6f), and S1 and S3 in a southern Levantine marine core (Langgut et al., 2011) (bottom panel, Fig. 5.6) have been interpreted as indicating warmer and wetter conditions (Langgut et al., 2011). Other palynological studies of the eastern Mediterranean had also inferred an increase in summer precipitation during times of sapropel formation (e.g., Rossignol-Strick, 1987, 1999; Wijmstra et al., 1990; Rossignol-Strick and Paterne, 1999).

With respect to the pollen data, Tzedakis (2009) questioned the reliability of these previous interpretations, and suggested that drought-resistant species or winter precipitation equivalent to the present-day regime could explain the observed trends, without the need to invoke enhanced summer precipitation. The inference that homogenous eastern Mediterranean SSS during times of sapropel deposition reflects increased local precipitation is also disputable, because freshwater inputs from the Nile would have been well-mixed throughout the eastern Mediterranean by efficient, counter-clockwise surface circulation. Moreover, a statistical assessment of stable oxygen isotope gradients through the Mediterranean basin for the time of S1 deposition indicated that strongest depletion clearly occurred in the Levantine region, in the vicinity of the Nile outlet (Rohling and De Rijk,

1999). Those authors also contested the calibration of $\delta^{18}O$ into SSS as used by Kallel et al. (1997, 2000), and these objections were given further quantitative weight by Rohling (1999) and Rohling et al. (2004). Hence, the model results of Meijer and Tuenter (2007) are intriguing, but they are not well supported by data and remain to be substantiated by other modelling studies.

Finally, we compare the above inferences with proxies of aeolian dust inputs into the eastern Mediterranean based on clay mineralogical data from core LC21 (Fig. 5.6d) as well as the ODP Site 967 dust record on its newly adjusted chronology (Fig. 5.6e). Relatively low kaolinite/chlorite ratios in sapropel intervals (Fig. 5.6d) imply reduced aeolian dust inputs from North Africa, which is consistent with a reduction in the dust source-area as vegetation cover expanded northwards with the monsoon rainbelt (Larrasoaña et al., 2003). Good agreement (in an opposite sense) between large-scale transitions in smectite/illite and kaolinite/chlorite ratios in LC21 is consistent with a common (monsoonal) forcing mechanism. Good agreement between changes in the clay ratios and the records of overshoots during sapropel intervals (Fig. 5.6) again supports the proposition that the overshoots predominantly reflect monsoon-related freshwater inputs into the eastern Mediterranean during precession minima/insolation maxima.

The ODP Site 967 dust proxy record also shows low values in S5, S4b, S3 and at the start of S1, in agreement with kaolinite/chlorite ratios, but inferred dust fluxes appear to be elevated in S4a and most of S1 (Fig. 5.6e). Previous work has demonstrated that on longer (million-year) timescales, dust-flux variations at ODP Site 967 show strong cyclicity in the precession band (Larrasoaña et al., 2003), with dust-flux minima corresponding to precession minima. Variations in kaolinite/chlorite in LC21 clearly follow the same trend, so an explanation is required for the discrepancies in detail between LC21 kaolinite/chlorite ratios and the ODP Site 967 dust proxy, during S4a and S1. The current data set does not allow a conclusive explanation, but it is striking that both discrepancies are closely associated with a ‘sapropel interruption’ due to centennial-scale cold spells with improved convective deep-water formation (evident in S4, and especially well known from S1 in core LC21 and throughout the eastern Mediterranean; Rohling et al., 1997; Rohling et al., 2002a; Mercone et al., 2001; Casford et al., 2003; Rohling and Pälike, 2005; Abu-Zied et al., 2008). In support of that notion, the elevated dust fluxes in sapropels S4a and S1 also correspond to temporary decreases in arboreal pollen (Fig. 5.6e,f). We tentatively propose that different timescales of response may exist for the processes of liberation and ablation of kaolinite than for ablation of haematite, and that these different timescales result in contrasting responses to brief, centennial-scale environmental changes.

5.4.2. Eastern Mediterranean climate during glacials

$Soreq_{residuals}$ are mainly negative in MIS 2, 4 and 6, and positive in MIS 3 (Fig. 5.6b). We will focus first on MIS 2, 4, and 6 (section 5.4.2.1) and then consider palaeo-environmental changes in the eastern Mediterranean during MIS 3 (section 5.4.2.2).

5.4.2.1. Colder glacial intervals (MIS 2, 4, 6)

Marine isotope stages 2, 4, and 6 correspond to relatively low dust fluxes (Fig. 5.6e) and mainly negative overshoots (Fig. 5.6c) which, together with negative $Soreq_{residuals}$, suggest an increase in net precipitation. This translates as either reduced evaporation, increased precipitation, or a combination of both.

The inferred increased precipitation and/or reduced evaporation agree with reconstructions of past lake levels in the Mediterranean borderlands, which found highstands at 24-27 ka BP in Lake Lisan, Israel (Bartov et al., 2002, 2004) and at 24-26 ka BP in Lake Kinneret, Israel (Hazan et al., 2005) (Fig. 5.6). These dates agree with the radiometrically-dated timing of beach deposits in Kastritsa Cave (Greece) at 24.5-28.5 ka BP, which were interpreted as shoreline deposits of previously elevated lake levels (Galanidou et al., 2000; Galanidou and Tzedakis, 2001). Similarly, a reconstruction of the "ELA" (equilibrium line altitude) of glaciers for the western and central Mediterranean during the LGM implies steep vertical gradients in atmospheric temperatures, and therefore local convective precipitation (Kuhlemann et al., 2008). Further evidence for an increase in effective moisture in the eastern Mediterranean during MIS 2-4 and 6 comes from Ma'ale Efrayim Cave, Israel, where speleothem growth was limited to these intervals only (Vaks et al., 2003).

The clay mineralogical data from core LC21 show lower (higher) average smectite/illite (kaolinite/chorite) ratios in MIS 2, 4, and 6 than in sapropel intervals, and minimum smectite/illite ratios are observed in MIS 4. At first glance, those observations might imply increased aridity. However, depleted smectite/illite ratios may also reflect a rise in Eurasian river discharge into the northeastern Mediterranean, relative to Nile inputs. Smectite/illite ratios in MIS 2-3 are comparable to those in the warmer MIS 5a and 5d (Fig. 5.6d), so distinguishing between smectite/illite values for (warmer) sapropel versus colder glacial intervals is not without ambiguity. Also, there is less covariation between smectite/illite and kaolinite/chlorite ratios during the colder intervals of the last glacial cycle, which suggests against a common mechanism driving clay mineral abundances. These observations call for

caution when interpreting clay mineralogical changes in core LC21 outside of sapropel times (boreal insolation maxima) in simple terms of aridity versus humidity; more complex controlling processes seem to be at work.

Palaeovegetation studies based on pollen records have also suggested increased aridity during the coldest glacial periods. Arboreal pollen taxa in a peat core from Tenaghi Philippon, Greece, were at a minimum in MIS 2 and 6, and up to 50% lower than present-day values in MIS 4 (Fig. 5.6f), while in the pollen zonation scheme of Langgut et al. (2011) (bottom panel, Fig. 5.6), zone IVc represents the coldest and driest interval of the last 86 kyr, with lowest tree abundances, and zone II is characterised by increasing aridification. Similar palynological interpretations of cold aridity in the Mediterranean during the last glacial period are common in the literature (e.g., Wijmstra et al., 1990; Cheddadi and Rossignol-Strick, 1995; Elenga et al., 2000)

The apparent dichotomy among climate reconstructions for the last glacial period in the Mediterranean region has been discussed in detail by Tzedakis (2007, 2009). Those reviews demonstrated that seemingly incompatible climatic inferences (e.g., increased aridity and precipitation) might be reconciled with more thorough proxy interpretations (e.g., accounting for the seasonality of precipitation and drought), and with the use of improved chronologies and high-resolution records. For example, increased storminess during glacial periods (e.g., Enzel et al., 2008; Kuhlemann et al., 2008) may have resulted in less frequent but more intense deluges (Prentice et al., 1992; Vaks et al., 2003), which coexisted with cold winters and summer drought. Results of the present study are compatible with this suggestion, but a conclusive synthesis cannot yet be offered.

5.4.2.2. MIS 3

$Soreq_{residuals}$ are positive for most of MIS 3, in contrast to MIS 2, 4 and 6, and coincide with above-average dust fluxes (Fig. 5.6b,e). Furthermore, there is good agreement in the timing of dust maxima and elevated $Soreq_{residuals}$ at around 30 and 60 ka BP; both records suggest increased net aridity during MIS 3. Interestingly, MIS 3 is the only period when the $\delta^{18}O_{speleo}$ and $\delta^{18}O_{ruber}$ overshoots diverge; the $\delta^{18}O_{ruber}$ overshoots are negative, whereas the $\delta^{18}O_{speleo}$ overshoots are positive (Fig. 5.6c). This divergence cannot be explained by a change in average annual temperatures or salinities because, under those circumstances, both records of overshoots would register excursions in the same direction. Considering that $\delta^{18}O_{ruber}$ is a summer signal (Rohling et al., 2004), and $\delta^{18}O_{speleo}$ is a winter/spring signal (Bar-Matthews et al., 1996), the divergent overshoots may reflect enhanced seasonality during MIS 3. In

that scenario, the eastern Mediterranean would have been characterised by net precipitation during summer and net evaporation during winter/spring. An alternative explanation for divergent overshoots is a stronger latitudinal gradient in atmospheric conditions over the Mediterranean between 30 and 35˚N, whereby warmer/wetter conditions to the north contrasted with a colder/drier climate to the south. It is important to note that these scenarios 1) are not mutually exclusive, and 2) invoke relative changes in effective moisture; so, for example, net precipitation (evaporation) in summer (winter) may reflect significantly reduced (enhanced) evaporation rather than changes in total precipitation. Evidence from other proxies is needed to help narrow down the possibilities.

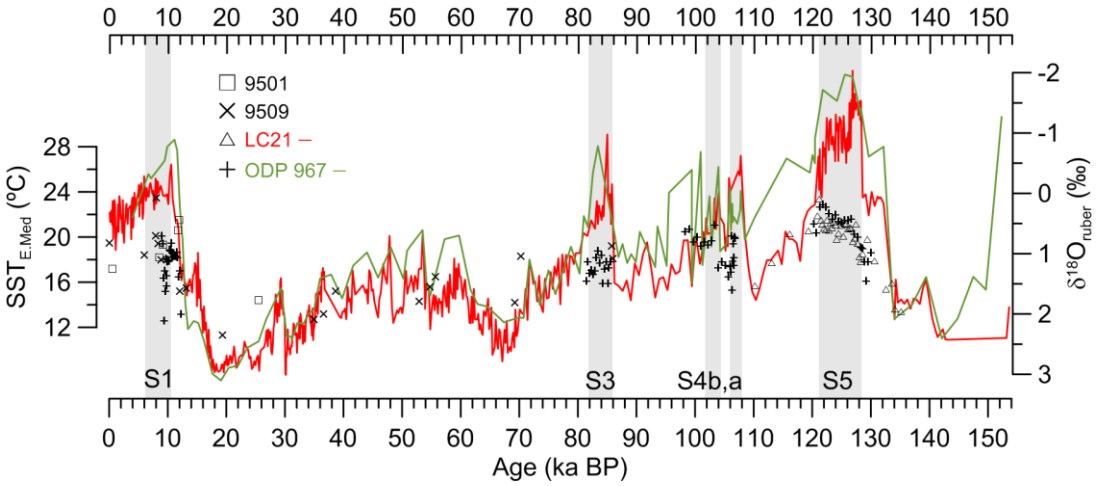

Figure 5.7 Sea surface temperature (SST) estimates from eastern Mediterranean marine cores and planktonic foraminiferal (*G. ruber*) $\delta^{18}O$ records from core LC21 (red) and ODP Site 967 (green). SST data are from core 9501 (south-eastern Levantine Basin, Almogi-Labin et al., 2009), core 9509 (eastern Levantine Basin, Almogi-Labin et al., 2009), core LC21 (southern Aegean Sea, Marino et al., 2007), and ODP Site 967 (eastern Levantine Basin, Emeis et al., 1998).

Due to analytical challenges, only few alkenone-derived sea surface temperature (SST) estimates exist for the eastern Mediterranean in MIS 3, but those available suggest values of 14-16˚C, which fall within the lower range of SST estimates for MIS 1 and 5 (Fig. 5.7). Regarding the palynological evidence, MIS 3 corresponds to Langgut et al.'s (2011) pollen zones III and IVa, and part of zone IVb (Bottom panel Fig. 5.6). Zone III climate was interpreted as more humid and variable, with significant fluctuations in pollen taxa. Zone IVa was considered to be characterised by more stable conditions with colder winters, and zone IVb was interpreted as warmer but with extensive aridity (Langgut et al., 2011). It is worth noting that this zonation scheme is based on pollen data from a marine core; hence, it is a distal signal that may reflect climatic heterogeneity between different pollen-source regions. Langgut et al. (2011) suggest that their zone III corresponds to an interval with

relatively high arboreal pollen in records from the northern Ghab Valley, Syria (Niklewski and Van Zeist, 1970), and Hula Lake, Israel (Weinstein-Evron, 1990), which are also thought to indicate wetter conditions, but the chronologies of these records may not be reliable (see Langgut et al., 2011 and references therein). Arboreal pollen abundance at Tenaghi Philippon (NE Greece) is lower in this interval than during interglacials, but is also highly variable, with peaks reaching up to 50% (Fig. 5.6f).

Overall, a picture emerges of major temporal and spatial variability in climate conditions in and around the eastern Mediterranean, during MIS 3. This likely resulted from regional responses to widespread climate instability at that time, such as the well-known 'Dansgaard-Oeschger' cycles in Greenland ice cores (e.g., Dansgaard et al., 1993; Grootes et al., 1993; Voelker et al., 2002; Rohling et al., 2003; North Greenland Ice Core Project Members, 2004; Siddall et al. 2010; and references therein). The eastern Mediterranean is particularly sensitive to outbreaks of cold, northerly airflows, relating to the position and strength of the Siberian high pressure cell (Saaroni et al., 1996; Lolis et al., 2002; Harding et al., 2009; Papadopoulos et al., 2012), and this appears to have been the case in the past (e.g., Rohling et al., 2002a; Casford et al., 2003; Marino et al., 2009; and refs therein). Given also that the eastern Mediterranean climate is influenced by a complex interplay between the temperate westerlies – including migrations of the polar front and subtropical jets on synoptic, seasonal, and interannual timescales – subtropical atmospheric pressure systems, and (indirectly via freshwater runoff) the East African summer monsoon (e.g., Larrasoaña et al., 2003; Kostopoulou and Jones, 2007; Harding et al., 2009), the proposed scenario of strong temporal and spatial variability in climate conditions during MIS 3 seems plausible.

5.5. Conclusions

Our multi-proxy suite of palaeo-environmental records from the eastern Mediterranean permits reconstructions of local climate conditions during successive intervals of sapropel deposition, and during four glacial periods (MIS 2-4, 6). Our results suggest that (net) humidity was not significantly elevated around the eastern Mediterranean during the deposition of sapropels S1, S3 and S4. Hence, water-column stratification at these times was predominantly controlled by monsoon-related freshwater run-off. However, local precipitation likely was increased during the deposition of S5, although more arid conditions may have occurred at the onset of S5. We also find evidence for increased net humidity during glacial periods MIS 2, 4, and 6, which can be explained by the seasonal timing and intensity of precipitation and drought. The most variable climatic conditions in the eastern Mediterranean over the last glacial cycle appear to have occurred during MIS 3. We propose

that global climatic instability at this time caused pronounced temporal and spatial environmental contrasts within the eastern Mediterranean region.

References

Abu-Zied, R.H., Rohling, E.J., Jorissen, F.J., Fontanier, C., Casford, J.S.L. Cooke, S. 2008. Benthic foraminiferal response to changes in bottom water oxygenation and organic carbon flux in the eastern Mediterranean during LGM to Recent times. Marine Micropaleontology 67, 46-68.

Almogi-Labin, A., Bar-Matthews, M., Shriki, D., Kolosovsky, E., Paterne, M., Schilman, B., Ayalon, A., Aizenshtat, Z., Matthews, A., 2009. Climatic variability during the last ~90 ka of the southern and northern Levantine Basin as evident from marine records and speleothems. Quaternary Science Reviews 28, 2882-2896.

Bachmann, O., Schoene, B., Schnyder, C., Spikings, R. 2010. The $^{40}Ar/^{39}Ar$ and U/Pb dating of young rhyolites in the Kos-Nisyros volcanic complex, Eastern Aegean Arc, Greece: Age discordance due to excess ^{40}Ar in biotite. Geochemistry, Geophysics, Geosystems 11, doi:10.1029/2010GC003073.

Bar-Matthews, M., Ayalon, A., Matthews, A., Sass, E., Halicz, L. 1996. Carbon and oxygen isotope study of the active water-carbonate system in a karstic Mediterranean cave: implications for palaeoclimate research in semiarid regions. Geochimica et Cosmochimica Acta 60, 337-347.

Bar-Matthews, M., Ayalon, A., Kaufman, A. 2000. Timing and hydrological conditions of Sapropel events in the Eastern Mediterranean, as evident from speleothems, Soreq Cave, Israel. Chemical Geology 169,145-156.

Bar-Matthews, M., Ayalon, A., Gilmour, M., Matthews, A., Hawkesworth, C.J. 2003. Sea-land oxygen isotopic relationships from planktonic foraminifera and speleothems in the Eastern Mediterranean region and their implication for paleorainfall during interglacial intervals. Geochimica et Cosmochimica Acta 67, 3181-3199.

Bartov, Y., Stein, M., Enzel, Y., Agnon, A., Reches, Z., 2002. Lake levels and sequence stratigraphy of Lake Lisan, the late pleistocene precursor of the Dead Sea. Quaternary Research 57, 9-21.

Bartov, Y., Goldstein, S.L., Stein, M., Enzel, Y., 2004. Catastrophic arid episodes in the Eastern Mediterranean linked with the North Atlantic Heinrich events. Geology 31, 439-442.

Biscaye, P.E. 1965. Mineralogy and sedimentation of recent deep-sea clay in the Atlantic Ocean and adjacent seas and oceans. Geological Society of America Bulletin 76, 803-832.

Bloemendal, J., deMenocal, P.B. 1989. Evidence for a change in the periodicity of tropical climate cycles at 2.4 Myr from whole-core magnetic susceptibility measurements. Nature 342, 897-900.

Bottema, S. 1995. The YD in the Eastern Mediterranean. Quaternary Science Reviews 14, 883-891.

Casford, J.S.L., Rohling, E.J., Abu-Zied,R., Cooke, S., Fontanier, C., Leng, M., Lykousis,V. 2002. Circulation changes and nutrient concentrations in the Late Quaternary Aegean Sea: A non-steady state concept for sapropel formation. Paleoceanography 17, 2000PA000601, 14.1-14.11.

Casford, J.S.L., Rohling, E.J., Abu-Zied, R.H.., Jorissen, F.J., Leng, M., Thomson, J. 2003. A dynamic concept for eastern Mediterranean circulation and oxygenation during sapropel formation. Palaeogeography, Palaeoclimatology, Palaeoecology 190, 103-119.

Cheddadi, R., Rossignol-Strick, M. 1995. Eastern Mediterranean quaternary paleoclimates from pollen and isotope records of marine cores in the Nile cone area. Paleoceanography 10, 291-300.

Clare, L., Rohling, E.J., Weninger, B., Hilpert, J. 2008. Warfare in Late Neolithic/ Early Chalcolithic Pisidia, southwestern Turkey. Climate induced social unrest in the late 7th millennium cal BC. Documenta Praehistorica 35 (Neolithic Studies 15), 65-92.

Dansgaard, W., Johnsen, S.J., Clausen, H.B., Dahl-Jensen, D., Gundestrup, N.S., Hammer, C.U., Hvidberg, C.S., Steffensen, J.P., Sveinbjornsdottir, A.E., Jouzel, J., Bond, G. 1993. Evidence for general instability of past climate from a 250-kyr ice-core record. Nature 364, 218-220.

deMenocal, P.B. 1995. Plio-Pleistocene African climate. Science 270, 53-59.

Ehrmann,W., Schmiedl, G., Hamann, Y., Kuhnt, T. 2007a. Distribution of clay minerals in surface sediments of the Aegean Sea: a compilation. International Journal of Earth Sciences 96, 769-780.

Ehrmann, W., Schmiedl, G., Hamann, Y., Kuhnt, T., Hemleben, C., Siebel, W. 2007b. Clay minerals in late glacial and Holocene sediments of the northern and southern Aegean Sea. Palaeogeography Palaeoclimatology Palaeoecology 249, 36-57.

Elenga, H., Peyron, O., Bonnefille, R., Jolly, D., Cheddadi, R., Guiot, J., Andrieu, V., Bottema, S., Buchet, G., Debeaulieu, J., Hamilton, A., Maley, J., Marchant, R., Perezobiol, R., Reille, M., Riollet, G., Scott, L., Straka, H., Taylor., D., van Campo, E., Vincens, A., Laarif, F., Jonson, H. 2000. Pollen-based biome reconstruction for Southern Europe and Africa 18,000 Yr BP. Journal of Biogeography 27, 621-634.

Emeis, K.-C., Schulz, H.-M., Struck, U., Sakamoto, T., Doose, H., Erlenkeuser, H., Howell, M., Kroon, D., Paterne, M. 1998. Stable isotope and alkenone temperature records

of sapropels from sites 964 and 967: constraining the physical environment of sapropel formation in the eastern Mediterranean Sea. In: A.H.F. Robertson, K.-C. Emeis, C. Richter, A. Camerlenghi (Eds.), Proceedings of the Ocean Drilling Program, Scientific Results 160. College Station, Texas, 309-331.

Enzel, Y., Amit, R., Dayan, U., Crouvi, O., Kahana, R., Ziv, B., Sharon, D. 2008. The climatic and physiographic controls of the eastern Mediterranean over the late Pleistocene climates in the southern Levant and its neighboring deserts. Global and Planetary Change 60, 165-192.

Eriksen, U., Friedrich,W.L., Buchardt, B., Tauber, H., Thomson, M.S. 1990. The Stronghyle Caldera: geological, paleontological and stable isotope evidence from radiocarbon-dated stromatolites from Santorini. In: D.A. Hardy, J. Keller, V.P. Galanopoulos, N.C. Flemming, T.H. Druitt (Eds.), Thera and the Aegean World III. Santorini, Greece, 139-150.

Fontugne, M.R., Calvert, S.E. 1992. Late Pleistocene variability of the carbon isotopic composition of organic matter in the eastern Mediterranean: monitor of changes in carbon sources and atmospheric CO_2 concentrations. Paleoceanography 7, 1-20.

Frumkin, A., Bar-Yosef, O., Schwarcz, H.P., 2011. Possible paleohydrologic and paleoclimatic effects on hominin migration and occupation of the Levantine Middle Paleolithic. Journal of Human Evolution 60, 437-451.

Galanidou, P., Tzedakis, P.C. 2001. New AMS dates from the Upper Palaeolithic Kastritsa. Proceedings of the Prehistoric Society 67, 271-278.

Galanidou, P., Tzedakis, P.C., Lawson, I.T., Frogley, M.R. 2000. A revised chronological and palaeoenvironmental framework for the Kastritsa rockshelter, northwest Greece. Antiquity 74, 349-355.

Grant, K.M., Rohling, E.J., Bar-Matthews, M., Ayalon, A., Medina-Elizalde, M., Bronk Ramsey, C., Satow, C., and Roberts, A.P., Rapid coupling between ice volume and polar temperature over the past 150 kyr. Nature 491, 744-747.

Grelaud, M., Marino, G., Ziveri, P., Rohling, E.J. 2012. Abrupt shoaling of the nutricline in response to massive freshwater flooding at the onset of the last interglacial sapropel event. Paleoceanography 27, PA3208, doi:10.1029/ 2012PA002288.

Grootes, P.M., Stuiver, M., White, J.W.C., Johnsen, S., Jouzel, J. 1993. Comparison of oxygen isotope records from the GISP2 and GRIP Greenland ice cores. Nature 366, 552-554.

Hamann, Y., Ehrmann, W.U., Schmiedl, G., Kuhnt, T. 2009. Modern and late Quaternary clay mineral distribution in the area of the SE Mediterranean Sea. Quaternary Research 7, 453-464.

Harding, A.E., Palutikof, J., Holt, T. 2009. The climate system. In: J.C. Woodward (Ed.), The physical geography of the Mediterranean. Oxford University Press, Oxford, 69-88.

Hazan, N., Stein, M., Agnon, A., Marco, S., Nadel, D., Negendank, J.F.W., Schab, M.J., Neev, D. 2005. The Late Quaternary limnological history of Lake Kinneret (Sea of Galille), Israel. Quaternary Research 63, 60-77.

Hoogakker, B.AA., Rothwell, R.G., Rohling, E.J., Paterne, M., Stow, D.A.V. 2004. Variations in terrigenous dilution in western Mediterranean Sea pelagic sediments in response to climate change during the last glacial cycle. Marine Geology 211, 21-43.

Kadosh, D., Sivan, D., Kutiel, H., Weinstein-Evron, M. 2004. A Late Quaternary paleoenvironmental sequence from Dor, Carmel Coastal Plain, Israel. Palynology 28, 143-157.

Kallel, N., Paterne, M., Duplessy, J.-C., Vergnaud-Grazzini, C., Pujol, C., Labeyrie, L., Arnold, M., Fontugne, M., Pierre, C. 1997. Enhanced rainfall in the Mediterranean region during the last sapropel event. Oceanologica Acta 20, 697-712.

Kallel, N., Duplessy, J.-C., Labeyrie, L., Fontugne, M., Paterne, M., Montacer, M. 2000. Mediterranean pluvial periods and sapropel fromation over the last 200 000 years. Palaeogeography, Palaeoclimatology, Palaeoecology 157, 45-58.

Kolodny, Y., Stein, M., Machlus, M. 2005. Sea-rain-lake relation in the Last Glacial East Mediterranean revealed by $\delta^{18}O$-$\delta^{13}C$ in Lake Lisan aragonites. Geochimica et Cosmochimica Acta 69, 4045- 4060.

Kostopoulou, E., Jones, P.D. 2007. Comprehensive analysis of the climate variability in the eastern Mediterranean. Part I: map-pattern classification. International Journal of Climatology 27, 1189-1214.

Kotthoff, U., Koutsodendris, A., Pross, J., Schmiedl, G., Bornemann, A., Kaul, C., Marino, G., Peyron, O., Schiebel, R., 2011. Impact of Lateglacial cold events on the northern Aegean region reconstructed from marine and terrestrial proxy data. Journal of Quaternary Science 26, 86-96.

Kroon, D., Alexander, I., Little, M., Lourens, L.J., Matthewson, A., Robertson, A.H.F., Sakamoto, T. 1998. Oxygen isotope and sapropel stratigraphy in the Eastern Mediterranean during the last 3.2 million years. In: A.H.F. Robertson, K.-C. Emeis, C. Richter, A. Camerlenghi (Eds.), Proceedings of the Ocean Drilling Program, Scientific Results 160. College Station, Texas, 181-189.

Kuhlemann, J., Rohling, E.J., Kumrei, I., Kubik, P., Ivy-Ochs, S., Kucera, M. 2008. Regional synthesis of Mediterranean atmospheric circulation during the Last Glacial Maximum. Science 321, 1338-1340.

Lang, N., Wolff, E.W. 2011. Interglacial and glacial variability from the last 800 ka in marine, ice and terrestrial archives. Climates of the Past 7, 361-380.

Langgut, D., Almogi-Labin, A., Bar-Matthews, M., Weinstein-Evron, M. 2011. Vegetation and climate changes in the South Eastern Mediterranean during the Last Glacial-Interglacial cycle (86 ka): new marine pollen record. Quaternary Science Reviews 30, 3960-3972.

Larrasoaña, J.C., Roberts, A.P., Rohling, E.J., Winklhofer, M., Wehausen, R. 2003. Three million years of monsoon variability over the northern Sahara. Climate Dynamics 21, 689-698.

Larrasoaña, J.C., Roberts, A.P., Rohling, E.J. 2008. Magnetic susceptibility of eastern Mediterranean marine sediments as a proxy for Saharan dust supply? Marine Geology 254, 224-229.

Lolis, C.J., Bartzokas, A., Katsoulis, B.D. 2002. Spatial and temporal 850 hPa air temperature and sea-surface temperature covariances in the Mediterranean region and their connection to atmospheric circulation. International Journal of Climatology 22, 663-676.

Lourens, L., Hilgen, F., Shackleton, N.J., Laskar, J., Wilson, D. 2004. The Neogene period. In: F.M. Gradstein, J.G. Ogg, A.G. Smith (Eds.), A Geologic Timescale 2004, Cambridge University Press, Cambridge, 409-440.

Marino, G., Rohling, E.J., Rijpstra, W.I., Sangiorgi, F., Schouten, S., Sinninghe Damsté, J.S. 2007. Aegean Sea as driver for hydrological and ecological changes in the eastern Mediterranean. Geology 35, 675-678.

Marino, G., Rohling, E.J., Sangiorgi, F., Hayes, A., Casford, J.S.L., Lotter, A.F., Kucera, M., Brinkhuis, H. 2009. Early and middle Holocene in the Aegean Sea: interplay between high and low latitude climate variability. Quaternary Science Reviews 28, 3246-3262.

Mayewski, P.A., Rohling, E.J., Stager, J.C., Karlén, W., Maasch, K., Meeker, L.D., Meyerson, E., Gasse, F., Van Kreveld, S., Holmgren, K., Lee-Thorp. J., Rosqvist, G., Rack, F., Staubwasser, M., Schneider, R.R., Steig, E. 2004. Holocene Climate Variability. Quaternary Research 62, 243-255.

McGarry, S., Bar-Matthews, M., Matthews, A., Vaks, A., Schilman, B., Ayalon, A. 2004. Constraints on hydrological and paleotemperature variations in the eastern Mediterranean region in the last 140 ka given by the δD values of speleothem fluid inclusions. Quaternary Science Reviews 23, 919-934.

Meijer, P. T., Tuenter, E. 2007. The effect of precession induced changes in the Mediterranean freshwater budget on circulation at shallow and intermediate depth. Journal of Marine Systems 68, 349-365.

Mercone, D., Thomson, J., Abu-Zied, R.H., Croudace, I.W., Rohling, E.J. 2001. High-resolution geochemical and micropalaeontological profiling of the most recent eastern Mediterranean sapropel. Marine Geology 177, 25-44.

Milner, A.M., Müller, U.C., Roucou, K.H., Collier, R.E.L., Pross, J., Kalaitzidis, S., Christianis, K., Tzedakis, P.C. 2013. Environmental variability during the Last Interglacial: a new high-resolution pollen record from Tenaghi Philippon, Greece. Journal of Quaternary Science 28,113-117.

Niklewski, J., Van Zeist, W. 1970. A Late Quaternary pollen diagram from northwestern Syria. Acta Botanica Neerlandica 19, 737-754.

North Greenland Ice Core Project Members. 2004. High-resolution record of Northern Hemisphere climate extending into the last interglacial period. Nature 431, 147-151.

Osborne, A.H., Vance, D., Rohling, E.J., Barton, N., Rogerson, M., Fello, N. 2008. A humid corridor across the Sahara for the migration "Out of Africa" of early modern humans 120,000 years ago. Proceedings of the National Academy of Sciences 105, 16444-16447.

Osborne, A., Marino, G., Vance, D., Rohling, E.J. 2010. Eastern Mediterranean surface water Nd during Eemian sapropel S5: monitoring northerly (mid latitude) versus southerly (sub tropical) freshwater contributions. Quaternary Science Reviews 29, 2473-2483.

Paillard, D. 1996. Macintosh Program performs time-series analysis. Eos Transactions, American Geophysical Union 77, 39.

Papadopoulos, V.P., Kontoyiannis, H., Ruiz, S., Zarokanellos, N. 2012. Influence of atmospheric circulation on turbulent air-sea heat fluxes over the Mediterranean Sea during winter. Journal of Geophysical Research 117, C03044, doi:10.1029/ 2011JC007455.

Poulos, S.E. 2009. Origin and distribution of the terrigenous component of the unconsolidated surface sediment of the Aegean floor: A synthesis. Continental Shelf Research 29, 2045-2060.

Prentice, I.C., Guiot, J., Harrison, S.P. 1992. Mediterranean vegetation, lake levels and palaeoclimate at the Last Glacial Maximum. Nature 360, 658-660.

Rohling, E.J. 1999. Environmental control on Mediterranean salinity and $\delta^{18}O$. Paleoceanography 14, 706-715.

Rohling, E.J., De Rijk. S. 1999. The Holocene climate optimum and last glacial maximum in the Mediterranean: the marine oxygen isotope record. Marine Geology 153, 57-75.

Rohling, E.J., Pälike, H. 2005. Centennial-scale climate cooling with a sudden cold event around 8,200 years ago. Nature 434, 975-979.

Rohling, E.J., Jorissen, F.J., De Stigter, H.C. 1997. 200 Year interruption of Holocene sapropel formation in the Adriatic Sea. Journal of Micropalaeontology 16, 97-108.

Rohling, E.J., Mayewski, P.A., Hayes, A., Abu-Zied, R.H., Casford, J.S.L. 2002a. Holocene atmosphere-ocean interactions: records from Greenland and the Aegean Sea. Climate Dynamics 18, 587-593.

Rohling, E.J., Cane, T.R., Cooke, S., Sprovieri, M., Bouloubassi, I., Emeis, K.C., Schiebel, R., Kroon, D., Jorissen, F.J., Lorre, A., Kemp, A.E.S. 2002b. African monsoon variability during the previous interglacial maximum. Earth and Planetary Science Letters 202, 61-75.

Rohling, E.J., Mayewski, P.A., Challenor, P. 2003. On the timing and mechanism of millennial-scale climate variability during the last glacial cycle. Climate Dynamics 20, 257-267.

Rohling, E.J., Sprovieri, M., Cane, T.R., Casford, J.S.L., Cooke, S., Bouloubassi, I., Emeis, K.C., Schiebel, R., Hayes, A., Jorissen, F.J., Kroon, D. 2004. Reconstructing past planktic foraminiferal habitats using stable isotope data: a case history for Mediterranean sapropel S5. Marine Micropaleontology 50, 89-123.

Rohling, E.J., Hopmans, E.C., Sinninghe-Damste, J.S. 2006. Water column dynamics during the last interglacial anoxic event in the Mediterranean (sapropel S5). Paleoceanography 21, PA2018, doi:10.1029/2005PA001237.

Rohling, E.J., Abu-Zied, R., Casford, J.S.L., Hayes, A., Hoogakker, B.A.A. 2009. The marine environment: present and past. In: J.C. Woodward (ed.), The Physical Geography of the Mediterranean. Oxford University Press, Oxford, 33-67.

Rossignol-Strick, M. 1985. Mediterranean quaternary sapropels, an immediate response of the African monsoon to variation of insolation. Palaeogeography, Palaeoclimatology, Palaeoecology 49, 237-263.

Rossignol-Strick, M. 1987. Rainy periods and bottom water stagnation initiating brine accumulation and metal concentrations: 1. the Late Quaternary. Paleoceanography 2, 333-360,

Rossignol-Strick, M. 1999. The Holocene climatic optimum and pollen records of sapropel 1 in the eastern Mediterranean, 9000–6000 BP. Quaternary Science Reviews 18, 515-530.

Rossignol-Strick, M., Paterne, M. 1999. A synthetic pollen record of the eastern Mediterranean sapropels of the last 1 Ma: implications for the time-scale and formation of sapropels. Marine Geology 153, 221-237.

Rossignol-Strick, M., Nesteroff, W., Olive, P., Vergnaud-Grazzini, C. 1982. After the deluge, Mediterranean stagnation and sapropel formation. Nature 295, 105-110.

Saaroni, H., Bitan, A., Alpert, P., Ziv, B. 1996. Continental polar outbreaks into the Levant and Eastern Mediterranean. International Journal of Climatology 16, 1175-1191.

Sakamoto, T., Janecek, T., Emeis, K.-C. 1998. Continuous sedimentary sequences from the Eastern Mediterranean Sea: composite depth sections. In: A.H.F. Robertson, K.-C. Emeis, C. Richter, A. Camerlenghi (Eds.), Proceedings of the Ocean Drilling Program, Scientific Results 160. College Station, Texas, 37-59.

Satow, C.G. 2012. The tephrostratigraphy of three, late Quaternary, Mediterranean marine cores. Royal Holloway, University of London. Unpublished thesis.

Schmiedl, G., Kuhnt, T., Ehrmann, W., Emeis, K.-C., Hamann, Y., Kotthoff, U., Dulski, P., Pross, J. 2010. Climatic forcing of eastern Mediterranean deep-water formation and benthic ecosystems during the past 22 000 years. Quaternary Science Reviews 29, 3006-3020.

Scrivner, A.E., Vance, D., Rohling, E.J. 2004. New neodymium isotope data quantify Nile involvement in Mediterranean anoxic episodes. Geology 32, 565-568..

Siddall, M., Rohling, E.J., Blunier, T., Spahni, R. 2010. Patterns of millennial variability over the last 500 ka. Climate of the Past 6, 295-303.

Stanley, D.J., Wingerath, J.G. 1996. Clay mineral distributions to interpret Nile cell provenance and dispersal I: lower River Nile to delta sector. Journal of Coastal Research 12, 911-929.

Torfstein, A., Goldstein, S.L., Kagan, E., Stein, M. 2013. Integrated multi-site U-Th chronology of the last glacial Lake Lisan. Geochimica et Cosmochimica Acta 104, 210-231.

Tuenter, E., Weber, S.L., Hilgen, F.J., Lourens, L.J. 2003. The response of the African summer monsoon to remote and local forcing due to precession and obliquity. Global and Planetary Change 36, 219-235.

Tzedakis, P.C. 2007. Seven ambiguities in the Mediterranean palaeoenvironmental narrative. Quaternary Science Reviews 26, 2042-2066.

Tzedakis, P.C. 2009. Cenozoic climate and vegetation change. In: J.C. Woodward (Ed.), The Physical Geography of the Mediterranean. Oxford University Press, Oxford, 89-137.

Tzedakis, P.C., Lawson, I.T., Frogley, M.R., Hewitt, G.M., Preece, R.C. 2002. Buffered vegetation changes in a Quaternary refugium: evolutionary implications. Science 297, 2044-2047.

Tzedakis, P.C., Frogley, M.R., Heaton, T.H.E. 2003. Last interglacial conditions in southern Europe: evidence from Ioannina, northwest Greece. Global and Planetary Change 36, 157-170.

Tzedakis, P.C., Hooghiemstra, H., Palike, H. 2006. The last 1.35 million years at Tenaghi Philippon: revised chronostratigraphy and long-term vegetation trends. Quaternary Sci. Rev. 25, 3416-3430.

Vaks, A., Bar-Matthews, M., Ayalon, A., Schilman, B., Gilmour, M., Hawkesworth, C.J., Frumkin, A., Kaufman, A., Matthews, A. 2003. Paleoclimate reconstruction based on the timing of speleothem growth and oxygen and carbon isotope composition in a cave located in the rain shadow in Israel. Quaternary Research 59, 182-193.

Vaks, A., Bar-Matthews, M., Ayalon, A., Matthews, A., Frumkin, A., Dayan, U., Halicz, L., Almogi-Laban, A., Schilman, B. 2006. Paleoclimate and location of the border between Mediterranean climate region and the Saharo–Arabian Desert as revealed by speleothems from the northern Negev Desert, Israel. Earth and Planetary Science Letters 249, 384-399.

Venkatarathnam, K., Ryan, W.B.F. 1971. Dispersal patterns of clay minerals in the sediments of the eastern Mediterranean Sea. Marine Geology 11, 261-282.

Voelker, A.H.L. and workshop participants. 2002. Global distribution of centennial-scale records for Marine Isotope Stage (MIS) 3: a database. Quaternary Science Reviews 21, 1185-1212.

Weinstein-Evron, M. 1990. Palynological history of the last pleniglacial in the levant. In: J.K. Kozlowski (Ed.), Feuilles de Pierre: les Industries à Pointes Foliacées du Paléolithique Supérieur Européen, vol. 42. ERAUL, Liège, pp. 9-25.

Wick, L., Lemcke, G., Sturm, M. 2003. Evidence of Late glacial and Holocene climatic change and human impact in Eastern Anatolia: high resolution pollen, charcoal, isotopic and geochemical records from the laminated sediments of Lake Van, Turkey. The Holocene 13, 665-675.

Wijmstra, T.A., Young, R., Witte, H.J.L. 1990. An evaluation of the climatic conditions during the Late Quaternary in northern Greece by means of multivariate analysis of palynological data and comparison with recent phytosociological and climatic data. Geologie en Mijnbouw 69, 243-251.

6 Summary and future work

The key findings of this study are outlined below, and are followed by a discussion of potential directions for future research which relate directly to this study.

6.1 Summary of results

The principle aim of this thesis was to develop a new, radiometrically based chronology for the 500 kyr Red Sea relative sea-level (RSL) record. This in turn would allow ice-volume phase relationships to be examined. It was found that:

1. There was good agreement in the timing of ice-volume fluctuations and polar climate changes over the last glacial cycle, particularly regarding Greenland (as opposed to Antarctic) temperature changes. The response times for ice-volume changes, and their rates of change, were within centuries of polar climate change, and rates of sea-level rise during major episodes of ice-volume reduction reached at least 1.2 m/century. These findings are especially pertinent in light of current global warming trends.

2. Over successive ice ages, ice-volume changes at glacial terminations generally lagged rising boreal mid-summer insolation and atmospheric CO_2 concentrations by 2-7 kyr. This finding supports the classical "Milankovitch Theory" of ice-age cycles, and suggests that CO_2-driven feedback processes were not responsible for initiating the transition to interglacial conditions. In detail, however, ice-volume phasings relative to key climate-system variables were different at each of the last five terminations.

Another significant outcome of the new RSL chronology was the opportunity to investigate monsoon variability in the context of global ice-volume changes. This strand of research was possible because the new RSL record is synchronised with East African summer monsoon (EAfSM) and East Asian monsoon (EAM) proxy records. It was found that:

1. Rapid, millennial-scale variability in summer and winter EAM proxies at glacial terminations can be explained by rapid rates of ice-volume reduction. This observation supports the bipolar see-saw hypothesis, whereby meltwater pulses into the North Atlantic at glacial terminations caused a lag in the (precession-driven) intensification of the summer EAM.

2. Ice-volume changes also appear to be related to synchronous monsoon variability among different monsoon systems of the northern hemisphere during periods of ice-volume minima, although pronounced regional phase offsets during glacial inceptions challenge the notion of a 'global monsoon'.

3. Regarding the EAfSM, inconsistent phasings between precession minima and EAfSM maxima strongly dispute the widespread use of a 3-kyr precession-lag to date EAfSM maxima before the Holocene. Instead, the timing of EAfSM maxima appears to be determined, during glacial inceptions, by insolation alone and, during full interglacial conditions, by changes in insolation and ice volume.

Finally, the new RSL record and an RSL-synchronised Mediterranean $\delta^{18}O$ record, permitted the first deconvolution of two key eastern Mediterranean $\delta^{18}O$ records into their component environmental signals, without the bias of source-water or ice-volume effects. These isotope residuals were then compared with local palaeoclimate proxy records. It was found that:

1. Local precipitation did not increase significantly during the deposition of sapropels S1, S3 and S4, implying that water-column stratification at these times was predominantly controlled by monsoon-related fresh-water run-off. However, there is evidence to suggest that net moisture availability in the region increased during the deposition of sapropel S5.

2. Evidence suggests that periods of elevated humidity also occurred during colder glacial intervals, and this can be explained by changes in the seasonality and intensity of precipitation and drought.

3. Marine isotope stage (MIS) 3 was characterised by the most variable climatic conditions in the eastern Mediterranean, with potentially strong seasonal contrasts and/or latitudinal gradients in precipitation and drought. This observation adds to a growing body of evidence for global climatic instability during MIS 3.

6.2. Future work

6.2.1. Ice-volume and monsoon variability

The reconstruction of relative sea-level (RSL) records using proxies of past variations in Mediterranean seawater $\delta^{18}O$ could be further explored. The 'Mediterranean method' of sea-level chronology in Grant et al. (2012) (Chapter 2) is restricted to the last glacial cycle primarily by the age of core LC21 sediments, and to a lesser degree by the resolution, length and dating of the Soreq Cave speleothem $\delta^{18}O$ record. (The latter extends to 177 ka BP, and sample resolution for U/Th-age and $\delta^{18}O$ data is best for 0-160 ka BP; Mira Bar-Matthews, pers. comm.). However, continuous sediment sequences have been recovered from the Eastern Mediterranean that date back to the Pliocene (Emeis et al., 1996; Larrasoaña et al., 2003), and these offer the potential for the construction of extensive RSL time-series. Key issues to be addressed are: (1) removal of the hydrological overprints on eastern Mediterranean $\delta^{18}O$; and (2) dating of sediments that pre-date the oldest dated sections of the Soreq Cave record.

Regarding (1), there are two main approaches. First, multi-species foraminiferal $\delta^{18}O$ data will illustrate which signals are common throughout the water column (i.e., the underlying basin-wide signal with a dominant glacial-cycle component), and which are clearly vertically stratified and/or regionally differentiated, and therefore characteristic of freshwater events (Rohling and De Rijk, 1999; Rohling, 1999; Rohling et al., 2004). Second, the record of sapropels (including post-depositionally reoxidised sapropels) indicates the timing of potential hydrological overprints on eastern Mediterranean $\delta^{18}O$; this record can be recognised using geochemical markers, such as Ba/Al (Higgs et al., 1994; Thomson et al., 1995), and palaeomagnetic evidence (Larrasoaña et al., 2006).

Regarding (2), a better understanding is emerging of sapropel timing relative to insolation using direct dating, and it is evident that each individual sapropel is differently phased relative to insolation on timescales finer than a few thousand years (Chapter 4). Nonetheless, a 'mean' phase relationship can be determined with uncertainties, and this newly established mean phase relationship can be applied (with uncertainties) to date precession-scale fluctuations in Eastern Mediterranean records with precisions of a few thousand years, similar to the work of Hilgen (1991), Hilgen et al. (1993) and Lourens et al. (1996, 2001). For sea-level variability in times before 160 ka BP, that level of precision is similar to, or better than, that achieved with radiometric dating of fossil coral sea-level benchmarks. The new, Mediterranean-based, method, however, will have the significant advantages of time-

series continuity, high temporal resolution, and extension of the sea-level record down to 3 Ma (and potentially further using other ODP cores).

Furthermore, low-latitude climate-proxy records (e.g., EAfSM maxima, Saharan dust fluxes) can be derived from the same core samples as those used for (potentially) reconstructing sea-level, thus enabling clarification of timing relationships between high- and low-latitude climate change before and after the 'middle Pleistocene transition' (see Clark et al., 2006). Finally, comparison of a longer (>1 Myr) sea-level record with a global stacked record of benthic foraminiferal $\delta^{18}O$ (Lisiecki and Raymo, 2005) and with a deep-sea temperature reconstruction (Elderfield et al., 2011) may help to clarify ice-volume:deep-sea $\delta^{18}O$ relationships over several glacial cycles.

In a separate development, the implications of our radiometrically-constrained, 500-kyr RSL record, and its phase relationships with respect to insolation, Antarctic temperature, CO_2, etc. (Chapter 3), need to be considered in much greater depth. For example: how do these observations fit with current theories of ice-age cycles? This question should be examined in the context of the relative importance of the eccentricity, obliquity and precession cycles, as well as that of external forcing (orbital configuration) versus internal climate feedbacks (e.g., CO_2, ice-sheet albedo, atmospheric moisture redistribution). The validity of inferred phase relationships depends on the minimum interval of age control in the RSL record, which is ~11 kyr (i.e., about half of a precession cycle) for the 150-500 kyr interval (Chapter 3). Therefore, another possible avenue of future research would be to investigate methods of improving this age control.

Finally, the generation of longer time series of East African summer monsoon (EAfSM) variability will allow the findings of Chapter 4 to be tested. For example: does the observed differentiation between EAfSM phasings during interglacial and non-interglacial periods – with respect to changes in insolation, global sea level, and monsoon-proxy records from different regions – hold true for several glacial cycles? The establishment of a global database of monsoon-proxy records would be particularly useful in this respect, since it would offer the best scope for a comprehensive analysis of monsoon phase relationships. The feasibility of an internally consistent database of vetted proxy records could also be explored.

In concrete terms regarding our future research, we have started with ODP Site 967, which will be the focus for much of this work, due to its location in the easternmost sector of the Mediterranean and its exisiting palaeomagnetic records (Larrasoaña et al., 2003). Down-core

sampling will be extended back to ~3 Myr-old sediments, in order to generate high-resolution records of 1) EAfSM variability, and 2) planktonic foraminiferal $\delta^{18}O$, from surface and sub-surface dwelling species.

6.2.2. Tephrochronology

The utility of establishing a tephra 'lattice' between archaeological and palaeoclimatic records has been demonstrated by Lowe et al. (2012) (Appendix C). This approach involves correlation of archaeological, terrestrial and marine records using geochemically-fingerprinted ash layers that are common to all of the cores/sites from which the records in question originate. Analysis of tephra shards from Eastern Mediterranean core LC21 and ODP Site 967 (Satow, 2012) and from northern Red Sea core GeoTü-KL17 (Christine Lane, pers. comm.), has resulted in the identification of tephra horizons that can be used as isochronic correlation tiepoints between these regions (Fig. 6.1). These ash deposits are linked to the Cape Riva (CR), Campanian Ignimbrite (CI), Pantellaria (P-11) and Kos Plateau Tuff (KPT) eruptions. Core LC21 contains the CI, P-11, and KPT; ODP Site 967 contains the CR and KPT; and core KL17 contains the CR and CI (Fig. 6.1). These results therefore improve the understanding of chronological relationships between these regions, which helps inter-regional palaeoclimate studies.

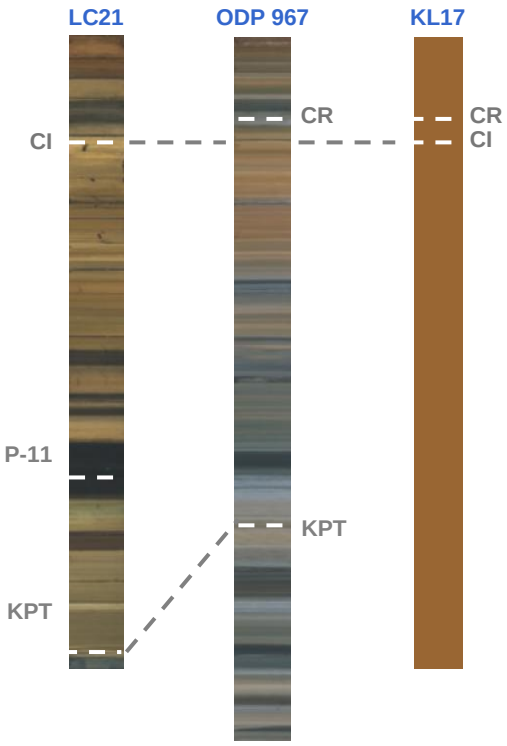

Figure 6.1
Photographs of Eastern Mediterranean sediments from core LC21 and ODP Site 967, with tephra horizons common to these cores and core KL17 from the northern Red Sea schematically indicated. The images are not to scale. The tephra horizons are from the Campanian Ignimbrite (CI), Pantellaria (P-11), Kos Plateau Tuff (KPT), and Cape Riva (CR) eruptions.

The P-11 tephra has also been confirmed in a terrestrial core from Lesvos, northern Aegean Sea (Mark Hardimann, pers. comm.), for which a pollen-derived palaeoclimate record is available, and in an archaeological sequence from Theopetra Cave, Greece (Dustin White, pers. comm.). There is therefore the possibility of a combined archaeological-palaeoclimatic study for the time interval encompassing the P-11, in a similar vein to the Lowe et al. (2012) study based on the CI (Appendix C). The likely proximal equivalent of the P-11 tephra - 'Unit P' - has K/Ar datings ranging between 132±6 ka BP and 134±6 ka BP (Mahood and Hildreth, 1986). Interpolated ages from oxygen-isotope stratigraphy are 129.1 ka BP (Tamburrino et al., 2012) and 133.5±1.6 ka BP (based on Grant et al., 2012), hence the timing of the P-11 tephra approximately coincides with glacial termination 2. In light of hypothesised 'windows of opportunity' with respect to migration pathways for hominid dispersals (Rohling et al., in press; Appendix A), which are inferred to have been determined by both sea level and regional climate, a cross-discipline study utilising the P-11 isochron would be a ideal target for future work.

It should be noted, however, that the P-11 tephra horizon has not (yet) been geochemically linked to proximal ash deposits. Potential correlations between the core LC21 and Lesvos palaeoclimate records, and the Theopetra Cave archaeological sequences, are therefore currently based upon the temporal coincidence of geochemically-specific tephra shards at these sites. Clearly, thorough sampling, dating and geochemical analyses of ash deposits proximal to the eruptive source of a tephra isochron are critical to the 'tephra-lattice' method, and the absence of this information limits the use of tephrochronology in sediment-core age models. For example, it is not (yet) possible to link many of the geochemically finger-printed tephras in core LC21 to a specific, radiometrically-dated eruption (Satow, 2012). Future developments in tephrostratigraphy will benefit palaeoclimate research in general, and Mediterranean/near-East palaeoclimate reconstructions in particular, by adding chronological constraints to proxy time-series.

6.2.3. Other cores/sites

Millennial-scale climate variability in the North Atlantic region during the last glacial period appears to be strongly reflected in palaeotemperature records from Western Mediterranean sediments (Cacho et al., 1999, 2002). New, high-resolution stable isotope, scanning x-ray fluorescence (XRF), and environmental magnetism records for ODP Site 975 (Menorca Rise, Western Mediterranean) have already been generated by Prof. Rohling's group. Together with similar proxy records from Eastern Mediterranean ODP Site 967 and core LC21, and with the Soreq-correlated RSL record, the combined dataset will allow a detailed

investigation of 1) the timing relationship between global ice-volume fluctuations and climate changes in the North Atlantic and western and eastern Mediterranean, and 2) basin-wide variability in Mediterranean palaeoceanography over (at least) the last entire glacial cycle.

Marine cores KL17 and KL23 from the northern Red Sea provide a geographical link between the Eastern Mediterranean and central Red Sea cores discussed in this study. The northern Red Sea is climatically at the intersection of North African/Eastern Mediterranean and Arabian/Indian atmospheric circulation and climate regimes, so sediments from cores KL17 and KL23 should register changes in the timing and intensity of long-term variability in these different systems. Establishing a chronologically-consistent east-west transect of climate/monsoon proxy records between Asia and the Atlantic should therefore be possible, by making use of tephra isochrons common to Red Sea and Mediterranean sediment cores, and sea-level records correlated with Chinese, Red Sea and Mediterranean climate records. I am a central part of a wider initiative in Prof. Rohling's group to explore these relationships.

References

Cacho, I., Grimallt, J.O., Pelejerlo, C., Canals, M., Sierro, F.J., Flores, J.A., Shackleton, N. 1999. Dansgaard-Oeschger and Heinrich event imprints in Alboran Sea paleotemperatures. Paleoceanography 14, , 698-705.

Cacho, I., Grimallt, J.O., Canals, M. 2002. Response of the Western Mediterranean Sea to rapid climatic variability during the last 50,000 years: a molecular biomarker approach. Journal of Marine Systems 33-34, 253-272.

Clark, P.U., Archer, D., Pollard, D., Blum, J.D., Rial, J.A., Brovkin, V., Mix, A.C., Pisias, N.G., Roy, M. 2006. The middle Pleistocene transition: characteristics, mechanisms, and implications for long-term changes in atmospheric pCO_2. Quaternary Science Reviews 25, 3150-3184.

Elderfield, H., Ferretti, P., Greaves, M., Crowhurst, S., McCave, I.N., Hodell, D., Piotrowski, A.M. 2012. Evolution of ocean temperature and ice volume through the mid-Pleistocene climate transition. Science 337, 704-709.

Emeis, K.-C., Robertson, A.H.F., Richter, C., and shipboard scientific party. 1996. Proceedings of the Ocean Drilling Program, Initial Reports, Leg 160. College Station, Texas.

Grant, K.M., Rohling, E.J., Bar-Matthews, Ayalon, A., Bronk Ramsey, C., M., Satow, C., Medina-Elizalde, M., Roberts, A.P. 2012. Rapid coupling between ice volume and polar temperature over the past 150,000 years. Nature 491, 744-747.

Hemming, S.R. 2004. Heinrich events: Massive late Pleistocene detritus layers of the North Atlantic and their global climate imprint. Reviews of Geophysics 42, RG1005, doi:10.1029/2003RG000128.

Higgs, N.C., Thomson, J., Wilson, T.R.S., Croudace, I.W. 1994. Modification and complete removal of eastern Mediterranean sapropels by postdepositional oxidation. Geology 22, 423-426.

Hilgen, F.J. 1991. Astronomical calibration of Gauss to Matuyama sapropels in the Mediterranean and implication for the geomagnetic polarity time scale. Earth and Planetary Science Letters 104, 226-244.

Hilgen, F.J., Lourens, L.J., Berger, A., Loutre, M.F. 1993. Evaluation of the astronomically calibrated time-scale for the late Pliocene and earliest Pleistocene. Paleoceanography 8, 549-565.

Larrasoaña, J.C., Roberts, A.P., Rohling, E.J., Winklhofer, M., Wehausen, R. 2003. Three million years of monsoon variability over the northern Sahara. Climate Dynamics 21, 689-698.

Larrasoaña, J.C., Roberts, A.P., Hayes, A., Wehausen, R., Rohling, E.J. 2006. Detecting missing beats in the Mediterranean climate rhythm from magnetic identification of oxidized sapropels in Ocean Drilling Program Leg 160 marine sediments. Physics of the Earth and Planetary Interiors 156, 283-293.

Lisiecki, L.E., Raymo, M.E. 2005. A Plio-Pleistocene stack of 57 globally distributed benthic $\delta^{18}O$ records. Paleoceanography 20, PA1003, doi:10.1029/2004PA001071.

Lowe, J., Barton, N., Blockley, S., Bronk Ramsey, C., Cullen, V.L., Davies, W., Gamble, C., Grant, K., Hardiman, M., Housley, R., Lane, C.S., Lee, S., Lewis, M., .MacLeod, A., Menzies, M.A., Müller, W., Pollard, M., Price, C., Roberts, A.P., Rohling, E.J., Satow, C., Smith, V.C., Stringer, C., Tomlinson, E.L., White, D., Albert, P.G., Arienzo, I., Barker, G., Borić, D., Carandente, A., Civetta, L., Ferrier, C., Gaudelli, J.L., Karkanas, P., Koumouzelis, M., Müller, U.C., Orsi, G., Pross, J., Rosi, M., Shalamanov-Korobar, L., Sirakov, N., Tzedakis, P.C. 2012. Volcanic ash layers illuminate the resilience of Neanderthals and early modern humans to natural hazards. Proceedings of the National Academy of Sciences, 109, 13532-13537.

Lourens, L.J., Antonarakou, A., Hilgen, F.J., van Hoof, A.A.M., Vergnaud-Grazzini, C., Zachariasse, W.J. 1996. Evaluation of the Plio-Pleistocene astronomical timescale. Paleoceanography 11, 391-413.

Lourens, L.J., Wehausen, R., Brumsack, H.J. 2001. Geological constraints on tidal dissipation and dynamical ellipticity of the Earth over the past three million years. Nature 409, 1029-1033.

Mahood, G.A., Hildreth, W. 1986. Geology of the peralkaline volcano at Pantelleria, Strait of Sicily. Bulletin of Volcanology 48, 143-172.

Rohling, E.J. 1999. Environmental controls on salinity and δ18O in the Mediterranean. Paleoceanography 14, 706-715.

Rohling, E.J., De Rijk. S. 1999. The Holocene Climate Optimum and Last Glacial Maximum in the Mediterranean: the marine oxygen isotope record. Marine Geology 153, 57-75.

Rohling, E.J., Sprovieri, M., Cane, T.R., Casford, J.S.L., Cooke, S., Bouloubassi, I., Emeis, K.C., Schiebel, R., Hayes, A., Jorissen, F.J., Kroon, D. 2004. Reconstructing past planktic foraminiferal habitats using stable isotope data: a case history for Mediterranean sapropel S5. Marine Micropaleontology 50, 89-123.

Rohling, E.J., Grant, K.M., Roberts, A.P., Larrasoana, J.C. Palaeoclimate variability in the Mediterranean and Red Sea regions during the last 500,000 years; implications for hominin migrations. Current Anthropology, in press.

Satow, C.G. 2012. The tephrostratigraphy of three, late Quaternary, Mediterranean marine cores. Royal Holloway, University of London. Unpublished thesis.

Tamburrino, S., Insinga, D.D., Sprovieri, M., Petrosino, P., Tiepolo, M. 2012. Major and trace element characterization of tephra layers offshore Pantelleria Island: insights into the last 200 ka of volcanic activity and contribution to the Mediterranean tephrochronology. Journal of Quaternary Science 27, 129-140.

Thomson, J., Higgs, N.C., Wilson, T.R.S., Croudace, I.W., de Lange, G.J., van Santvoort, P.J.M. 1995. Redistribution and geochemical behaviour of redox-sensitive elements around S1, the most recent eastern Mediterranean sapropel. Geochimica et Cosmochimica Acta 59, 3487-3501.

Appendix A

Palaeoclimate variability in the Mediterranean and Red Sea regions during the last 500,000 years; implications for hominin migrations

Eelco J. Rohling, Katharine M. Grant, Andrew P. Roberts, Juan-Cruz Larrasoaña

Manuscript submitted to Current Anthropology (in review)

Author contributions: EJR led the review and wrote the paper; KMG, APR and JCL contributed to discussion of the presented data, figure preparation and significant manuscript refinement. Author affiliations are listed in the manuscript.

Palaeoclimate variability in the Mediterranean and Red Sea regions during the last 500,000 years; implications for hominin migrations

Eelco J. Rohling[1], Katharine M. Grant[1], Andrew P. Roberts[2], Juan-Cruz Larrasoaña[3]

1. School of Ocean and Earth Science, University of Southampton, National Oceanography Centre, Southampton, SO14 3ZH, UK.
2. Research School of Earth Sciences, The Australian National University, Canberra ACT 0200, Australia.
3. Instituto Geológico y Minero de España, Unidad de Zaragoza, Zaragoza 50006, Spain.

Abstract

The Mediterranean-Red Sea region has played an important role in the dispersal of hominids and other species between Africa and the rest of the world. Climate and sea level are often inferred as major controls on the "opening and closing" of migration pathways for these dispersals. We present an overview of the modern climate of the region, and how this changed through the last 500,000 years. This provides a context for consideration of the role of climate variability in anthropological and archaeological developments at the interface between Africa and Eurasia. First, we find that there have been episodes of generally (globally) increased millennial-scale climate variability at 40-80 ka, 160-200 ka, 320-340 ka, 360-380 ka, 400-440 ka, and 460-480 ka. Potential implications include intermittent habitat fragmentation, which may have affected developments and migrations of hominins and their food sources. Next, we find that passageways across the Sahara Desert, as well as the "northern out-of-Africa route" from Egypt into the Levant, were intermittently open during pluvial phases that were strongly related to orbital insolation maxima. For the "southern out-of-Africa route", across the Bab-el-Mandab narrows in the southern Red Sea, there is no such evident relationship. Instead, we present a novel interpretation of combined sea-level and regional climate control on potential migrations via the southern route, which identifies a series of "windows of opportunity" within the last half million years, which date to 458-448, 340-345, 272-265, 145-140, and 70-65 thousand years ago (ka). The "window" of 145-140 ka may be relevant for an early colonisation of Arabia at around 127 ± 16 ka. The "window" of 70-65 ka agrees well with age estimates of 65 +5/–8 ka for the final out-of-Africa migration by the anatomically modern human founder group of all non-Africans, which is thought to have taken the southern route. At any time, use of the southern route must have involved navigation or rafting across a marine strait of at least 6 km width, because there has never been a dry land bridge across the Red Sea within the last 500,000 years. The inferences that hominin dispersals were controlled by pluvials in currently hyperarid regions, and emerged shelves during times of sea-level lowstand, imply that many potential sites for fossil evidence will now either be buried under shifting sands and/or deflated, or be submerged under tens to a hundred metres of seawater. Once migrations via any route had reached the Eurasian margins of the Mediterranean Sea, populations would have benefited from great diversity of terrain and microclimates, drainage patterns, and accentuated relief with many rock shelters and caves, which would have been conducive to a relatively rich variety of exploitable plant and animal food sources, and of camp locations. Conditions remained relatively favourable throughout that region even during severe glacials, especially in lowlands and coastal plains, with potential to range into higher elevations during periods with milder conditions.

1. Introduction

The Mediterranean-Red Sea region occupies a zone that is influenced by four major climate systems. From northwest to southeast, these are:(1) the temperate westerlies that affect Europe, the western Mediterranean, and the northern sector of the eastern Mediterranean; (2) the dry subtropical conditions that dominate the southern and eastern sectors of the Mediterranean basin, as well as the entire Red Sea region; (3) the African monsoon, which affects Mediterranean conditions through inflow of major rivers (Nile, and in the past other North African drainage systems) and which has caused past contractions and expansions of the Sahara desert; and (4) the Indian Ocean monsoon, which causes seasonal wind reversals over the southern Red Sea region, up to latitudes of 20 to 25°N. No significant rainfall is associated with the Indian Ocean monsoon over the Red Sea and Arabian Peninsula today, but the monsoon's summer rainfall domain may have shifted onto the SE margin of the Arabian Peninsula (i.e., Yemen and Oman) during insolation-driven monsoon maxima such as that of the Early-Middle Holocene (Conroy and Overpeck, 2011).

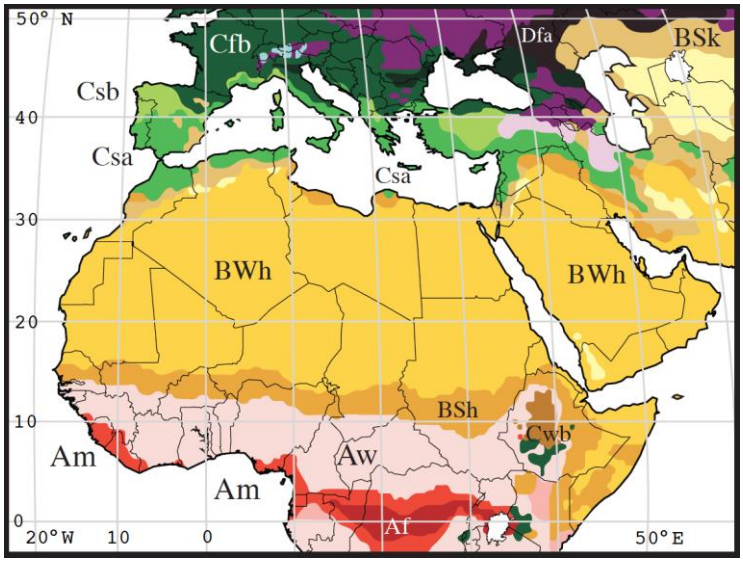

Figure 1.Summary map of the main climate zones in the study region using the Köppen-Geiger climate classification. C is warm temperate; B is arid; A is equatorial; D is snow; s is summer dry; f is fully humid; S is steppe; W is desert; w is winter dry; m is monsoonal; a is hot summer; b is warm summer; k is cold arid; and h is hot arid. Modified after Kottek et al. (2006).

Climatic gradients over the Mediterranean and Red Sea region are well illustrated by the updated Köppen-Geiger climate classification (Kottek et al., 2006) (Figure1). Important measures of climate variability through time are obtained from a variety of methods, such as pollen data, lake levels, stable isotopes from a variety of sedimentary archives, faunal changes, etc. These data especially supply information about changes in regional temperature and precipitation regimes. In addition, the Red Sea has in the past decade become a key region for reconstruction of continuous records of sea-level fluctuations (Rohling et al., 1998, 2008a, 2009b, 2010; Siddall et al., 2003, 2004; Grant et al., in review). Finally, the presence of vast deserts to the south of the Mediterranean and around the Red Sea gives rise to large wind-blown dust fluxes into these basins, and reconstructions of those fluxes through time – notably using marine sediment cores – also reveal important changes in regional climate conditions.

In this paper, we present an overview of the modern climate of the region, and of the main changes that have been reconstructed from palaeoclimate proxy records for the last

500,000 years. This overview provides a context for consideration of the role of climate variability in anthropological and archaeological developments at the interface between Africa and Europe.

2. Modern climatic setting

2.1. Mediterranean

We summarise modern Mediterranean climate conditions following the recent review of Rohling et al. (2009a).The classical Mediterranean climate is characterised by warm and dry summers, and mild and wet winters. Mean annual precipitation along the Mediterranean ranges from less than 0.12 m in North Africa, to over 2.00 m in portions of southwest Turkey and in the eastern Adriatic Sea along the slopes of the Dinaric Alps (Naval Oceanography Command, 1987). Total evaporation in the entire Mediterranean increases toward the east, with an average of 1.45 m y^{-1} (Malanotte-Rizzoli and Bergamasco, 1991) to 1.57 m y^{-1} (Béthoux and Gentili, 1994).

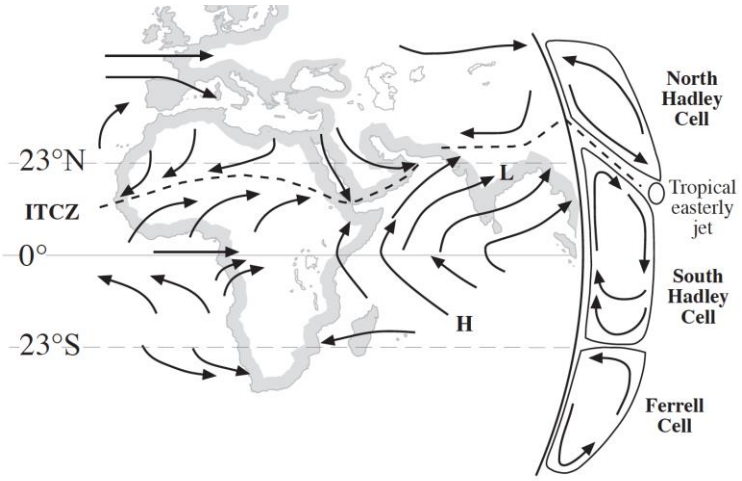

Figure 2.Atmospheric circulation pattern during Northern Hemisphere summer. The main winds are indicated as arrows. ITCZ = Inter-Tropical Convergence Zone; H = areas of high sea-level pressure; L = areas of low sea-level pressure. From an adaptation in Rohling et al. (2009) after Rossignol-Strick (1985) and Reichart (1997).

The classical Mediterranean climate is a result of the region's location on the transition between temperate westerlies that dominate over central and northern Europe, and the subtropical high-pressure belt over North Africa (Figure 2) (Boucher, 1975; Lolis et al., 2002). In summer, subtropical high-pressure conditions (and drought) extend from the southeast in a northwestward direction over most of the Mediterranean. Polar front depressions may still reach the western Mediterranean, but they only exceptionally penetrate the eastern Mediterranean (Rohling and Hilgen, 1991). During winter, the subtropical conditions shift southward, and the northern sector of the Mediterranean becomes influenced by the temperate westerlies, with associated Atlantic depressions that track eastward over Europe. These depression influences extend from the Mediterranean southeastward across the Levant and into the northernmost sector of the Red Sea (e.g., Goodfriend, 1991; Matthews et al., 2000;Bar-Matthews et al., 2003;Arz et al., 2003a; McGarry et al., 2004; Trommer et al., 2010).

Polar and continental air masses over Europe are channelled into the Mediterranean basin through gaps in the mountainous topography of the northern Mediterranean

margin. During winter and spring, intense cold and dry air flows through the lower Rhone Valley to reach the Gulf of Lions (the "Mistral"), and similar flows extend over the Adriatic and Aegean Seas (the "Bora" and "Vardar"), where they cause strong evaporation and sea-surface cooling (e.g., Leaman and Schott, 1991; Saaroni et al., 1996; Poulos et al., 1997; Maheras et al., 1999; Casford et al., 2003; and references therein). The northerly air flows into the western and eastern Mediterranean are determined by interaction between an intense low over the central or eastern Mediterranean, and northeastward extension of the Azores High (over Iberia, France, and southern Britain) or westward ridging of the Siberian High toward northwestern Europe and southern Scandinavia (Maheras et al., 1999; Lolis et al., 2002). Persistent winter low pressure conditions over the region result from high Mediterranean sea-surface temperatures (Lolis et al., 2002).

The most pronounced basin-wide cold winter events complement cold conditions over Europe, and develop in association with positive sea-level pressure anomalies to the west or northwest of the British Isles and particularly low pressure over the Mediterranean. An important aspect of winter variability concerns cyclogenesis (formation of new depressions), which governs precipitation in the northeastern and south-central sectors of the Mediterranean. Some Atlantic depressions may enter the (western) basin, but most cyclones observed in the Mediterranean form over the basin itself (Rumney, 1968; Trigo et al., 1999), when cold and relatively dry northerly air flows extend over warm sea surfaces in the northern sectors of the basin. Thus, winter cyclones are linked to North Atlantic systems, given that they represent either (occasional) direct entries of Atlantic synoptic systems into the Mediterranean basin, or secondary lows formed when Atlantic systems interact with the Alps and lead to cyclogenesis within the basin (Trigo et al., 2000).

Over the Mediterranean Sea, cyclogenesis is most frequent over the Gulf of Genoa and Ligurian Sea, but the Aegean Sea is also a major centre for winter cyclogenesis (Trewartha, 1966; Rumney, 1968; Boucher, 1975; Cantu, 1977; Trigo et al., 1999). Most Genoan depressions track over Italy, thereby affecting the Adriatic region, and thence in a generally eastward direction toward the Aegean Sea and/or northern Levantine seas (Trewartha, 1966; Rumney, 1968; Trigo et al., 1999; Lolis et al., 2002). These depressions, along with those that develop over other centres of cyclogenesis, cause the winter precipitation that is characteristic of modern Mediterranean climate. Geological archives indicate that Mediterranean depressions have controlled Mediterranean climate in the Levant as an enduring feature over glacial-interglacial timescales (Goodfriend, 1991;Matthews et al., 2000; Bar-Matthews et al., 2003; McGarry et al., 2004).

Summer rainfall is low around the Mediterranean region, especially in eastern and southeastern sectors. Some cyclogenesis occurs around Cyprus and the Middle East in summer, but adiabatic descent in the upper troposphere – related to the Asian summer monsoon – precludes deep convection over the region, and so causes the prevalence of dry summer conditions (Rodwell and Hoskins, 1996; Trigo et al., 1999).

The African monsoon does not reach directly into the Mediterranean basin, and there is no evidence that it ever did during the Quaternary. It does, however, have (or, more appropriately, used to have) a "remote" influence on the basin through Nile River discharge. Prior to the anthropogenic control of the Nile, its average discharge was 8.4×10^{10} m^3 yr^{-1} (4.5×10^{10} m^3 yr^{-1} in low-flood years to 15.0×10^{10} m^3 yr^{-1} in high-flood

years), which from the mid 1960s has dwindled to nearly nothing (Nof, 1979; Said, 1981; Wahbi and Bishara, 1981; Béthoux, 1984; Rohling and Bryden, 1992). During the pre-damming instrumental era, a strong (3-fold) interannual variability has been noted between high and low discharge years, mainly due to variability in the monsoon-fed contribution of the Blue Nile and Atbara rivers (see data summary in Rohling et al., 2009a).

The Nile River comprises two different systems: the White Nile, which drains the equatorial uplands of Uganda in a regular, permanent manner; and the Blue Nile and Atbara, which drain highly seasonal (summer) African monsoon precipitation from the Ethiopian highlands. Summarising the pre-damming Nile hydrology after Adamson et al. (1980) and Williams et al. (2000), it appears that up to 30% of the annual discharge of the Nile originated from the White Nile, and a minimum of 70% from the Blue Nile/Atbara. The winter flow was dominated (83%) by the steady White Nile contribution, and the Blue Nile/Atbara component provided 90% of the summer flow (with a peak over August-October). The White Nile discharge has a much smaller ratio of change between its annual peak and lowest monthly value, with a maximum between late September and January.

It should be noted that the Nile has not always been the only route for drainage of African monsoon precipitation into the Mediterranean. During past monsoon maxima (related to orbitally induced insolation maxima), the extent of the Sahara desert was much reduced, and there was northward routing of drainage from the central Saharan watershed into the Mediterranean along the wider North African margin (see below for details).

2.2. Red Sea

The Red Sea basin is entirely situated in an arid zone with very low humidity. Coastal stations record annual rainfall figures of less than 20 mm in the north and 50 to 100 mm in the south (Pedgley, 1974). Riverine flow into the basin is negligible due to the basin's small watershed (Morcos, 1970; Maillard and Soliman, 1986; Siddall et al., 2004) (Figure 3). One of the larger systems that drains into the Red Sea is the Baraka (Tokar) wadi in Sudan (Figure 1), which today is active 40–70 days per year (mainly during autumn). Wadi Baraka discharges between 200 and 970×10^6 m^3 water at 18.5°N into the Red Sea (Whiteman, 1971; Trommer et al., 2011), which is equivalent to a maximum of only 2 mm y^{-1} when distributed over the entire Red Sea surface area. Thus, river inflow and precipitation are negligible throughout the Red Sea region, especially when contrasted with the high rates of evaporation, which seasonally reach 2 m y^{-1} or more (Privett, 1959; Morcos, 1970; Pedgley, 1974; Maillard and Soliman, 1986; see also Fenton et al., 2000; Siddall et al., 2004). Evaporation over the Red Sea is seasonally affected by atmospheric circulation changes that are related to the Indian Ocean monsoon. The most notable feature is a seasonal wind reversal over the southern Red Sea, the general nature of which is discussed below. For more details and modeling, see Jiang et al. (2009).

During winter (October to May), reduction of sensible heat radiation occurs over the cold landmass of central Asia that is enhanced by snow-induced high albedo (reflection of insolation) over the Tibetan Plateau and Himalayas. This results in a quasi-stable high-pressure system that extends from Mongolia to central Europe, Turkey and Arabia. The cold, descending air leads to a radial outflow of cold dry air toward low-pressure areas over the relatively warm Indian Ocean. The inter-tropical convergence zone (ITCZ) is

displaced southward in winter, to 20°S over East Africa, and the winter northeast monsoon blows across the Arabian Sea and the Gulf of Aden toward central Africa (Morcos, 1970). A general southeasterly wind circulation results between a continental depression over central Africa and a continental anticyclone that extends from Asia to Arabia. Channeling by the rift geometry of the Red Sea coast then causes strong (6.7-9.3 m s^{-1}) winds to blow from the south or south-southeast over the southern half of the Red Sea, up to about 20°N (e.g., Morcos, 1970; Patzert, 1972). Throughout October to December, there is a convergence between these south-southeasterlies and the north-northwesterly winds that prevail year-round over the northern Red Sea. This convergence occupies a north-south zone across the Red Sea at around 20°N (Pedgley, 1974; Jiang et al., 2009), which varies in size and is characterised by low-pressure calms (Morcos, 1970). Jiang et al. (2009) demonstrated that the position of the convergence zone may be determined by gaps in the topography, notably the Tokar Gap some 50 km inland from the Tokar delta on the Sudan coast, which acts as an outlet of surface wind from the Red Sea basin in winter (and as an inlet in summer; see below).

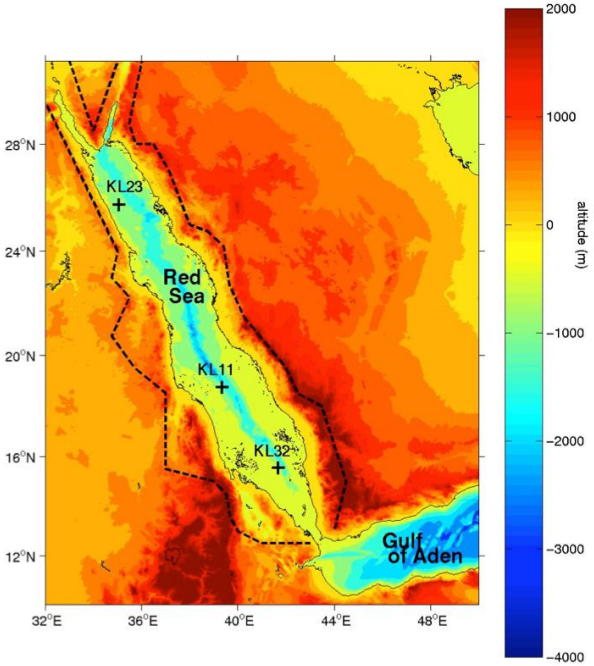

Figure 3. Topographic map of the Red Sea basin. The dashed line delineates the Red Sea watershed. Numbers refer to key sediment core locations (not used here). From Siddall et al. (2004).

During summer (June to September), the monsoon system is reversed. The spring melt reduces albedo over central Asia and insolation increases, thereby causing the landmass to warm. This warms the air above, causing it to rise, creating a quasi-stable low-pressure system over northern India (less than 995 mb; Morcos, 1970), which extends over Pakistan to the Persian Gulf. The updraft causes humid, relatively cool, maritime air to flow in from the area of higher pressure over the now relatively cool Indian Ocean. Latent heat release from condensation/precipitation against the flanks of the Himalayas fuels further deepening of the continental low-pressure cell, and consequently more inflow of maritime air, which reinforces the system. The ITCZ reaches its most northerly position (20°N) in July and becomes identified with the front of the southwest monsoon. This passes north of Aden and the southwest monsoon flows in a clockwise direction over East Africa, the Gulf of Aden, and the Arabian Sea, toward the main monsoon low of northern India (Morcos, 1970). At this time, a general northwesterly circulation is set up on the

western side of the summer Asiatic low-pressure cell. This causes relatively weak (2.4-4.4 m s^{-1}) north-northwesterly or northwesterly winds to dominate over the entire length of the Red Sea (e.g., Morcos, 1970; Patzert, 1972).

Jiang et al. (2009) analysed regional patterns superimposed on the general along-axis wind systems, which are more zonal (W-E or E-W) in nature and that are related to gaps in the topography along the basin, such as the Tokar Gap. There are eastward blowing wind jets in summer (mainly through the Tokar Gap), and westward blowing wind jets in winter, from the Saudi Arabian margin (mainly over the northern Red Sea). Wind speeds in these surface jets can reach 10 to 15 m s^{-1}, and Jiang et al. (2009) provide clear evidence of atmospheric dust entrainment over the Red Sea. Jiang et al. (2009) further note that: "*… other strong zonal winds … blow from the Egyptian coast eastward across the Red Sea longitudinal axis … . This … can also drive dust storms … .*"

In the northernmost Red Sea, records of past climate change have detected an influence of SE Mediterranean climate influences that extend across the Middle East (Arz et al., 2003a; Legge et al., 2006; Trommer et al., 2010).Contemporary climatology suggests that this link functions through winter frontal rainfall associated with Cyprus lows (El-Fandy, 1946; Morcos, 1970).

3. Past climate variability

3.1. Glacial-Interglacial changes

Throughout the last three million years, climate variability over the entire study region has been dominated by the impacts of the global ice age cycles, which were particularly prominent during the last 500,000 years (e.g., Lisiecki and Raymo, 2005), with variability that is forced by cyclic changes in the Earth-Sun orbital configuration. The astronomical forcing of climate takes place due to three main processes, namely: changes in the eccentricity of Earth's orbit around the sun, with climate impacts in approximately 100 and 400 thousand year cycles; changes in the tilt of the Earth's rotational axis, with impacts on climate in 41 thousand year cycles; and precession of the equinoxes, with climate impacts in cycles of 19 and 23 thousand year durations(e.g., Milankovitch, 1941; Hays et al., 1976; Berger, 1977; Imbrie and Imbrie, 1980, 1986).

Glaciations were strongly focused on the North American and northern Eurasian locations of continental ice sheets, but the impacts on climate were global. This had global implications for sea level, with fluctuations between interglacial highstands up to +10m (Rohling et al., 2008, 2009b; Kopp et al., 2009;Muhs et al., 2011) and glacial lowstands at –120m or lower relative to present sea level (Rohling et al., 1998a; Waelbroeck et al., 2000). Methods for constructing continuous records of sea level variability now exist for the last half million years(Waelbroeck et al., 2000; Siddall et al., 2003; Rohling et al., 2009b, 2010). Model-based deconvolutions of deep-sea stable oxygen isotope records have also been used to extend the record over many millions of years (Bintanja et al., 2005; DeBoer et al., 2010, 2011), but these still require independent validation (Figure 4).

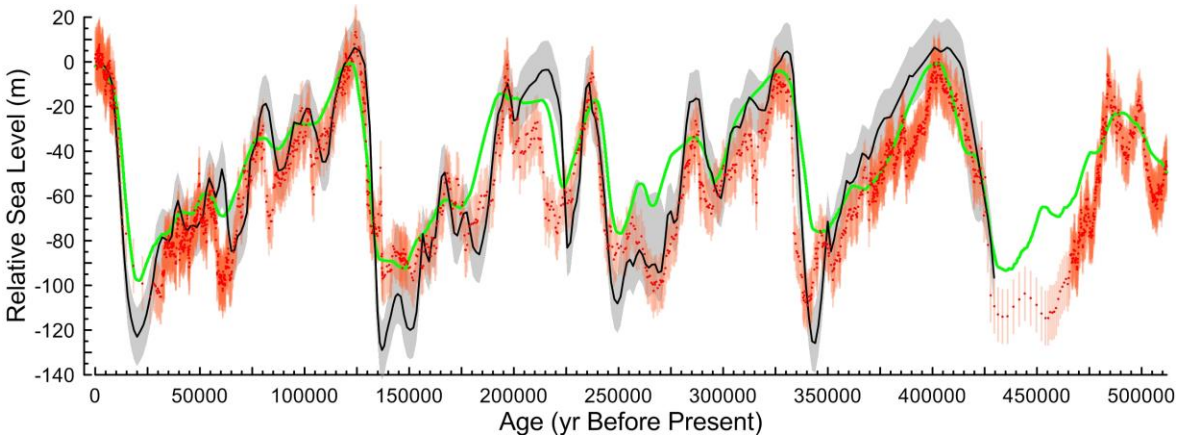

Figure 4. Comparison between three approaches for reconstructing continuous records of sea-level variations. Black is Waelbroeck et al. (2002) based on coral-calibrated deep-sea stable oxygen isotope data, with uncertainties (grey). Green is the reconstruction of De Boer et al. (2010, 2011) from a model-based deconvolution of deep-sea stable oxygen isotope records into a temperature and a sea-level component, following the method of Bintanja et al. (2005). Red dots with orange (2σ) uncertainty bars represent the Red Sea reconstruction on a U-Th adjusted chronology (Rohling et al., 2009b, 2010). From Rohling et al. (2012).

Along with enlarged land-ice volumes, another defining characteristic of glacials was widespread cooling (e.g., CLIMAP project members, 1976; MARGO project members, 2009;Schneider von Deimling et al., 2006; Rohling et al., 2012).In the study region, cooling produced a strong gradient from west to east through the Mediterranean and then to the southeast along the axis of the Red Sea. Relative to the present, glacial sea surface temperatures in summer were reduced by 8±2°C in the westernmost Mediterranean, 5±2°C around Sicily, and 3±2°C in the easternmost Mediterranean; winter sea surface temperatures were reduced by 5±2°C, 3±1°C, and 0-2.5°C, respectively (Hayes et al., 2005).In the Red Sea, glacial-interglacial differences in sea surface temperature were of the order of 3-4°C (Arz et al., 2003b; Trommer et al., 2011), with a bias toward summer. These estimates for the Red Sea are in agreement with estimates for the western Arabian Sea (see compilation of Rohling et al., 2012).

Terrestrial temperature contrasts between glacials and interglacials are typically around 1.3 or 1.5 times larger than sea surface temperature contrasts (Braconnot et al., 2007; Laîné et al., 2009). This agrees with estimates by Kuhlemann et al. (2008) of terrestrial temperature reductions of 12°C in the northwest Mediterranean region, 7.5°C around Sicily, and 6°C or less to the south and east of Crete. Thus, mean glacial-interglacial temperature contrasts of 4-6°C are expected on land around the Red Sea.

A notable southward displacement of climate zones also occurred in glacials on both orbital and sub-orbital timescales (e.g., Wang et al., 2004, 2006), as well as global lowering of the snow line and associated vertical compression of vegetation zones (e.g., Broecker and Denton, 1989; Barmawidjaja et al., 1993; Klein et al., 1995; Kuhlemann et al., 2008). Such snowline and vegetation displacements were particularly strongly expressed in the mountain ranges along the northern margin of the Mediterranean (Kuhlemann et al., 2008).

In a general sense, summer circulation/monsoons were weakened in the northern hemisphere during glacial periods, and winter circulation/monsoons strengthened(e.g., Rohling et al., 2003, 2009c and references therein).

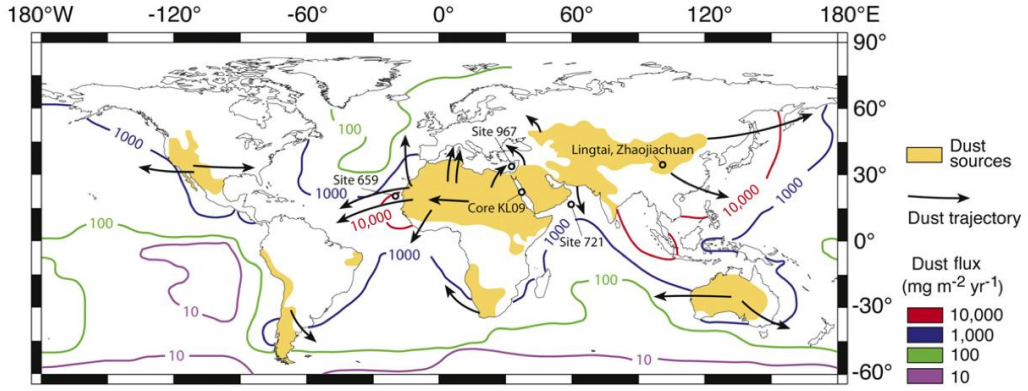

Figure 5.Major global dust sources and locations of dust records. Dust flux contours (mg m^{-2} yr^{-1}) are shown in oceans surrounding dust sources (after Duce et al., 1991). Locations of dust records discussed are indicated (Ocean Drilling Program sites 659 (Tiedemann et al., 1994), 721 (deMenocal et al., 1991), and 967 (Larrasoaña et al., 2003), core KL09 (this study) and the Zhaojiachuan and Lingtai loess sections (Sun et al., 2006)). Site KL09 is the Red Sea record presented in Rohling et al. (2008b, 2009b) and Roberts et al. (2011). From Roberts et al. (2011).

Overall, atmospheric dust transport was strongly intensified during glacials (e.g., Mayewski et al., 1997; Larrasoaña et al., 2003; Rohling et al., 2003; Ruth et al., 2007; Lambert et al., 2008; Winckler et al., 2008; Trauth et al., 2009; Roberts et al., 2011), which attests to increased aridity, stronger winds, and reduced vegetation cover (reduced soil cohesion). However, even within the Mediterranean and Red Sea region, there can be considerable spatial differences in dust flux histories because of spatially different conditions in the various dust source areas. The western Mediterranean receives dust from northwest Africa/western Sahara, while the eastern Mediterranean receives dust from the eastern Sahara (Libya, Egypt). The Red Sea receives influxes of wind-blown dust from the easternmost Sahara, Sudan, and Saudi Arabia (Middleton and Goudie, 2001; Hickey and Goudie, 2007; Jiang et al., 2009) (Figure 5). On millennial timescales, dust variability from various source areas varies considerably within and around the Mediterranean and Red Seas; these variations do not seem to be systematic between the two basins (Roberts et al., 2011) (Figure 6). This suggests considerable regional differences in the temporal variability of vegetation cover, soil cohesion, and wind patterns/intensities.

Ice-core records from Greenland and Antarctica reveal that glacial periods were characterised by strong temperature fluctuations on millennial timescales (Figure 7). Antarctic ice-core records reveal climate variability that was less abrupt and of smaller amplitude than that observed in Greenland (Blunier et al., 1998; EPICA community members, 2006). Continuous records of sea-level variability, developed from Red Sea oxygen isotope records, indicate that, within the last glacial cycle, global ice volume fluctuated on millennial timescales with a rhythm close to that of variability observed in Antarctic climate records (Siddall et al., 2003, 2008; Rohling et al., 2004, 2009b; Grant et al., in review).

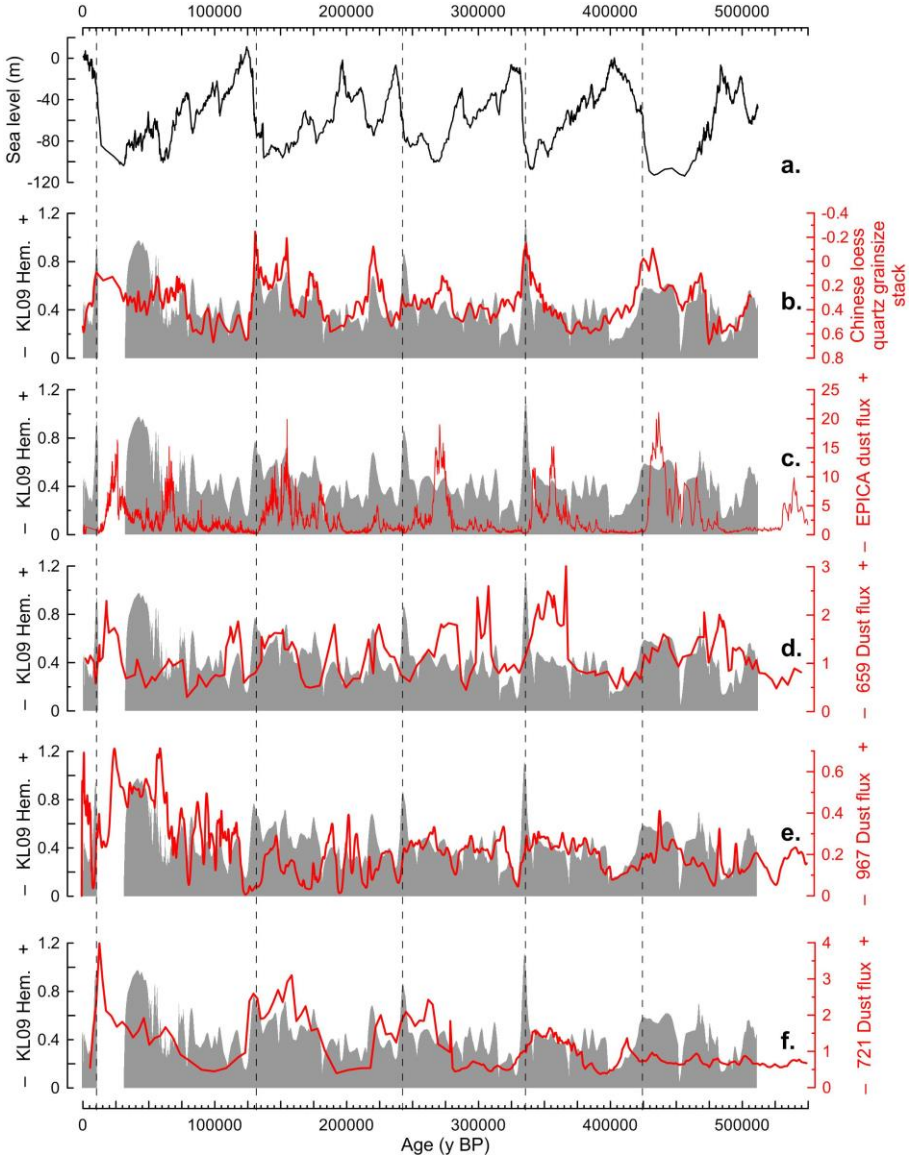

Figure 6. Comparison of sea level and dust records for the Red Sea, circum-Sahara region, and Chinese Loess Plateau. (a) Central Red Sea sea-level reconstruction (Rohling et al., 2009b, 2010). (b) Environmental magnetic IRM900 mT@AF120 mT proxy for windblown hematite (Hem.) in Red Sea core KL09 (grey) compared to the stacked Chinese loess grainsize record from Zhaojiachuan and Lingtai, Chinese Loess Plateau (red; from Sun et al., 2006, with minor age adjustments in Roberts et al., 2011). Panels (c), (d), (e), and (f), respectively, compare the Red Sea dust record (grey shading) with dust records from EPICA Dome C, Antarctica (Lambert et al., 2008), ODP Site 659, off northwest Africa (Tiedemann et al., 1994), ODP Site 967, Eastern Mediterranean Sea (Larrasoaña et al., 2003), and ODP Site 721, Arabian Sea (deMenocal et al., 1991). Vertical dashed lines coincide with Red Sea dust peaks at the glacial terminations and are shown to assist comparisons between panels. The Red Sea records are shown for consistency on same (Rohling et al., 2009b, 2010) chronology as used in Roberts et al. (2011). This chronology is (subtly) updated within the last 150,000 years in Figures 7 and 8, based on the latest age controls developed by Grant et al. (in review).

Greenland ice-core records and North Atlantic marine sediment records provide evidence of particularly strong climate fluctuations that have become known as Dansgaard-Oeschger cycles, which include the particularly cold Heinrich events (e.g., Grootes et al., 1993; Dansgaard et al., 1993; Broecker, 2000; Hemming, 2004). In many records, these millennial-scale fluctuations appear as an alternation between 'more intense' and 'less intense' glacial conditions, and the Heinrich events are often particularly cold/intense.

Western Mediterranean sea-surface temperature strongly fluctuated in close agreement with the Dansgaard-Oeschger cycles and Heinrich events (Rohling et al., 1998b;Cacho et al., 1999, 2000, 2001; Martrat et al., 2004; Frigola et al., 2007).

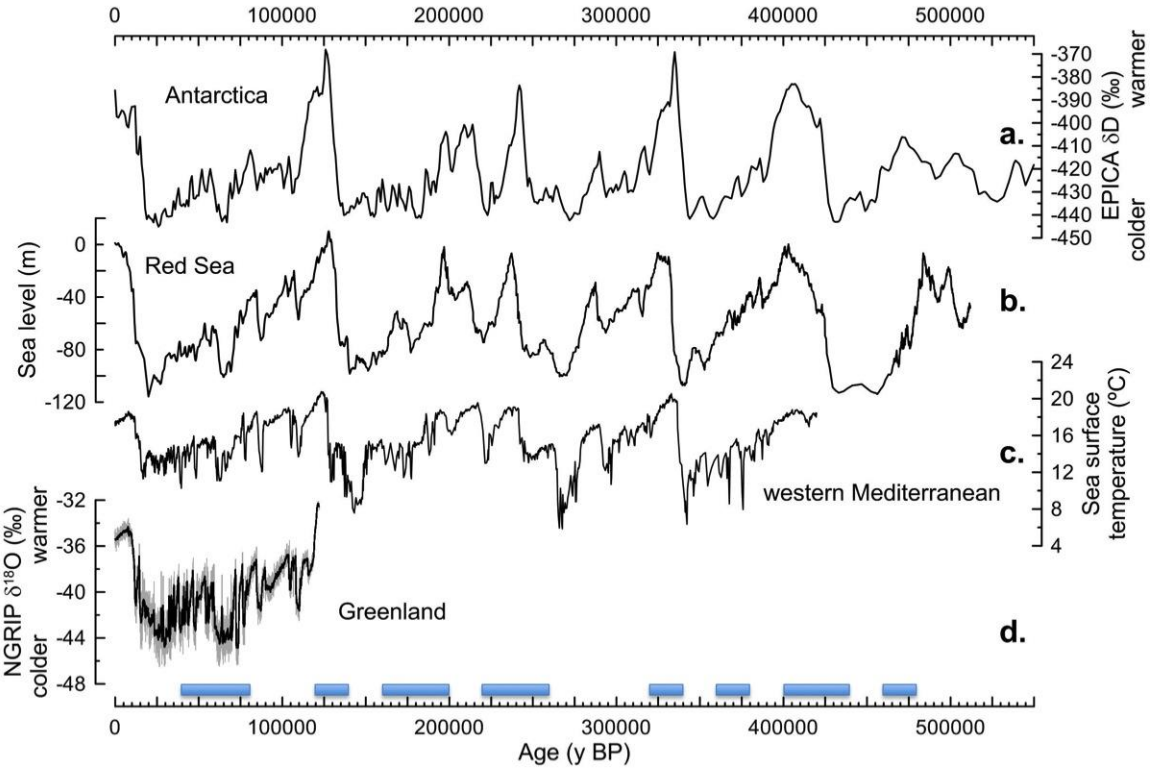

Figure 7. Comparison of different records of climate variability including polar ice core records, sea level, and Mediterranean temperature variability. (a) The EPICA Dome C ice-core stable hydrogen isotope proxy for temperature, Antarctica (Jouzel et al., 2007); (b) the Red Sea sea-level record in the pre-150 ka interval on the chronology of Rohling et al. (2009b, 2010) and in the post-150 ka interval on the latest chronology using the age constraints developed by Grant et al. (in review); (c) sea surface temperature in the Alboran Sea, westernmost Mediterranean (Martrat et al., 2004); and (d) in grey the stacked North-GRIP ice-core oxygen isotope proxy for temperature, Greenland (Wolff et al., 2010), and – for clarity – in black a 21-point moving average smoothing. Blue bars at the bottom indicate intervals of particularly pronounced millennial-scale climate variability, after the analysis of Siddall et al. (2010).

Dansgaard-Oeschger oscillations in the Northern Hemisphere were related to Antarctic (southern hemisphere) temperature cycles, through a systematic out-of-phase relationship (e.g., Blunier et al., 1998; Blunier and Brook, 2001; Stocker and Johnsen, 2003; EPICA community members, 2006). In this relationship, which has become known as the 'bipolar temperature see-saw', the magnitude of warming in the southern hemisphere is proportional to the duration of cold episodes in the northern hemisphere (e.g., Stocker and Johnsen, 2003; EPICA community members, 2006). Siddall et al. (2010) identified during which intervals of the last 500,000 years such millennial-scale climate variability has been particularly pronounced, and found that this was the case at 40-80 ka, 120-140 ka, 160-200 ka, 220-260 ka, 320-340 ka, 360-380 ka, 400-440 ka, and 460-480 ka (Figure 7). Because of the global nature of this variability, it may be expected that

these intervals of generally enhanced climate variability will be noticeable in record from Africa and Eurasia, even if the exact nature of the variability may differ between regions.

Northern high-latitude cooling events particularly affected the northern sectors of the Mediterranean region, due to cold air outbreaks that were channelled toward the basin through gaps in the mountain ranges along its northern limits, which also triggered atmospheric instability over the Mediterranean with implications for regional precipitation regimes (e.g., Rohling et al., 1998, 2002b; Casford et al., 2003; Frigola et al., 2007; Kuhlemann et al., 2008). Thus, vegetation (pollen) records from the western Mediterranean and northern sector of the eastern Mediterranean also reflect the strong impacts of northerly (Greenland-style) climate influences (e.g., Allen et al., 1999; Tzedakis, 1999, 2009; Moreno et al., 2002; Sánchez-Goñi et al., 2002;Tzedakis et al., 2004; Müller and Pross, 2007; Kotthoff et al., 2008).

From the Red Sea area, relatively little is known about climate variability. It was always dry, with high windblown dust input, but this input nevertheless reveals intensity variations that are closely similar to those observed on the Chinese Loess Plateau (Roberts et al., 2011). This suggests that the main climate influences over the central Red Sea (with respect to windblown dust input) were dominated by atmospheric circulation/wind changes that reflect the larger westerlies-dominated northern hemisphere climate variability and Indian-Asian monsoon variability (e.g., Porter and An, 1995; Rohling et al., 2003).

3.2. African monsoon changes

Superimposed upon the glacial cycles, the entire Mediterranean region is strongly affected by monsoon intensity variations, which are dominated by northern hemisphere insolation changes that mainly reflect the influences of precession and eccentricity (e.g., Rossignol-Strick, 1985; Kutzbach and Street-Perrott, 1985; Kutzbach and Guetter, 1986; Kutzback and Gallimore, 1988; COHMAP members, 1988). African monsoon maxima are well known to have been associated with insolation maxima. Freshwater flooding from the African margin into the Mediterranean during these times caused collapse of deep-water formation, eventually resulting in deep-water anoxia. These events are easily recognised in eastern Mediterranean sedimentary sequences due to the fact that organic carbon preservation led to the formation of characteristic black organic rich layers, called sapropels (e.g., Rohling, 1994 and references therein).

The Mediterranean sapropel record reflects the more intense African monsoon maxima, and individual sapropels have been dated(Hilgen, 1991; Hilgen et al., 1993; Kroon et al., 1998; Emeis et al., 2000; Lourens et al., 1996, 2001) based on the ages of precession-driven insolation maxima that are known from astronomical solutions (Milankovitch, 1941; Berger 1978; Laskar et al., 2004). A particularly straightforward summary table of ages is given for the main sapropels by Kroon et al. (1998), after Lourens et al. (1996). These datings may be important for archaeological, anthropological, and biogeographical studies, because they provide a chronological framework that may help to date and understand, for example, past migration pulses through the Sahara desert region (e.g., Osborne et al., 2008; Drake et al., 2011), or past humid phases associated with fossil hominid finds (e.g., McDougall et al., 2005, 2008; Brown et al., 2012).The sapropel record indicates that there have been more than a hundred of such strongly developed African monsoon maxima over the past couple of million years.

During times with intensified African monsoon circulation, the spatial extent of the Sahara Desert was much reduced, which has become known as “greening of the Sahara”, when the African monsoon penetrated further northward than today. This penetration was partly due to orbital forcing, and partly resulted from northward expansion of vegetation into the previously more reflective desert, which in turn triggered further northward penetration of the monsoon front in a “vegetation-albedo feedback process” (e.g., Brovkin et al., 1998; Claussen et al., 1998; Foley et al., 2003). During intense monsoon maxima, the monsoon front appears to have penetrated northward past the central Saharan watershed (at about 21°N), and seasonal run-off occurred from the central Saharan mountains into the eastern Mediterranean along the wider North African margin (Rohling et al., 2002a, 2004; Osborne et al., 2008; Paillou et al., 2009; Drake et al., 2011). Such drainages will have presented green corridors along which humans and animals may have migrated across the otherwise arid region (Osborne et al., 2008; Drake et al., 2011).These ideas integrate a wide variety of evidence for past increases in precipitation and water-availability throughout the currently hyper-arid Sahara, including the distributions of animal and human fossils, sedimentological data, lake-level reconstructions, etc. (e.g., Pachur and Braun, 1980; Gaven et al., 1981; Szabo et al., 1995; Gasse, 2000; Mandell and Simmons, 2001; Pachur, 2001; Cremaschi, 2002; Kuper and Kröpelin, 2006; Pachur and Altmann, 2006; Armitage et al., 2007; Drake et al., 2011).Records of African monsoon variability reveal that centennial to millennial-scale decreases/collapses in monsoon intensity occurred during several monsoon maxima, and that these roughly coincided with intrusions of northerly cooling events into the Mediterranean basin (e.g., Gasse 2000; Mercone et al., 2001; Rohling et al., 2002a,b, 2004; Casford et al., 2003; Scrivner et al., 2004; Osborne et al., 2008).

It is important to note that there is no evidence that the African monsoon penetrated at any time directly into the Mediterranean basin. Rainfall gradient and isotope reconstructions in the Levant indicate that rain in that region was always sourced from the north and west, from the Mediterranean, even during monsoon maxima (Goodfriend, 1991; Matthews et al., 2000; Bar-Matthews et al., 2003; McGarry et al., 2004; Vaks et al., 2007). Moreover, Tzedakis (2009) presented a compelling case that times of insolation-driven African monsoon maxima were not characterised by enhanced summer precipitation around the northern and eastern Mediterranean, as had been often inferred before (e.g., Rohling and Hilgen, 1991; Tzedakis, 2009; and references therein).Pollen data indicate that summer aridity was enhanced at these times and that any enhanced rainfall likely took place in winter(with some possible regional exceptions); i.e., typical Mediterranean climate conditions were intensified (Tzedakis, 2009).

During opposite phases of the precession cycle, the monsoon was weak, and the (hyper-)arid Sahara desert was spatially extended, similar to the present, without water-courses crossing it to the wider North African margin. Orbital cyclicity in the African monsoon is obvious in records of wind-blown dust fluxes from the Sahara (e.g., Wehausen and Brumsack, 2000;Lourens et al., 2001; Larrasoaña et al., 2003; Trauth et al., 2009), which reflects insolation forcing of the African monsoon.

3.3. Indian monsoon changes

Variations in the Indian Ocean monsoon circulation, which affect the wind-field over the southern sector of the Red Sea region, have been documented especially by marine

sedimentary records from the Arabian Sea (e.g., Prell and Kutzbach, 1987; Clemens and Prell, 1990, 2003; Clemens et al., 1991; Sirocko et al., 1993; Rostek et al., 1997; Reichart et al., 1998; Schultz et al., 1998; Almogi-Labin et al., 2000; Schmiedl and Leuschner, 2005;Ivanochko et al., 2005) and by speleothem records from Oman and Socotra (Burns et al., 2003, 2004; Fleitmann et al., 2003a,b, 2004, 2007).Long Arabian Sea records provide convincing evidence for a predominant control of orbital precession and thus insolation on the Indian monsoon intensity, similar to the African monsoon. Speleothem data from Oman (Fleitmann et al., 2003a,b, 2004, 2007) indicate that the precipitation regime of the Indian Ocean monsoon expanded to affect the southeastern margin of the Arabian Peninsula during the Early to Middle Holocene summer southwest Monsoon maximum, whereas that region currently (during the opposite precession phase) is unaffected (Conroy and Overpeck, 2011).

Trommer et al. (2011) described the timing of a somewhat more humid interval in the central Red Sea Bakala (Tokar) wadi catchment, and found that this started immediately following the last interglacial sea-level highstand, and lasted several thousand years. This relative timing agrees with the period of deposition of the deep-sea anoxic event known as sapropel S5 in the eastern Mediterranean, which is also recognised as a humid interval in the speleothem record of Soreq cave, Israel, which reflects the last interglacial African monsoon maximum (Bar-Matthews et al., 1997, 1999, 2000, 2003). U-series dating of the Soreq cave record demonstrates that the last interglacial African monsoon maximum dates to 128-120 thousand years ago (ka). This agrees with datings from Dongge cave, China, for the last interglacial maximum of the Asian monsoon, from 129.3±0.9 to 119.6±0.6 ka (Yuan et al., 2004). On millennial scales, therefore, the timing of monsoon maxima seems to be roughly similar for all three major monsoon systems (African, Indian, and Southeast Asian).

Red Sea records contain no evidence for any major precipitation/vegetation changes associated with monsoon maxima; the area appears to have remained (hyper) arid. Monsoon variability, however, affected Red Sea oceanography through changes in the wind-field over the basin (Biton et al., 2010; Trommer et al., 2011), and strong wind-blown dust variations over time support the notion of important fluctuations in wind forcing over the basin (Rohling et al., 2008b; Roberts et al., 2011).

Millennial-scale variability in wind-blown dust records of the central Red Sea is coherent with millennial-scale changes in Arabian Sea productivity (Schultz et al., 1998; Rohling et al., 2008b), as well as with Chinese loess records (Porter and An, 1995; Sun et al., 2006; Roberts et al., 2011). This links Arabia with winter-dominated climate variability as recorded in Greenland ice core records (Rohling et al., 2003). In short, there is good evidence that colder conditions in Greenland coincided with intensified winter-type atmospheric circulation over Asia, which also affected Arabia, possibly through the winter (northeast) monsoon.

4. Implications and Conclusions

4.1.Conditions relevant to proposed migration routes across the southern Red Sea

4.1.1. Sea level

The intense ice-age cycles of the last 500,000 years have been associated with important variability in global sea level, over a range of 120m or more below the present to perhaps 10 m above the present (Figure 4). The Strait of Bab-el-Mandab in the southern Red Sea,

which connects the basin with the open ocean, is highly sensitive to sea-level change because it is (today) only 137 m deep. This is of the same order as past sea-level drops during glacial maxima, and there have consequently been many proposals of a potential migration route across the Southern Red Sea, assuming that a passage between Africa and Arabia may have emerged during times of maximum glacial sea-level lowstands.

Fernandes et al. (2006) evaluated the concept of emergence of a southern landbridge between Africa and Arabia, and concluded that there is no evidence for it at any time during the last 500,000 years. Emergence of a landbridge in the strait would lead rapidly to desiccation within the highly evaporative Red Sea, with deposition of evaporites within a matter of several centuries in the open basin and within a matter of years to decades in shallow coastal environments. Moreover, there is evidence of substantial persistent local water depths above the sill in the strait of at least 15 m (Fernandes et al., 2006), and up to 35 m (Biton et al., 2008); for the last glacial maximum, the passage depth has been estimated as up to 25±4 m (Lambeck et al., 2011). For lower water depths, inflow from the open ocean would have become sufficiently restricted for basin-wide development of extreme salinities in excess of about 75 psu. There is evidence that salinities at times rose above 49 psu, causing local extinction of planktonic foraminifera (Fenton et al., 2000 and refs. therein). However, salinities remained below 75 psu, given that higher values would have caused also the local extinction of all pteropods and all benthic foraminifera, which did not happen (Rohling et al., 1998; Fenton et al., 2000).

Regardless of the above, the strait passage was much shallower and narrower than today, during glacial sea-level lowstands (Rohling et al., 1998; Siddall et al., 2004; Lambeck et al., 2011). This is especially clearly illustrated by a recent advanced reconstruction of strait morphology during the last glacial maximum (Lambeck et al., 2011), which takes into account detailed hydrographic data for the present-day strait, sea level change during the last glacial maximum, and a model for isostatic change components. Lambeck et al. (2011) also present arguments about older glacial lowstands, and support the notion that an open passage remained in existence. In summary, it is evident from the combined studies that any migration across the southern Red Sea during glacial sea-level lowstands would have: (a) benefited from the fact that the marine passage was strongly reduced in width; and (b) definitely included some element of swimming, rafting, or navigation.

4.1.2. Climate conditions

Another important control on potential migrations across the Southern Red Sea concerns regional climatic conditions. For example, was enough water and food available to sustain migrating animals/humans on either side of the Strait? This question has come to the fore because of a recent proposal (Armitage et al., 2011) that an early wave of human migration out of Africa occurred across the southern Red Sea, with migration toward and across the strait region during the penultimate glacial maximum (the 'Saalian'), and subsequent spreading across/along the Arabian Peninsula during the monsoon maximum of the last interglacial (about 128-120 ka).

Red Sea sedimentary records provide important insights into regional climatic conditions. Windblown dust concentrations have been measured in exactly the same sedimentary sequences that were used to reconstruct the Red Sea sea-level record. This dust record clearly illustrates that the transition between the Saalian glacial and the last interglacial was characterised by extreme fluxes of windblown dust, which reflects high winds and

pronounced aridity in the region (Roberts et al., 2011). Organic geochemical data, also from the same sample sequence, demonstrate that (lightly) enhanced humidity in the Red Sea region – the most likely local expression of the last interglacial summer monsoon maximum – first developed only after the sea-level highstand had peaked and sea level had started to drop again (Trommer et al., 2011). Data from Oman suggest that relatively more humid conditions may have started to develop earlier from about 135 ka (Fleitmann et al., 2003b;Vaks et al., 2007), a little later than in the eastern Sahara (from 140 ka; Szabo et al., 1995; Osmond and Dabous, 2004; Vaks et al., 2007).

It would be an oversimplification to assume a simple succession from low sea-level to favourable climate for migration across the Arabian Peninsula during the transition from the Saalian glacial to the last interglacial. The data instead reveal considerable complexity across that transition, highlighting that the sea-level lowstand and the climatically more favourable conditions were separated by at least 5,000 years of arid regional conditions and sharp sea-level rise (Roberts et al., 2011).This does not exclude the possibility that the southern route out of Africa was employed at this time. But if it was, then the animals/humans involved must have been resilient to significantly adverse environmental conditions. We note that a similar sequence of events is observed for almost all glacial terminations. In the next section, we elaborate a new view of more promising migration intervals.

4.1.3. A new concept: “windows of opportunity” for southern migration out of Africa
Our sea-level and wind-blown dust records, sampled from the same central Red Sea sediment sequence (Rohling et al., 2008b, 2009b, 2010; Roberts et al., 2011) are shown in Figure 8. The last 150,000 years are shown on a new chronology (Grant et al., in review), which is tightly constrained relative to the U-Th dated Soreq Cave record from Israel (Bar-Matthews et al., 1997, 1999, 2000, 2003). Prior to 150 ka, the records are shown on a chronology developed (Rohling et al., 2009) by correlation with the Antarctic EPICA Dome C temperature proxy record on the EDC3 chronology (Jouzel et al., 2007), with an adjustment that accounts for radiometric datings of past sea-level highstands (Rohling et al., 2010).

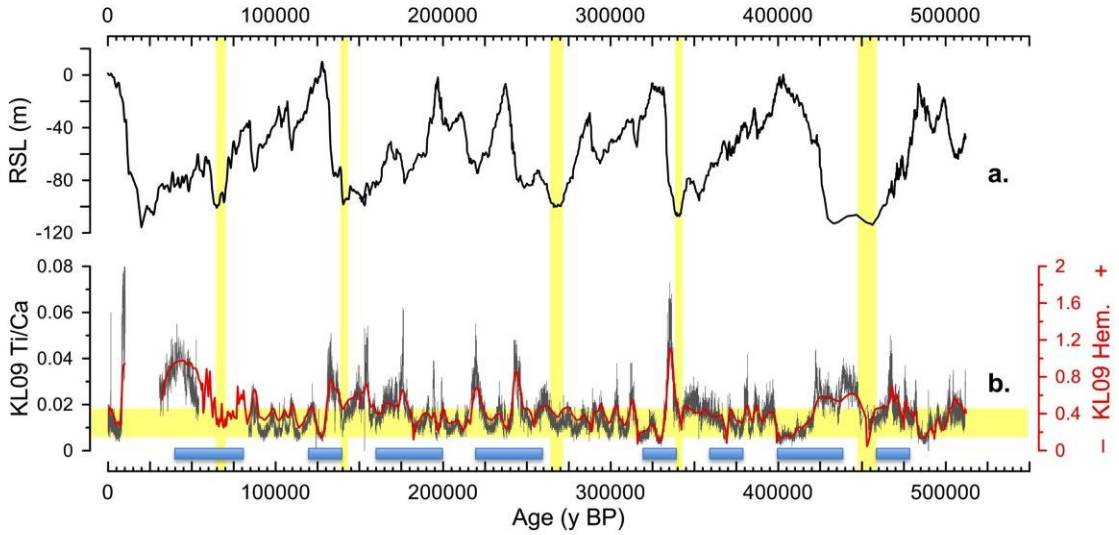

Figure 8. Direct comparison between: (a) the latest version of the Red Sea sea-level reconstruction, with the pre-150 ka interval on the chronology of Rohling et al. (2009b, 2010) and the post-150 ka interval on the new chronology of Grant et al. (in review); and (b) central Red Sea dust proxy data, including the Ti/Ca ratio from core-scanning XRF analysis (grey), and hematite concentration data from environmental magnetic analyses (red) (see also Rohling et al., 2008b; Roberts et al., 2011).Data originate from a single sampling of the same sedimentary sequence, which ensures unambiguous phase relationships between the various records. Yellow bars are explained in the text. Blue bars indicate intervals of particularly pronounced millennial-scale climate variability, after the analysis of Siddall et al. (2010) (see also Figure 7).

The horizontal yellow bar in Figure 8 highlights relatively low dust fluxes, similar to those of the Holocene. During times with such relatively low dust fluxes, we infer that the regional climate may have been most favourable for habitation/migration, in contrast to the intervening intervals with high dust fluxes, which attest to more intense winds and lower soil cohesion due to even lower soil moisture and even more scarce vegetation cover than today. The vertical yellow bars identify periods when both: (a) sea level stood 100 m or more below the present, so that the marine connection to be crossed in the Strait of Bab el Mandab would have been only some 6 km wide (cf. Last Glacial Maximum reconstruction of Lambeck et al., 2011); and (b) dust fluxes were relatively low. These highlighted intervals therefore represent periods with relatively favourable conditions ("windows of opportunity") for potential migrations between northeast Africa and southeast Arabia via a southern route. There is increasing evidence that the southern route was used for the final migration out of Africa by anatomically modern humans (AMH) (e.g., Derricourt, 2005; Fernandes et al., 2012).

The highlighted periods of significant sea-level lowstands were also characterised by emerged continental shelves around the Arabian Peninsula. These provided excellent habitation and migration potential for animals and humans, especially if the enhanced

hydraulic head due to sea-level lowering led to enhanced freshwater seepage on the emerged shelves from groundwater reservoirs (e.g., Parker and Rose, 2008). Such seepage exists even today on the shelves, in submarine form (Parker and Rose, 2008; Ghoneim, 2008).The emerged shelves may therefore have presented an excellent habitat with gentle topography, freshwater availability, and an abundance of coastal/marine resources. If emerged shelves were key migration/habitation zones, then much of the anthropological record may now be under water.

A number of "windows of opportunity" for migration along the southern route out of Africa within the last half million years are highlighted in Figure 8. These "windows" date to about 458-448, 340-345, 272-265, 145-140, and 70-65 ka. The interval of 145-140 ka may be relevant with respect to a tentative early migration of AMH that led to early inhabitation at the Hormuz region of the Arabian Gulf with an oldest dating of 127 ±16 ka (Armitage et al., 2011). That population is thought to have been ''unsuccessful' in that it did not leave any decendants (Fernandes et al., 2012). Instead, all non-African humans originate from a more recent migration out of Africa, dated with various molecular clock approaches at around 57 to 65 ka, with an upper age bound of 65-70 ka based on east African data (Fernandes et al., 2012). This age range of 65 +5/−8 ka is in remarkable agreement with our "window of opportunity" of 65-70 ka for a southern-route out of Africa migration. The chronological uncertainties for our records in that interval are less than 1000 years (Grant et al., in review). Haplotype dispersal maps suggest that the migration at around 65 ka followed the southern route out of Africa, and that Arabia was the first staging post in the spread of AMH around the world (Fernandes et al., 2012).

4.2. Conditions relevant to habitation of, and migration through, the Sahara

Migration potential through the Sahara Desert was comprehensively assessed by Drake et al. (2011). Their abstract says it all: "*… both animals and humans populated it* [the Sahara] *during past humid phases. … More animals crossed via this route than used the Nile corridor …* [and] *… many of these species are aquatic. This dispersal was possible because during the Holocene humid period the region contained a series of linked lakes, rivers, and inland deltas comprising a large interlinked waterway, channeling water and animals into and across the Sahara … . This system was last active in the early Holocene when many species appear to have occupied the entire Sahara. Human dispersals were influenced by this distribution … . Lacustrine sediments show that the "green Sahara" also existed during the last interglacial (~125 ka) and provided green corridors that could have formed dispersal routes at a likely time for the migration of modern humans out of Africa.*" Both periods highlighted in that study are well-known insolation-driven African monsoon maxima. The Holocene period is known to correspond to eastern Mediterranean sapropel S1, and the last interglacial period to sapropel S5 (e.g., Rohling and Hilgen, 1991; Rohling et al., 2002a, 2004; Scrivner et al., 2005; Osborne et al., 2008).

Archaeological observations around exclusively rain-fed depressions on the Libyan Plateau suggest that monsoonal summer rains from central Africa periodically penetrated at least as far north as Kharga (roughly 25°N) during the Holocene monsoon maximum despite the fact that conditions during that pluvial phase seem to have remained drier than during earlier Quaternary pluvial phases (Mandel and Simmons, 2001). This suggestion that the Holocene monsoon maximum was of a relatively low intensity, compared with previous Quaternary monsoon maxima, has been corroborated by quantitative reconstructions of impacts of the Holocene and last interglacial monsoon

maxima in the eastern Mediterranean (Rohling, 1999; Rohling et al., 2004). Hence, past monsoon maxima – datings for which can be obtained from the astronomical ages of insolation-driven monsoon maxima (Hilgen 1991; Hilgen et al., 1993; Kroon et al., 1998; Emeis et al., 2000; Lourens et al., 1996, 2001) – represent times of enhanced humidity that may have been crucial for migrations through the otherwise hyperarid Sahara 'barrier' between sub-Saharan Africa and the Mediterranean/Levantine regions.

As mentioned above, several African monsoon maxima (e.g., the Holocene and last interglacial) have been interrupted by centennial to millennial-scale periods of reduced monsoon intensity. Hence, potential routes for migration through the Sahara region remained intermittent, subject to periodic returns of harsh conditions.

Finally, hypotheses that invoke an importance of periods of rapid, millennial-scale climate variability for developments and/or migrations of hominins and their food sources, for example through intermittent habitat fragmentation, may benefit from the objectively identified episodes of generally (globally) enhanced millennial-scale climate variability (Siddall et al., 2010). We have indicated these intervals (40-80 ka, 120-140 ka, 160-200 ka, 220-260 ka, 320-340 ka, 360-380 ka, 400-440 ka, and 460-480 ka) in Figures 7 and 8.

4.3. Conditions relevant to migrations through the Levant

Conditions for migrations through the Levant are normally poor, because of hyperarid conditions in the Sinai-Negev region. However, data from a N-S array of caves highlight a window of time between 140 and 110 ka when this region was intermittently more humid (especially between 133 and 122 ka), and thus more hospitable (Vaks et al., 2007).This closely matches data that indicate more humid conditions in the Egyptian Sahara (Osmond and Dabous, 2004), which suggests a high probability that a pathway existed through the Levant for migrations out of Africa between about 140 and 110 ka, with possible extension to 85 ka, after which hyperarid conditions were re-established (Vaks et al., 2007).

Derricourt (2005) reviewed climatic and archaeological studies to conclude that the Levantine route was the most likely route of early (pre-85 ka) migrations out of Africa, in contrast to the youngest (post-85 ka) migration, which he links more to a southern route across the Bab-el-Mandab Strait (see above). Early AMH finds from Qafzeh and Skhul in the Near Eastdate to between 119±18 and 81±13 ka(e.g., Grün et al., 2005; Shea, 2008; Armitage et al., 2011; Petraglia, 2011). Genetic data indicate that this migration did not leave any descendants in the modern human population outside Africa, which instead can be traced back to a migration out of Africa that took place around 65 ka, likely via a southern route (Fernandes et al., 2012; see above).

For Levantine migration routes, the key control may have been exerted by development of pluvial episodes, as recorded and accurately dated in cave speleothem deposits (e.g., Derricourt, 2005; Vaks et al., 2007; Shea, 2008). These intermittently more humid conditions in the Levant are closely related to monsoon maxima associated with northern hemisphere insolation maxima. It should be emphasised that monsoon maxima, with "greening of the Sahara", were not limited to only interglacial insolation maxima, but occurred also during insolation maxima within glacial times (e.g., Larrasoaña et al., 2003; Liu et al., 2012).

The control by pluvials that applies to the Levantine route is considerably more straightforward than the "windows of opportunity" control we have proposed in section 4.1.3. for the southern route, which requires a combination of low sea level and concomitant interludes of relatively favourable climate conditions. These "windows of opportunity" are not simply aligned with monsoon maxima, but instead reflect millennial-scale episodes of relatively favourable climate within glacial maxima.

4.4. Conditions along the European margin of the Mediterranean

The European margin of the Mediterranean has been strongly affected by intense climate swings that originate in the North Atlantic region, as recorded in Greenland ice cores. Cold events were transmitted to the Mediterranean by northerly air outbreaks through gaps in the mountainous topography around the northern margin of the Mediterranean, especially over the northwest Mediterranean, the Adriatic Sea, and the Aegean (e.g., Rohling et al., 1998b, 2002b; Moreno et al., 2002; Casford et al., 2003; Frigola et al., 2007; Kuhlemann et al., 2008). During the Holocene, a strong temporal coincidence has been found between the northerly cooling events and archaeological transitions in the northeastern sector of the Mediterranean region (Clare et al., 2008). Because of resultant atmospheric instabilities within the Mediterranean basin, northerly cooling events may have had an amplified effect on snowline lowerings and vegetation-zone migrations in the Mediterranean region (e.g., Kuhlemann et al., 2008; and references therein).

Despite this glacial variability, the Mediterranean region during glacial times was a refugium with relatively mild conditions for plants and animals, avoiding the much more severe climatic stress over the main Eurasian landmass to the north of the Alps/Carpathians (e.g., Tzedakis, 2009; Blondel, 2009). The region's great diversity of terrain and microclimates, drainage patterns, and accentuated relief with many rock shelters and caves, would have been conducive to a relatively rich variety of exploitable plant and animal food sources, and of camp locations. From a climatic point of view, therefore, it is likely that habitation and migration were possible throughout this region even during severe glacials, especially in lowlands and coastal plains, and with potential to range into higher elevations during periods with milder conditions.

Acknowledgements

This paper contributes to UK Natural Environment Research Council projectsNE/E01531X/1 (RESET), NE/I009906/1 (iGlass), and NE/H004424/1.EJR acknowledges further support from a Royal Society-Wolfson Research Merit Award.

References

Adamson, D.A., Gasse, F., Street, F.A., and Williams, M.A.J., 1980. Late Quaternary history of the Nile. *Nature, 288*, 50–55.

Allen, J.R.M., Brandt, U., Brauer, A., Hubberten, H.W., Huntley, B., Keller, J., Kraml, M., Mackensen, A., Mingram, J., Negendank, J.F.W., Nowaczyk, N.R., Oberhänsli, H., Watts, W.A., Wulf, S., and Zolitschka, B., 1999. Rapid environmental changes in southern Europe during the last glacial period. *Nature, 400***,** 740–743.

Almogi-Labin, A., Schmiedl, G., Hemleben, Ch., Siman-Tov, R., Segl, M., and Meischner, D., 2000. The influence of the NE winter monsoon on productivity changes in the Gulf of Aden, NW Arabian Sea, during the last 530 ka as recorded by benthic foraminifera. *Mar. Micropaleontol., 40*, 295–319.

Armitage, S.J., Drake, N.A., Stokes, S., El-Hawat, A., Salem, M., White, K., Turner, P., and McLaren, S.J., 2007. Multiple phases of North African humidity recorded in lacustrine sediments from the Fazzan Basin, Libyan Sahara. *Quat. Geochron., 2*, 181–186.

Armitage, S.J., Jasim, S.A., Marks, A.E., Parker, A.G., Usik, V.I., and Uerpmann, H.P., 2011. The southern route "Out of Africa": evidence for an early expansion of modern humans into Arabia. *Science, 331*, 453–456.
Arz, H.W., Lamy, F., Pätzold, J., Müller, P.J., and Prins, M., 2003a. Mediterranean moisture source for an early-Holocene humid period in the Northern Red Sea. *Science, 300*, 118–121.
Arz, H.W., Pätzold, J., Müller, P.J., and Moammar, M.O., 2003b. Influence of Northern Hemisphere climate and global sea level rise on the restricted Red Sea marine environment during termination I, *Paleoceanography, 18*, 1053, doi:10.1029/2002PA000864.
Bar-Matthews, M., Ayalon, A., Gilmour, M., Matthews, A., and Hawkesworth, C.J., 2003. Sea-land oxygen isotopic relationships from planktonic foraminifera and speleothems in the Eastern Mediterranean region and their implication for paleorainfall during interglacial intervals. *Geochim. Cosmochim. Acta, 67*, 3181–3199.
Bar-Matthews, M., Ayalon, A., and Kaufman, A., 1997. Late Quaternary paleoclimate in the eastern Mediterranean region from stable isotope analysis of speleothems at Soreq Cave, Israel. *Quat. Res., 47*,155–168.
Bar-Matthews, M., Ayalon, A., and Kaufman, A., 2000. Timing and hydrological conditions of Sapropel events in the Eastern Mediterranean, as evident from speleothems, Soreq Cave, Israel. *Chem. Geol., 169*,145–156.
Bar-Matthews, M., Ayalon, A., Kaufman, A., and Wasserburg, G.J., 1999. The Eastern Mediterranean paleoclimate as a reflection of regional events: Soreq Cave, Israel. *Earth Planet. Sci. Lett., 166*,85–95.
Barmawidjaja, D.M., Rohling, E.J., Van der Kaars, W.A., Vergnaud-Grazzini, C., and Zachariasse, W.J., 1993. Glacial conditions in the northern Molucca Sea region (Indonesia). *Paleogeogr., Palaeoclimatol., Palaeoecol., 101,* 147–167.
Berger, A., 1977. Support for the astronomical theory of climatic change. *Nature, 269*, 44–45.
Béthoux, J.P., 1984. Paleo-hydrologie de la Mer Mediterranee au cours des derniers 20 000 ans. *Oceanol. Acta*, *7*, 43–48.
Béthoux, J.P., and Gentili, B., 1994. The Mediterranean Sea, a test area for marine and climatic interactions, in: Malanotte-Rizzoli, P., and Robinson, A.R. (eds.), *Ocean Processes in Climate Dynamics: Global and Mediterranean Examples*, Kluwer Academic Publishers, Netherlands, 239–254.
Bintanja, R., van de Wal, R.S.W., and Oerlemans, J., 2005. Modelled atmospheric temperatures and global sea levels over the past million years. *Nature, 437*, 125–128.
Biton, E., Gildor, H., and Peltier, W.R., 2008. Relative sea level reduction at the Red Sea during the Last Glacial Maximum. *Paleoceanography, 23*, PA1214, doi:10.1029/2007PA001431.
Biton, E., Gildor, H., Trommer, G., Siccha, M., Kucera, M., van der Meer, M.T.J., and Schouten, S., 2010. Sensitivity of Red Sea circulation to monsoonal variability during the Holocene: an integrated data and modeling study.*Paleoceanography, 25*, PA4209, doi:10.1029/2009PA001876.
Blondel, J., 2009. The nature and origin of the vertebrate fauna, in: Woodward, J.C. (ed.) *The PhysicalGeography of the Mediterranean*, Oxford University Press, Oxford, pp. 139–163.
Blunier, T. and Brook, E., 2001. Timing of millennial-scale climate change in Antarctica and Greenland during the last glacial period. *Science, 291*, 109–112.
Blunier, T., Chapellaz, J., Schwander, J., Dällenbach, A., Stauffer, B., Stocker, T.F., Raynaud, D., Jouzel, J., Clausen, H.B., Hammer, C.U., and Johnsen, S.J., 1998. Asynchrony of Antarctic and Greenland climate change during the last glacial period. *Nature, 394*, 739–743.
Boucher, K., 1975. *Global climate*, The English University Press Ltd., London, 326 pp.
Braconnot, P., Otto-Bliesner, B.,Harrison, S.,Joussaume, S.,Peterchmitt, J.Y.,Abe-Ouchi, A.,Crucifix, M.,Driesschaert, E.,Fichefet, Th.,Hewitt, C.D.,Kageyama, M.,Kitoh, A.,Laîné, A.,Loutre, M.F., Marti, O.,Merkel, U.,Ramstein, G.,Valdes, P.,Weber, S.L.,Yu, Y., and Zhao, Y.,2007. Results of PMIP2 coupled simulations of the mid-Holocene and Last Glacial Maximum – Part 1: experiments and large-scale features. *Clim. Past, 3*, 261–277.
Broecker, W.S., 2000. Abrupt climate change: causal constraints provided by the paleoclimate record. *Earth-Sci. Rev., 51*, 137–154.
Broecker, W.S., and Denton, G.H., 1989. The role of ocean-atmosphere reorganizations in glacial cycles. *Geochim. Cosmochim. Acta, 53*, 2465–2501.
Brovkin, V., Claussen, M., Petoukhov, V., and Ganopolski, A., 1998. On the stability of the atmosphere–vegetation system in the Sahara/Sahel region, *J. Geophys. Res., 103*, 31613–31624.
Brown, F.H., McDougall, I., and Fleagle, J.G., 2012. Correlation of the KHS Tuff of the Kibish Formation to volcanic ash layers at other sites, and the age of early *Homo sapiens* (Omo I and Omo II), *J. Human. Evol.* Doi: 10.1016/j.jhevol.2012.05.014.
Burns, S.J., Fleitmann, D., Matter, A., Kramers, J., and Al-Subbary, A.A., 2003. Indian Ocean climate and an absolute chronology over Dansgaard/Oeschger Events 9 to 13. *Science, 301*, 1365–1367.

Burns, S.J., Fleitmann, D., Matter, A., Kramers, J., and Al-Subbary, A.A., 2004. Indian Ocean climate and an absolute chronology over Dansgaard/Oeschger events 9 to 13: correction. *Science, 305*, 1567.
Cacho, I., Grimalt, J.O., Pelejero, C., Canals, M., Sierro, F.J., Flores, J.A., and Shackleton, N.J., 1999. Dansgaard-Oeschger and Heinrich event imprints in Alboran Sea paleotemperatures. *Paleoceanography, 14*, 698–705.
Cacho, I., Grimalt, J.O., Sierro, F.J., Shackleton, N.J., and Canals, M., 2000. Evidence of enhanced Mediterranean thermohaline circulation during rapid climate coolings. *Earth Planet. Sci. Lett., 183*, 417–429.
Cacho, I., Grimalt, J.O., Canals, M., Sbaffi, L., Shackleton, N.J., Schönfeld, J., and Zahn, R., 2001. Variability of the western Mediterranean Sea surface temperatures during the last 25,000 years and its connection with the northern hemisphere climatic changes. *Paleoceanography, 16*, 40–52.
Cantu, V., 1977. The climate of Italy, in: Wallen,C.C. (ed.), *Climates of Central and Southern Europe - World Survey of Climatology, 6*. Elsevier, Amsterdam, 127–183.
Casford, J.S.L., Rohling, E.J., Abu-Zied, R.H., Jorissen, F.J., Leng, M., and Thomson, J., 2003. A dynamic concept for eastern Mediterranean circulation and oxygenation during sapropel formation. *Palaeogeogr., Palaeoclimatol., Palaeoecol.*, *190*, 103–119.
Clare, L., Rohling, E.J., Weninger, B., and Hilpert, J., 2008. Warfare in Late Neolithic/ Early Chalcolithic Pisidia, southwestern Turkey. Climate induced social unrest in the late 7th millennium calBC. *Documenta Praehistorica, 35* (Neolithic Studies 15), 65–92.
Claussen, M., Brovkin, V., Ganopolski, A., Kubatski, C., and Petoukhov, V., 1998. Modelling global terrestrial vegetation–climate interaction, *Phil. Trans. R. Soc. Lond., 353,* 53–63.
Clemens, S.C., and Prell, W.L., 1990. Late Pleistocene variability of Arabian Sea summer monsoon winds and continental aridity: eolian records from the lithogenic component of deep-sea sediments. *Paleoceanography, 5*,109–145.
Clemens, S.C., and Prell, W.L., 2003. A 350,000 year summer-monsoon multi-proxy stack from the Owen Ridge, northern Arabian Sea. *Mar. Geol., 201*, 35–51.
Clemens, S.C., Prell, W.L., Murray, D., Shimmield, G., and Weedon, G., 1991. Forcing mechanisms of the Indian Ocean monsoon. *Nature, 353*, 720–725.
CLIMAP project members, 1976. The surface of the ice-age Earth. *Science, 191*, 1131–1137.
COHMAP members, 1988. Climatic changes of the last 18,000 years: observations and model simulations. *Science, 241*, 1043–1052.
Conroy, J.L., and Overpeck, J.T., 2011. Regionalization of present-day precipitation in the greater monsoon region of Asia. *J. Clim., 24*, 4073–4095.
Cremaschi, M., 2002. Late Pleistocene and Holocene climatic changes in the central Sahara; the case study of the south-western Fezzan, Libya, in: Hassan, F.A. (ed.), *Droughts, Food and Culture – Ecological Change and Food Security in Africa's Later Prehistory*, Kluwer/Plenum, New York, pp. 65–81.
Dansgaard, W., Johnsen, S.J., Clausen, H.B., Dahl-Jensen, D., Gundestrup, N.S., Hammer, C.U., Hvidberg, C.S., Steffensen, J.P., Sveinbjornsdottir, A.E., Jouzel, J., and Bond, G., 1993. Evidence for general instability of past climate from a 250 kyr ice core. *Nature, 364*, 218–219.
De Boer, B., van de Wal, R.S.W., Bintanja, R., Lourens, L.J., and Tuenter, E., 2010. Cenozoic global ice-volume and temperature simulations with 1-D ice-sheet models forced by benthic $\delta^{18}O$ records. *Annals Glaciol., 51*, 23–33.
De Boer, B., van de Wal, R.S.W., Lourens, L.J., and Bintanja, R., 2011. Transient nature of the Earth's climate and the implications for the interpretation of benthic records. *Palaeogeogr., Palaeoclimatol., Palaeoecol.*, in press (on-line available), doi: 10.1016/ j.palaeo.2011.02.001.
deMenocal, P., Bloemendal, J., and King, J., 1991. A rock-magnetic record of monsoonal dust deposition to the Arabian Sea: evidence for a shift in the mode of deposition at 2.4 Ma. *Proc. ODP., Sci. Res., 177*, 389–407.
Derricourt, R., 2005. Getting "out of Africa": sea crossings, land crossingsand culture in the hominin migrations. *J. World Prehist., 19*, 119–132.
Drake, N.A., Blench, R.M., Armitage, S.J., Bristow, C.S., and White, K.H., 2011. Ancient watercourses and biogeography of the Sahara explain the peopling of the desert. *Proc. Natl. Acad. Sci. USA, 108*, 458–462.
Duce, R.A., Liss, P.S., Merrill, J.T., Atlas, E.L., Buat-Menard, P., Hicks, B.B., Miller, J.M., Prospero, J.M., Arimoto, R., Church, T.M., Ellis, W., Galloway, J.N., Hansen, L., Jickells, T.D., Knap, A.H., Reinhardt, K.H., Schneider, B., Soudine, A., Tokos, J.J., Tsunogai, S., Wollast, R., and Zhou, M., 1991. The atmospheric input of trace species to the world ocean. *Global Biogeochem. Cycles, 5*, 193–259.
El-Fandy, M.G., Barometric lows of Cyprus. *Quat. J. Roy. Meteorol. Soc., 72*, 291–306.

Emeis, K.C., Sakamoto, T., Wehausen, R., and Brumsack, H.J., 2000. The sapropel record of the eastern Mediterranean Sea – results of Ocean Drilling Program Leg 160. *Palaeogeogr., Palaeoclimatol., Palaeoecol., 158*, 371-395.

EPICA community members, 2006. One-to-one coupling of glacial climate variability in Greenland and Antarctica. *Nature, 444*, 195–197.

Fenton, M., Geiselhart, S., Rohling, E.J., and Hemleben, C., 2000. Aplanktonic zones in the Red Sea. *Mar. Micropaleontol., 40*, 277–294.

Fernandes, C., Rohling, E.J., and Siddall, M., 2006. Absence of Quaternary Red Sea land bridges: biogeographic implications. *J. Biogeogr., 33*, 961–966.

Fernandes, V., Alshamali, F., Alves, M., Costa, M.D., Pereira, J.B., Silva, N.M., Cherni, L., Harich, N., Cerny, V., Soares, P., Richards, M.B., and Pereira, L., 2012. The Arabian cradle: mitochondrial relicts of the first steps along the southern route out of Africa, *Am. J. Human Genetics, 90*, doi: 10.1016/j.ajhg.2011.12.010, 1–9.

Fleitmann, D., Burns, S.J., Mangini, A., Mudelsee, M., Kramers, J., Villa, I., Neff, U., Al-Subarry, A., Buettner, A., Hippler, D., and Matter, A., 2007. Holocene ITCZ and Indian monsoon dynamics recorded in stalagmites from Oman and Yemen (Socotra). *Quat. Sci. Rev., 26*, 170–188.

Fleitmann, D., Burns, S.J., Mudelsee, M., Neff, U., Kramers, J., Mangini, A., and Matter, A., 2003a. Holocene forcing of the Indian monsoon recorded in a stalagmite from Southern Oman. *Science, 300*, 1737–1739.

Fleitmann, D., Burns, S.J., Neff, U., Mangini, A., and Matter, A., 2003b. Changing moisture sources over the last 330,000 years in Northern Oman from fluid-inclusion evidence in speleothems. *Quat. Res., 60*, 223–232.

Fleitmann, D., Burns, S.J., Neff, U., Mudelsee, M., Mangini, A., and Matter, A., 2004. Palaeoclimatic interpretation of high-resolution oxygen isotope profiles derived from annually laminated speleothems from Southern Oman. *Quat. Sci. Rev., 23*, 935–945.

Foley, J.A., Coe, M.T., Scheffer, M., and Wang, G., 2003. Regime shifts in the Sahara and Sahel: interactions between ecological and climatic systems in Northern Africa. *Ecosystems*, *6*, 524–539.

Frigola, J., Moreno, A., Cacho, I., Canals, M., Sierro, F.J., Flores, J.A., Grimalt, J.O., Hodell, D.A., and Curtis, J.H., 2007. Holocene climate variability in the western Mediterranean region from a deepwater sediment record. *Paleoceanography, 22*, PA2209, doi:10.1029/2006PA001307.

Gasse, F., 2000. Hydrological changes in the African tropics since the Last Glacial Maximum, *Quat. Sci. Rev., 19*, 189–211.

Gaven, C., Hillaire-Marcel, C., and Petit-Maire, N., 1981. A Pleistocene lacustrine episode in southeastern Libya. *Nature, 290*, 131–133.

Ghoneim, E., 2008. Optimum groundwater locations in the northern United Arab Emirates. *Int. J. Rem. Sens., 29*, 5879–5906.

Goodfriend, G.A., 1991. Holocene trends in ^{18}O in land snail shells from the Negev Desert and their implications for changes in rainfall source areas. *Quat. Res., 35*, 417–426.

Grant, K.M., Rohling, E.J., Bronk Ramsey, C., Bar-Matthews, M., Satow, C., Medina-Elizalde, M., and Roberts, A.P., in review. Rapid response of ice volume to polar temperature variations. *Nature* in review.

Grootes, P.M., Stuiver, M., White, J.W.C., Johnsen, S., and Jouzel, J., 1993. Comparison of oxygen isotope records from the GISP2 and GRIP Greenland ice cores. *Nature, 366*, 552–554.

Grün, R., Stringer, C., McDermott, F., Nathan, R., Porat, N., Robertson, S., Taylor, L., Mortimer, G., Eggins, S., and McCulloch, M., 2005. U-series and ESR analyses of bones and teeth relating to the human burials from Skhul. *J. Hum. Evol., 49*, 316–334.

Hayes, A., Kucera, M., Kallel, N., Sbaffi, L., and Rohling, E.J., 2005. Glacial Mediterranean sea surface temperatures reconstructed from planktonic foraminiferal assemblages.*Quat. Sci. Rev., 24*, 999–1016.

Hays, J.D., Imbrie, J., and Shackleton, N.J., 1976. Variations in the earth's orbit: pacemaker of the ice ages. *Science, 194*, 1121–1132.

Hemming, S.R., 2004. Heinrich events: massive Late Pleistocene detritus layers of the North Atlantic and their global imprint. *Rev. Geophys., 42*, 1–43.

Hickey, B., and Goudie, A.S., 2007. The use of TOMS and MODIS to identify dust storm source areas: the Tokar delta (Sudan) and the Seistan basin (south west Asia), in: Goudie, A.S., and Kalvoda,J. (eds.), *Geomorphological Variations*, P3K, Prague, pp. 37–57.

Hilgen, F.J., 1991. Astronomical calibration of Gauss to Matuyama sapropels in the Mediterranean and implication for the geomagnetic polarity time scale. *Earth Planet. Sci. Lett., 104*, 226–244.

Hilgen, F.J., Lourens, L.J., Berger, A., and Loutre, M.F., 1993. Evaluation of the astronomically calibrated time-scale for the late Pliocene and earliest Pleistocene. *Paleoceanography, 8*, 549–565.

Imbrie, J., and Imbrie, J.Z., 1980. Modeling the climatic response to orbital variations. *Science, 207*, 943–953.

Imbrie, J., and Imbrie, K.P., 1986. *Ice Ages: Solving the Mystery*. Harvard University Press, Cambridge Mass., 224 pp.
Ivanochko, T.S., Ganeshram, R.S., Brummer, G.J.A., Ganssen, G., Jung, S.J.A., Moreton, S.G., and Kroon, D., 2005. Variations in tropical convection as an amplifier of global climate change at the millennial scale. *Earth Planet. Sci. Lett., 235*, 302–314.
Jiang, H., Farrar, J.T., Beardsley, R.C., Chen, R., and Chen, C., 2009. Zonal surface wind jets across the Red Sea due to mountain gap forcing along both sides of the Red Sea. *Geophys. Res. Lett., 36*, L19605, doi:10.1029/2009GL040008.
Jouzel, J., Masson-Delmotte, V., Cattani, O., Dreyfus, G., Falourd, S., Hoffmann, G., Minster, B., Nouet, J., Barnola, J.M., Chappellaz, J., Fischer, H., Gallet, J.C., Johnsen, S., Leuenberger, M., Loulergue, L., Luethi, D., Oerter, H., Parrenin, F., Raisbeck, G., Raynaud, D., Schilt, A., Schwander, J., Selmo, E., Souchez, R., Spahni, R., Stauffer, B., Steffensen, J.P., Stenni, B., Stocker, T.F., Tison, J.L., Werner, M., and Wolff., E.W., 2007. Orbital and millennial Antarctic climate variability over the past 800,000 years. *Science, 317*, 793–797.
Klein, A.G., Isacks, B., and Bloom, A.L., 1995. Modern and last glacial maximum snowline in Peru and Bolivia: implications for regional climatic change. *Bull. Inst. Fr. Etudes Andines, 24*, 607–617.
Kopp, R.E., Simons, F.J., Mitrovica, J.X., Maloof, A.C., and Oppenheimer, M., 2009. Probabilistic assessment of sea level during the last interglacial stage. *Nature, 462*, 863–868.
Kottek, M., Grieser, J., Beck, C., Rudolf, B., and Rubel, F.,2006. World map of the Köppen-Geiger climate classification updated. *Meteorol. Z.*, *15*, 259–263.
Kotthoff, U., Muller, U.C., Pross, J., Schmiedl, G., Lawson, I.T., and Schulz, H., 2008. Lateglacial and Holocene vegetation dynamics in the Aegean region: an integrated view based on pollen data from marine and terrestrial archives. *Holocene, 18*, 1019–1032.
Kroon, D., Alexander, I., Little, M., Lourens, J.L., Matthewson, A., Robertson, A.H.F., and Sakamoto, T., 1998. Oxygen isotope and sapropel stratigraphy in the Eastern Mediterranean during the last 3.2 million years. *Proc. ODP Sci. Res., 160*, 181–190.
Kuhlemann, J., Rohling, E.J., Kumrei, I., Kubik, P., Ivy-Ochs, S., and Kucera, M., 2008. Regional synthesis ofMediterranean atmospheric circulation during the Last Glacial Maximum. *Science, 321*, 1338–1340.
Kuper, R., and Kröpelin, S., 2006. Climate-controlled Holocene occupation in the Sahara: motor of Africa's evolution. *Science, 313*, 803–807.
Kutzbach, J.E., and Gallimore, R.G., 1988. Sensitivity of a coupled atmosphere/mixed layer ocean model to changes in orbital forcing at 9000 years. *J. Geophys. Res., 93*, 803–821.
Kutzbach, J.E., and Guetter, P.J., 1986. The influence of changing orbital parameters and surface boundary conditions on climate simulations for the past 18,000 years. *J. Atmos. Sci., 43*, 1726–1759.
Kutzbach, J.E., and Street-Perrott, F.A., 1985. Milankovitch forcing in the level of tropical lakes from 18 to 0 kyr . *Nature, 317*, 130–134.
Laîné, A., Kageyama, M.,Braconnot, P.,and Alkama, R.,2009. Impact of greenhouse gas concentration changes on surface energetics in IPSL-CM4: regional warming patterns, land-sea warming ratios, and glacial-interglacial differences. *J. Clim., 22*, 4621–4635.
Lambeck, K., Purcell, A., Fleming, N.C., Vita-Finzi, C., Alsharekh, A.M., and Bailey, G.M., 2011.Sea level and shoreline reconstructions for the Red Sea: isostatic and tectonic considerations and implications for hominin migration out of Africa.*Quat. Sci. Rev., 30*, 3542–3574.
Lambert, F., Delmonte, B., Petit, J.R., Bigler, M., Kaufmann, P.R., Hutterli, M.A., Stocker, T.F., Ruth, U., Steffensen, J.P., and Maggi, V., 2008. Dust-climate couplings over the past 800,000 years from the EPICA Dome C ice core. *Nature, 452*, 616–619.
Larrasoaña, J.C., Roberts, A.P., Rohling, E.J., Winklhofer, M., and Wehausen, R., 2003. Three million years of monsoon variability over the northern Sahara. *Clim. Dyn., 21*, 689–698.
Leaman, K.D., and Schott, F.A., 1991. Hydrographic structure of the convection regime in the Gulf of Lions: Winter 1987. *J. Phys. Oceanogr.*, *21*, 575–598.
Legge, H.L., Mutterlose, J., and Arz, H.W., 2006. Climatic changes in the northern Red Sea during the last 22,000 years as recorded by calcareous nannofossils.*Paleoceanography, 21*, PA1003, doi:10.1029/2005PA001142.
Lisiecki, L.E., and Raymo, M.E., 2005. A Plio-Pleistocene stack of 57 globally distributed benthic $\delta^{18}O$ records. *Paleoceanography, 20*, PA1003 doi:10.1029/2004PA001071.
Liu, Q., Larrasoaña, J.C., Torrent, J., Roberts, A.P., Rohling, E.J., Liu, Z., and Jiang, Z., 2012. New constraints on climate forcing and variability in the circum-Mediterranean region from magnetic and geochemical observations of sapropels S1, S5 and S6. *Palaeogeogr., Palaeoclimatol., Palaeoecol.,* in press (on-line available).

Lolis, C.J., Bartzokas, A., and Katsoulis, B.D., 2002. Spatial and temporal 850 hPa air temperature and sea-surface temperature covariances in the Mediterranean region and their connection to atmospheric circulation.*Int. J. Climatol.*, *22*, 663–676.
Lourens, L.J., Antonarakou, A., Hilgen, F.J., van Hoof, A.A.M., Vergnaud-Grazzini, C., and Zachariasse, W.J., 1996. Evaluation of the Plio-Pleistocene astronomical timescale. *Paleoceanography, 11*, 391–413.
Lourens, L.J., Wehausen, R., and Brumsack, H.J., 2001. Geological constraints on tidal dissipation and dynamical ellipticity of the Earth over the past three million years. *Nature, 409*, 1029–1033.
Maheras, P., Xoplaki, E., Davies, T., Martin-Vide, J., Bariendos, M., and Alcoforado, M.J., 1999. Warm and cold monthly anomalies across the Mediterranean basin and their relationship with circulation; 1860–1990. *Int. J. Climatol.*, *19,* 1697–1715.
Maillard, C., and Soliman, G., 1986. Hydrography of the Red Sea and exchanges with the Indian Ocean in summer. *Oceanol. Acta, 9*, 249–269.
Malanotte-Rizzoli, P., and Bergamasco, A., 1991. The wind and thermally driven circulation of the eastern Mediterranean Sea. Part II: the baroclinic case. *Dyn. Atmos. Oceans, 15*, 355–419.
Mandel, R.D., and Simmons, A.H., 2001. Prehistoric occupation of Late Quaternary landscapes near Kharga Oasis, western desert of Egypt. *Geoarchaeology, 16*, 95–117.
MARGO project members (Waelbroeck, C., Paul, A., Kucera, M., Rosell-Melé, A., Weinelt, M., Schneider, R., Mix, A.C., Abelmann, A., Armand, L., Bard, E., Barker, S., Barrows, T.T., Benway, H., Cacho, I., Chen, M.-T., Cortijo, E., Crosta, X., de Vernal, A., Dokken, T., Duprat, J., Elderfield, H., Eynaud, F., Gersonde, R., Hayes, A., Henry, M., Hillaire-Marcel, C., Huang, C.-C., Jansen, E., Juggins, S., Kallel, N., Kiefer, T., Kienast, M., Labeyrie, L., Leclaire, H., Londeix, L., Mangin, S., Matthiessen, J., Marret, F., Meland, M., Morey, A.E., Mulitza, S., Pflaumann, U., Pisias, N.G., Radi, T., Rochon, A., Rohling, E.J., Sbaffi, L., Schäfer-Neth, C., Solignac, S., Spero, H., Tachikawa, K., Turon, J.-L.), 2009. Constraints on the magnitude and patterns of ocean cooling at the Last Glacial Maximum. *Nature Geosci., 2*, 127–132.
Martrat, B., Grimalt, J.O., Lopez-Martinez, C., Cacho, I., Sierro, F.J., Flores, J.A., Zahn, R., Canals, M., Curtis, J.H., and Hodell, D.A., 2004. Abrupt temperature changes in the western Mediterranean over the past 250,000 years. *Science, 306*, 1762–1765.
Matthews, A., Ayalon, A., and Bar-Matthews, M., 2000. D/H ratios of fluid inclusions of Soreq Cave (Israel) speleothems as a guide to the Eastern Mediterranean Meteoric Line relationships in the last 120 ky, *Chem. Geol., 166*, 183–191.
Mayewski, P.A., Meeker, L.D., Twickler, M.S., Whitlow, S., Yang, Q., Lyons, W.B., and Prentice, M., 1997. Major features and forcing of high-latitude northern hemisphere atmospheric circulation using a 110,000-year-long glaciochemical series. *J. Geophys. Res., 102*, 26,345–26,366.
McDougall, I., Brown, F.H., and Fleagle, J.G., 2005. Stratigraphic placement and age of modern humans from Kibish, Ethiopia. *Nature, 433*, 733–736.
McDougall, I., Brown, F.H., and Fleagle, J.G., 2008. Sapropels and the age of hominins Omo I and II, Kibish, Ethiopia. *J. Human Evol., 55*, 409–420.
McGarry, S., Bar-Matthews, M., Matthews, A., Vaks, A., Schilman, B., and Ayalon, A., 2004. Constraints on hydrological and paleotemperature variations in the eastern Mediterranean region in the last 140 ka given by the δD values of speleothem fluid inclusions. *Quat. Sci. Rev., 23*, 919–934.
Mercone, D., Thomson, J., Abu-Zied, R.H., Croudace, I.W., and Rohling, E.J., 2001. High-resolution geochemical and micropalaeontological profiling of the most recent eastern Mediterranean sapropel. *Mar. Geol., 177*, 25–44.
Middleton, N.J., and Goudie, A.S., 2001. Saharan dust: sources and trajectories. *Trans. Inst. British Geogr., 26*, 165–181.
Milankovitch, M., 1941. *Kanon der Erdbestrahlung und seine Anwendung auf das Eiszeitenproblem*, Special Publications Vol. 132, vol. 33 of Section Mathematics and Natural Sciences. Royal Serbian Academy, Belgrade.
Morcos, S.A., 1970. Physical and chemical oceanography of the Red Sea. *Oceanogr. Mar. Biol., 8*, 73–202.
Moreno, A., Cacho, I., Canals, M., Prins, M.A., Sánchez-Goñi, M.F., Grimalt, J.O., and Weltje, G.J., 2002. Saharan dust transport and high-latitude glacial climatic variability: the Alboran Sea record. *Quat. Res., 58*, 318–328.
Muhs, D., Simmons, K.R., Schumann, R.R., and Halley, R.B., 2011. Sea-level history of the past two interglacial periods: new evidence from U-series dating of reef corals from south Florida. *Quat. Sci. Rev., 30*, 570–590.
Müller, U., and Pross, J., 2007. Lesson from the past: present insolation minimum holds potential for glacial inception. *Quat. Sci. Rev., 26*, 3025–3029.
Naval Oceanography Command, 1987. *U.S. Navy climatic study of the Mediterranean Sea* (Naval Oceanography Command Detachment, Asheville, North Carolina), 342 pp.
Nof, D., 1979. On man-induced variations in the circulation of the Mediterranean Sea. *Tellus*, *31*, 558–564.

Osborne, A.H., Vance, D., Rohling, E.J., Barton, N., Rogerson, M., and Fello, N., 2008. A humid corridor across the Sahara for the migration "Out of Africa" of early modern humans 120,000 years ago. *Proc. Natl. Acad. Sci. USA*, *105*, 16444–16447.
Osmond, J.K., and Dabous, A.A., 2004, Timing and intensity of groundwater movement during Egyptian Sahara pluvial periods by U-series analysis of secondary U in ores and carbonates. *Quat. Res., 61*, 85–94.
Pachur, H.J., 2001. HolozäneKlimawechselin den nördlichen Subtropen, *Nova Acta Leopoldina NF88, 331*, 109–131.
Pachur, H.J., and Altmann, N., 2006. *Die Ostsahara im Spätquartär*, Springer, Berlin.
Pachur, H.J., and Braun, G., 1980. The paleoclimate of the central Sahara, Libya and the Libyan Desert, *Palaeoecol. Afr., 12*, 351–363.
Paillou, P., Schuster, M., Tooth, S., Farr, T., Rosenqvist, A., Lopez, S., and Malezieux, J.M., 2009. Mapping of a major paleodrainage system in eastern Libya using orbital imaging radar: the Kufrah River. *Earth Planet. Sci. Lett., 277*, 327–333.
Parker, A.G., and Rose, J.I., 2008. Climate change and human origins in southeastern Arabia. *Proc. Sem. Arabian Studies, 38*, 25–42.
Patzert, W.C., 1974. Wind induced reversal in Red Sea circulation. *Deep-Sea Res., 21*, 109–121.
Pedgley, D.E., 1974. An outline of the weather and climate of the Red Sea. *Publ. Cent. Natl. Exploit. Oceans Actes Colloq., 2*, 9–21.
Petraglia, M.D., 2011. Trailblazers across Arabia. *Nature, 470*, 50–51.
Porter, S.C., and An, Z., 1995. Correlation between climate events in the North Atlantic and China during the last glaciation. *Nature, 375*, 305–308.
Poulos, S.E., Drakopoulos, P.G., and Collins, M.B., 1997. Seasonal variability in sea surface oceanographic conditions in the Aegean Sea (eastern Mediterranean): an overview. *J. Mar. Sys.*, *13*, 225–244.
Prell, W.L., and Kutzbach, J.E., 1987. Monsoon variability over the past 150,000 years. *J. Geophys. Res., 92*, 8411–8425.
Privett, D.W., 1959. Monthly charts of evaporation from the North Indian Ocean, including the Red Sea and Persian Gulf. *Quart. J. Meteorol. Soc., 85*, 424–428.
Reichart, G.J., 1997. Late Quaternary variability of the Arabian Sea monsoon and oxygen minimum zone. *Geologica Ultraiectina, 154*, pp. 174.
Reichart, G.J., Lourens, L.J., and Zachariasse, W.J., 1998. Temporal variability in the northern Arabian Sea oxygen minimum zone (OMZ) during the last 225,000 years. *Paleoceanography, 13*, 607–621.
Roberts, A.P., Rohling, E.J., Grant, K.M., Larrasoaña, J.C., and Liu, Q., 2011. Atmospheric dust variability from major global source regions over the last 500,000 years. *Quat. Sci. Rev., 30*, 3537-3541.
Rodwell, M.J., and Hoskins, B.J., 1996. Monsoons and the dynamics of deserts. *Quart. J. Roy. Meteorol. Soc.*, *122*, 1385–1404.
Rohling, E.J., 1994. Review and new aspects concerning the formation of Mediterranean sapropels. *Mar. Geol., 122*, 1–28.
Rohling, E.J., 1999. Environmental controls on salinity and $\delta^{18}O$ in the Mediterranean. *Paleoceanography, 14,* 706–715.
Rohling, E.J., and Bryden, H.L., 1992. Man-induced salinity and temperature increases in western Mediterranean Deep Water. *J. Geophys. Res.*, *97*, 11191–11198.
Rohling, E.J., and Hilgen, F.J., 1991. The eastern Mediterranean climate at times of sapropel formation: a review. *Geol. Mijnb., 70,* 253–264.
Rohling, E.J., Abu-Zied, R., Casford, J.S.L., Hayes, A., and Hoogakker, B.A.A., 2009a. The marine environment: present and past, in: Woodward, J.C. (ed.) *The PhysicalGeography of the Mediterranean*, Oxford University Press, Oxford, pp. 33–67.
Rohling, E.J., Cane, T.R., Cooke, S., Sprovieri, M., Bouloubassi, I., Emeis, K.C., Schiebel, R., Kroon, D., Jorissen, F.J., Lorre, A., and Kemp, A.E.S., 2002a. African monsoon variability during the previous interglacial maximum. *Earth Planet. Sci. Lett., 202*, 61–75.
Rohling, E.J., Fenton, M., Jorissen, F.J., Bertrand, P., Ganssen, G., and Caulet, J.P., 1998a. Magnitudes of sea-level lowstands of the past 500,000 years. *Nature, 394*, 162–165.
Rohling, E.J., Grant, K., Bolshaw, M., Roberts, A.P., Siddall, M., Hemleben, Ch., and Kucera, M., 2009b. Antarctic temperature and global sea level closely coupled over the past five glacial cycles. *Nature Geosci., 2,* 500–504.
Rohling, E.J., Grant, K., Hemleben, Ch., Siddall, M., Hoogakker, B.A.A., Bolshaw, M., and Kucera, M., 2008a. High rates of sea-level rise during the last interglacial period. *Nature Geosci., 1*, 38–42.
Rohling, E.J., Grant, K., Hemleben, Ch., Kucera, M., Roberts, A.P., Schmeltzer, I., Schulz, H., Siccha, M., Siddall, M., and Trommer, G., 2008b. New constraints on the timing and amplitude of sea level fluctuations during Marine Isotope Stage 3. *Paleoceanography*, *23*, PA 3219, doi:10.1029/2008PA001617.

Rohling, E.J., Hayes, A., Kroon, D., De Rijk, S., and Zachariasse, W.J., 1998b. Abrupt cold spells in the NW Mediterranean. *Paleoceanography, 13*, 316–322.
Rohling, E.J., Liu, Q., Roberts, A.P., Stanford, J.D., Rasmussen, S.O., Langen, P.L., and Siddall., M., 2009c. Controls on the East Asian monsoon during the last glacial cycle, based on comparison between Hulu Cave and polar ice-core records. *Quat. Sci. Rev., 28*, 3291–3302.
Rohling, E.J., Marsh, R., Wells, N.C., Siddall, M., and Edwards, N., 2004. Similar melt-water contributions to glacial sea-level variability from Antarctic and northern ice sheets. *Nature, 430*, 1016–1021.
Rohling, E.J., Mayewski, P.A., and Challenor, P., 2003. On the timing and mechanism of millennial-scale climate variability during the last glacial cycle, *Clim. Dyn., 20*, 257–267.
Rohling, E.J., Mayewski, P.A., Hayes, A., Abu-Zied, R.H., and Casford, J.S.L., 2002b. Holocene atmosphere-ocean interactions: records from Greenland and the Aegean Sea. *Clim. Dyn., 18*, 587–593.
Rohling, E.J., Medina-Elizalde, M., Shepherd, J.G., Siddall, M., and Stanford, J.D., 2012. Sea surface temperature sensitivity to radiative forcing of climate over several glacial cycles. *J. Clim.*, 10.1175/2011JCLI4078.1, in press.
Rohling, E.J., Sprovieri, M., Cane, T.R., Casford, J.S.L., Cooke, S., Bouloubassi, I., Emeis, K.C., Schiebel, R., Hayes, A., Jorissen, F.J., and Kroon, D., 2004. Reconstructing past planktic foraminiferal habitats using stable isotope data: a case history for Mediterranean sapropel S5, *Mar. Micropaleontol., 50*, 89–123.
Rossignol-Strick, M., 1985. Mediterranean Quaternary sapropels, an immediate response of the African monsoon to variation of insolation. *Palaeogeogr., Palaeoclimatol. Palaeoecol., 49*, 237–263.
Rostek, F., Bard, E., Beaufort, L., Sonzogni, C., and Ganssen, G., 1997. Sea surface temperature and productivity records for the past 240 kyr in the Arabian Sea. *Deep Sea Res. II, 44***,** 1461–1480.
Rumney, G.R., 1968. *Climatology and the World's Climates*. Macmillan, New York, 656 pp.
Ruth, U., Bigler, M., Röthlisberger, R., Siggaard-Andersen, M.L., Kipfstuhl, J., Goto-Azuma, K., Hansson, M.E., Johnsen, S.J., Lu, H., and Steffensen, J.P., 2007. Ice core evidence for a very tight link between North Atlantic and east Asian glacial climate. *Geophys. Res. Lett., 34*, L03706, doi:10.1029/2006GL027876.
Saaroni, H., Bitan, A., Alpert, P., and Ziv, B., 1996. Continental Polar outbreaks into the Levant and Eastern Mediterranean.*Int. J. Climatol.*, *16*, 1175–1191.
Said, R., 1981. *The Geological Evolution of the River Nile*. Springer-Verlag, New York, 151 pp.
Sánchez-Goñi, M.F., Cacho, I., Turon, J.L., Guiot, J., Sierro, F.J., Peypouquet,J.P., Grimalt, J.O., and Shackleton, N.J., 2002. Synchroneity between marine and terrestrial responses to millennial scale climatic variability during the last glacial period in the Mediterranean region. *Clim. Dyn., 19*,95–105.
Schmiedl, G., and Leuschner, D.C., 2005. Oxygenation changes in the deep western Arabian Sea during the last 190,000 years: productivity versus deepwater circulation. *Paleoceanography, 20*, PA2008, doi:10.1029/2004PA001044.
Schneider von Deimling, T., Ganopolski, A., Held, H., and Rahmstorf, S., 2006. How cold was the Last Glacial Maximum? *Geophys. Res. Lett., 33*, L14709, doi: 10.1029/2006GL026484.
Schulz, H., von Rad, U., and Erlenkeuser, H., 1998. Correlation between Arabian Sea and Greenland climate oscillations of the past 110,000 years. *Nature, 393*, 54–57.
Scrivner, A.E., Vance, D., and Rohling, E.J., 2004. New neodymium isotope data quantify Nile involvement in Mediterranean anoxic episodes. *Geology, 32*, 565–568.
Shea, J.J., 2008. Transitions or turnovers? Climatically-forced extinctions of Homo sapiens and Neanderthals in the east Mediterranean Levant. *Quat. Sci. Rev., 27*, 2253–2270.
Siddall, M., Rohling, E.J., Almogi-Labin, A., Hemleben, Ch., Meischner, D., Schmeltzer, I., and Smeed, D.A., 2003. Sea-level fluctuations during the last glacial cycle. *Nature, 423*, 853–858.
Siddall, M., Rohling, E.J., Blunier, T., and Spahni, R., 2010. Patterns of millennial variability over the last 500 ka.*Clim. Past, 6,* 295–303.
Siddall, M., Rohling, E.J., Thompson, W.G., and Waelbroeck, C., 2008. Marine isotope stage 3 sea level fluctuations: data synthesis and new outlook. *Rev. Geophys., 46*, RG4003, doi:10.1029/2007RG000226.
Siddall, M., Smeed, D.A., Hemleben, Ch., Rohling, E.J., Schmeltzer, I., and Peltier, W.R., 2004. Understanding the Red Sea response to sea level.*Earth Planet. Sci. Lett., 225*, 421–434*.*
Sirocko, F., Sarnthein, M., Erlenkeuser, H., Lange, H., Arnold, M., and Duplessy, J. C., 1993. Century-scale events in monsoonal climate over the past 24,000 years. *Nature, 364*, 322–324.
Stocker, T.F. and Johnsen, S.J., 2003. A minimum thermodynamic model for the bipolar seesaw. *Paleoceanography, 18*, 1087, doi:10.1029/2003PA000920.
Sun, Y., Clemens, S.C., An, Z., and Yu, Z., 2006. Astronomic timescale and palaeoclimatic implication of stacked 3.6-Myr monsoon records from the Chinese Loess Plateau. *Quat. Sci. Rev.,25*, 33–48.
Szabo, B,J., Haynes, C.V.Jr, and Maxwell, T.A., 1995. Ages of Quaternary pluvial episodes determined by uranium-series and radiocarbon dating of lacustrine deposits of eastern Sahara. *Palaeogeogr., Palaeoclimatol., Palaeoecol., 113*, 227–242.

Tiedemann, R., Sarnthein, M., and Shackleton, N.J., 1994. Astronomical timescale for the Pliocene Atlantic $\delta^{18}O$ and dust flux records of Ocean Drilling Program site 659. *Paleoceanography, 9*, 619–638.
Trauth, M.H., Larrasoaña, J.C., and Mudelsee, M., 2009. Trends, rhythms and events in Plio-Pleistocene African climate. *Quat. Sci. Rev., 28*, 399–411.
Trewartha, G.T., 1966. *The Earth's Problem Climates*. Methuen & Co., London, 334 pp.
Trigo, I.F., Davies, T.D., and Bigg, G.R., 1999. Objective climatology in the Mediterranean region. *J. Clim., 12*, 1685–1696.
Trigo, I.F., Davies, T.D., and Bigg, G.R., 2000. Decline in Mediterranean rainfall caused by weakening of Mediterranean cyclones. *Geophys. Res. Lett., 27*, 2913–2916.
Trommer, G., Siccha, M., Rohling, E.J., Grant, K., van der Meer, M., Schouten, S., Hemleben, Ch., and Kucera, M., 2010. Millennial scale variability in Red Sea circulation in response to Holocene insolation forcing. *Paleoceanography, 25*, PA3203, doi:10.1029/2009PA001826.
Trommer, G., Siccha, M., Rohling, E.J., Grant, K., van der Meer, M.T.J., Schouten, S., Baranowski, U., and Kucera, M., 2011. Sensitivity of Red Sea circulation to sea level and insolation forcing during the last interglacial. *Clim. Past, 7*, 941–955.
Tzedakis, P.C., 1999. The last climatic cycle at Kopais, central Greece. *J. Geol. Soc. Lond., 156*, 425–434.
Tzedakis, P.C., 2009. Cenozoic climate and vegetation change, in: Woodward, J.C. (ed.) *The PhysicalGeography of the Mediterranean*, Oxford University Press, Oxford, pp. 89–137.
Tzedakis, P.C., Frogley, M.R., Lawson, I.T., Preece, R.C., Cacho, I., and de Abreu, L., 2004. Ecological thresholds and patterns of millennial-scale climate variability: the response of vegetation in Greece during the last glacial period. *Geology, 32*, 109-112.
Vaks, A., Bar-Matthews, M., Ayalon, A., Matthews, A., Halicz, L., and Frumkin, A., 2007. Desert speleothems reveal climatic window for African exodus of early modern humans. *Geology, 35*, 831–834.
Waelbroeck, C., Labeyrie, L., Michel, E., Duplessy, J.C., McManus, J.F., Lambeck, K., Balbon, E., and Labracherie, M., 2002. Sea-level and deep water temperature changes derived from benthic foraminifera isotopic records. *Quat. Sci. Rev., 21*, 295–305.
Wahby, S.D., and Bishara, N.F., 1981. The effect of the river Nile on Mediterranean water, before and after the construction of the High Dam at Aswan, in: Martin, J.M.,Burton, J.D.,and Eisma,D. (eds.), *River Inputs to Ocean Systems.* UNEP-UNESCO, Switzerland, 311–318.
Wang, X.F., Auler, A.S., Edwards, R.L., Cheng, H., Cristalli, P.S., Smart, P.L., Richards, D.A., and Shen, C.C., 2004. Wet periods in northeastern Brazil over the past 210 ka linked to distant climate anomalies. *Nature, 432*, 740–743.
Wang, X., Auler, A.S., Edwards, R.L., Cheng, H., Ito, E., and Solheid, M., 2006. Interhemispheric anti-phasing of rainfall during the last glacial period. *Quat. Sci. Rev.,25*, 3391–3403.
Wehausen, R., and Brumsack, H.J., 2000. Chemical cycles in Pliocene sapropel-bearing and sapropel-barren eastern Mediterranean sediments. *Palaeogeogr., Palaeoclimatol., Palaeoecol., 158*, 325–352.
Whiteman, A., 1971. *The Geology of the Sudan Republic*. Clarendon Press, Oxford, 290 pp..
Williams, M.A.J., Adamson, D.A., Cock, B., and McEvedy, R., 2000. Late Quaternary environments in the White Nile region, Sudan. *Global Planet. Change*, *26,* 305–316.
Winckler, G., Anderson, R.F., Fleisher, M.Q., McGee, D., and Mahowald, N., 2008. Covariant glacial-interglacial dust fluxes in the equatorial Pacific and Antarctica. *Science, 320*, 93–96.
Wolff, E.W., Chappellaz, J., Blunier, T., Rasmussen, S.O., and Svensson, A., 2010. Millennial-scale variability during the last glacial: the ice core record. *Quat. Sci. Rev.,29*, 2828–2838.
Yuan, D., Cheng, H., Edwards, R.L., Dykoski, C.A., Kelly, M.J., Zhang, M., Qing, J., Lin, Y., Wang, Y., Wu, J., Dorale, J.A., An, Z., and Cai, Y., 2004. Timing, duration, andtransitions of the last interglacial Asian monsoon. *Science*, *304,* 575–578.

Appendix B

Atmospheric dust variability from Arabia and China over the last 500,000 years

Andrew P. Roberts, Eelco J. Rohling, Katharine M. Grant, Juan-Cruz Larrasoaña, Qingsong Liu

Manuscript published in: Quaternary Science Reviews 30, 3537-3541 (2011)

Author contributions: APR led the study and wrote the paper; EJR designed the study and contributed to significant manuscript refinement; KMG performed isotope, geochemical and magnetic analyses on Red Sea core KL09, and contributed to manuscript refinement; JCL and QL contributed to discussion of the results and manuscript refinement. Author affiliations are listed in the manuscript.

Quaternary Science Reviews 30 (2011) 3537–3541

Contents lists available at SciVerse ScienceDirect

Quaternary Science Reviews

journal homepage: www.elsevier.com/locate/quascirev

Rapid communication

Atmospheric dust variability from Arabia and China over the last 500,000 years

Andrew P. Roberts*, Eelco J. Rohling, Katharine M. Grant, Juan C. Larrasoaña[1], Qingsong Liu[2]

School of Ocean and Earth Science, University of Southampton, National Oceanography Centre, European Way, Southampton SO14 3ZH, UK

ARTICLE INFO

Article history:
Received 27 April 2011
Received in revised form
9 September 2011
Accepted 13 September 2011
Available online 21 October 2011

Keywords:
Aeolian dust
Climate
Radiative perturbation
Glacial
Interglacial

ABSTRACT

Atmospheric mineral dust aerosols affect Earth's radiative balance and are an important climate forcing and feedback mechanism. Dust is argued to have played an important role in past natural climate changes through glacial cycles, yet temporal and spatial dust variability remain poorly constrained, with scientific understanding of uncertainties associated with radiative perturbations due to mineral dust classified as "very low". To advance understanding of the dust cycle, we present a high-resolution dust record from the Red Sea, sourced principally from Arabia, with a precise chronology relative to global sea level/ice volume variability. Our record correlates well with a high-resolution Asian dust record from the Chinese Loess Plateau. Importing our age model from the Red Sea to the Chinese Loess Plateau provides a first detailed millennial-scale age model for the Chinese loess, which has been notoriously difficult to date at this resolution and provides a basis for inter-regional correlation of Chinese dust records. We observe a high baseline of dust emissions from Arabia and China, even through interglacials, with strong superimposed millennial-scale variability. Conversely, the distal EPICA Dome C Antarctic ice core record, which is widely used to calculate the radiative impact of dust variations, appears biased to sharply delineated glacial/interglacial contrasts. Calculations based on this Antarctic dust record will therefore overestimate the radiative contrast of atmospheric dust loadings on glacial/interglacial timescales. Additional differences between Arabian/Asian and circum-Saharan records reveal that climate models could be improved by avoiding 'global mean' dust considerations and instead including large-scale regions with different dust source variability.

1. Introduction

Wind-borne mineral dust can influence climate both directly and indirectly (Tegen et al., 1996; Kaufman et al., 2002; Maher et al., 2010). Dust can influence climate directly because it changes the radiative properties of the atmosphere by scattering and absorbing solar and terrestrial radiation (IPCC, 2007). Dust also acts as ice nuclei in clouds (Sassen et al., 2003) and modifies cloud properties, which influences the formation and lifetime of clouds and affects Earth's radiative balance (Spracklen et al., 2008) and the hydrological cycle (e.g., Arimoto, 2001). Dust deposition onto the ocean surface may affect climate indirectly by supplying iron as a micronutrient to Fe-limited waters, thereby fertilizing phytoplankton productivity (Martin et al., 1991; Jickells et al., 2005; Wolff et al., 2006; Boyd and Ellwood, 2010). Increased productivity results in drawdown of atmospheric CO_2; subsequent export of biogenic carbon from surface to deep ocean waters can lead to long-term geological sequestration of carbon (e.g., Martinez-Garcia et al., 2009). It is therefore well established that aeolian dust responds to, and has a direct role in, climate change (Jickells et al., 2005; Maher et al., 2010).

It remains a crucial goal of climate research to understand the dust cycle, how it is involved in climate forcing, and how the dust cycle responds to changing climate. Anthropogenic changes to land use have been demonstrated to have major impacts on dust generation (e.g., Mulitza et al., 2010). Dust cycle models for the coming centuries predict large changes in aeolian transport from land to sea in response to anthropogenic change (e.g., Mahowald et al., 2006). Such modelling depends on understanding feedbacks between dust aerosols and radiative forcing for the past and present and the effects of dust flux changes on ocean fertilization and productivity-related atmospheric CO_2 change. One key requirement is a global view of spatial and temporal variability in dust fluxes from the major dust-producing regions, including the Sahara, Arabia, central Asia, Patagonia, and Australia (Fig. 1). The northern hemisphere is responsible for up to 80% of the global atmospheric dust loading,

* Corresponding author. Present address: Research School of Earth Sciences, The Australian National University, Canberra ACT 0200, Australia
E-mail address: andrew.roberts@anu.edu.au (A.P. Roberts).
[1] Present address: Instituto Geológico y Minero de España, Unidad de Zaragoza, Manuel Lasala 44 9B, Zaragoza 50006, Spain.
[2] Present address: Paleomagnetism and Geochronology Laboratory (SKL-LE), Institute of Geology and Geophysics, Chinese Academy of Sciences, Beijing 100029, People's Republic of China.

0277-3791/$ – see front matter © 2011 Elsevier Ltd. All rights reserved.
doi:10.1016/j.quascirev.2011.09.007

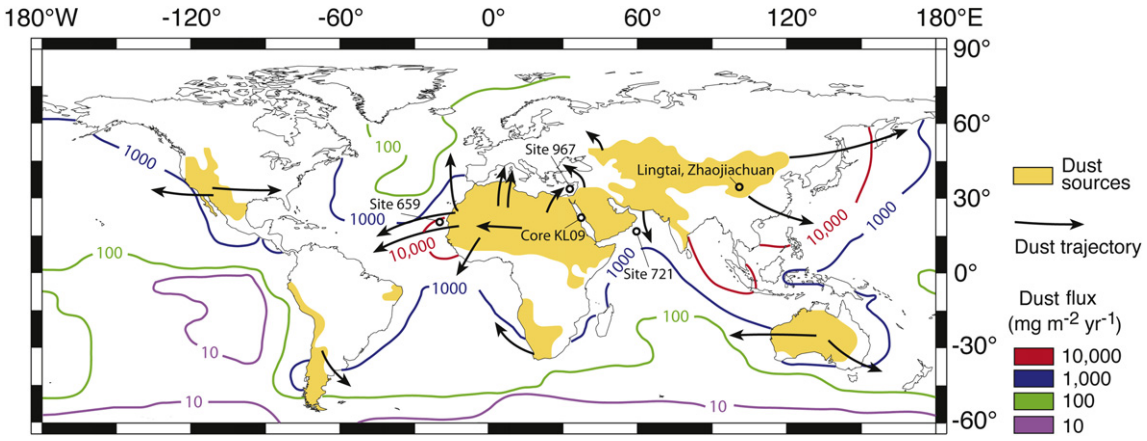

Fig. 1. Major global dust sources and locations of dust records. Dust flux contours (mg m^{-2} yr^{-1}) are shown in oceans surrounding dust sources (after Duce et al., 1991). Locations of dust records discussed are indicated (ODP sites 659 (Tiedemann et al., 1994), 721 (deMenocal et al., 1991), and 967 (Larrasoaña et al., 2003), core KL09 (this study) and the Zhaojiachuan and Lingtai loess sections (Sun et al., 2006)). Note that Antarctica lies in a distal region with low dust flux.

with the Sahara estimated to provide 40–60% of the global dust supply (Prospero et al., 2002; Maher et al., 2010). The dust belt from Arabia to the Chinese Loess Plateau represents the next major supplier of northern hemisphere dust, with Arabia producing 10–20% of global dust emissions (Maher et al., 2010). Trauth et al. (2009) compiled the longest available dust records sourced from the Sahara and Arabia. Despite the fact that these records are astronomically tuned, the records lack millennial resolution.

We present here a new dust record from marine sediment core KL09 from the central Red Sea (latitude = 19°57′36″N; longitude = 38°8′18″E; water depth = 814 m), for which Arabia, and to a lesser extent eastern North Africa, are the dominant dust sources (Stein et al., 2007), and from which we have published detailed records of relative sea level (RSL) variations for the last 5 glacial cycles that span the past 520 kyr (Rohling et al., 2009). This record has the advantage that it has a U–Th validated chronology for the major glacial/interglacial sea level changes (Rohling et al., 2010), which enables us to make a detailed comparison between our dust record and those from polar ice cores to assess spatial and temporal dust flux variability in different regions. Crucially, our dust record is co-registered with (i.e., measured on the same samples as) the RSL record from core KL09. Hence, the phase relationship of these records (Fig. 2a) is absolute. We compare our dust record with other regional dust records and discuss these comparisons in terms of their implications for understanding the global dust cycle.

2. Methods

We use an environmental magnetic proxy for haematite content, with which we have developed aeolian dust records for hyper-arid Saharan (Larrasoaña et al., 2003) and Arabian sources (Rohling et al., 2008). The proxy is an isothermal remanent magnetization (IRM) that was imparted to samples using an inducing field of 900 mT, followed by alternating field (AF) demagnetization at 120 mT ($IRM_{900\ mT@AF120\ mT}$). The IRM was imparted using an impulse magnetizer, with AF demagnetization and remanence measurements made using a 2-G Enterprises superconducting rock magnetometer with in-line demagnetization capability at the National Oceanography Centre, Southampton (NOCS), UK (Roberts, 2006). Measurements were made on continuous discrete samples taken at ~1 cm stratigraphic intervals. $IRM_{900\ mT@AF120\ mT}$ has been validated as an aeolian dust proxy through significant correlations between Fe and Ti abundances in the Red Sea (Rohling et al., 2008), as is also demonstrated for core KL09 in Fig. 2b. Elemental abundances were measured using an ITRAX core-scanning X-ray fluorescence system (Croudace et al., 2006), with measurements made at 0.5 mm stratigraphic increments at NOCS prior to sub-sampling for stable isotopic (as presented by Rohling et al. (2009)) and environmental magnetic measurements.

3. Results and discussion

Global dust fluxes during the last few glacial cycles are usually recognised to have been higher during glacial stages and lower during interglacials (e.g., Lambert et al., 2008; Winckler et al., 2008; Maher et al., 2010). In contrast, the highest dust fluxes in our Red Sea record coincide with glacial terminations (dashed lines in Fig. 2a) rather than with glacial stages, although dust fluxes overall were higher during glacials than during interglacials. We observe a strong similarity between our Red Sea dust record and those from the Chinese Loess Plateau (Fig. 2c and d; Sun et al., 2006). Mean quartz grain size is widely used as a proxy for wind strength on the Chinese Loess Plateau (Porter and An, 1995; Sun et al., 2006), and is plotted in Fig. 2c for two Chinese loess records and a stack of these records (Sun et al., 2006) beside our Red Sea dust record. Despite the strong similarity between the Red Sea and Chinese data sets, there appear to be chronological offsets in detail. Orbitally tuned chronologies exist for the Chinese loess (e.g., Sun et al., 2006), but the ages obtained by Sun et al. (2006) for several geomagnetic reversals in the Chinese loess remain inconsistent with those of the standard geomagnetic polarity timescale (Cande and Kent, 1995). The persistence of age offsets for geomagnetic reversals in the chronology of Sun et al. (2006) demonstrates that the longstanding problem with the chronology of the Chinese loess (cf. Liu et al., 2008) is not completely resolved. Construction of millennial-scale chronologies is notoriously difficult because of a lack of suitable material for precise dating. The signal similarity between the Red Sea and Chinese dust records suggests that they document the same climate variability and that it is appropriate to correlate the Chinese loess record to the Red Sea dust record. Correlation of dust records from the Red Sea and Chinese Loess Plateau (Fig. 2) provides a solution to the problem of dating the Chinese loess because the Red Sea chronology is tied through our RSL record (Rohling et al., 2009) to a sound U–Th chronology for sea level variations on glacial/interglacial timescales (Rohling et al., 2010). We use the stacked quartz grain size record of Sun et al. (2006) and tune it to our Red Sea dust record (Fig. 2d). This enables us to export

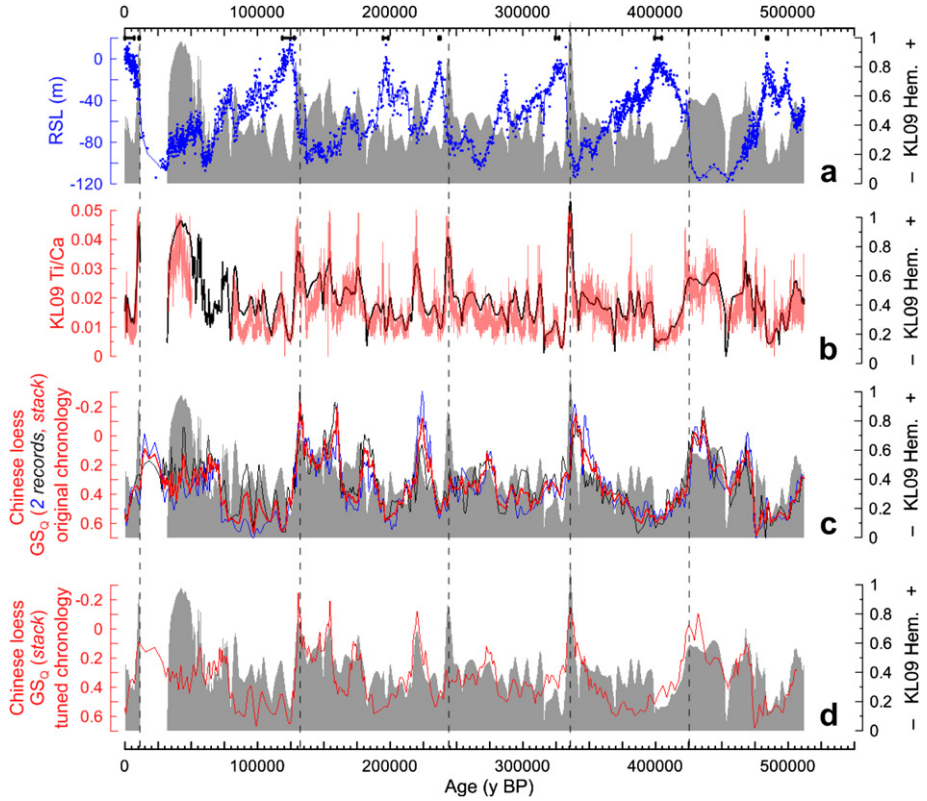

Fig. 2. Comparison of sea level and dust records for the Red Sea and Chinese Loess Plateau. (a) Sea level (blue) and dust (grey shading) for Red Sea core KL09 (sea level after Rohling et al. (2009), with chronology tied to U–Th dating of corals from Rohling et al. (2010); black tie points at top of panel). (b) Two dust proxies from Red Sea core KL09, including Ti/Ca ratio (pink) and the $IRM_{900\ mT@AF120\ mT}$ haematite (Hem.) proxy (black). (c) Comparison of our Red Sea dust record (grey shading) with two representative dust records (quartz grain size (GS_Q)) from Zhaojiachuan (blue) and Lingtai (black), Chinese Loess Plateau, on their own age model (from Sun et al., 2006), with a stack of the two records (red). (d) Comparison of our Red Sea dust record (grey shading) with the stacked Chinese loess record (red) after tuning to the Red Sea chronology of Rohling et al. (2010). R^2 values improve from 0.15 to 0.28 (for $n = 1582$ data points) after tuning (both correlations are statistically significant at $P = 0.01$). Vertical dashed lines denote dust spikes at glacial terminations. (For interpretation of the references to colour in this figure legend, the reader is referred to the web version of this article.)

a millennial chronology to the Chinese loess for the first time, for synchronizing Chinese loess records to global climate signals. Relative to sea-level/ice-volume changes, our dust chronology is precise on millennial timescales because both signals are obtained from the same samples. In an absolute (U–Th equivalent) sense, the chronology of the Red Sea sequences is well defined on glacial/interglacial timescales (Rohling et al., 2010). However, although the absolute chronology through parts of the sequence could still be subjected to fine-tuning on millennial timescales (e.g., Rohling et al., 2008), age control through the studied record should be considered accurate to within ±5 kyr.

The major dust maxima that stand out in the Red Sea and Chinese loess records at the early stages of glacial terminations II, III, IV and V (Fig. 2d) are not systematically present in Antarctic (Fig. 3b) (Lambert et al., 2008), Saharan (Fig. 3c and d) (Tiedemann et al., 1994; Larrasoaña et al., 2003) or low-resolution Arabian (Fig. 3c) (deMenocal et al., 1991) records. A dust spike also occurs at termination I in our Red Sea record, but it is less visible in Fig. 3 because the immediately underlying interval is obscured by an indurated aplanktonic zone (Rohling et al., 2008). The apparent absence of systematic dust peaks in the deglaciations in near-Saharan marine records may result from inadequate resolutions and/or chronological uncertainties. Improved records are needed to investigate this in detail.

Winckler et al. (2008) concluded that there is a high degree of correlation between dust fluxes in the equatorial Pacific and Antarctica. The Antarctic EPICA Dome C ice core dust record (Lambert et al., 2008) has therefore been used to represent an inter-hemispheric response of dust generation to climate change on glacial/interglacial timescales (Köhler et al., 2010). The Antarctic record is genuinely different from the records shown in Fig. 3. Antarctica is a remote depositional site, whereas our records are located within globally significant ablation zones (Fig. 1).

Similarity between Red Sea and Chinese dust records suggests an atmospheric teleconnection across two major northern hemisphere dust producing regions. The abrupt climate variations documented in Greenland ice cores (Dansgaard et al., 1993) have been detected in the Chinese loess (Porter and An, 1995), Arabian Sea (Schulz et al., 1998) and Red Sea (Rohling et al., 2008). However, we here document for the first time that a detailed similarity exists between dust signals from China and Arabia, and that dust variability in these areas may be significantly different from that in circum-Saharan records (cf. Trauth et al., 2009). The observed dust peaks at deglaciations in the Arabia–China dust belt (Fig. 2d) appear to coincide with North Atlantic Heinrich events at the last 5 glacial terminations (Hodell et al., 2008). Heinrich events have been linked to intensified winter conditions with stronger westerly circulation over Eurasia, weakened summer monsoons and increased aridity in Eurasian deserts (Jin et al., 2007), and reduced summer monsoon-related upwelling in the Arabian Sea (Schulz et al., 1998). Large-scale atmospheric teleconnections therefore provide a credible explanation for the observed close relationship between variations in widely separated dust sources (Fig. 2d). By comparison, Saharan deflation is more related to changes in aridity associated with the position of the inter-

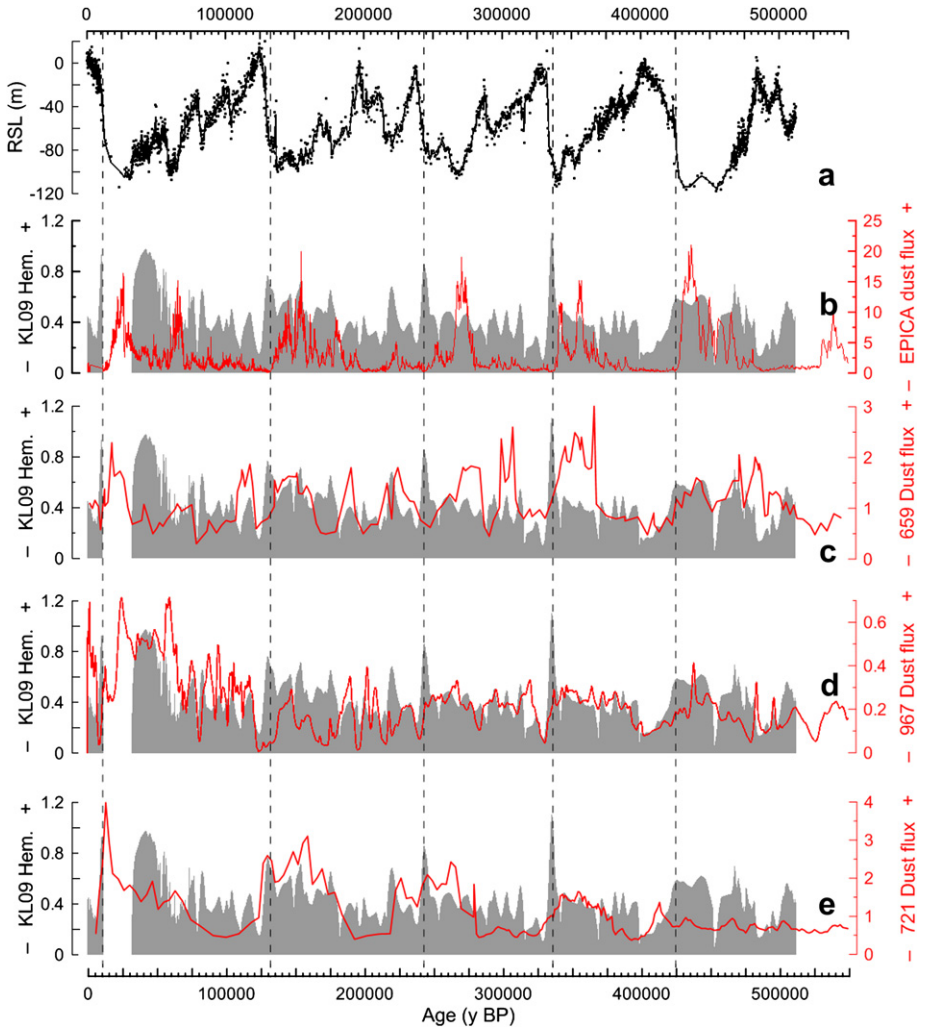

Fig. 3. Comparison of sea level and dust records from the Red Sea with those from Antarctica and around North Africa. (a) Sea level as in Fig. 2a. Comparison of dust records from core KL09 (grey shading) and (b) EPICA Dome C, Antarctica (Lambert et al., 2008); (c) ODP Site 659, off northwest Africa (Tiedemann et al., 1994); (d) ODP Site 967, Eastern Mediterranean Sea (Larrasoaña et al., 2003); and (e) ODP Site 721, Arabian Sea (deMenocal et al., 1991). Vertical dashed lines denote dust spikes at glacial terminations.

tropical convergence zone and to the intensity of tropical easterlies (e.g., Larrasoaña et al., 2003; Itambi et al., 2009). While millennial-scale Saharan dust responses to Dansgaard–Oeschger and Heinrich events have been documented in high-resolution marine records (Moreno et al., 2002; Itambi et al., 2009), the largest Saharan dust fluxes occurred in glacials rather than during glacial terminations (e.g., Itambi et al., 2009), as is also shown in the records compiled in Fig. 3.

4. Conclusions

We conclude first that large regional differences in dust fluxes from major dust producing regions indicate that understanding global dust cycle variability on glacial/interglacial timescales requires separate treatment of the easterly-dominated low-latitude Sahara and the westerly-dominated dust belt from Arabia to China. Modelling studies can be improved by incorporating regional zones with different source variability. Second, dust flux patterns for the Arabia–China dust belt also contrast with the Antarctic ice core records (Lambert et al., 2008) that are increasingly used to assess climatic responses to changes in radiative forcing (e.g., Köhler et al., 2010). The distal response records from Antarctica have sharply delineated glacial/interglacial contrasts compared to the more proximal records shown in Figs. 2 and 3, which have a much higher total dust flux, a higher baseline of dust emissions through interglacials, and considerable high-frequency variability throughout the records. Studies that rely on Antarctic dust records to represent global atmospheric dust loadings will therefore erroneously overestimate the radiative contrast of aerosol loadings on glacial/interglacial timescales. Furthermore, the radiative forcing effect of atmospheric dust at low latitudes is up to an order of magnitude greater than at polar latitudes (Claquin et al., 2003). Third, further proximal dust flux records are needed from all major global dust source regions in order to properly constrain the spatial and temporal source variability and radiative impact of atmospheric dust loadings for use in climate models. Such records should resolve millennial-scale responses of the dust cycle to abrupt climate changes. Fourth, correlation of our Red Sea record with Chinese loess records makes it possible to export our U–Th validated chronology, which enables millennial-scale correlation of the Chinese records with other global records for the first time.

Acknowledgements

This study contributes to UK Natural Environment Research Council projects NE/C003152/1, NE/H004424/1 and NE/E01531X/1.

References

Arimoto, R., 2001. Eolian dust and climate: relationships to sources, tropospheric chemistry, transport and deposition. Earth-Science Reviews 54, 29–42.

Boyd, P.W., Ellwood, M.J., 2010. The biogeochemical cycle of iron in the ocean. Nature Geoscience 3, 675–682.

Cande, S.C., Kent, D.V., 1995. Revised calibration of the geomagnetic polarity time scale for the late Cretaceous and Cenozoic. Journal of Geophysical Research 100, 6093–6095.

Claquin, T., Roelandt, C., Kohfeld, K.E., Harrison, S.P., Tegen, I., Prentice, I.C., Balkanski, Y., Bergametti, G., Hansson, M., Mahowald, N., Rodhe, H., Schulz, M., 2003. Radiative forcing of climate by ice-age atmospheric dust. Climate Dynamics 20, 193–202.

Croudace, I.W., Rindby, A., Rothwell, R.G., 2006. ITRAX: description and evaluation of a new multi-function X-ray core scanner. In: Geological Society of London Special Publication, vol. 267, 51–63.

Dansgaard, W., Johnsen, S.J., Clausen, H.B., Dahl-Jensen, D., Gundestrup, N.S., Hammer, C.U., Hvidberg, C.S., Steffensen, J.P., Sveinbjörnsdottir, A.E., Jouzel, J., Bond, G., 1993. Evidence for general instability of past climate from a 250-kyr ice-core record. Nature 364, 218–220.

deMenocal, P., Bloemendal, J., King, J., 1991. A rock-magnetic record of monsoonal dust deposition to the Arabian Sea: evidence for a shift in the mode of deposition at 2.4 Ma. Proceedings of the Ocean Drilling Program, Scientific Results 177, 389–407.

Duce, R.A., Liss, P.S., Merrill, J.T., Atlas, E.L., Buat-Menard, P., Hicks, B.B., Miller, J.M., Prospero, J.M., Arimoto, R., Church, T.M., Ellis, W., Galloway, J.N., Hansen, L., Jickells, T.D., Knap, A.H., Reinhardt, K.H., Schneider, B., Soudine, A., Tokos, J.J., Tsunogai, S., Wollast, R., Zhou, M., 1991. The atmospheric input of trace species to the world ocean. Global Biogeochemical Cycles 5, 193–259.

Hodell, D.A., Channell, J.E.T., Curtis, J.H., Romero, O.E., Röhl, U., 2008. Onset of "Hudson Strait" Heinrich events in the eastern North Atlantic at the end of the middle Pleistocene transition (~640 ka)? Paleoceanography 23, PA4218. doi:10.1029/2008PA001591.

Intergovernmental Panel on Climate Change, 2007. Changes in atmospheric constituents and in radiative forcing. In: Climate Change 2007: The Physical Science Basis. Contribution of Working Group I to the Fourth Assessment Report of the Intergovernmental Panel on Climate Change. Cambridge University Press.

Itambi, A.C., von Dobeneck, T., Mulitza, S., Bickert, T., Heslop, D., 2009. Millennial-scale northwest African droughts related to Heinrich events and Dansgaard–Oeschger cycles: evidence in marine sediments from offshore Senegal. Paleoceanography 24, PA1205. doi:10.1029/2007PA001570.

Jickells, T.D., An, Z.S., Anderson, K.K., Baker, A.R., Bergametti, G., Brooks, N., Cao, J.J., Boyd, P.W., Duce, R.A., Hunter, K.A., Kawahata, H., Kubilay, N., laRoche, J., Liss, P.S., Mahowald, N., Prospero, J.M., Ridgwell, A.J., Tegen, I., Torres, R., 2005. Global iron connections between desert dust, ocean biogeochemistry, and climate. Science 308, 67–71.

Jin, L., Chen, F., Ganopolski, A., Claussen, M., 2007. Response of East Asian climate to Dansgaard/Oeschger and Heinrich events in a coupled model of intermediate complexity. Journal of Geophysical Research 112, D06117. doi:10.1029/2006JD007316.

Kaufman, Y.J., Tanré, D., Boucher, O., 2002. A satellite view of aerosols in the climate system. Nature 419, 215–223.

Köhler, P., Bintanja, R., Fischer, H., Joos, F., Knutti, R., Lohmann, G., Masson-Delmotte, V., 2010. What caused earth's temperature variations during the last 800,000 years? Data-based evidence on radiative forcing and constraints on climate sensitivity. Quaternary Science Reviews 29, 129–145.

Lambert, F., Delmonte, B., Petit, J.R., Bigler, M., Kaufmann, P.R., Hutterli, M.A., Stocker, T.F., Ruth, U., Steffensen, J.P., Maggi, V., 2008. Dust-climate couplings over the past 800,000 years from the EPICA Dome C ice core. Nature 452, 616–619.

Larrasoaña, J.C., Roberts, A.P., Rohling, E.J., Winklhofer, M., Wehausen, R., 2003. Three million years of monsoon variability over the northern Sahara. Climate Dynamics 21, 689–698.

Liu, Q., Roberts, A.P., Rohling, E.J., Zhu, R., Sun, Y., 2008. Post-depositional remanent magnetization lock-in and the location of the Matuyama-Brunhes geomagnetic reversal boundary in marine and Chinese loess sequences. Earth and Planetary Science Letters 275, 102–110.

Maher, B.A., Prospero, J.M., Mackie, D., Gaiero, D., Hesse, P.P., Balkanski, Y., 2010. Global connections between aeolian dust, climate and ocean biogeochemistry at the present day and at the last glacial maximum. Earth-Science Reviews 99, 61–97.

Mahowald, N.M., Muhs, D.R., Levis, S., Rasch, P.J., Yoshioka, M., Zender, C.S., Luo, C., 2006. Changes in atmospheric mineral aerosols in response to climate: last glacial period, preindustrial, modern, and doubled carbon dioxide climates. Journal of Geophysical Research 111, D10202. doi:10.1029/2005JD006653.

Martin, J.H., Gordon, R.M., Fitzwater, S.E., 1991. The case for iron. Limnology and Oceanography 36, 1793–1802.

Martinez-Garcia, A., Rosell-Melé, A., Geibert, W., Gersonde, R., Masqué, P., Gaspari, V., Barbante, C., 2009. Links between iron supply, marine productivity, sea surface temperature, and CO_2 over the last 1.1 Ma. Paleoceanography 24, PA1207. doi:10.1029/2008PA001657.

Moreno, A., Cacho, I., Canals, M., Prins, M.A., Sánchez-Goñi, M.-F., Grimalt, J.O., Weltje, G.J., 2002. Saharan dust transport and high-latitude glacial climatic variability: the Alboran Sea record. Quaternary Research 58, 318–328.

Mulitza, S., Heslop, D., Pittauerova, D., Fischer, H.W., Meyer, I., Stuut, J.-B., Zabel, M., Mollenhauer, G., Collins, J.A., Kuhnert, H., Schulz, M., 2010. Increase in African dust flux at the onset of commercial agriculture in the Sahel region. Nature 466, 226–228.

Porter, S.C., An, Z., 1995. Correlation between climate events in the North Atlantic and China during the last glaciation. Nature 375, 305–308.

Prospero, J.M., Ginoux, P., Torres, O., Nicholson, S.E., Gill, T.E., 2002. Environmental characterization of global sources of atmospheric soil dust identified with the NIMBUS 7 Total Ozone Mapping Spectrometer (TOMS) absorbing aerosol product. Reviews of Geophysics 40, 1002. doi:10.1029/2000RG000095.

Roberts, A.P., 2006. High-resolution magnetic analysis of sediment cores: strengths, limitations and strategies for maximizing the value of long-core magnetic data. Physics of the Earth and Planetary Interiors 156, 162–178.

Rohling, E.J., Grant, K., Hemleben, C., Kucera, M., Roberts, A.P., Schmeltzer, I., Schulz, H., Siccha, M., Siddall, M., Trommer, G., 2008. New constraints on the timing of sea level fluctuations during early to middle marine isotope stage 3. Paleoceanography 23, PA3219. doi:10.1029/2008PA001617.

Rohling, E.J., Grant, K., Bolshaw, M., Roberts, A.P., Siddall, M., Hemleben, C., Kucera, M., 2009. Antarctic temperature and global sea level closely coupled over the past five glacial cycles. Nature Geoscience 2, 500–504.

Rohling, E.J., Braun, K., Grant, K., Kucera, M., Roberts, A.P., Siddall, M., Trommer, G., 2010. Comparison between Holocene and marine isotope Stage-11 sea-level histories. Earth and Planetary Science Letters 291, 97–105.

Sassen, K., DeMott, P.J., Prospero, J.M., Poellot, M.R., 2003. Saharan dust storms and indirect aerosol effects on clouds: CRYSTAL-FACE results. Geophysical Research Letters 30, 1633. doi:10.1029/2003GL017371.

Schulz, H., von Rad, U., Erlenkeuser, H., 1998. Correlation between Arabian Sea and Greenland climate oscillations of the past 110,000 years. Nature 393, 54–57.

Spracklen, D.V., Carslaw, K.S., Kulmala, M., Kerminen, V.M., Sihto, S.L., Riipinen, I., Merikanto, J., Mann, G.W., Chipperfield, M.P., Wiedensohler, A., Birmili, W., Lihavainen, H., 2008. Contribution of particle formation to global cloud condensation nuclei concentrations. Geophysical Research Letters 35, L06808. doi:10.1029/2007GL033038.

Stein, M., Almogi-Labin, A., Goldstein, S.L., Hemleben, C., Starinsky, A., 2007. Late Quaternary changes in desert dust inputs to the Red Sea and Gulf of Aden from $^{87}Sr/^{86}Sr$ ratios in deep-sea cores. Earth and Planetary Science Letters 261, 104–119.

Sun, Y., Clemens, S.C., An, Z., Yu, Z., 2006. Astronomic timescale and palaeoclimatic implication of stacked 3.6-Myr monsoon records from the Chinese Loess Plateau. Quaternary Science Reviews 25, 33–48.

Tegen, I., Lacis, A.A., Fung, I., 1996. The influence on climate forcing of mineral aerosols from disturbed soils. Nature 380, 419–422.

Tiedemann, R., Sarnthein, M., Shackleton, N.J., 1994. Astronomical timescale for the Pliocene Atlantic $\delta^{18}O$ and dust flux records of Ocean Drilling Program site 659. Paleoceanography 9, 619–638.

Trauth, M.H., Larrasoaña, J.C., Mudelsee, M., 2009. Trends, rhythms and events in Plio-Pleistocene African climate. Quaternary Science Reviews 28, 399–411.

Winckler, G., Anderson, R.F., Fleisher, M.Q., McGee, D., Mahowald, N., 2008. Covariant glacial-interglacial dust fluxes in the equatorial Pacific and Antarctica. Science 320, 93–96.

Wolff, E.W., Fischer, H., Fundel, F., Ruth, U., Twarloh, B., Littot, G.C., Mulvaney, R., Röthlisberger, R., de Angelis, M., Boutron, C.F., Hansson, M., Jonsell, U., Hutterli, M.A., Lambert, F., Kaufmann, P., Stauffer, B., Stocker, T.F., Steffensen, J.P., Bigler, M., Siggaard-Andersen, M.L., Udisti, R., Becagli, S., Castellano, E., Severi, M., Wagenbach, D., Barbante, C., Gabrielli, P., Gaspari, V., 2006. Southern ocean sea-ice extent, productivity and iron flux over the past eight glacial cycles. Nature 440, 491–496.

Appendix C

Volcanic ash layers illuminate the resilience of Neanderthals and early modern humans to natural hazards

John Lowe, Nick Barton, Simon Blockley, Christopher Bronk Ramsey, Victoria L. Cullen, William Davies, Clive Gamble, **Katharine Grant**, Mark Hardiman, Rupert Housley, Christine S. Lane, Sharen Lee, Mark Lewis, Alison MacLeod, Martin Menzies, Wolfgang Müller, Mark Pollard, Catherine Price, Andrew P. Roberts, Eelco J. Rohling, Chris Satow, Victoria C. Smith, Chris B. Stringer, Emma L. Tomlinson, Dustin White, Paul Albert, Ilenia Arienzo, Graeme Barker, Dušan Borić, Antonio Carandente, Lucia Civetta, Catherine Ferrier, Jean-Luc Guadelli, Panagiotis Karkanas, Margarita Koumouzelis, Ulrich C. Müller, Giovanni Orsi, Jörg Pross, Mauro Rosi, Ljiljiana Shalamanov-Korobar, Nikolay Sirakov, and Polychronis C. Tzedakis

Manuscript published in: Proceedings of the National Academy of Sciences 109, 13532-13537 (2012)

Author affiliations and contributions are listed in the manuscript.

Volcanic ash layers illuminate the resilience of Neanderthals and early modern humans to natural hazards

John Lowe[a,1], Nick Barton[b], Simon Blockley[a], Christopher Bronk Ramsey[c], Victoria L. Cullen[c], William Davies[d], Clive Gamble[d], Katharine Grant[e], Mark Hardiman[a], Rupert Housley[a], Christine S. Lane[c], Sharen Lee[c], Mark Lewis[f], Alison MacLeod[a], Martin Menzies[g], Wolfgang Müller[g], Mark Pollard[c], Catherine Price[b], Andrew P. Roberts[h], Eelco J. Rohling[e], Chris Satow[a], Victoria C. Smith[c], Chris B. Stringer[f], Emma L. Tomlinson[g], Dustin White[b,d], Paul Albert[g], Ilenia Arienzo[i], Graeme Barker[j], Dušan Borić[k], Antonio Carandente[i], Lucia Civetta[l], Catherine Ferrier[m], Jean-Luc Guadelli[m], Panagiotis Karkanas[n], Margarita Koumouzelis[n], Ulrich C. Müller[o], Giovanni Orsi[i], Jörg Pross[o], Mauro Rosi[p], Ljiljiana Shalamanov-Korobar[q], Nikolay Sirakov[r], and Polychronis C. Tzedakis[s]

[a]Department of Geography, Royal Holloway University of London, Surrey TW20 0EX, United Kingdom; [b]Institute of Archaeology, Oxford University, Oxford OX1 2PG, United Kingdom; [c]Research Laboratory for Archaeology and the History of Art, Oxford University, Oxford OX1 3QY, United Kingdom; [d]Archaeology Department, University of Southampton, National Oceanography Centre, Southampton SO17 1BF, United Kingdom; [e]School of Ocean and Earth Science, University of Southampton, Hampshire SO14 3ZH, United Kingdom; [f]Palaeontology Department, Natural History Museum, London SW7 5BD, United Kingdom; [g]Department of Earth Sciences, Royal Holloway University of London, Surrey TW20 0EX, United Kingdom; [h]Research School of Earth Sciences, Australian National University, Acton ACT 0200, Australia; [i]Istituto Nazionale di Geofisica e Vulcanologia, Sezione di Napoli, Osservatorio Vesuviano, 80124 Naples, Italy; [j]McDonald Institute for Archaeological Research, University of Cambridge, Department of Archaeology and Anthropology, Cambridge CB2 3ER, United Kingdom; [k]Cardiff School of History, Ancient History, Archaeology and Religion, Cardiff University, Cardiff CF10 3EU, United Kingdom; [l]Dipartimento di Scienze Fisiche, Università Federico II, 80126 Naples, Italy; [m]De la Préhistoire à l'Actuel: Culture, Environnement et Anthropologie, Préhistoire, Palèoenvironnement, Patrimonie, Unité Mixte de Recherche 5199 Centre National de la Recherche Scientifique, Université Bordeaux 1, 33405 Talence Cedex, France; [n]Ephoreia of Palaeoanthropology–Speleology of Southern Greece, 116 36 Athens, Greece; [o]Institute of Geosciences, Goethe University Frankfurt, 60438 Frankfurt am Main, Germany; [p]Dipartimento di Scienze della Terra, Università di Pisa, 56126 Pisa, Italy; [q]National Institution Museum of Macedonia, Skopje, Republic of Macedonia; [r]National Institute of Archaeology and Museum of Bulgarian Academy of Sciences, Prehistory, Sofia 1000, Bulgaria; and [s]Department of Geography, University College London, London WC1E 6BT, United Kingdom

Edited by Richard G. Klein, Stanford University, Stanford, CA, and approved June 18, 2012 (received for review March 17, 2012)

Marked changes in human dispersal and development during the Middle to Upper Paleolithic transition have been attributed to massive volcanic eruption and/or severe climatic deterioration. We test this concept using records of volcanic ash layers of the Campanian Ignimbrite eruption dated to *ca.* 40,000 y ago (40 ka B.P.). The distribution of the Campanian Ignimbrite has been enhanced by the discovery of cryptotephra deposits (volcanic ash layers that are not visible to the naked eye) in archaeological cave sequences. They enable us to synchronize archaeological and paleoclimatic records through the period of transition from Neanderthal to the earliest anatomically modern human populations in Europe. Our results confirm that the combined effects of a major volcanic eruption and severe climatic cooling failed to have lasting impacts on Neanderthals or early modern humans in Europe. We infer that modern humans proved a greater competitive threat to indigenous populations than natural disasters.

During the last glacial stage, between *ca.* 100 and 30 ka B.P., anatomically modern humans (AMHs) migrated from Africa to eventually reach Europe, bringing them increasingly into contact with indigenous Neanderthals (1). The latter experienced marked population decline from *ca.* 40 ka B.P. on and had largely disappeared by 30 ka B.P. (2). Over the same period, climate oscillated markedly between cold interludes—the most extreme of which are termed Heinrich Events (HEs)—and significantly warmer Interstadial periods (3). The warm transitions were particularly abrupt (within a few decades) in the North Atlantic region and Europe. Hominins were driven from large tracts of northern Europe during the cold episodes but were able to recolonize when conditions ameliorated (1). Over time, they also developed more advanced stone tool kits, created increasingly sophisticated ornamental and ritual objects, and formed closer social networks, both heralding and signaling the transition from Middle to Upper Paleolithic cultures (4). Some of these changes appear suddenly in the archaeological record, suggesting rapid assimilation of or replacement by new technologies (5). However, it remains unknown to what degree these innovations were stimulated by abrupt climatic changes that periodically tested the resiliency of hominin survival skills.

Climate is considered by some to have been the main cause of Neanderthal demise, by either progressive population attrition over several cold intervals, culminating in a terminal decline around 40 ka B.P. (6), or population collapse during a particularly severe HE at around 48 ka B.P. (7). Either way, it is assumed that AMHs had developed competitive advantages that enabled them to recolonize and survive in Europe more effectively than Neanderthals. Others, however, consider that climate change alone cannot explain Neanderthal demise, because they had already survived a long series of marked climatic oscillations. Suggested contributory factors include conflict with and displacement by invading AMHs (8) or the environmental impacts of the Campanian Ignimbrite (CI) volcanic ash, deposited at around 40 ka B.P. The CI eruption was the largest within the Mediterranean area during the last 200 ka (9). It liberated some 250–300 km^3 volcanic ash, which spread over a large sector of Central and Eastern Europe; the injection of such huge amounts of ash and volatiles (including sulfurous gases) into the atmosphere is likely to have caused a volcanic winter (10). Because this eruption occurred during the cold HE4 interval, it has led to speculation that the combination of a severe climatic downturn and widespread ash deposition either immediately drove Neanderthals out of parts of Europe, leaving the territory free for

Author contributions: J.L., N.B., S.B., C.B.R., W.D., C.G., M.M., M.P., A.P.R., E.J.R., C.B.S., and D.W. designed research; S.B., V.L.C., K.G., M.H., R.H., C.S.L., S.L., M.L., A.M., E.J.R., C.S., V.C.S., E.L.T., D.W., P.A., G.B., M.K., and P.C.T. performed research; N.B., C.B.R., V.L.C., C.G., K.G., M.H., R.H., C.S.L., S.L., M.L., A.M., M.M., W.M., M.P., C.P., A.P.R., E.J.R., C.S., V.C.S., C.B.S., E.L.T., D.W., P.A., I.A., G.B., D.B., A.C., L.C., C.F., J.-L.G., P.K., U.C.M., G.O., J.P., M.R., L.S.-K., N.S., and P.C.T. analyzed data; M.H., C.S.L., and D.W. created figures; R.H. updated the program database; C.S.L. and E.L.T. compiled Tables S2–S5; and D.W. gained access to protected archaeological sites in southeast and east Europe; and J.L., C.B.R., W.D., C.G., M.M., A.P.R., E.J.R., C.B.S., and D.W. wrote the paper.

The authors declare no conflict of interest.

This article is a PNAS Direct Submission.

See Commentary on page 13471.

[1]To whom correspondence should be addressed. E-mail: j.lowe@rhul.ac.uk.

This article contains supporting information online at www.pnas.org/lookup/suppl/doi:10.1073/pnas.1204579109/-/DCSupplemental.

subsequent colonization by AMHs (11), or triggered more gradual in situ cultural and evolutionary changes, enabling AMHs to outcompete and finally, supplant the Neanderthals (12).

These hypotheses are difficult to test, however, because of chronological uncertainties that blur the precise timing of archaeological and geologic events (6). Whereas climate was capable of major swings within a human lifespan (3), it is seldom possible to link cultural and environmental responses to such abrupt shifts with similar chronological precision because of common sedimentary complications in archaeological and geologic sequences (13) and dating uncertainties that, for the period under consideration, are typically centennial to millennial in scale (14). Robust tests of proposed causal links between climate change, environmental response, and cultural adaptations during the Middle and Upper Paleolithic, therefore, require more secure dating and correlation of archaeological and geologic records. Here, we show how recent discoveries of nonvisible volcanic ash markers, termed cryptotephra, are helping to synchronize archaeological and environmental records by linking horizons of precisely the same age between widely scattered sites (15).

Results

Until recently, investigation of past volcanic eruptions has relied on the study of either proximal volcanic deposits (found close to volcanoes) or distal but visible ash layers. For example, visible ash of the CI was used to synchronize Paleolithic records from sites in southern Italy (16) and Russia (17, 18). Focusing only on visible volcanic ash layers, however, limits the number of isochrons that can be used as well as the geographic range over which they can be traced. Recent research has shown that nonvisible ash layers (Fig. 1) can also be detected in marine and terrestrial sequences (19). Consisting mainly of tiny glass particles (commonly <150 μm in size) that are recoverable in the laboratory by density separation methods, discrete layers of cryptotephra travel farther from source than their visible counterparts and frequently yield sufficient glass for analysis using geochemical fingerprinting methods (*Methods*).

Here, we report discoveries of the CI, including cryptotephra layers, detected in important archaeological sites. We have extracted CI tephra from (*i*) an ancient paludal sequence at Tenaghi Philippon, Greece; (*ii*) marine core LC21 located in the southeast Aegean Sea; (*iii*) Africa in the Haua Fteah Cave sequence in Libya; and (*iv*) four important central European archaeological cave sequences: Klissoura, Golema Pesht, Kozarnika, and Tabula Traiana (Fig. 2 and Table S1). To confirm its role as a valid, precise correlation marker, we also generated a robust dataset of the proximal chemical composition of the CI (21), against which the chemical signatures of distal CI layers have been compared (Fig. 3 and Tables S2– S5). The results provide a secure common isochronous marker, which directly ties marine and terrestrial paleoenvironmental records with archaeological sequences over an expanded region that includes sites from both south and north of the Mediterranean.

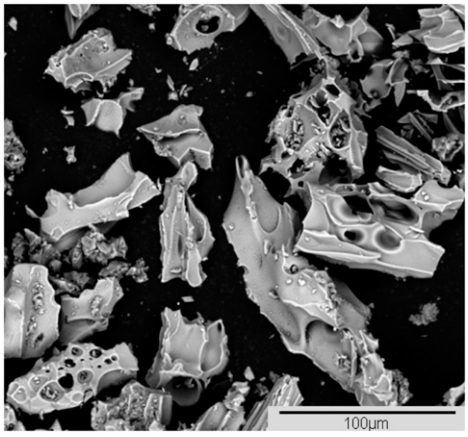

Fig. 1. Scanning electron photomicrograph of distal cryptotephra shards associated with the visible Campanian Ignimbrite layer in the Tenaghi Philippon sequence. (Photo by Suzanne MacLachlan, British Ocean Sediment Core Research Facility, National Oceanography Centre, Southampton.)

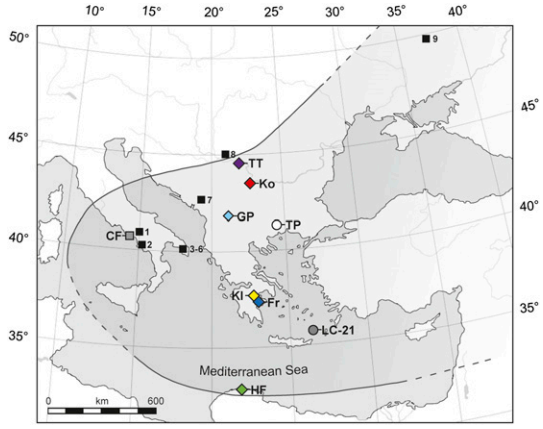

Fig. 2. Map of the preservation limits of visible layers of the CI (curved line in ref. 20), the location of its source at Campi Flegrei (CF), and positions of sites referred to in the text (symbols are explained in Fig. 3). Letters indicate sites examined within the Response of Humans to Abrupt Environmental Transitions Project: Fr, Franchthi; GP, Golema Pesht; HF, Haua Fteah; Kl, Klissoura; Ko, Kozarnika; LC-21, EC-MAST2 PALAEO-FLUX cruise 1995, "Long Core 21"; TP, Tenaghi Philippon; TT, Tabula Traiana. Numbers refer to other sequences mentioned in the text: 1, Serino; 2, Castelcivita; 3, Cavallo; 4, Uluzzo; 5, Uluzzo C; 6, Bernardini; 7, Crvena Stijina; 8, Oase; 9, Kostenki 14.

The CI eruption occurred during the last glacial cycle, just after the onset of a millennial-scale cold stadial that encompassed HE4, a northern hemisphere-wide climatic event of extreme cold and aridity (22). We confirm this temporal relationship with identification of the CI in high-resolution paleoclimate records from the southeast Aegean Sea (core LC21) and a terrestrial sequence from Greece (Tenaghi Philippon) (7), where the climatic event is identified by increased aridity and a sharp reduction in tree pollen (Fig. 4). This area is known to be highly sensitive to cooling events triggered by northerly incursions of cold and dry continental air through gaps in the surrounding mountain ranges (23). By synchronizing the paleoclimatic and archaeological records using the CI, we find results that contradict prevailing hypotheses about the effects of volcanic activity and climate on Neanderthals and AMHs (11, 12).

Discussion

Assessment. In Europe, Upper Paleolithic (UP) industries, such as the Aurignacian, are clearly associated with modern humans and typically appear after the CI (24, 25), but some occurrences are radiocarbon-dated to older than 40 ka B.P. (26), which is the case with fossil evidence from Oase that lacks archaeological association (27). Although Neanderthals are known to postdate the CI eruption in Iberia and perhaps, elsewhere (28, 29), the terminal Middle Paleolithic (MP) industries at our studied sites in Eastern Europe all predate the CI considerably, from which they are separated by sterile or UP deposits. In Italy, UP deposits underlie the CI in at least six sites (Serino, Castelcivita, Cavallo, Uluzzo, Uluzzo C, and Bernardini) (24, 30), and AMH fossils are reportedly associated with transitional UP records at Grotta del Cavallo (31); the term transitional in this context is explained in *SI Text*. Synchronization of records using the CI, therefore, confirms that Neanderthal survival and modern human expansion were characterized by significant spatial heterogeneity (patchiness) across Europe.

Farther east, in the southern Balkans, the CI caps MP deposits at Crvena Stijena in Montenegro (32) and a nondiagnostic assemblage at Franchthi Cave in Greece (33), whereas it also caps

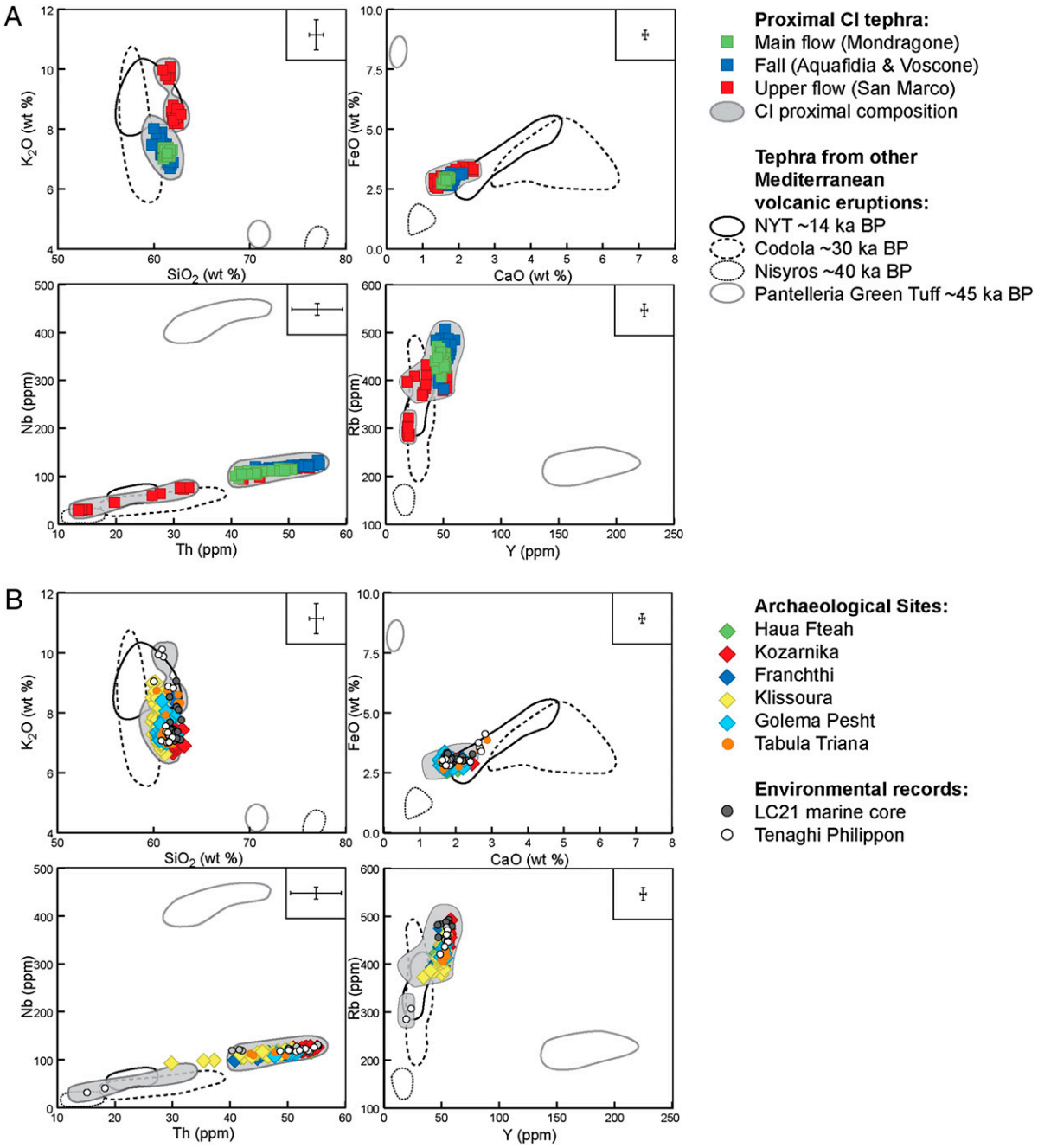

Fig. 3. (*A*) Selected major and trace element biplots with delineation of the compositional ranges of pumice matrix glasses from proximal tephra fall and flow units from the CI (gray-filled envelope) using the same discriminant source. (*B*) Compositional correlation of the distal tephra fall units from this study with the CI tephra. For comparison on all graphs, the compositional fields for four well-known Mediterranean volcanic eruptions are also plotted. The Neapolitan Yellow Tuff (NYT) is the second largest known eruption of the CF after the CI tephra. The Codola Tephra from Vesuvius, the Nisyros Island Tephra (Upper Member), and the Pantelleria Green Tuff are all found as far-traveled tephra layers and occurred within ±20 ka of the CI eruption. Representative 2σ uncertainty ranges are shown (*A*, *Upper Right* and *B*, *Upper Right*) for each biplot based on precision established from secondary standard analyses (Tables S2–S5).

a layer with transitional Uluzzian-type industry at Klissoura Cave 1, Greece (34) (Fig. 5). In contrast, the CI overlies early UP levels in Kozarnika Cave, Bulgaria (35), Tabula Traiana Cave, Serbia, and Golema Pesht Cave, Macedonia (36). In Russia, early UP layers are within or considerably below the CI at the Kostenki–Borshchevo sites, and hence, a good case can be made for AMH presence in the central Russian Plain before the CI eruption (18, 37). In most of these cases, therefore, with the exception of sites in Greece and Montenegro, modern humans and early UP demonstrably predate the CI at 40 ka B.P.

Distal CI deposits in the Haua Fteah Cave sediment sequence, Libya, allow for isochronous correlation between Paleolithic sites in Europe and Africa. At Haua Fteah, the CI is located within a continuous sequence of UP locally termed the Dabban culture, and hence, it postdates the start of the Dabban industry (38). Below the Dabban, in the same sequence, are deposits containing MP industries and two modern human jawbones, which show that modern human remains predate the CI at Haua Fteah (39). In Morocco, early modern humans have been recorded by at least 100 ka (40), and in Egypt, early modern humans have

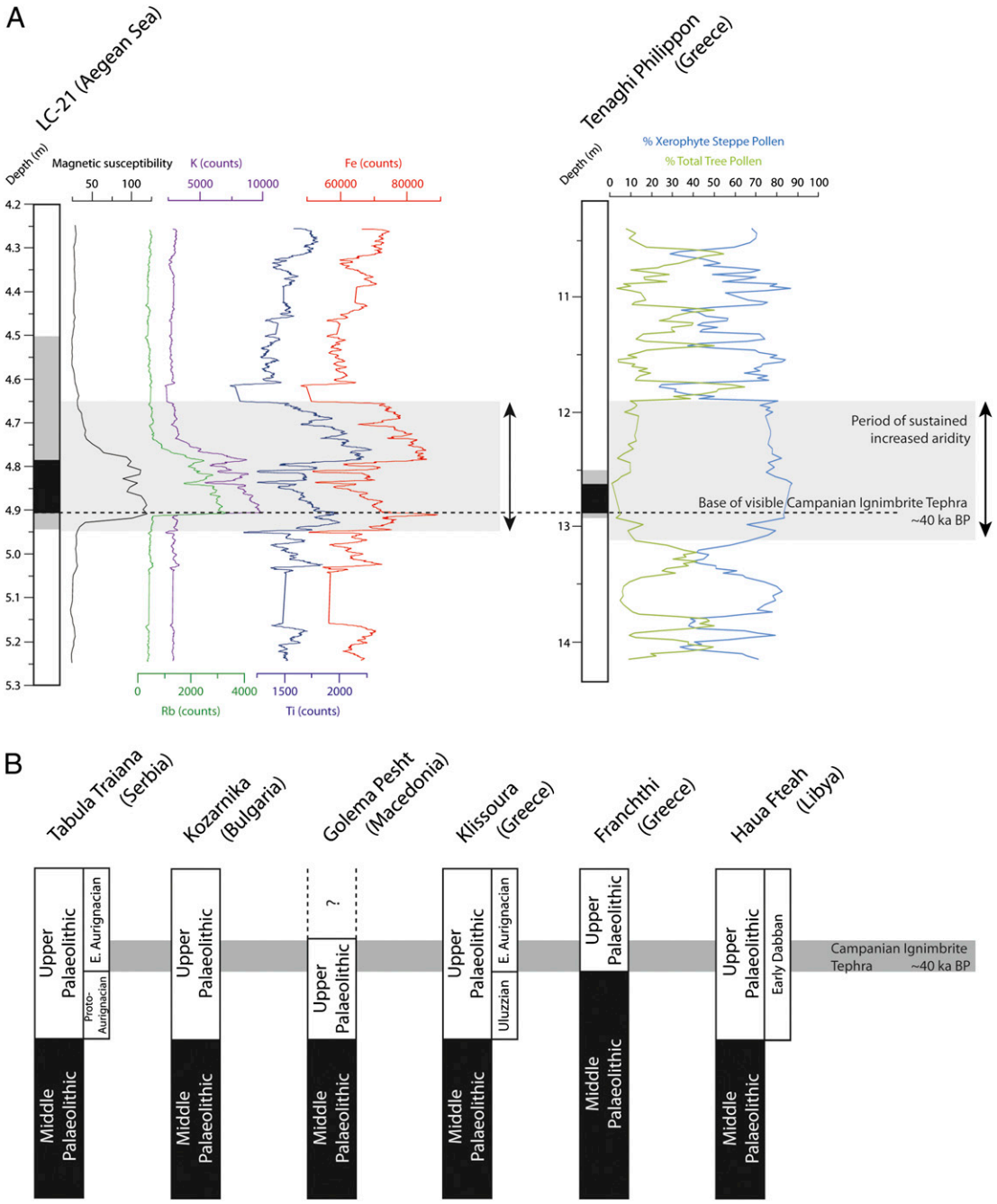

Fig. 4. (*A*) Position of the CI (black, visible glass shards; gray, cryptotephra) with respect to proxy evidence for a period of dry conditions in the eastern Mediterranean considered to approximate HE4. In core LC21, peaks in concentrations of magnetic susceptibility, Rb, and K correspond to peak CI tephra influx, whereas the longer-lasting high values for Ti and Fe reflect higher atmospheric dust influx. The marked reduction in tree pollen percentages in the Tenaghi Philippon sequence is also considered to reflect adversely dry conditions. The CI occurs early in this dry phase, which dates it to the lower part of HE4. (*B*) Schematic representation of the position of the CI with respect to the MP to UP transition in six of the archaeological sequences investigated within the Response of Humans to Abrupt Environmental Transitions Project.

been recorded by, perhaps, 60 ka (41). Thus, modern humans clearly existed in North Africa well before the CI eruption, and no adverse effects on activities since that event can be detected.

By tracing the CI ash in cryptotephra form to new sites in Eastern Europe, our results provide an unambiguous datum that reveals how the timing of the arrival of AMH industries was spatially complex in Eastern Europe, with some sites recording Aurignacian type industries much earlier than others. Recent developments in radiocarbon and luminescence dating and the routine redating of important Paleolithic sites, such as Geissenklösterle, are also revealing that AMHs were present in parts of Europe significantly earlier than considered before (42). Our method, however, now shown in two continents, provides a fixed datum against which to corroborate and test these advances. We envisage a future where the debate about major transitions in human evolution can be based on the unambiguous alignment of the stratigraphical evidence within an isochronic lattice, such as can be provided by tephra layers. Tracing the CI, as we have done here, provides an index to this future.

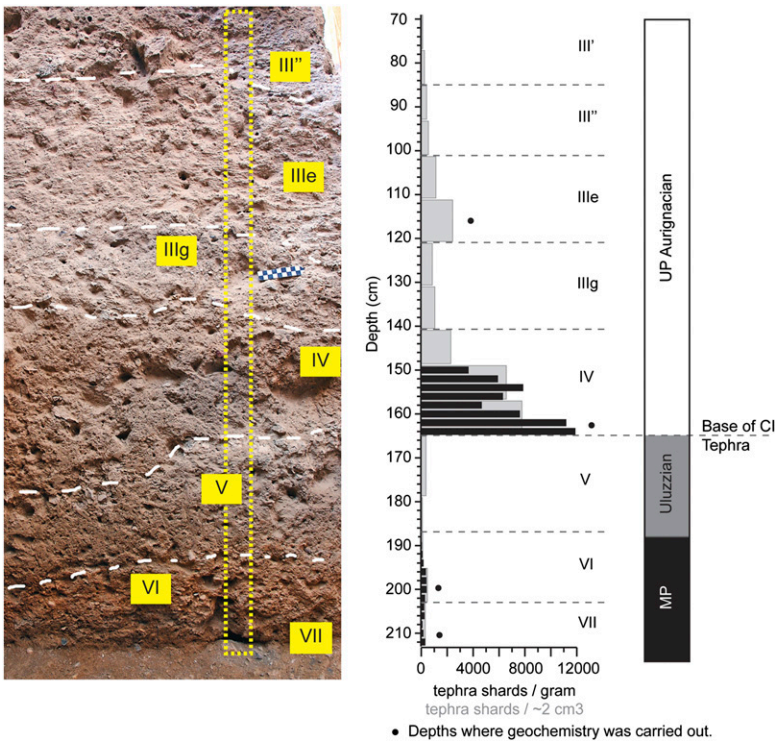

Fig. 5. The archaeological sequence in Klissoura Cave 1 in the Peloponnese of southern Greece preserves a long record of Paleolithic occupation, which is represented by Mousterian, early UP Uluzzian (layer V), Aurignacian (layers IV and III), and epipaleolithic industries (34). The dotted rectangle indicates one of the columns that was systematically investigated for tephra content, with results shown in *Right*. The CI occurs as a sharp peak at the interface of layers V and IV, which provides an important chronostratigraphic marker horizon for the Uluzzian and earliest Aurignacian levels at the site. Overlying this tephra peak, upward recirculation of CI shards through the sequence is a result of postdepositional anthropogenic and biogenic processes. A second concentration of tephra, chemically distinguished from the CI but not yet assigned to a specific source, has been identified in layer VI/VII.

Implications. The MP to UP transition began before the CI eruption in both North Africa and Europe, similar to AMH dispersal in the latter region, which implies that neither the eruption nor the HE4 cold/arid event could have been the primary driver of cultural changes and population dispersals or regional Neanderthal extinction in Northern and Eastern Europe over this period. These insights require reconsideration of the prevailing concept of straightforward, environmentally driven replacement, because both Neanderthals and early modern humans seem to have been more resilient to environmental crises than previously supposed. Although a recent assessment of Neanderthal mtDNA variation (43) indicates that Neanderthals in Eastern Europe showed overall population continuity until they became extinct, our results imply that such extinction is likely to have occurred long before the CI eruption.

With respect to the impacts on humans of the CI eruption, there must have been different outcomes in areas proximal or distal to the volcanic source. Proximal sites such as Serino, for example, located only ~50 km east of the Campi Flegrei would have felt the full impact, and it is, therefore, likely that populations here were devastated; the early Aurignacian at Serino is capped by a thick CI ash layer, with no evidence of subsequent site reoccupation. Most of our newly identified CI records, however, are from sites considerably more distal from Campania, where the effects are likely to have been less severe; here, we see no evidence of continental-scale, long-term impact on hominin species.

Our results indicate that Neanderthal extinction in Europe was not associated with the CI eruption. Furthermore, in view of the continuous records of human occupation over the MP to UP transition preserved at Klissoura, Kozarnika, Tabula Traiana, and Golema Pesht, we also question the posited scale of the impact of HE4 cooling on Neanderthal demise. AMHs also seem to have been widespread throughout much of Europe before the CI eruption; thus, Neanderthal and AMH population interactions must have occurred before 40 ka B.P. Given the spatially complex nature of the Neanderthal and AMH evidence listed here, there may have been considerable variability in the timing of such encounters across Eastern Europe and Italy. Our evidence indicates that, on a continental scale, modern humans were a greater competitive threat to indigenous populations than the largest known volcanic eruption in Europe, even if combined with the deleterious effects of climatic cooling. We propose that small population numbers and high mobility may have initially saved the Neanderthals but that they were ultimately outperformed in this capacity by AMHs.

Methods

To underpin our study, proximal CI stratigraphies were sampled for geochemical analysis, the results of which are based on unaltered juvenile clasts collected from both pyroclastic fall and flow deposits. At each site, multiple proximal samples were taken to (*i*) ensure spatial and temporal coverage and (*ii*) include any variations in vesicularity, phenocryst content, and/or color. To test for the possible presence of cryptotephra layers, which may be less than 1 mm in thickness, the full vertical interval represented at each archaeological or geologic site needed to be examined in its entirety. To test for the presence/absence of the CI tephra at archaeological cave sites, including possible cryptotephra, sediments were sampled during active excavations or from accessible standing stratigraphic sections that required minimal cleaning. Systematic sampling involved collection of small amounts (15–20 g) of in situ deposits at 2-cm consecutive and contiguous intervals along continuous vertical profiles. When possible, multiple section profiles at each site were sampled, and all samples were identified with reference to the site datum and other relevant provenience information. At each site, all sedimentary deposits dating between *ca.* 60 and 25 ka B.P. were sampled; therefore, if any tephra layers were identified, they could be directly and unambiguously associated to both other lithostratigraphic units at the site and recovered archaeological materials.

All archaeological, marine, and lake sediment sequences were investigated for the presence of cryptotephra using published protocols (44). Contiguous subsamples were analyzed, and the stratigraphic positions of cryptotephra layers were determined with a minimum depth resolution of ±1–2 cm. Details of sites referred to here, which were systematically examined for presence of CI and other tephra layers, are provided in Table S1.

Chemical characterization of single tephra shard samples was conducted in two stages using microanalytical techniques to measure the volcanic glass compositions in both proximal and distal samples (21, 45, 46). Major elements were analyzed using a Jeol JXA8600 electron probe microanalyzer with wavelength dispersive spectroscopy (EPMA-WDS) at the Research Laboratory

for Archeology and the History of Art, University of Oxford. An accelerating voltage of 15 kV, 6 nA beam current, and a 10-μm beam were used. The EPMA WDS was calibrated using a suite of mineral standards (47); 9–11 elements were measured in each sample with varying count times: (Na, 10 s; Si, Al, K, Ca, Fe, and Mg, 30 s; Ti, Mn, and Cl, 40 s; P, 60 s). Trace element analysis of the same grains was carried out using laser ablation inductively coupled plasma MS with an Agilent 7500ce inductively coupled plasma MS coupled to a 193-nm Resonetics M-50 ArF (193 nm) eximer laser ablation system with a two-volume ablation cell at the Department of Earth Sciences, Royal Holloway University of London (45, 48). Laser spot sizes of 57, 34, and 25 μm were used according to the sample area available for analysis. The repetition rate was 5 Hz, and both sample and gas blank count times were 40 s. Quantification used NIST612 with ^{29}Si as the internal standard and was corrected using ^{43}Ca (full details of analytical and data reduction methods are in refs. 20 and 45). Secondary glass standards (MPI-DING Suite) were analyzed between and within EPMA WDS and laser ablation inductively coupled plasma MS analytical runs to check instrumental precision and accuracy (21, 45, 47, 48). These data are reported with the other chemical data in Tables S2–S5.

ACKNOWLEDGMENTS. This research was funded by the United Kingdom Natural Environment Research Council through a Response of Humans to Abrupt Environmental Transitions (RESET) Consortium Grant awarded to four collaborating institutions: Royal Holloway University of London (Grant NE/E015905/1); Oxford University (Grant NE/E015670/1); Natural History Museum, London (Grant NE/E015913/1); and University of Southampton (Grant NE/E01531X/1). The research at Kozarnika was undertaken within the framework of an international cooperation between the Unité Mixte de Recherche 5199, Centre National de la Recherche Scientifique, De la Préhistoire à l'Actuel: Culture, Environnement et Anthropologie, Préhistoire, Paléoenvironnement, Patrimonie of Université Bordeaux 1 (J.-L.G.) and the National Institute of Archaeology of the Bulgarian Academy of Sciences (N.S.) under the financial support of the Advisory Committee of the Archaeological Researches Abroad (Mission Préhistorique Française en Bulgarie du Nord, MAEE, France), Centre National de la Recherche Scientifique, the Region Aquitaine, the Bulgarian Academy of Sciences, Université Bordeaux 1 (exceptional funding in 2004), the Max Planck Institute for Evolutionary Anthropology, Department of Human Evolution (2004), and the Stichting Horizon foundation; thanks are extended to all of these organizations. This publication is contribution no. RHOX/0016 of the Royal Holloway and Oxford Tephrochronology Research Network (RHOXTOR) research initiative (http://c14.arch.ox.ac.uk/rhoxtor/).

1. Gamble C, Davies W, Pettitt P, Richards M (2004) Climate change and evolving human diversity in Europe during the last glacial. *Philos Trans R Soc Lond B Biol Sci* 359: 243–253.
2. Stringer C (2006) *Neanderthals Revisited: New Approaches and Perspectives*, eds Harvati K, Harrison T (Springer, Heidelberg), pp 315–324.
3. Andersen KK, et al. (2004) High-resolution record of Northern Hemisphere climate extending into the last interglacial period. *Nature* 431:147–151.
4. Bar-Yosef O (2002) The Upper Paleolithic Revolution. *Annu Rev Anthropol* 31: 363–393.
5. Teyssandier N (2008) Revolution or evolution: The emergence of the upper paleolithic in Europe. *World Archaeol* 40:493–519.
6. Tzedakis PC, Hughen KA, Cacho I, Harvati K (2007) Placing late Neanderthals in a climatic context. *Nature* 449:206–208.
7. Müller UC, et al. (2011) The role of climate in the spread of modern humans into Europe. *Quat Sci Rev* 30:273–279.
8. Herrera KJ, Somarelli JA, Lowery RK, Herrera RJ (2009) To what extent did Neanderthals and modern humans interact? *Biol Rev Camb Philos Soc* 84:245–257.
9. Barberi F, et al. (1978) The campanian ignimbrite: A major prehistoric eruption in the Neapolitan area (Italy). *Bull Volcanol* 41:10–31.
10. Costa A, et al. (2012) Quantifying volcanic ash dispersal and impact of the campanian ignimbrite super-eruption. *Geophys Res Lett*, 10.1029/2012GL051605.
11. Golovanova LV, et al. (2010) Significance of ecological factors in the Middle to Upper Paleolithic Transition. *Curr Anthropol* 51:655–691.
12. Fedele FG, Giaccio B, Hajdas I (2008) Timescales and cultural process at 40,000 BP in the light of the Campanian Ignimbrite eruption, Western Eurasia. *J Hum Evol* 55: 834–857.
13. Roebroeks W (2008) Time for the Middle to Upper Paleolithic transition in Europe. *J Hum Evol* 55:918–926.
14. Blockley SPE, Ramsey CB, Higham TFG (2008) The Middle to Upper Paleolithic transition: Dating, stratigraphy, and isochronous markers. *J Hum Evol* 55:764–771.
15. Lowe D (2011) Tephrochronology and its application: A review. *Quat Geochronol* 6: 107–153.
16. de Vivo B, et al. (2001) New constraints on the pyroclastic eruptive history of the Campanian Volcanic Plain (Italy). *Contrib Mineral Petrol* 73:47–65.
17. Holliday VT, et al. (2007) Geoarchaeology of the Kostenki-Borschevo sites, Don River Valley, Russia. *Geoarchaeology* 22:181–228.
18. Hoffecker JF, et al. (2008) From the Bay of Naples to the River Don: The Campanian Ignimbrite eruption and the Middle to Upper Paleolithic transition in Eastern Europe. *J Hum Evol* 55:858–870.
19. Bourne A, et al. (2010) Tephrostratigraphical record of the last c. 105,000 years obtained from core PRAD 1-2 in the Central Adriatic Sea. *Quat Sci Rev* 29:3079–3094.
20. Fedele FG, Giaccio B, Isaia R, Orsi G (2003) *Volcanism and Earth's Atmosphere*, eds Robock A, Oppenheimer C (AGU Geophys, Washington, DC), pp 301–325.
21. Tomlinson E, et al. (2012) Geochemistry of the Phlegrean Fields (Italy) proximal sources for major Mediterranean tephras: Implications for the dispersal of Plinian and co-ignimbritic components of explosive eruptions. *Geochim Cosmochim Acta*, 10.1016/j.gcA.2012.05.043.
22. Rohling EJ, Mayewski P, Challenor P (2003) On the timing and mechanism of millennial-scale climatic variability during the last glacial cycle. *Clim Dyn* 20:257–267.
23. Rohling EJ, Mayewski P, Abu-Zied R, Casford J, Hayes A (2002) Holocene atmosphere-ocean interactions: Records from Greenland and the Aegean Sea. *Clim Dyn* 18:587–593.
24. Giaccio B, et al. (2006) *When Neanderthals and Modern Humans Met*, ed Conard NJ (Kerns Verlag, Tübingen, Germany), pp 343–375.
25. Bar-Yosef O, Zilhão J, eds (2002) Towards a definition of the Aurignacian. *Proceedings of Symposium Held in Lisbon, Portugal, June 25–30, 2002* (Instituto Português de Arqueologia, Lisbon Portugal).
26. Szmidt CC, Normand C, Burr G, Hodgins G, LaMotta S (2010) AMS ^{14}C dating the Protoaurignacian/early Aurignacian of Isturitz, France. Implications for Neanderthal-modern human interaction and the timing of technical and cultural innovations in Europe. *J Archaeol Sci* 37:758–768.
27. Zilhão J, et al. (2007) *Rethinking the Human Revolution: New Behavioural and Biological Perspectives on the Origin and Dispersal of Modern Humans*, eds Mellars P, Boyle K, Bar-Yosef O, Stringer C (McDonald Institute Archaeological Research Monographs, Cambridge, UK), pp 249–262.
28. Higham T, Ramsey CB, Karavanić I, Smith FH, Trinkaus E (2006) Revised direct radiocarbon dating of the Vindija G1 Upper Paleolithic Neandertals. *Proc Natl Acad Sci USA* 103:553–557.
29. Crevecoeur I, et al. (2010) The Spy VI child: A newly discovered Neandertal infant. *J Hum Evol* 59:641–656.
30. Mussi M (2001) *Earliest Italy: An Overview of the Italian Paleolithic and Mesolithic* (Plenum, New York).
31. Benazzi S, et al. (2011) Early dispersal of modern humans in Europe and implications for Neanderthal behaviour. *Nature* 479:525–528.
32. Morley MW, Woodward JC (2011) The Campanian Ignimbrite (Y5) tephra at Crvena Stijena Rockshelter, Montenegro. *Quat Res* 75:683–696.
33. Douka K, Perlès C, Valladas H, Vanhaeren M, Hedges REM (2011) Franchthi Cave revisited: The age of the Aurignacian in south-eastern Europe. *Antiquity* 85:1131–1150.
34. Stiner MC, Kozlowski JK, Kuhn SL, Karkanas P, Koumouzelis M (2010) Klissoura Cave 1 and the Upper Paleolithic of southern Greece in cultural and ecological context. *Eurasian Prehist* 7:309–321.
35. Sirakov N, et al. (2007) Nouveau faciès lamellaire du début de Paléolithique supérieur dans les Balkans. *Revue d'Archéologie Préhistorique, PALÉO* 19:131–144.
36. Shalamanov-Korobar L (2008) *The Palaeolithic of the Balkans*, eds Darlas A, Mihailović D (BAR International Series 1819, Oxford), pp 85–92.
37. Sinitsyn AA, Hoffecker JF (2006) Radiocarbon dating and chronology of the Early Upper Paleolithic at Kostenki. *Quat Int* 152-153:164–174.
38. Barker G, et al. (2010) The Cyrenaican Prehistory Project 2010: The fourth season of investigations of the Haua Fteah cave and its landscape, and further results from the 2007–2009 fieldwork. *Libyan Studies* 41:63–88.
39. McBurney CBM (1967) *The Haua Fteah in Cyrenaica* (Cambridge Univ Press, Cambridge, UK).
40. Hublin J-J, McPherron SP, eds (2012) *Modern Origins: A North African Perspective* (Springer, Berlin).
41. Vermeersch PM (2010) *South-Eastern Mediterranean Peoples Between 130,000 and 10,000 Years Ago*, ed Garcea EAA (Oxbow Books, Oxford), pp 66–88.
42. Higham T, et al. (2012) Testing models for the beginnings of the Aurignacian and the advent of figurative art and music: The radiocarbon chronology of Geißenklösterle. *J Hum Evol* 62:664–676.
43. Dalén L, et al. (2012) Partial genetic turnover in Neandertals: Continuity in the east and population replacement in the west. *Mol Biol Evol*, 10.1093/molbev/mss074.
44. Blockley SPE, et al. (2005) A new and less destructive laboratory procedure for the physical separation of distal glass tephra shards from sediments. *Quat Sci Rev* 24: 1952–1960.
45. Tomlinson EL, Thordarson T, Müller W, Thirlwall MF, Menzies MA (2010) Microanalysis of tephra by LA-ICP-MS—strategies, advantages and limitations assessed using the Thorsmörk Ignimbrite (Southern Iceland). *Chem Geol* 279:73–89.
46. Smith VC, Isaia R, Pearce NJG (2011) Tephrostratigraphy and glass compositions of post-15 kyr Campi Flegrei eruptions: Implications for eruption history and chronostratigraphic markers. *Quat Sci Rev* 30:3638–3660.
47. Jochum KP, et al. (2006) MPI-DING reference glasses for in situ microanalysis: New reference values for element concentrations and isotope ratios. *Geochem Geophys Geosyst*, 7:Q02008, 44 pp.
48. Müller W, Shelley M, Miller P, Broude S (2009) Initial performance metrics of a new custom designed ArF eximer LA-ICP-MS system coupled to a two-volume laser ablation cell. *J Anal At Spectrom* 24:209–214.